FORSCHUNGSZENTRUM JÜLICH GmbH KFA

Volcanic Tremor and Magma Flow

edited by

R. Schick and R. Mugiono

Scientific Series of the International Bureau Volume 4

Forschungszentrum Jülich GmbH
Scientific Series of the International Bureau

VOLCANIC TREMOR AND MAGMA FLOW

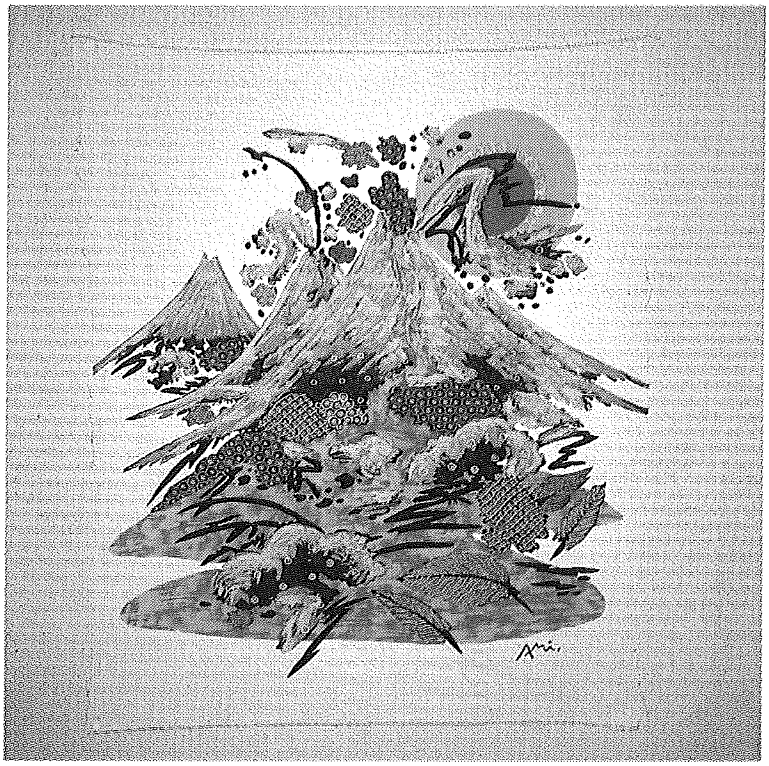

edited by
R. Schick and R. Mugiono

with Contributions by
W. Brüstle, T. Dahm, D. Emter, A. Fadeli, M. Hellweg, S.B. Kirbani, E. Meier, G. Meinhardt, J. Neuberg, P. Rydelek, R. Schick, D. Seidl, J. Strigl, P.S. Wayudi, W. Zürn

German-Indonesian-Cooperation
in Scientific Research and Technological Development

The title page shows 'Gunung Merapi and its Interior', in the original a batik painting by Yogakarta artist Ami. The reproduction on the back cover 'Molten Rock inside Gunung Merapi' was painted in the batik by Eri, sister of Ami. There is a striking similarity in this painting to turbulent flow patterns of fluids with high viscosity.

Herausgeber und Vertrieb: Forschungszentrum Jülich GmbH
ZENTRALBIBLIOTHEK
Postfach 1913 · D-5170 Jülich
Telefon (02461) 61-5368 · Telefax (02461) 61-6103

Druck: D. Gehler, Graphische Kunstanstalt Düren

Scientific Series of the International Bureau, Volume 4

ISSN 0938-7676

ISBN 3-89336-058-1

Preface.

The Government of the Federal Republic of Germany has signed a series of agreements on bilateral cooperation in scientific research and technological development with a considerable number of countries around the world. Among these are Third World countries in the developing stage or on the threshold of industrialization. The general goals of the national German research and technology policy are also applicable to these governmental agreements. Bilateral cooperation is aimed at to contribute to the broadening of scientific knowledge, to safeguard natural resources and the environment, and to improve the living and working conditions of the population through an increase of the economic strength and of the competitiveness on the international markets. Through the strengthening of the scientific-technological infrastructure as a prerequisite for industrialization, through the joint implementation of projects, and through the exchange of scientists and engineers a contribution to solve the most urgent problems in the partner countries can be achieved, helping thus to narrow the technological gap existing between the developed and the developing world.

On March 20, 1979, a governmental agreement on cooperation in scientific research and technological development with the Republic of Indonesia was signed. On the German side, the responsible Federal Ministry for Research and Technology has entrusted the Forschungszentrum Jülich through its International Bureau with the organisation and coordination of this cooperation. Funds are put at the disposal of the International Bureau to at least partially help financing these bilateral efforts. Among the manifold contacts established in the past decade to strengthen the bilateral links between the Republic of Indonesia and the Federal Republic of Germany the partnership between the Laboratory of Geophysics, Physics Department, Faculty of Mathematics and Natural Sciences, Gadjah Mada University, Yogyakarta and the Institute of Geophysics, University of Stuttgart play an outstanding role. The scientific results of 10 years of fruitful cooperation investigating the volcanological activities of Mount Merapi in Central Java are documented in the presented book and compared with Mount Etna in Sicily, another major volcano in the world. The expectation on both sides is great that these results go beyond the mere scientific merits and will also yield ways and means to work out methods of predicting the volcano's activities for the benefit and safety of the numerous population living nearby.

Bilateral cooperation has sometimes to surmount difficulties which do not necessarily occur on the national level. These difficulties have to do with the cultural and ethnic differences into which the partners are embedded, with administrative and infrastructural mismatching, and last but not least with distances making communication tedious and time consuming. These difficulties have to be compensated by the personal engagement of the scientists involved and an understanding and acceptance of the other's cultural background. Thanks are due to the two project leaders, Prof. R. Mugiono and Prof. R. Schick, whose scientific qualification and reputation is out of question and who have proven that these difficulties can be overcome, also by mutual esteem and comprehension. Their ability to motivate the rising generation of young Indonesian scientists to engage in these investigations and their willingness to adjust to the idiosyncracies of each other's culture have been instrumental in making this cooperation a success. This success confirms the political concept of bilateral cooperation and justifies the expenditures incurred over the past years and covered from various sources. Thanks are also due to all those that have contributed financially to these efforts.

This preface would not be complete without the sincere expression of hope that the personal, political and economic preconditions of the past may prevail on both sides into the future, allowing thus to continue what has proven to be an outstanding success.

D. Nentwich
Head
International Bureau
Forschungszentrum Jülich

Contents

Introduction.

'I forgot to say that the noise made by the bubbling lava is not great, heard as we heard it from our lofty perch. It makes three distinct sounds-a rushing, a hissing, and a coughing or puffing sound, and if you stand on the brink and close your eyes it is no trick at all to imagine that you are sweeping down a river on a large low-pressure steamer, and that you hear the hissing of the steam about her boilers, the puffing from her escape pipes and the churning rush of water abaft her wheels' (Mark Twain: Roughing it, Am. Publ. Corp., 1879).

Earthquakes and volcanic action have always been linked together in the consciousness of mankind. Until the end of the 19th century, the great majority of Earth scientists ('the plutonists') supported the opinion that all earthquakes are of volcanic origin. Indeed, it was the simultaneous occurrence of volcanoes and earthquakes in Italy which led to the founding there of modern seismology. The first seismograph station of modern design was established at Vesuvius in the year 1855. It was constructed by Palmieri, who gained the further distinction of becoming the first director of a university institute for the physics of the Earth in Naples. After 1860, he made the earliest attempt at correlating the eruptive activity at Vesuvius with instrumentally observed ground vibrations, finding seismic signals which systematically preceded volcanic eruptions.

It was Hoernes, an Austrian geologist, who around 1885 introduced the classification of earthquakes as rock-fall earthquakes, volcanic earthquakes and tectonic or dislocation earthquakes. He realized the importance of dislocation earthquakes and their correlation with tectonic processes in the earth, but his ideas were initially heavily attacked by the plutonists. The San Francisco earthquake of 1906 gave the tectonists the final clear and incontrovertible evidence: earthquakes are fracture processes of non-volcanic origin. A new epoch in seismology started, and the close relationship between volcanology and seismology ended.

The newly opened quantitative fields of earthquake investigation attracted the attention of most seismologists. Few Earth scientists read the now classical paper by the Japanese seismologist Omori, who in 1911 described long-lasting and non-impulsive seismic wave trains associated with eruptive activity at volcanoes in Japan. Omori named these vibrations 'volcanic tremor'. It was the same kind of ground motion which, for instance, was continously felt in Jakarta during the great paroxysm of Krakatau in 1883.

It was not only the new understanding of earthquake mechanisms which caused seismologists to abandon the study of volcanic earthquakes. Impulsive and clearly separable wave groups are discernible in seismograms of non-volcanic origin, which may be interpreted in terms illuminating the structure and composition of the Earth. By contrast, the apparently stochastic seismic signals which constitute volcanic tremor may be misrepresented as volcanic noise, and some textbooks actually include discussion of this subject along with ground noise of the human and meteorological variety. Less than 50 papers were published on volcanic tremor between 1911 and 1970, a tiny fraction of the number of papers written on earthquake sources and seismic wave propagation. Only in recent years has the sheltered status of volcano seismology changed. The observation of volcanic tremor and related signals at Volcanoes like Etna, Stromboli, St. Helens, Redoubt, Izu-Oshima, Nevado del Ruiz and Merapi, has demonstrated that volcanic tremor cannot be dismissed as 'simply coloured Gaussian noise', but carries, within its structure and temporal variation, important and unique information on the internal dynamics and mechanism of a volcano.

Most scientists nowadays see the origin of volcanic tremor in the unsteady flow of magma and gas in the interior of the volcano. Thus the study of volcanic tremor has become a branch of flow acoustics. With this conceptual development in tremor investigation, the conclusions which can be drawn on the internal dynamics of a volcano, and perhaps more importantly, on the assessment of volcanic risk, are weakened by enormous difficulties. It is often hard just to distinguish seismogram traces arising from fluid motion from those caused by pressure release in the solid part of the volcano. Volcanic tremor is only a collective name for numerous kinds of seismic signals generated by volcanic activity. With some sorts of transient signals, as for instance observed at Merapi, doubt still remains whether such wave groups (B-type volcanic earthquakes in Minakame's classification), are actually caused by fluid pressure instabilities. It is impossible to rule out explanations in terms of crack mechanisms in the solid part of the volcano (e.g. shear failure with low fracture velocity, tensional fractures associated with the opening of fissures and magma intrusion, or, for Merapi, gravitational sliding of the magma dome).

Clearly, seismology alone is insufficient to understand volcanic tremor. Fluid sources are mechanically different from the brittle fractures of earthquakes, and accordingly have to be studied with specific methods, which, in particular, treat the fluid dynamic instabilities that seem to play a key role in the origin of volcanic eruptions. The shallow understanding of volcanic tremor is partly attributable to the overwhelming influence of earthquake seismology in providing recording and interpretation techniques unsuitable for volcanic tremor investigations. The cooperation of physicists and engineers, working experimentally and theoretically in the field of vibration analysis and two-phase flow, is needed to establish a proper framework of scientific knowledge, which will help in understanding the cause of volcanic eruptions, and in estimating volcanic risk for countries like Indonesia, where dangerous volcanic terrain is home to more and more citizens of an increasing population.

This book contains 12 articles on volcanic tremor: possible mechanisms of origin, resonance effects and source dimensions, source locations, temporal variations of occurrence, correlations with eruptive activity, wave characteristics, investigations into nonlinear processes, recordings of 'activity parameters', and the design of tiltmeters which may supplement seismometers. The data comes from volcanological investigations at Merapi in Central Java (Indonesia) and Etna in Sicily (Italy). These two volcanoes have opposite petrology, and happen also to have contrasting tectonic settings: Merapi, in the Indonesian island arc, is situated in a typical subduction zone, while Etna, in Eastern Sicily, seems to be controlled by a fissure system of strike slip and normal faulting. This affords an interesting comparative study of the origin and nature of tremor.

The book is a result of a bilateral cooperation project in physical volcanology between the Republic of Indonesia and the Federal Republic of Germany. We owe special thanks to D. Nentwich from the Kernforschungsanlage Jülich (now Forschungszentrum Jülich) who encouraged us to start the cooperation nearly ten years ago, and who helped in many aspects of the organization. We acknowledge assistance from our respective universities, the Gadjah-Mada-University, Yogyakarta, and the University of Stuttgart. Financial support came from the Forschungszentrum Jülich, the Badan Pengkajian dan Penerapan (B.P.P.T.) and Lembaga Ilmu Pengetahuan Indonesia (L.I.P.I.), Jakarta, and the Deutsche Forschungsgemeinschaft (D.F.G.), Bonn. The data from Mt. Etna kindly were made available by the Istituto di Scienze della Terra, Catania, and we would like to thank M. Cosentino, G. Lombardo and G. Patané for their support.

We are convinced that the articles in this book will encourage future cooperative work.

Stuttgart and Yogyakarta, December 1990 *R. Schick* *R. Mugiono*

Signal characteristics of volcanic tremor during change from low to high activity

Wolfgang Brüstle

Institut für Geophysik, Rich.-Wagner-Str. 44, D-7000 Stuttgart-1
F.R. Germany

Abstract

The short period seismic record with energy mainly between 1 and 4 Hz just before and after the onset of an Etna, 1977 eruption is investigated. Evolution of amplitude and frequency characteristics of volcanic tremor is followed by calculating power spectra, amplitude probabilities, phase portraits, instantaneous frequencies and phasor walks. This is done first for the original seismogram data and then again for narrow-band filtered traces representing single resonators in the source. It appears that even more than the high-frequency original seismogram, its envelope with spectral content below 0.2 Hz can reveal the source dynamics causing volcanic tremor.

In the pre-eruption period, a significant cross-correlation between single resonators as well as a moderately high fractal dimension of about 8 is found. During the eruption, tremor amplitudes have increased by a factor 10, contribution of the individual resonators to the spectrum is completely changed and no longer correlated. Fractal dimension has become undeterminably high.

In contrast to earlier hypotheses, this example shows a considerable degree of interrelation and self-organization within the volcano source before, and unorganized, highly chaotic appearence during the eruption. This is in accordance with higher magma flow velocities and a higher degree of turbulence during the eruption.

1 Introduction

Analysis of volcanic tremor records is faced with the problem of instationarity. Usual time series analysis and statistics of transient data is based on stationarity, and thus requires invariance of amplitude probability density and of auto-correlation function for infinite time. Dealing with real world data, we can redefine stationarity as a stationarity of limited degree (weak stationarity, i.e. stationarity of order q, if the first q statistical moments, i.e. linear mean, variance, skew, kurtosis etc. are invariant) and as a stationarity of limited time duration (quasi-stationarity). Tremor data inevitably have to be termed instationary, if the order q is chosen higher than about 3 and also, if the time interval, in which stationarity is tested, is too small (compared to an average period of the tremor amplitude variation) or too long (compared to the total duration of a tremor storm, for example). In between there may well be time spans where quasi-stationarity can be assumed. In fact, tremor records may reveal quasi-stationarity over hours and even days displaying stable conditions of their internal magma source system. To learn more about the changes of magma flow dynamics, however, tremor records shortly before, during and after periods of transient and instationary character have to be studied.

A single one-component tremor record of Etna, December 1977, containing a so-called 'tremor storm' was selected for an exemplary study. I will focus on quasi-stationary time spans immediately before and after a truly instationary transition from low to high tremor amplitudes accompanying the onset of an eruption. In comparison of these two time spans, we hope to draw conclusions concerning the change of physical state in the volcano source. Is there a critical parameter indicative of the transition from low-amplitude tremor before and high-amplitude tremor during an eruption?

2 Basic data

Quoting the Smithsonian Bulletin, there was a sequence of eruptions on Etna, NE-crater cone starting November, 2 1977 lasting until January, 4 1978. On several days within this time, lava flowed a few kilometers down the E-flank of Etna, tephra was ejected hundreds of meters above the vent, and small earthquakes were felt in nearby villages. One of these eruption events took place on December 29, 1977 lasting from about 9:00 hrs to about 15:00 hrs local time (seismically seen as a tremor-storm, Fig. 1).

Seismogram data were recorded on magnetic tape from a velocity-type vertical-component 1-Hz-seismometer at the site Monte Vetore (MVT, see Cosentino et al., 1989) on Etna S-flank at a crater distance of 6.5 km. For the present study, data were played back, low-pass filtered with a cut-off at 5 Hz and sampled with a rate of 12.5 Hz. Run tests (see for instance Bendat and Piersol, 1971) on short (3 min), medium (10 min) and long term (30 min) values of linear mean and variance of data amplitudes were performed in order to detect underlying very-long-period trends of non-volcanic origin. No such trends were found in segments 1, 2 and 3 prior to the eruption (in the following called 'low-amplitude section') and in the segments 6, 7 and 8 ('high-amplitude section') just after the transition to high activity. On the basis of stable means, variances and auto-correlation functions, these two time spans are now termed 'quasi-stationary' and investigated in more detail with standard and advanced signal analysis procedures. The transition segments 4 and 5, where amplitudes increase by about a factor of 10, are instationary.

Fig. 1, upper part, shows the seismogram data assembled in continuous segments of 30 minutes length each. Peak-to-peak amplitude is about $100 \mu m/s$ ground velocity at its maximum. This 8-hour-record is mapped in frequency domain (Fig. 1, bottom) in an attempt to visualize consistency of spectral features. The map shows power spectral values based on a grid of 100 frequencies and 80 epochs. Power spectra calculation is done as below for Fig. 2, but using sliding time segments.

In the following, the first part of this record will be examined in closer detail. The total linear mean is removed first. Then power spectra for successive non-overlapping segments 1 to 8 are calculated, each time averaging over 86 subsegments with 50 % overlap using a Welch window. Frequency resolution is 0.02 Hz and reliability is characterized by a standard deviation of

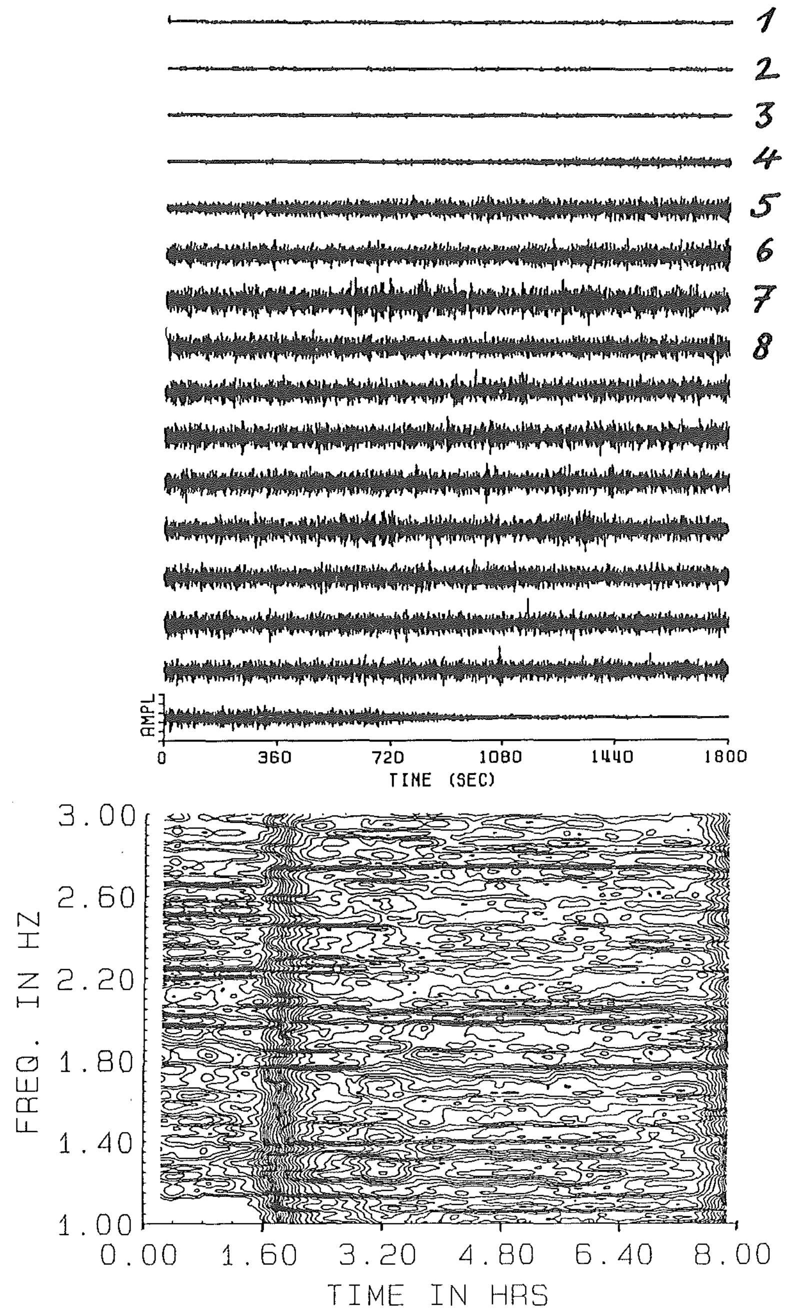

Figure 1: Top: Etna, 1977 tremor record plotted in continuous 30-minute segments, amplitude is 100 $\mu m/s$ for full scale as indicated for the last segment, segments 1 to 8 are investigated later in closer detail. Bottom: Logarithmic power spectral density map in the dominant seismogram spectral band of 1 to 3 Hz.

about 10 % of the spectral values. Power spectral density is normalized such, that the total power obtained by integrating from 0 to Nyquist frequency (6.25 Hz) equals the data variance. Spectra (Fig. 2) are fairly stable in the low-amplitude section segments 1 to 3 and again in the high-amplitude section segments 6 to 8. Spectra 4 and 5 show the transition, but as there is no stationarity, they cannot be regarded significant. Here the trade-off conflict between confidence of spectral estimation and quasi-stationarity in shorter time segments can not be settled. Possibly a Maximum-Entropy spectral analysis (*MESA*) with spectral reliability even from short time segments (e.g. Seidl, et al. 1990) could give more insight.

As already seen in the map of Fig. 1 at the bottom, there are several significant spectral peaks, persistent throughout all segments, differing however in relative strength. In the low-amplitude section, most prominent is a very narrow spectral peak at 2.225 Hz (in the following termed: 'peak a') with a half bandwidth of only 0.025 Hz (formally corresponding to a resonator quality factor of 90, see below). In the high-amplitude section the strongest peak is situated at about 1.25 Hz ('peak e').

Standard signal analysis is performed for the low-amplitude segments 1 to 3 (Fig. 3) and for the high-amplitude segments 6 to 8 (Fig. 4), each time in panels on the left for the basic seismogram data and in panels on the right for the seismogram envelope (see below). From top to bottom, Fig. 3 and Fig. 4 display first the data (again successive time intervals row after row) and second their auto-correlation function (both exemplarily only for segment 2 and segment 7, respectively, as the adjacent segments look very similar). Third is power spectrum and fourth amplitude probability density, each for the total of segments 1 until 3 and segments 6 until 8, respectively. Auto-correlation functions are calculated from 30 minutes data, and plotted in a significant time window symmetrically with lag zero in the middle of it. Power spectral calculation resembles that of Fig. 2, but now averaging over 90 minutes of data. Frequency of occurence of data amplitudes are counted in histograms of 30 and 25 equidistant classes in between the extremal values and normalized to the total number of data. Standard one- and two-

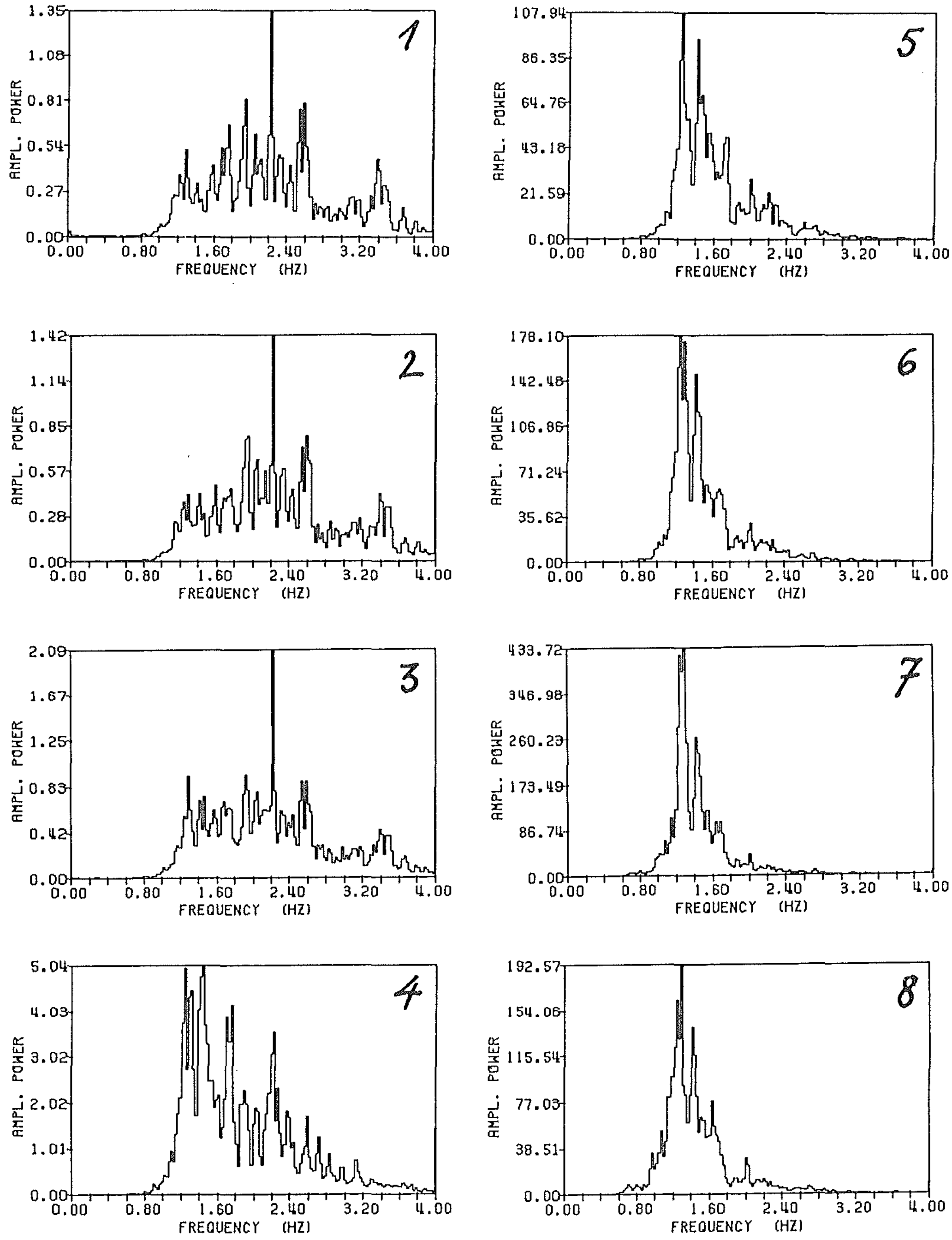

Figure 2: Sequence of power spectra for segments 1 to 8, scales are linear, plotted is power density in $\mu m^2/s$. Quasi-stationarity is given in the low-amplitude segments 1, 2, 3 and in the high-amplitude segments 6, 7, 8.

parameter probability density functions were probed to fit these histograms.

3 Envelope

The envelope is non-linearly related to the seismogram from which it is derived. Basically it is therefore a new data series in a lower frequency band, however completely different from the low-frequency seismic energy. As the envelope should reflect the overall shape of the tremor seismogram without minor wiggles, an appropriate low-passed version is taken.

I have considered three off-line methods for calculating the seismogram envelope:
a. as an 'instantaneous amplitude' of the seismogram (Farnbach, 1975), calculated for instance using the Hilbert transform (Liu and Kosloff, 1981);
b. connecting consecutive local maximum or minimum values of the seismogram, respectively;
c. removing the linear mean, then rectifying to the positive or negative side and low-pass filtering the seismogram.

Testing the three methods with various algorithms, they lead to completely coinciding results for envelope frequencies below about 0.5 Hz. Low-pass filtering is warranted in any case, as high-frequency small local extrema in the seismogram are undesired in the envelope. After some trials I decided to regard the one-sided (positive) envelope low-passed through a second order (12 db/octave) non-phase-shifting Butterworth filter with 0.2 Hz corner frequency to be the envelope further investigated. (Envelopes are plotted two-sided though to enhance clearness). Due to the lower frequency content, envelope data are decimated down to 3.125 Hz sampling, and due to the filter, amplitudes are diminished to about half of the original.

Comparing Fig. 3 and Fig. 4 for differences between seismogram and envelope data, as well as for differences between low- and high-amplitude sections, we notice:
Seismogram auto-correlation main lobe (lag zero) and side lobes reflect the prevailing spectral peak ('peak a' in segments 1, 2, 3 and 'peak e' in seg-

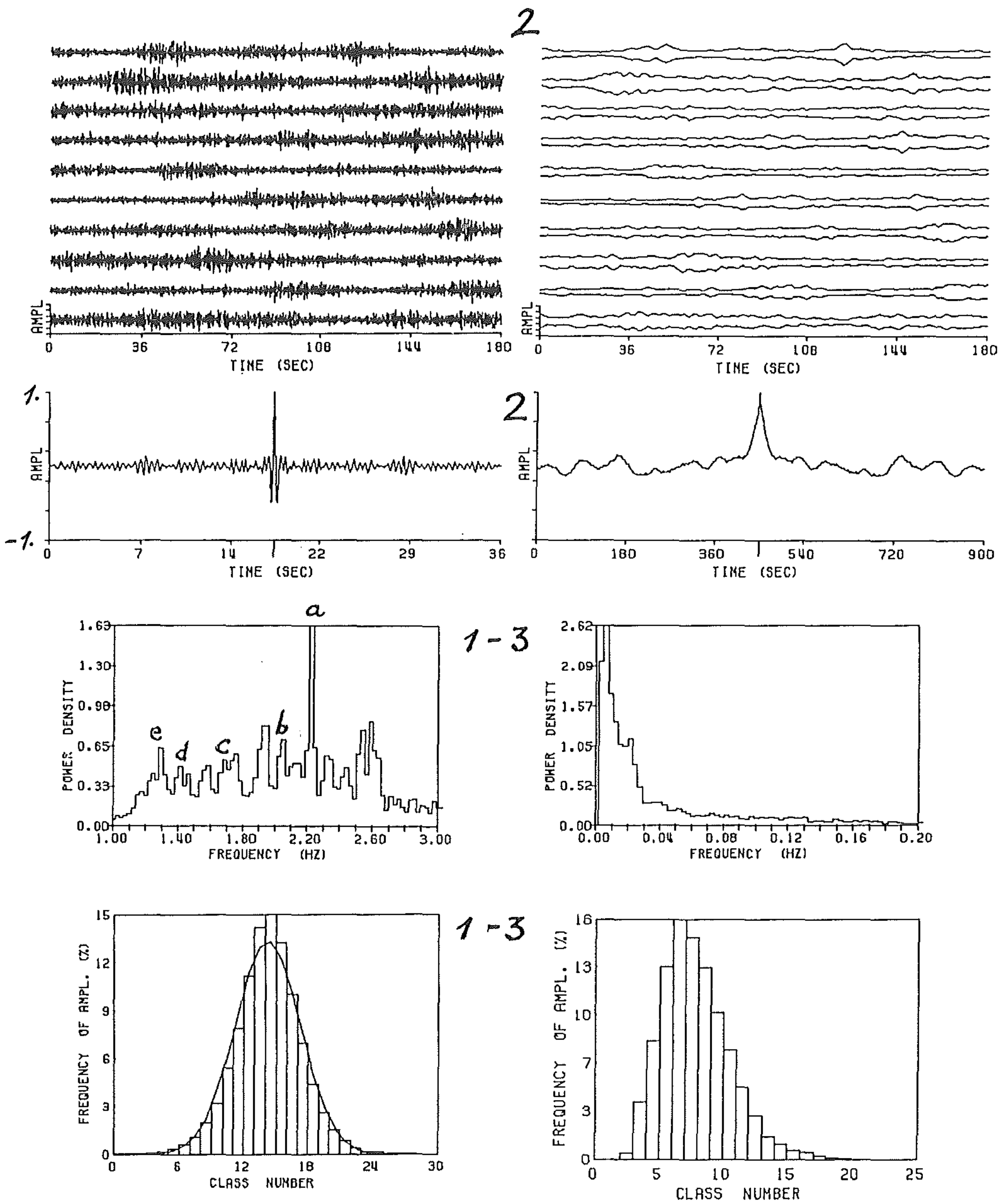

Figure 3: Low-amplitude section: Segments 1 until 3, or exemplary segment 2, as denoted. Left: Seismogram (full scale 10 $\mu m/s$). Right: Envelope. Top: Data. Second: Auto-correlation (lag zero in the middle). Third: Power spectrum ($\mu m^2/s$), peaks at the left are denoted 'a' to 'e'. Bottom: Amplitude probability (in %, classes span the data range).

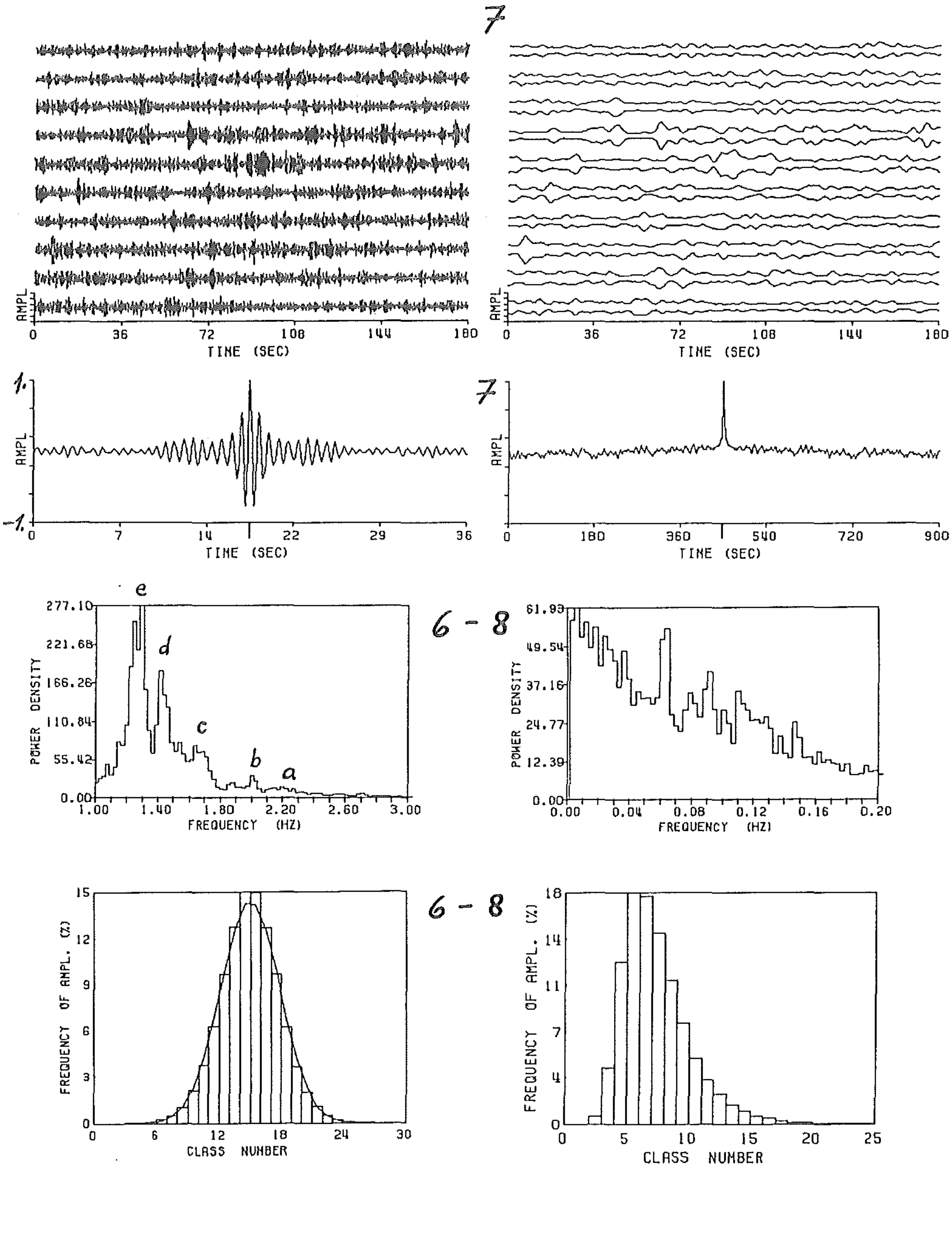

Figure 4: High-amplitude section: Segments 6 until 8 or exemplary segment 7, as denoted. As Fig. 3, but seismogram is 100 $\mu m/s$ for full scale.

ments 6, 7, 8). Envelope auto-correlation functions have an effective main-lobe width of 45 s and 15 s, respectively, corresponding to (less significant) peaks in the spectra. This is interpreted as a longer temporal coherence in the low-amplitude than in the high-amplitude section.

Envelope power spectra are generally of a shape proportional to the inverse of frequency. Besides some minor peaks, the spectra tend to culminate at zero frequency due to the envelope offset. As the linear mean is removed (in case of the envelope, this is done only for spectral calculation), leakage contaminates a few bins adjacent to frequency zero. Envelope spectra have resolution 0.003 Hz and standard deviation 20 %.

Amplitude probabilities for the seismogram itself resemble normal distributions throughout. The chi-squared test, however, discards a normal distribution on high significance level: kurtosis, and for segment 1 to 3 also skew, of the data distributions are significantly non-zero. Perfect normal distributions would have to be expected for completely stochastic data. On the other hand, normal distributions are very likely anyway, as by linear transformations any kind of distribution tends to become Gaussian.

The amplitude distribution for the envelope (amplitudes zero to maximum) resembles probability density functions of Weibull (see Schmidt and Tondl, 1986, chapter 10, 11), in particular also of Rayleigh type. (The envelopes of normal-distributed bandpassed random series are Rayleigh distributed). So far, no one- or two-parameter function, however, fitted the data sufficiently well to draw conclusions.

4 Chaos analysis

I try to describe the chaotic behaviour of the tremor by analyzing a single-variable time series, using the Grassberger and Procaccia, 1963 algorithm for estimation of the correlation dimension. Calculations of Strigl, 1991 (this volume) have shown for various examples, that if there is a strange attractor underlying tremor seismograms, it is certainly of very high dimension and thus not determinable for the time being. Analyzing low- and high-amplitude section of the present Etna record with series consisting of 20000 points, I arrived at the same conclusion. As I believe that envelope data characterize a new and even more basic dynamical system in the volcano, the envelope is probed within the fractal scheme instead of the seismogram itself.

We start from the data series x_i, with indices i running from 1 to n, equidistantly sampled at intervalls Δt. Then choosing an embedding dimension m, the trajectory in m dimensions is given by the vectors $\vec{x_i}$:

$$\vec{x_i} = (x_i,\ x_{i+\tau},\ x_{i+2\tau},\ \ldots,\ x_{i+(m-1)\tau})$$

with indices of $\vec{x_i}$ from $i = 1$ to $n - (m-1)\tau$. Now let p be the number of pairs $\vec{x_i}$, $\vec{x_j}$ with distances (maximum norm) smaller than a radius r. Self-pairs $(i - i)$, and near neighbours $(|i - j| \leq 4)$, are not counted. If for sufficiently large m, the graph of $log(p)$ versus $log(r)$ still exhibits a (nearly) constant slope over a sufficiently large range of $log(r)$, and if then for further increase of m, the slope does not change any more (saturation), this slope equals the correlation dimension d and is thus one particular measure of fractal dimension. There are many recommendations, restrictions and potential pitfalls connected with the Grassberger-Procaccia algorithm, which cannot be discussed here. I rather refer to Strigl, 1991 (this volume) and the literature quoted there.

Just two very important points need to be commented on. First it is the proper choice of the delay index τ. The issue of choosing $\tau \geq 2$ is to avoid strong linear relation between components of $\vec{x_i}$. In case of oversampling, too small τ can possibly feign a (too low) d. Too large τ can lead to overestimation or failure to detect d, as the relation of components of $\vec{x_i}$ tends to become random. In between there is a stable τ-intervall. Recipes for selecting a proper τ are for example: 'Determine τ according to a quarter of the dominant period for quasi-periodic data', or in other cases: 'Determine τ according to the half-width of the auto-correlation main lobe'. Analyzing the envelope data ($\Delta t = 0.32s$), I determine τ equal 3 to 4 as a lower bound for suitable τ-values from the smallest visible period in the data, and τ equal 25 to 70 as an upper bound from the auto-correlation functions, see

Fig. 3 and Fig. 4 respectively.

Second, as the number of data n for one run is concerned, I have taken all 17000 envelope points of the total section 1-3 and again of the total section 6-8. My opinion is, that d as the slope of a regression line can significantly be determined from data $log(p(r))$, which span at least half a unit of $log(r)$. This puts the highest correlation dimension d possibly determinable in the present case to about 15 (Ruelle, 1990), and the embedding dimension m to be tested for such d up to a maximum of about 40.

It was tried to map strange attractors in various ways of graphing the trajectories. Even though one cannot hope to see high-dimensional attractors in projections of their phase space onto two or three dimensions, I do plot some two-dimensional phase portraits. Each subfigure in Fig. 5 contains 1000 data points x_i, in the top part taken from the envelope in the low-amplitude section (segment 2), in the middle from the envelope in the high-amplitude section (segment 7), and at the bottom, for comparison, from random envelope data. To produce the latter, I take normal-distributed random numbers of asserted stationarity, remove the linear mean and shape their spectrum by band-passing between 1 and 3 Hz to get a random tremor seismogram. This seismogram is then rectified and 0.2-Hz-low-pass filtered in the same procedure as before to get a simulated random envelope.

On the right side of Fig. 5, subfigures show phase portraits $\dot{x}_i$ versus x_i, where $\dot{x}_i$ is simply calculated as the first-order central difference $(x_{i+1} - x_{i-1})/2\Delta t$. On the left side of Fig. 5, subfigures are quasi-phase-portraits $x_{i+\tau}$ versus x_i with $\tau = 4$, the data taken from the same time intervals as on the right side.

We can see, that the portraits taken out of segment 2 are considerably more structured than those of segment 7, which resemble the result for random numbers. Increasing the number of points up to 17000 and trials with τ from 2 to 64, do not change this picture. True Poincaré maps could not be obtained, since obviously there is no prevailing frequency in the envelope and no forcing frequency known a priori. Attractors cannot be seen, which was to be expected.

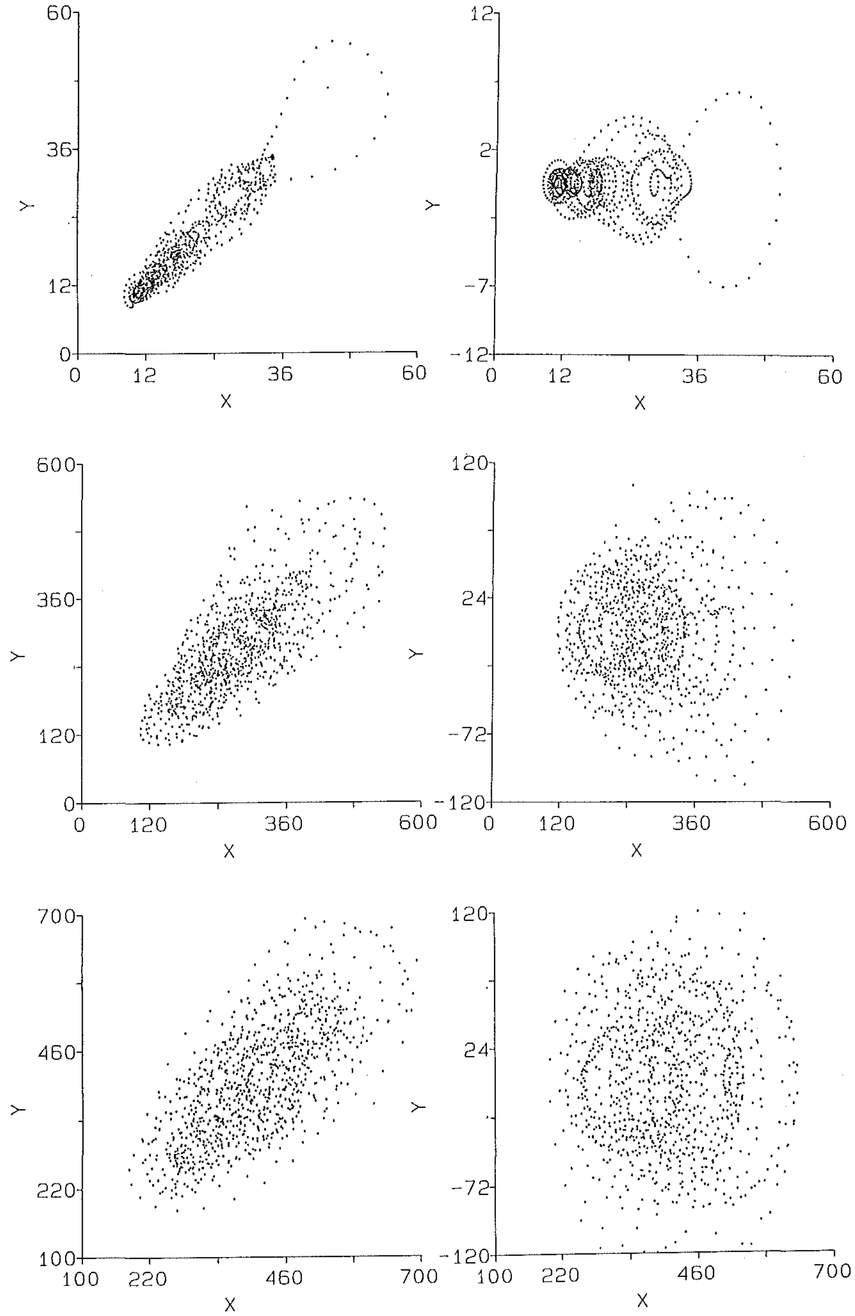

Figure 5: Phase-portraits: 1000 envelope points. Top: Taken from segment 2. Middle: Taken from segment 7. Bottom: Taken from random seismogram envelope. Left side: X is x_i, Y is x_{i+4}. Right side: X is x_i, Y is $\dot{x}_i$. Amplitudes in $\mu m/s$ and $\mu m/s^2$ multiplied by 30.

Fig. 6 presents the results of the correlation dimension calculations, from top to bottom for the low-amplitude section envelope, the high-amplitude section envelope, and for the envelope simulated from random numbers. Each time $n = 17000$ points were used. Parameter τ was varied from 2 up to 64 in steps of a factor 2, with only a small difference in the results. I prefer to present the results mainly for $\tau = 4$. Variation of the cut-off frequency (used for low-pass filtering the envelope) over an octave to the higher and to the lower side of 0.2 Hz did not alter the results.
Left-side panels of Fig. 6 show $log(p)$ versus $log(r)$ for embedding dimensions $m = 5, 15, 25, 35$ (in each panel successively from upper left to lower right) and the straight lines fitted in an intermediate region. In the right-side panels of Fig. 6, correlation dimension d is plotted versus m.
In the low-amplitude section (Fig. 6, top) these slopes do not change any more for m bigger than about 15, putting d to 7 for $\tau = 4$ and, as an upper bound, to 9 for $\tau = 64$. Thus I feel sure saying, that d is about 8. In the high-amplitude section (Fig. 6, middle) there is no saturation, nor is there saturation in the case of the completely stochastic data (Fig. 6, bottom). Some scatter in the $d(m)$ curves for higher m arises from uncertainties to determine the slope.

5 Narrow band filter

The tremor source can be assumed as being composed of individual 'oscillators' or 'resonators' radiating in individual frequency bands (Seidl et al., 1990). For brevity, I use the term 'resonator' in the following without any physical interpretation just as an abstract model to denote the source of a quasi-harmonic signal related to a peak in the tremor-seismogram spectrum. The stable spectral peaks demonstrated in Fig. 2, promoted the idea to split up the seismogram data by narrow band-pass filtering into individual 'resonator seismograms'. Without closer inspection, I have selected 5 peaks from the power spectra (see Fig. 3 and Fig. 4), i.e.: 'peak a' at a center frequency of 2.225 Hz, 'peak b' at 2.02 Hz, 'peak c' at 1.65 Hz, 'peak d' at 1.45 Hz, and 'peak e' at 1.25 Hz. Quasi-harmonic seismograms

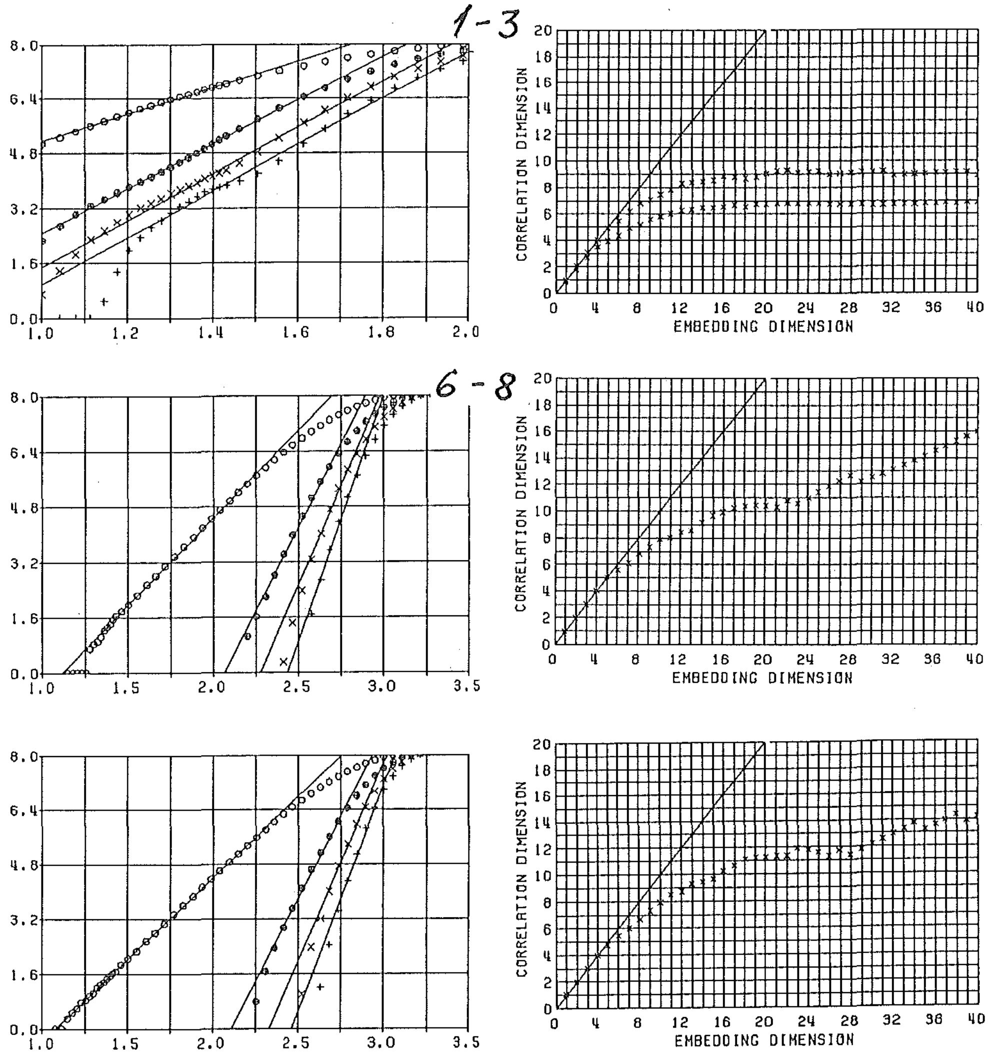

Figure 6: Correlation dimension: 17000 envelope points. Top: Segments 1 until 3. Middle: Segments 6 until 8. Bottom: From random seismogram envelope. Left: Slopes for $m = 5, 15, 25, 35$ (see text). Right: Correlation dimension d versus embedding dimension m. Delay τ is 4 throughout, except panel upper right, where lower curve is for $\tau = 4$ and upper curve for $\tau = 64$.

were obtained first by a 0.1-Hz-bandwidth non-phase-shifting Butterworth bandpass filter, centered at these frequencies. The filter is of order 6, such that the bands are sufficiently well separated. A 0.2-Hz-bandwidth filter gave similar results. Fig. 7, left side shows a 1-minute sample portion cut out of segment 2. From top to bottom, seismogram and filtered traces 'e', 'd', 'c', 'b', and 'a' are given, each time normalized to the trace maximum.

The notion 'frequency', originally deduced from the inverse of a prevailing period measured in a time record, is ambivalent if seen from the view of the Fourier-spectrum, *MESA*-spectrum or even from the concept of the 'instantaneous frequency'. The instantaneous frequency, calculated as the time derivative of the instantaneous phase of the complex envelope (Farnbach, 1975), can be seen as a measure of frequency, momentarily dominating in an infinitesimally small time interval.
Attempts to follow the instantaneous frequency in the non-filtered tremor seismograms were not successful yet. Taking the filtered seismograms representing the resonators, their instantaneous frequency is fairly equal to the center frequency of the filter employed (as far as resolution permits to say), except where the respective envelope approaches zero. Near to these signal constrictions, frequency is undefined and this numerically produces the spikes. Fig. 7, right side, gives the instantaneous frequencies plotted versus time, each on a scale from 0 to 3 Hz, derived from the filtered traces 'e', 'd', 'c', 'b' and 'a' from Fig. 7, left side.

In Fig. 8, a whole seismogram-segment is displayed, for filter 'a' at the left and filter 'e' at the right. Low-amplitude segments 2 are on top, high-amplitude segments 7 at bottom. More obvious than in the original seismograms (Fig. 3 and Fig. 4), there is a 'beating-like' structure in the filtered traces. Can these wave-packages be interpreted as properties of the resonator model? Are they bursts of energy radiation from respective single resonators? We have to keep in mind though, that the impulse response of the producing band-pass has an effective length of about 15 s. So this may be a characteristic pulse length in these traces.
I also construct the envelopes of these filtered seismograms, and search for

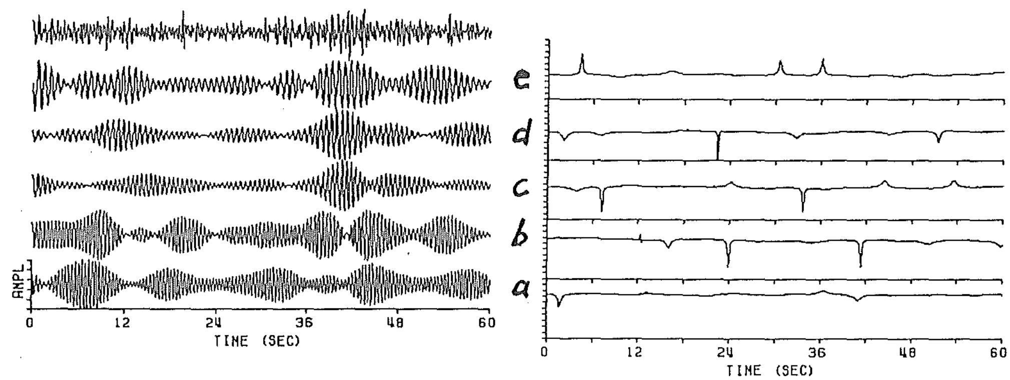

Figure 7: Single-resonator seismograms: 1-minute portions of narrow-band filtered seismograms (left) according to peaks 'a', 'b', 'c', 'd', 'e', and their instantaneous frequencies each on a 0-to-3 Hz scale (right).

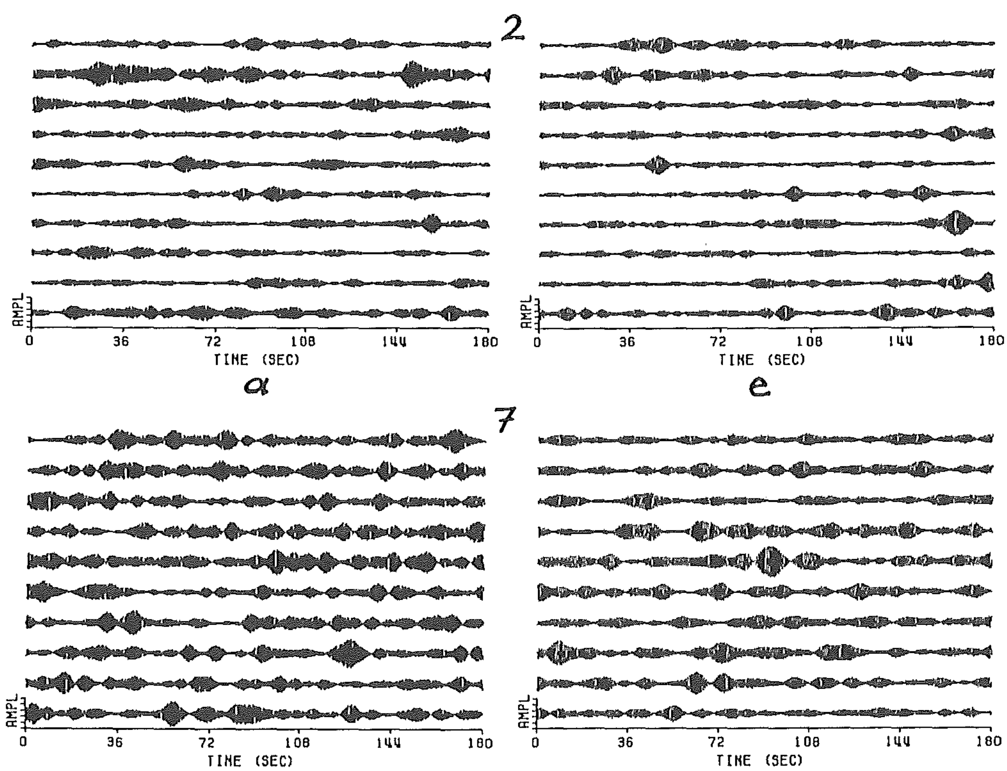

Figure 8: Single-resonator seismograms: Top: Segment 2. Bottom: Segment 7. Left: Peak 'a'. Right: Peak 'e'. Subfigures have the scales: top: 4 $\mu m/s$, bottom: 15 $\mu m/s$ at the left and 60 $\mu m/s$ at the right.

temporal coherence and periodicities of the resonators in auto-correlation functions and power spectra of respective envelopes. They, and the amplitude probabilities too, resemble altogether very much their respective counterparts of the total envelope in Fig. 3 and Fig. 4, right sides, respectively, and are not shown here. From a few test calculations, I suspect that for the correlation dimension d, too, there is no principal difference between the envelopes of the individual narrow-band and the parent envelope of the original seismograms. (A slight increase of d was observed though). Hence on a long-term perspective, the single resonators seem to behave as the overall source as far as amplitude and frequency characteristics of integral type are concerned.

We may ask whether there is an internal relation between the resonators. If so, it is certainly not very strong, as no clear congruence of the envelopping curves (see for instance Fig. 8) is obvious. Cross-correlation functions (using *FFT* and the biased but more-accurate estimation formula, Priestley, 1981) between the envelopes from filtered seismograms, denoted 'a', 'b', 'c', 'd' and 'e' as derived from respective resonator peaks, are calculated from segment 2 and segment 7 data. In Fig. 9, some of these cross-correlations are shown, denoted 'ab', 'cd', 'de', 'ae', for respective correlations. Zero lag is in the middle (at 900 s on the time scale of the plotted window). Negative lags correspond, for example taking 'ab' correlating 'a' and 'b', to 'b' shifted to the right of 'a', and vice versa. Rear ends, though uncontaminated by wrap-around effects, are less significant, as 'a' and 'b' then overlap only to one-half of their length.

In the low-amplitude section all cross-correlations peak at lag zero with a coefficient as high as 0.3 to 0.4 (from Fisher-test we have a 99 %-confidence for these values within 10 %-bounds). Examples for segment 2 are given in Fig. 9, second subfigure from top. The main lobes have an effective width of about 40 s, as have the respective auto-correlation main lobes of the 'a'- to 'e'- envelopes (examples denoted 'aa' and 'ee' in Fig. 9, subfigure on top, upper two traces), and has also the total envelope (Fig. 3, second on the right).

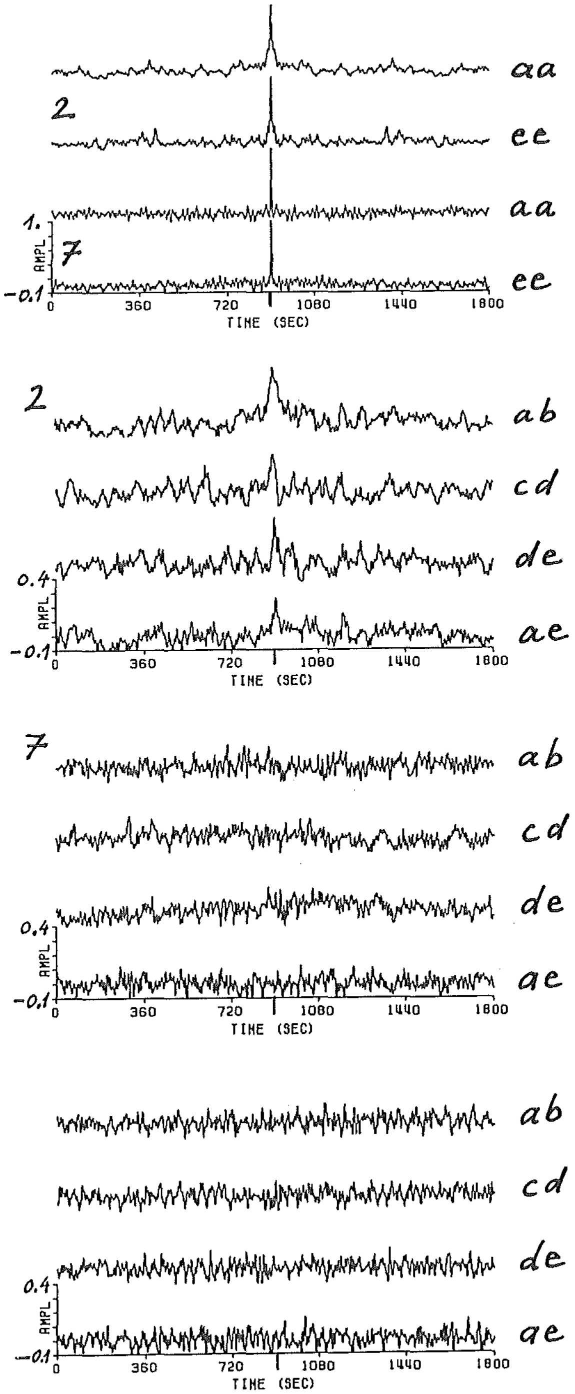

Figure 9: Correlograms from single-resonator envelopes: First on top: Auto-correlations. From second to bottom: Cross-correlations. Data are from segments 2 and 7 as indicated and from random seismogram envelopes for the bottom subfigure. Correlation couples denote peaks 'a' to 'e'. Lag zero is in the middle of the time windows shown.

There is no significant correlation in the high-amplitude section (Fig. 9, third from top, for segment 7). Correlation noise is then ± 0.1 as it is in the example of correlating simulations 'a', 'b', 'c', 'd', and 'e' deduced from random seismograms and processed step by step in exactly the same manner as the real data so far (Fig. 9, bottom). To my feeling, in this case, comparison with random numbers resembling the data as close as possible gives better confidence than formalized statistical test procedures.

Hence we may presume that there is significant coupling of the resonators in the low-amplitude section, which then disappeares in the high-amplitude section.

6 Phasor walks

We have seen in the power spectra of Fig. 2, that the relative power of the single resonators varies considerably from low- to high-amplitude section. How about the phase? Let

$$\tilde{x}(f_k) = \Delta t \sum_{i=1}^{n} x_i \, e^{-2\pi j f_k (i-1)\Delta t}$$

be the discrete Fourier transform of the series x_i with i from 1 to n, evaluated for frequency f_k. (j is the imaginary unit). There is no point to take the result of this sum, neither the absolute nor the complex value, into serious consideration, as its error its 100 % for any n, and it corresponds energetically to a very narrow ($1/(n\Delta t)$) frequency bin containing f_k. The idea is, however, to inspect the phasor path in the complex plane ($\mathrm{Im}(\tilde{x})$ versus $\mathrm{Re}(\tilde{x})$ plane), on which the final $\tilde{x}(f_k)$ value is reached walking from $n = 1$ to successively increasing n. To learn to know this method (see e.g. Rydelek and Sacks, 1989), I advocate to follow the walks of quasi-harmonic, amplitude-modulated, sweep, and random series. In short, it can be said, that if spectral energy for f_k is strong and there is a stable phase function over a stretch of time, then the walk proceeds in a fairly straight manner; change of phase, however, produces change of walk direction, instationarities in the time series produce instationarities of the walk pattern.

Going back to the non-filtered seismogram (Fig. 3 and Fig. 4, left), we follow the phasor walks exemplary of 'peak a' for the frequency $f_k = 2.225\ Hz$. (The same result can of course be obtained from the respective filtered version, Fig. 8, left side). Fig. 10, top part from left to right arethe walks in segments 2, 3, ($n = 22500$ points each) and 1 until 3 (total $n = 67500$), in the Im($\tilde{x}$)- versus Re($\tilde{x}$)-plane, each time normalized to the extremal values on either axes. Fig. 10, middle part, gives the same for segments 6, 7, and 6 until 8. At the bottom, once again, is the result obtained from a closely matched random seismogram for comparison.

Without any quantitative interpretation, we can see that the walks in the low-amplitude section are much smoother (and over some time even fairly straight) than in the high-amplitude section. However, even there appear to be some more regular parts in between totally irregular ones (see segment 6). Alltogether, the high-amplitude section resembles random walks more than straight ones.

Doing the same for the other peak frequencies, one gets similar, but also in the low-amplitude section somewhat irregular walks. From attempts to smoothen the curves by averaging over frequencies adjacent to f_k while walking from point to point, no clearer results have been obtained so far. For now, I can just report the indication, that the low-amplitude section apparently has a higher degree of order than the high-amplitude section.

7 Conclusions

Analysing the envelope of tremor seismogram amplitudes rather than the seismogram itself has several objectives.

Formally, the (squared) envelope of a tremor seismogram can be taken as a smoothed intensity curve, proportional to energy flux from of the overall tremor source.

It has also been observed on Etna, that visible eruptive parameters (for example strength of ash ejection, height of lava fountains) are in correlation with averaged tremor intensities (Riuscetti and Schick, personal communication).

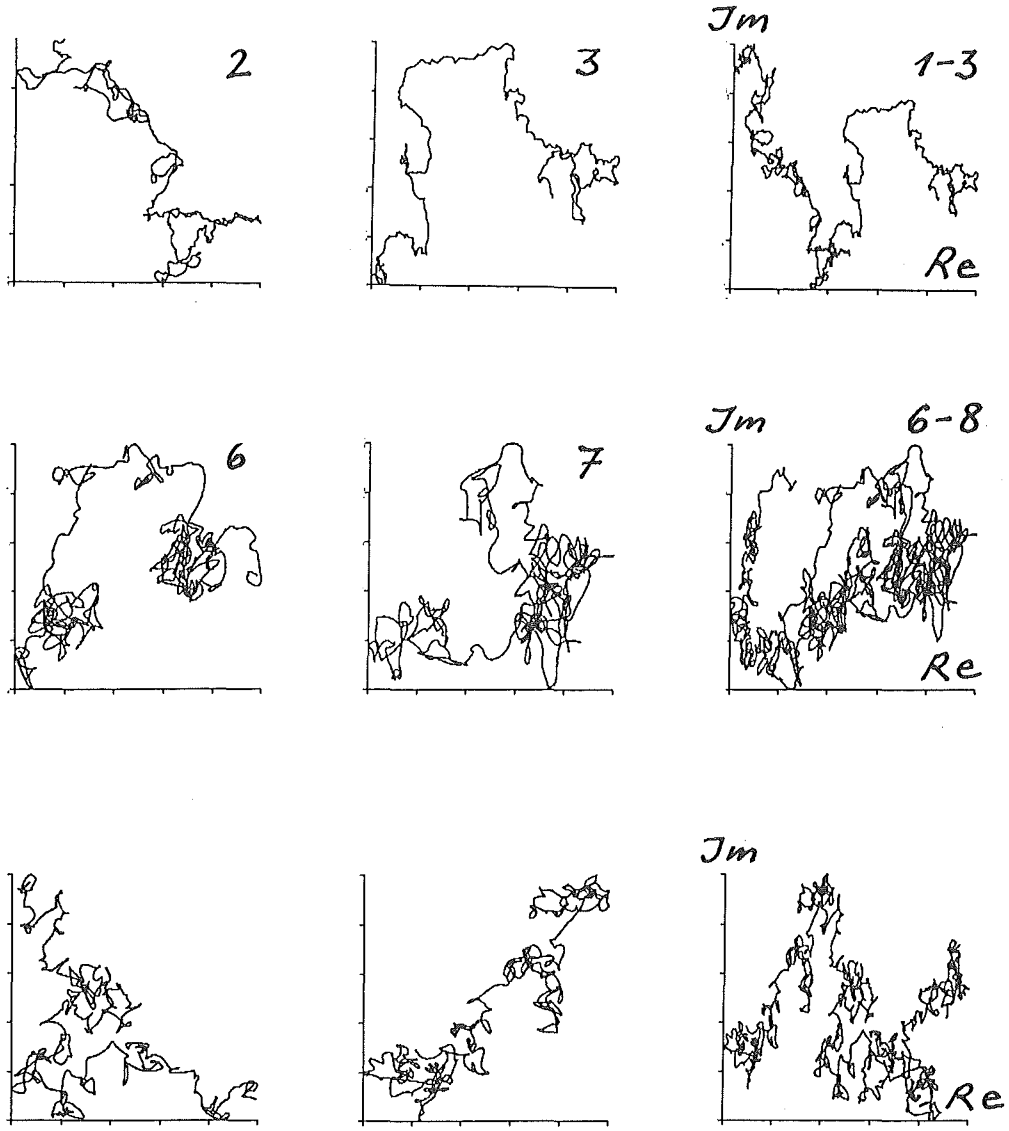

Figure 10: Seismogram phasor walks for frequency 2.225 Hz (peak 'a'): Real (Re) and imaginary (Im) part of the complex Fourier transform. Top: Low-amplitude section segments 1 to 3. Middle: High-amplitude section segments 6 to 8. Bottom: random seismogram segments. Individual amplitude normalization in each subfigure.

Comparing the tremor source with a damped oscillator system excited by external forces (for example Riuscetti et al., 1977), the peak frequencies in the seismogram spectrum can be related to eigenfrequencies, the bandwidths possibly to internal damping of the oscillators. These peak frequencies, in the present example situated in the range from 1 to 3 Hz, act as carrier frequencies, which are amplitude modulated mainly due to a variation of the force system exciting the oscillators (then also called resonators). Hence the seismogram envelope contains the information about the energy feeding system driving the resonators, rather than about the resonators themselves. Physically, stable spectral peaks have been connected to geometrical properties of the resonators (length of magma filled dykes, radius of magma chambers etc.) and also to material properties of flowing magma (e.g. viscosity). The envelope data characteristics may now be interpreted in terms of properties of the underlying source system of tremor origin. Moreover, going to an even longer time scale, the envelope of the envelope represents a source system which again underlies the latter.

The envelope is non-linearly related to its original seismogram, and basically a new data series in a considerably lower frequency band, however different from the low-frequency seismic energy, which could eventually be detected by a long-period seismometer. Envelope frequencies are affected by influences of wave propagation through the volcano (e.g. absorption, to mention one) only to a minor degree. As for the lower frequency content, envelopes can digitally be obtained on more economic sampling rates.

The present results are based on an exemplary record of tremor transition from low to high activity reflecting the transition from the pre-eruption into the eruption phase of the volcano. The main result is that prior to eruption there is a higher degree of order in the tremor source than during the eruption. This is argumented from evidence of more structured phase portraits, moderately high fractal dimension, significant correlation of resonators and more regular phasor walks observed in the pre-eruption section, contrasting to irregular, not-correlated, highly chaotic pictures within the eruption. Contrary to earlier hypotheses saying that chaotic systems become more deterministic if forced into stronger motion, I found that this is not true for the tremor source in the present case.

The most likely physical reason for tremor origin is turbulent magma flow inside the volcano (Schick, 1988). Thus the present finding is in accordance with higher magma flow velocities and a higher degree of turbulence during the eruption than before. Similar observations have been made in various fields of fluid dynamics (see articles in Mayer-Kress, 1986 for examples).

The seismogram envelope has played the key role in this study and has helped to unravel the chaos a little bit. I recommend, to consider the envelope in further tremor investigations.

Acknowledgements

I thank Professor R. Schick for stimulating this study and for his advice throughout. Istituto di Scienze della Terra, Catania, Italy kindly provided the tremor data. I am grateful to J. Strigl for his correlation dimension code and for fruitful discussions. The phasor-walk method was pointed out to me by Dr. W. Zürn. I appreciated helpful comments from Drs. D. Seidl and W. Zürn who reviewed the manuscript. This work was supported by the Deutsche Forschungsgemeinschaft.

References

Bendat, J.S., and A.G. Piersol, Random data analysis and measurement procedures, Wiley, New York, 1971.

Cosentino, M., G. Lombardo, and E. Privitera, A model for internal dynamical process on Mt Etna, Geophys. J., 97, 367-379, 1989.

Farnbach, J.S., The complex envelope in seismic signal analysis, Bull. Seism. Soc. Am., 65, 951-962, 1975.

Liu, H.-P., and D.D. Kosloff, Numerical evaluation of the Hilbert transform by the Fast Fourier Transform (*FFT*) technique, Geophys. J. R. astr. Soc., 67, 791-799, 1981.

Mayer-Kress, G., (ed.), Dimensions and entropies in chaotic systems: quantification of complex behavior, Proceedings of an international workshop at the Pecos River Ranch New Mexico, Springer, Berlin, 1986.

Priestley, M.B., Spectral analysis and time series, vol. 1 and vol. 2, Academic Press, London, 1981.

Riuscetti, M., R. Schick, and D. Seidl, Spectral parameters of volcanic tremors at Etna, J. Volc. Geoth. Res., 2, 289-298, 1977.

Ruelle, C.B., Deterministic chaos: the science and the fiction, Proc. R. Soc. Lond., A427, 241-248, 1990.

Rydelek, P.A., and I.S. Sacks, Testing the completeness of earthquake catalogues and the hypothesis of self-similarity, Nature, 337, 251-253, 1989.

Schick, R., Volcanic tremor-source mechanisms and correlation with eruptive activity, Natural Hazard, 1, 125-144, 1988.

Schmidt, G., and A. Tondl, Non-linear vibrations, Cambridge University Press, Cambridge, 1986.

Seidl, D., S.B. Kirbani, and W. Brüstle, Maximum entropy spectral analysis of volcanic tremor using data from Etna (Sicily) and Merapi (central Java), Bull. Volcanol., 52, 460-474, 1990.

Smithsonian Bulletin, Natural Science Event Bulletin, Scientific Event Alert Network, Smithsonian Institution, Museum of Natural History, Washington, D.C., Vol. 2, No. 11 and 12, 1977.

Strigl, J., Dimensional analysis of volcanic tremor, 1991 (this volume).

VOLCANIC TREMOR RECORDINGS: POLARIZATION ANALYSIS

Dieter Seidl

Seismologisches Zentralobservatorium Gräfenberg, Krankenhausstr. 1-3, D-8520 Erlangen, Germany

Margaret Hellweg

United States Geological Survey, 345 Middlefield Road, Menlo Park, CA 94025, USA

Introduction

The main source of volcanic tremor can be modelled as an ensemble of randomly excited acoustic resonators. The resonators are thought to be magma-filled conduits and dikes driven by turbulent pressure fluctuations in the magma-gas flow field (see for example Schick 1988). This qualitative understanding of the source mechanism leaves three basic questions of tremor seismology unanswered:

1. Can the individual resonators be resolved and located?
2. What are the dynamics of the elementary wave radiation process?
3. What are the spatial characteristics of the tremor wavefield?

The standard monitoring techniques using short-period and vertical seismometers can shed no further light on these questions. Two extensions of the recording and time series analysis methods are necessary to reveal the tremor source mechanism:

1. Recordings should be made in the nearfield of the tremor source with a portable array of broadband three-component seismometers to determine the frequency-wavenumber power spectrum and the spatial coherence of the wavefield.
2. Methods for the analysis of time series must be developed to extract the wavefield of the individual resonators from the tremor recording. A single resonator can then be characterized in terms of its frequency-wavenumber-polarization radiation pattern.

At present, very few tremor recordings exist from small, portable arrays (for example Dietel, et al., 1989; Ferrazzini, et al., 1990). Recordings have, however, been made using a vertical broadband seismometer at Torre del Filosofo, Mt. Etna (Sicily). Seidl et al. (1990) have analysed the data using the maximum entropy spectral analysis method (MEM) to resolve the power spectra radiated by the individual resonators. This station was colocated with a short-period three-component velocity seismometer. Using these recordings, a method of frequency-polarization decomposition was developed to further characterize the individual resonators. It combines maximum entropy spectral analysis with polarization analysis of bandpass filtered tremor recordings.

Restoration of tremor recordings

Tremor is normally recorded using short-period seismometers with velocity transducers. For many methods of time domain processing such as polarization analysis or coherence measurements, it is advantageous to convert the short-period velocity seismograms to displacement seismograms and extend the bandwidth to longer periods. This restoration problem can be solved for the random tremor time series by recursive filtering in the time domain.

If $H_V(s)$ is the transfer function of the recording velocity seismometer and D(s) denotes the Laplace (L) transform of the ground displacement, the L-transform of the velocity seismogram V(s) is given by

$$V(s) = H_V(s)\,D(s) = \frac{s^3}{s^2 + 2h_0\omega_0 s + \omega_0^2} D(s), \qquad (1)$$

where h_0 and $T_0 = 2\pi/\omega_0$ are the damping constant and the period of the recording seismometer, respectively.

If the ground motion with L-transform D(s) is recorded by a displacement seismometer with the transfer function $H_D(s)$ the L-transform of the displacement seismogram U(s) is given by

$$U(s) = H_D(s)D(s) = \frac{s^2}{s^2 + 2h_1\omega_1 s + \omega_1^2} D(s), \qquad (2)$$

where h_1 and $T_1 = 2\pi/\omega_1$ are the damping constant and the period of the simulated displacement seismometer, respectively.

The conversion formula follows from equations (1) and (2):

$$U(s) = \frac{H_D(s)}{H_V(s)} = \frac{s^2 + 2h_0\omega_0 s + \omega_0^2}{s^2 + 2h_1\omega_1 s + \omega_1^2}\frac{1}{s}V(s). \tag{3}$$

Using the bilinear z-transformation equation (3) can be converted into two difference equations:

$$w_t = a_0 v_t + a_1 v_{t-1} + a_2 v_{t-2} - b_1 w_{t-1} - b_2 w_{t-2} \tag{4}$$

$$u_t = c_0(w_t + w_{t-1}) + u_{t-1} \tag{5}$$

Equations (4) and (5) describe a two-step recursive filter which converts the discrete recorded velocity seismogram v_t into a simulated displacement seismogram u_t. The first output w_t is the velocity seismogram of a seismometer with period T_1 (usually $T_1 > T_0$), the second step integrates w_t to the displacement seismogram u_t. The formulas for the filter coefficients are given by Seidl (1980). The upper limit for the restoration period T_1 depends mainly on the low-frequncy seismometer noise and can be found by gradually increasing the period T_1 until the seismogram u_t becomes unstable. A high pass filter can be applied to w_t to reduce the low frequency seismometer noise.

Polarization analysis of 3-component tremor recordings

The tremor time series is a superposition of wavegroups which produce the many peaks in the periodogram power spectrum. MEM analysis reveals narrow spectral peaks with center frequencies f_n and bandwidths B_n excited in each short time segment. A narrow bandpass filter, (f_n, B_n), can extract the particle motion associated with the peak from the three components of the recording. The particle motion can be described as a random vector

$$\vec{u}(t) = \{u_x(t), u_y(t), u_z(t)\}\ \exp(j\omega_n t) \tag{6}$$

where the complex amplitudes of the three components

$$u_k(t) = a_k(t)\exp[j\phi_k(t)] \quad k = x, y, z \tag{7}$$

are slowly varying time functions of instantaneous amplitude and phase. The kinematic parameters of the three-dimensional particle motion can be determined using the methods of polarization analysis.

For a random process, the trajectory method of Matsumura (1981), a method of least squares fitting, can be used to determine the polarization ellipsoids in the frequency bands of the maximum entropy spectral peaks.

Given are m samples of the discrete narrow-band particle motion vector $\vec{u} = \{u_{xt}, u_{yt}, u_{zt}\}$, $t = 1, m$. The unit vectors $\vec{n} = \{n_x, n_y, n_z\}$ must be found, so that the squared sum of the projections of vector $\vec{u_t}$ onto $\vec{n}$ has extreme values under the constraint $n_x^2 + n_y^2 + n_z^2 = 1$. Using the Lagrange multipliers method, the extreme value problem can be formulated as:

$$g = \sum_{t=1}^{t=m} [u_{xt}n_x + u_{yt}n_y + u_{zt}n_z]^2 - l(n_x^2 + n_y^2 + n_z^2 - 1) \qquad (8)$$

where the extreme values of g are determined by setting the partial derivatives $\partial g/\partial n_x, \partial g/\partial n_y, \partial g/\partial n_z$ to zero. This gives the following homogeneous linear system of equations in matrix form:

$$\begin{pmatrix} C_{xx}(0) & C_{xy}(0) & C_{xz}(0) \\ C_{yx}(0) & C_{yy}(0) & C_{yz}(0) \\ C_{zx}(0) & C_{zy}(0) & C_{zz}(0) \end{pmatrix} \begin{pmatrix} n_x \\ n_y \\ n_z \end{pmatrix} = l \begin{pmatrix} n_x \\ n_y \\ n_z \end{pmatrix}, \qquad (9)$$

where

$$C = \begin{pmatrix} \sum u_{xt}u_{xt} & \sum u_{xt}u_{yt} & \sum u_{xt}u_{zt} \\ \sum u_{yt}u_{xt} & \sum u_{yt}u_{yt} & \sum u_{yt}u_{zt} \\ \sum u_{zt}u_{xt} & \sum u_{zt}u_{yt} & \sum u_{zt}u_{zt} \end{pmatrix}. \qquad (10)$$

C is the coherence matrix consisting of the auto-covariances C_{ii} and the cross-covariances C_{ik} for the zero lag time. The solution of equation (9) gives the eigenvalues l_1, l_2 and l_3, and the corresponding eigenvectors $\vec{n_1}, \vec{n_2}, \vec{n_3}$ of the coherence matrix C.

When the three eigenvalues, $l_1 > l_2 > l_3$, are different, the three orthogonal eigenvectors $\vec{e}_k = \sqrt{l_k}\,\vec{n}_k$, $k = 1, 3$, determine the axes of an ellipsoid with major axis $\sqrt{l_1}$, intermediate axis $\sqrt{l_2}$ and minor axis $\sqrt{l_3}$.

In the special case of unpolarized motion, the cross-covariances are all zero and the auto-covariances are all equal. In this case, the three eigenvalues are equal, $l_1 = l_2 = l_3 = l$, and the resulting polarization ellipsoid is a sphere of radius $\sqrt{l}$.

For a narrowband random process described by equation (6), the coherence time, t_c, is defined as the time interval during which the amplitude and phase of the complex displacement vector remain nearly constant. For a narrow band random time series with bandwidth B and center frequency f_0, t_c can be approximated by:

$$t_c\, B \approx 1/\pi \tag{11}$$

To obtain a reasonably stable polarization ellipsoid, the analysis time interval t_a must be less than t_c. Statistically independent polarization ellipsoids can therefore only be determined by repeating the measurement at time intervals greater than the coherence time. If such polarization diagrams show nearly the same polarization ellipsoids, then the tremor wavefield producing a spectral peak with center frequency f_0 and bandwidth B must consist of many wavegroups with a dominant propagation azimuth and polarization. On the other hand, if the polarization ellipoids have a broad distribution, the tremor wavefield must consist of several independent wavegroups propagating in various directions. Many measurements must be made to determine whether the wavefield has completely randomly distributed propagation azimuths and polarizations or whether there are several dominant directions.

The following procedure for analysing three component recordings of volcanic tremor uses a combination of restoration, spectral analysis and polarization analysis to recover information about the tremor source.

1. Periodogram power spectrum: Estimation of periodogram power spectra P(f) and correction for the seismometer transfer function H(f) by $P(f)/|H(f)|^2$ to determine the maximum period T_{max} for time domain restoration.

2. Time domain restoration: Restoration of recorded seismograms by simulating a displacement seismometer with period $T_1 = T_{max}$ using the recursive filter in equations (4) and (5).

3. Maximum entropy spectra: Determination of the optimum MEM order by adapting the histogram of the MEM peak frequencies to the periodogram power spectrum.

4. Bandpass filtering: Isolation of the particle motion $\vec{u}(t, f_m)$ within a narrow bandwidth around a MEM spectral peak f_m by time domain bandpass filtering.

5. Polarization analysis: Determination of the polarization ellipsoids for analysis intervals less than the coherence time using the trajectory method.

6. Parameter compression: Statistical analysis of the parameters (coherence times, spectral peak frequencies, axes and unit vectors of polarization ellipsoids) into averaged time functions or histograms for interpretation or activity monitoring.

Polarization analysis using Mt. Etna tremor recordings

The method has been applied to data recorded at Torre del Filosofo, Mt. Etna (Sicily), on July 11, 1988, during a state of normal activity. Figure 1 shows velocity recordings of 1 Hz seismometers for the vertical (Z), north (N, approximately radial to central crater) and east (E) component, together with seismograms restored to simulate the response of a displacement seismometer with period 2.5 s.

Figure 2 shows the periodogram power spectra for the simulated displacement recordings. The spectra are estimated for a 34 min time interval using record sectioning in 100 segments (length 20.4 s), Welch windowing and segment overlapping by one-half of segment length. The power is mainly concentrated in the horizontal plane with a broad spectral maximum in the frequency interval [0.6 Hz,1.2 Hz] common to all three components.

The maximum entropy method (MEM) reveals several very narrow-band peaks with center frequencies at 0.63, 0.73, 0.83, 0.88, 0.93, 0.98, 1.03 and 1.12 Hz. The most frequently occurring peak is at 0.93 Hz with a bandwidth of about 0.02 Hz. Figure 3 shows the maximum entropy spectra for six 16 s time intervals which include the dominant 0.93 Hz peak. In addition, the figure shows the polarization ellipses in the horizontal (N-E) and vertical (R-Z, R direction taken as the azimuth of the major axis of the

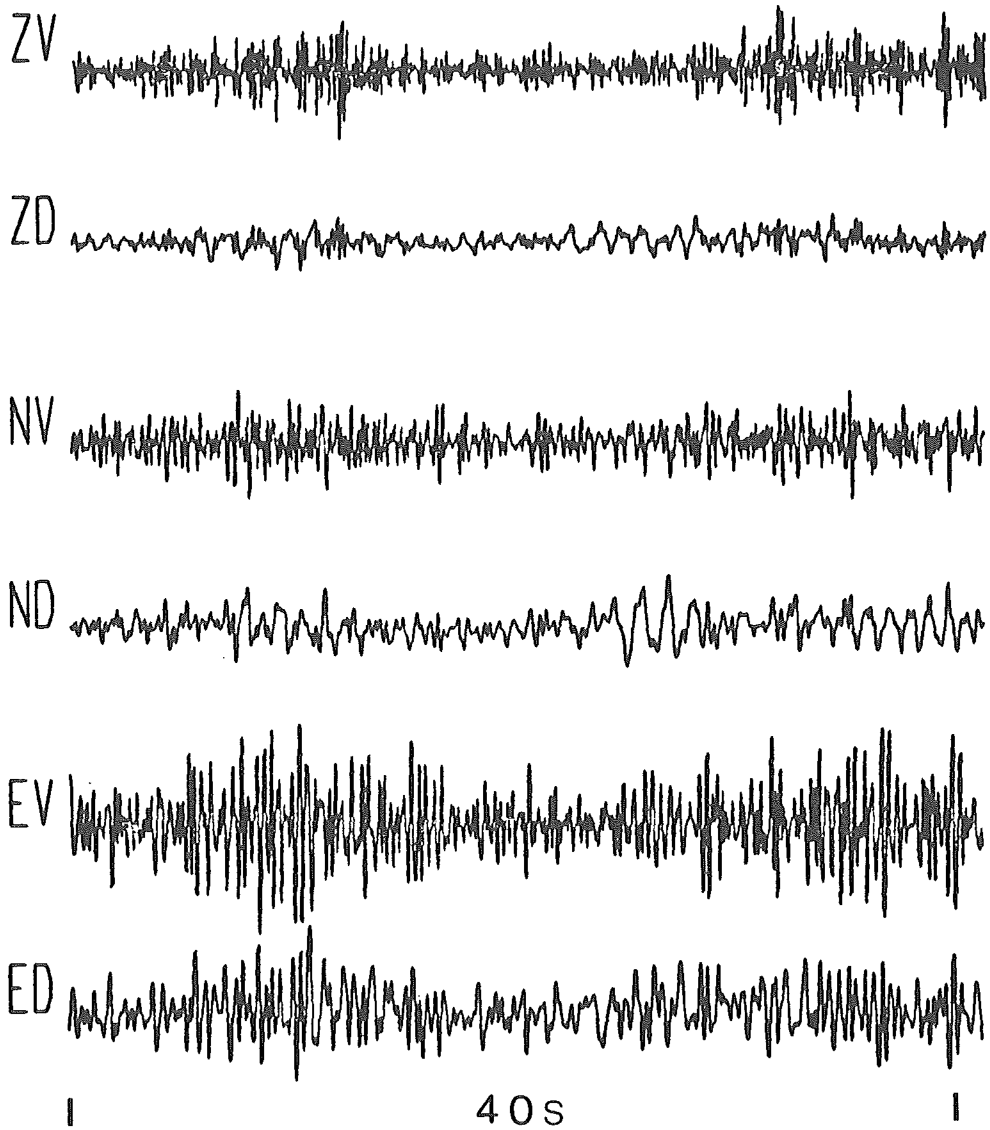

Figure 1: Three-component (Z vertical, N north or about radial to central crater, E east) tremor section (41 s) showing velocity seismograms (V) recorded at Torre del Filosofo, Etna (Sicily) and simulated displacement seismograms (D).

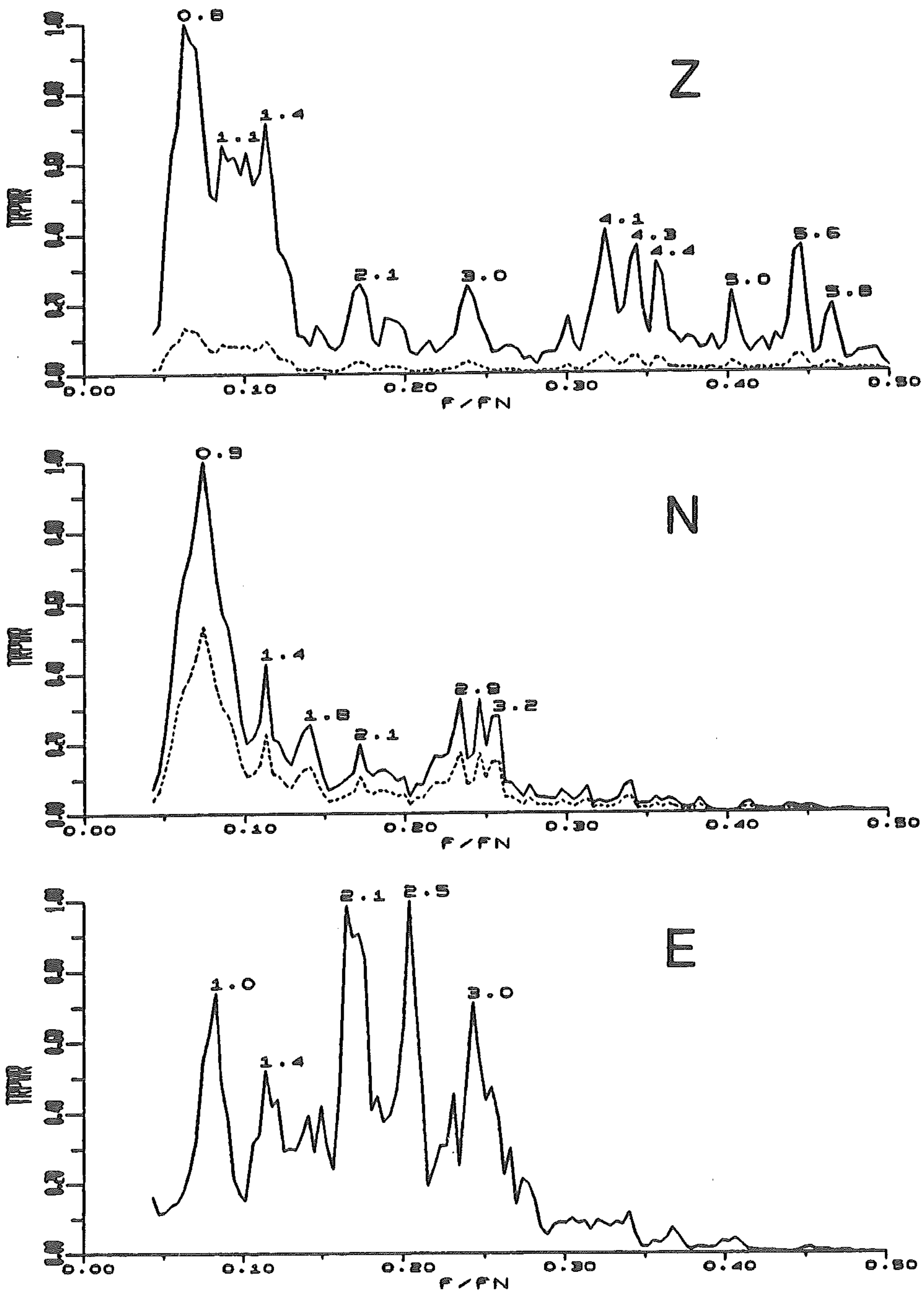

Figure 2: Power spectra (arbitrary units) for vertical (Z) and horizontal (N north, E east) ground displacement, normalized to full scale (solid) and to the E-component (dashed), respectively. Nyquist frequency f_N=12.5 Hz. The numbers indicate the peak frequencies in Hz.

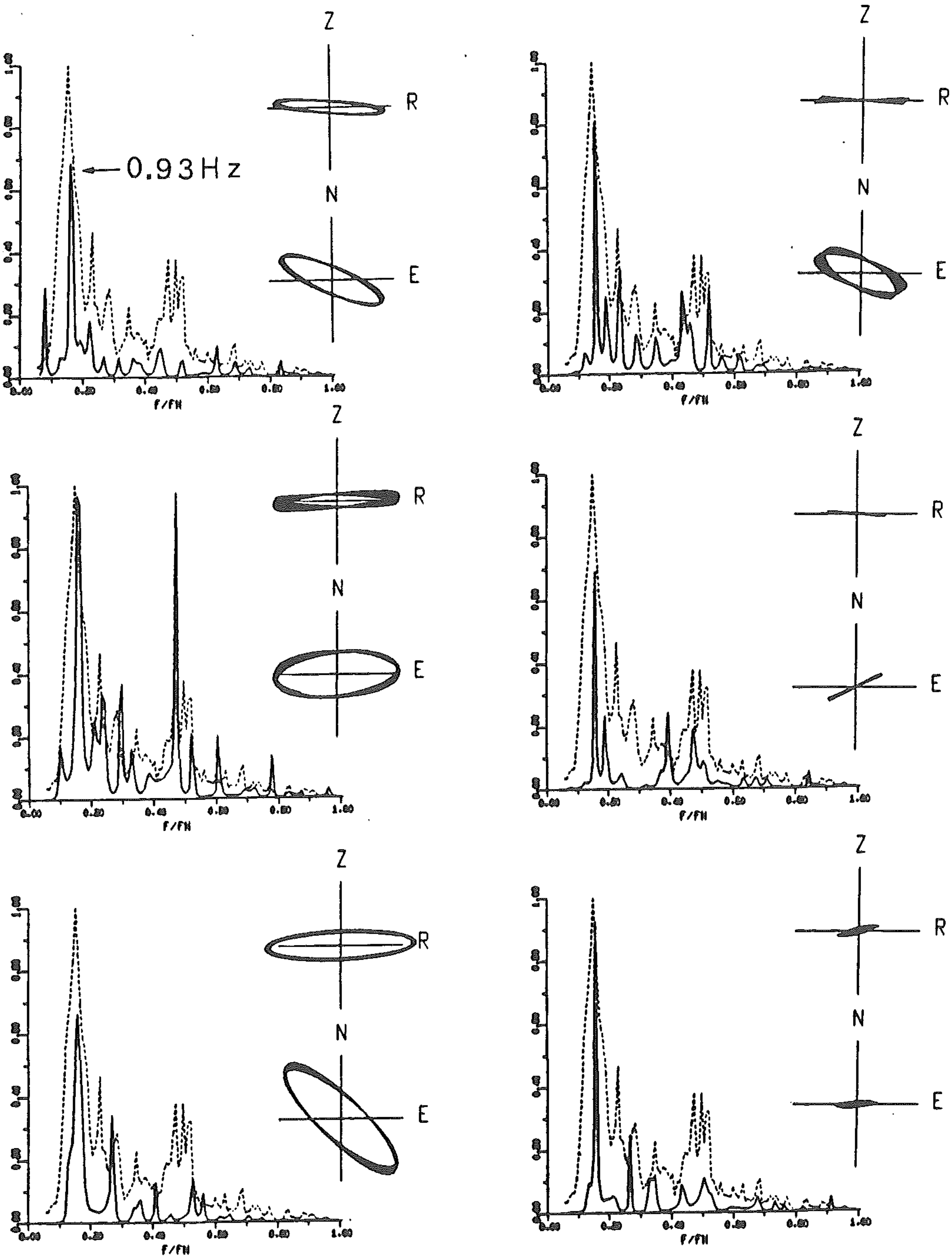

Figure 3: Power spectrum (dashed; Figure 1) and maximum entropy spectra (solid) for the N-component with particle motion ellipses for the frequency band around the most frequent 0.93 Hz peak.

N-E ellipse) planes for a frequency band B=0.02 Hz around the 0.93 Hz peak. For the polarization analysis, the restored displacement time series has been bandpass-filtered at 0.93 Hz with a bandwidth of B=0.02 Hz to include only this peak.

According to equation (11), the coherence time t_c corresponding to this bandwidth is about $t_c \approx 16$ s. For the independent analysis intervals $t_a \approx t_c$ in figure 3 coherent polarization ellipsoids are observed but with large variations in the orientation and ellipticity of the horizontal ellipses.

Figure 4 confirms this observation. It shows the variation of the polarization ellipses in both planes for a sequence of successive time intervals with $t_a = 4.0$ s. The diagrams on each line show a systematic change of polarization parameters, ellipticity and orientation, during a coherence interval, t_c. Stepping through the diagrams vertically in steps of t_c, a more random variation is observed in the horizontal plane. This indicates that the wavegroups in the narrow band of the 0.93 Hz peak are propagating in many azimuthal directions. The tremor wavefield may be generated either by several independent point sources, a moving source or an extended source.

The polar histogram in Figure 5 shows the fraction of the 34 minutes of the recording interval for which each azimuth was measured. It has a nonuniform distribution with a maximum between 20 and 30 degrees. Figure 6 shows analogous determinations of distribution for the incidence angle. During the whole analysis interval, the particle motion in the 0.93 Hz peak remains nearly horizontal confirming the results of the periodogram analysis which showed that the power is concentrated in the horizontal plane.

Frequently the polarization ellipsoid remains constant for a polarization time interval, t_p, greater than the coherence time t_c, before changing rapidly to a new stable direction. The polarization diagrams below the histogram in Figure 5 show two typical polarization episodes. Notice that each diagram shows two intervals of fairly constant polarization between which the major axis has rotated by nearly 90 degrees.

When the polarization time, t_p, for which the polarization remains constant is larger than the coherence time t_c due to the bandpass filter, then the particle motion is caused by a wavetrain in this frequency band with a

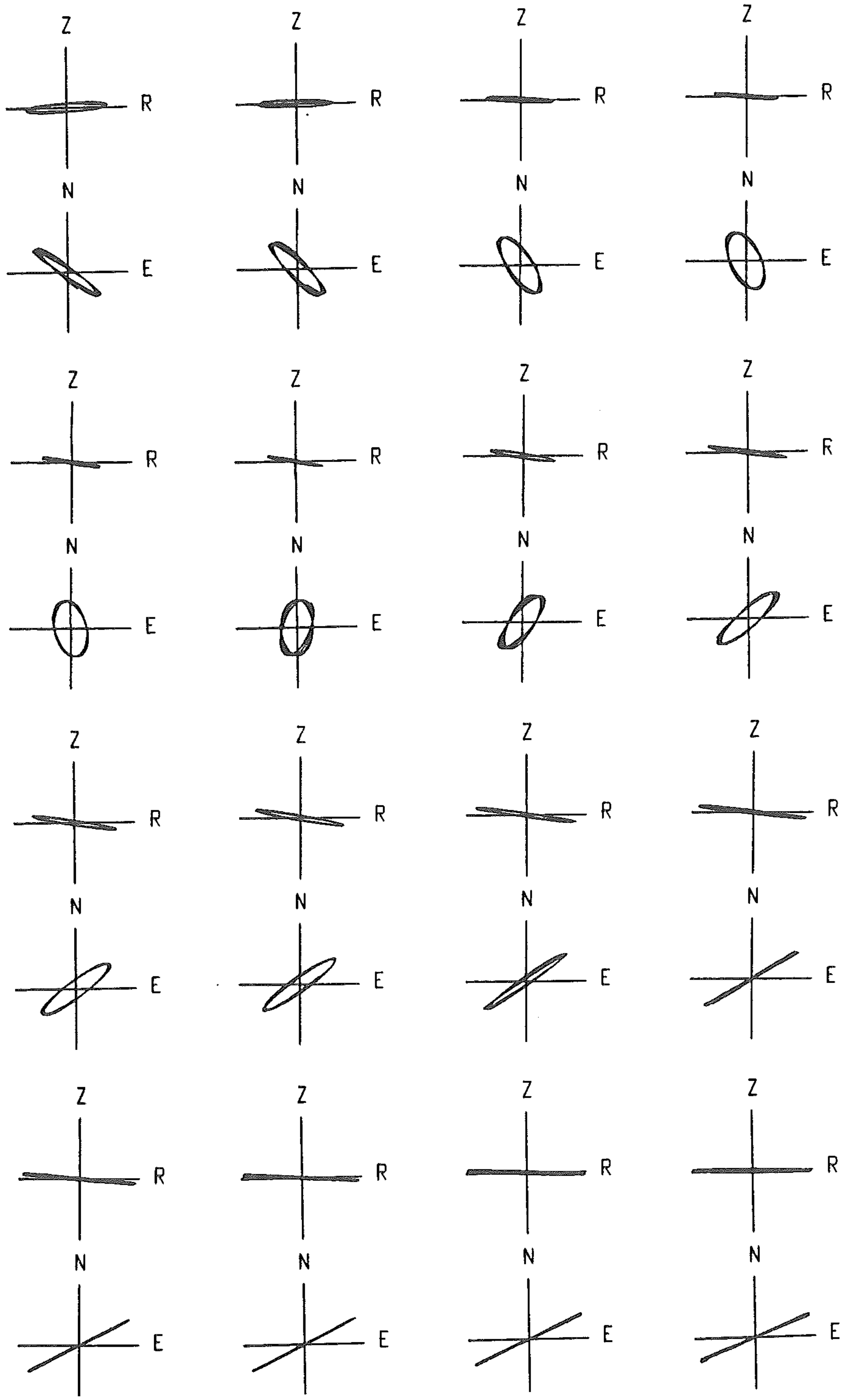

Figure 4: Sequential series of polarization ellipses in the frequency band around the 0.93 Hz peak.

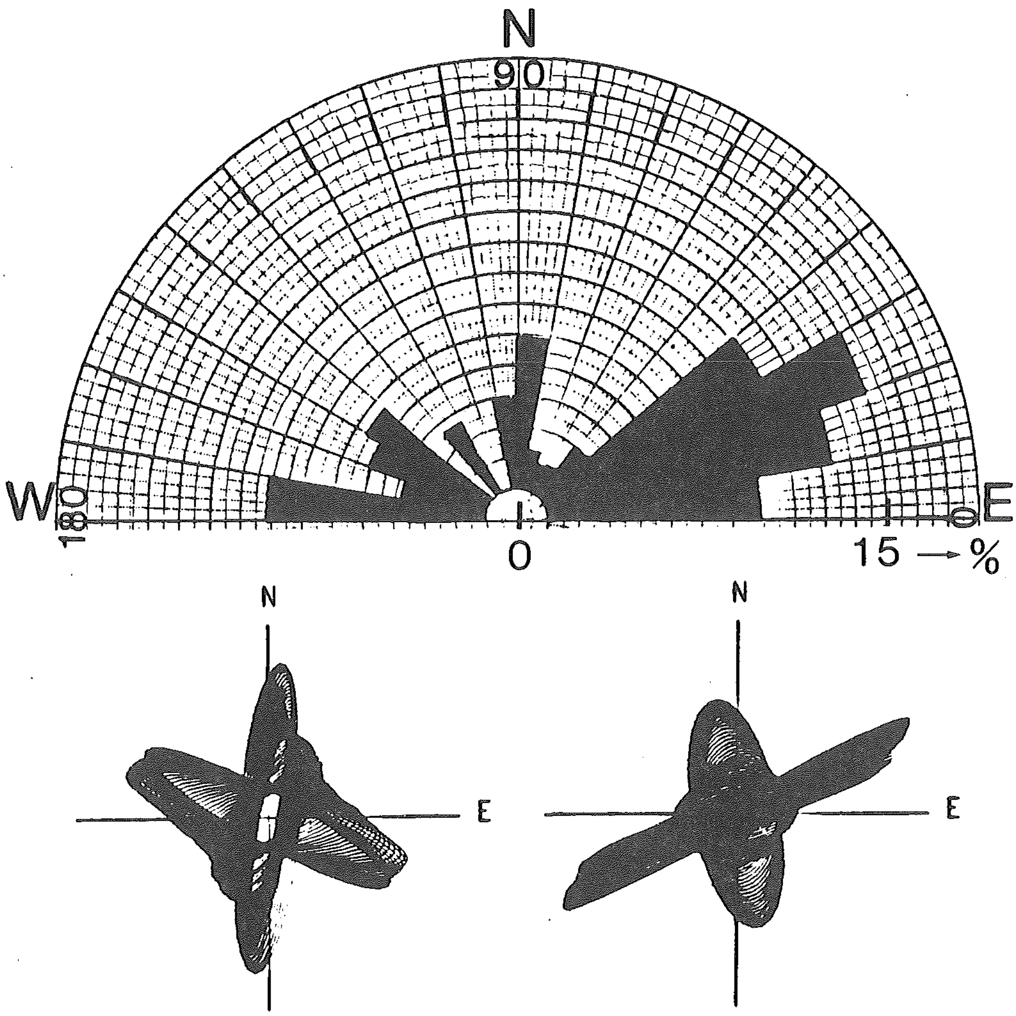

Figure 5: Azimuth histogram for the major axes of the polarization ellipsoids in the 0.93 Hz band. The particle motion diagrams illustrate some dominant azimuth sectors for two time intervals of 164 s.

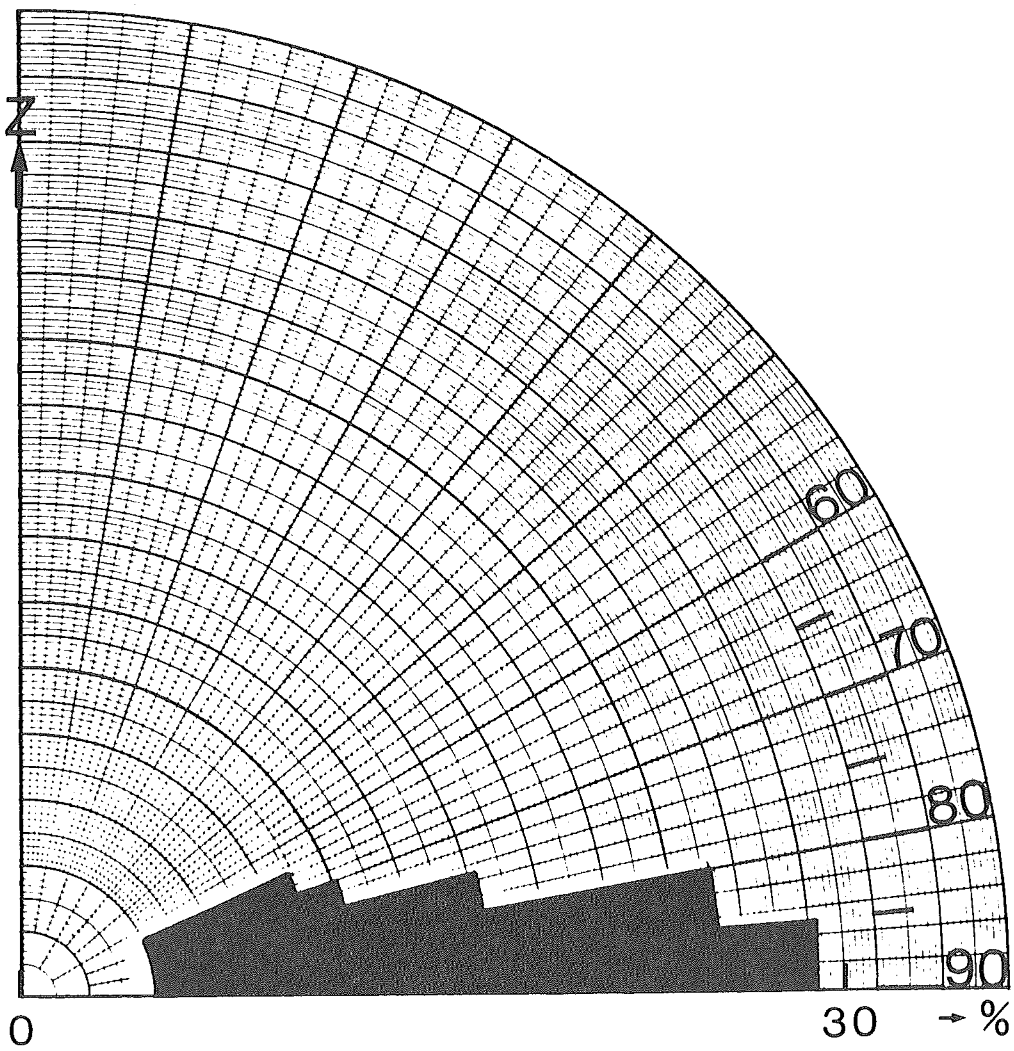

Figure 6: Histogram for the incidence angles of the major axes of the polarization ellipsoids in the 0.93 Hz band.

bandwidth $B_p = 1/(\pi * t_p) < B_c$ (f_p and B_p are the maximum frequency and the bandwidth of the peak). From t_p the quality factor, Q, defined by $1/Q = B_p/f_p$, can be calculated using equation (11):

$$Q = \pi \, f_p \, t_p \tag{12}$$

The intervals of coherent polarization,t_p, show large time variations. The maximum values for the azimuth interval [30 deg, 40 deg] are of the order of magnitude $t_p \approx 80$ s, corresponding to Q-values of about 230. Polarization analysis is thus a method for determining the quality factors of the spectral peaks of the individual wavetrains.

Conclusions

The tremor wavefield consists of many overlapping wavegroups radiated by discrete sources in the volcano. The standard periodogram power spectrum P(f) describes the frequency distribution of the total power of the source ensemble averaged over time intervals of some 10 min. P(f) can therefore be used as an estimator for activity monitoring.

To resolve the elemetary radiation processes of the individual sources the tremor time series must be decomposed into the single wavegroups. Using a single-component recording the maximum entropy method can be applied to separate P(f) into short-term spectra (Seidl et al.,1990).

Using a three-component recording, the maximum entropy method can be combined with trajectory polarization analysis to determine the vector motion of the wavegroups associated with a given power peak. It has resolved the displacement tremor motion recorded at station Torre del Filosofo (Mt. Etna) in the narrow frequency band around the most frequent 0.93 Hz maximum entropy spectral peak. The polarization is mainly horizontal with two predominant, approximately orthogonal azimuths, almost radial and transverse to the central crater. The ellipses in the horizontal motion show time variations with coherent polarization over intervals up to 80 s and rapid transitions between these steady states. These observed times of coherence indicate a bell-like resonance associated with the 0.93 Hz peak, for example the oscillation of an acoustic resonator (Schick, 1988), a block vibration driven by magma pressure variations or a fluid-driven crack (Chouet, et al., 1987). Since Torre del Filosofo is located in a distance of about 1.5

km from the crater, it is possible that the observed mainly horizontal polarization and its rapid time variations could be explained by the near-field waves radiated by a moving extended source or by a pair of coupled sources.

To distinguish between various models of sources and propagation effects, it is necessary to record the tremor near-wavefield with a small portable network of three-componenet broadband seismometers. Measuring the spatial and temporal coherence and polarization in the frequency bands of the discrete sources it will be possible to determine the hypocenters of the sources and to reveal the physics of the elementary radiation processes.

References

Chouet, B., R. Koyanagi and K. Aki: Origin of volcanic tremor in Hawaii, Part II: Theory and discussion.
U.S. Geological Survey Prof. Paper, 1350, 1259-1280, 1987.

Dietel, C., B. Chouet, K. Aki, V. Ferrazini, P. Roberts and R. Koyanagi: Data summary for dense GEOS array observations of seismic activity associated with magma transport at Kilauea volcano, Hawaii.
Open-File Report 89-113, U.S. Geological Survey, Menlo Park, California, 171 p., 1989.

Ferrazini, V., K. Aki and B. Chouet: Characteristics of seismic waves composing Hawaiian volcanic tremor and gas-piston events observed by a near-source array.
J.Geophys.R., 1990 (in press)

Matsumura, S.: Three-dimensional expression of seismic particle motions by the trajectory ellipsoid and its application to the seismic data observed in the Kanto district, Japan.
J.Phys.Earth 29, 221-239, 1981.

Schick, R.: Volcanic tremor-source mechanism and correlation with eruptive activity.
Natural Hazard 1, 125-144, 1988.

Seidl, D.: The simulation problem for broad-band seismograms.
J. Geophys. 48, 84-93, 1980.

Seidl, D., S.B. Kirbani and W. Brüstle: Maximum entropy spectral method of volcanic tremor using data from Etna (Sicily) and Merapi (central Java).
Bull.Volcanol. 52, 460-474, 1990.

Acknowledgements: We thank R. Schick and the Istituto di Scienze della Terra, Catania for supplying the digital tremor recordings , J. Wassermann (University Munich) for computational assistance and H. Rademacher, B. Chouet and D. Hill for critically reading the manuscript and for many stimulating suggestions.

VOLCANIC TREMOR OBSERVED DURING VARIOUS STAGES OF MAGMA DOME BUILDING ACTIVITY ON MERAPI (CENTRAL JAVA, INDONESIA)

SRI BROTOPUSPITO KIRBANI

Physics Department, Gadjah Mada University, Sekip Unit III, P.O.Box BLS 21, Yogyakarta, Indonesia.

Abstract

In middle of October 1986, a lava dome building started, lasting about one month at the summit area of Mount Merapi. During that time 1.5 million cubic meters of additional volume grew over an old lava dome. Volcanic tremor with different spectral patterns has been observed before, during and after the doming period. This paper deals with possible source mechanisms explaining the characteristic of the tremor spectra.

Keywords : Volcanic Tremor - Spectral Patterns - Merapi Dome Building.

Introduction

Mount Merapi is one of the most active volcanoes in the world, located in Central Java, with a summit height of 2911 m. Since the beginning of the 11th century, Merapi has shown a large variety of volcanic activities, for instance lava dome building and eruptions with various gas contents (*Hartman, 1935*).

Between October and November 1986, Merapi showed lava dome building with 1.5 million cubic meter additional volume (*Anonymous, 1987 ; Ratdomopurbo, 1989*). There were various kinds of volcanic tremor (*Kirbani, 1990*) observed since July 1986 to February 1987 which accompanied the various stages of the dome building. The tremor showed significant variations in the spectral composition.

Data Acquisition

A seismic network consisting of 3 stations (KLT, LBH, and KKN) at the volcano and a fourth station (MTK) located 50 km south of Merapi, delivered the data for this research (fig. 1). A 1 Hz vertical seismometer (*L4A by Mark-Products*) is in use at each station. Radio telemetry (*FM, made by Lennartz Electronics, FRG*) is used for data transmission. The data acquisition system using magnetic tape recording has a dynamic range of about 50 db (0.1 - 50 μm/s) and a frequency bandwidth of 1 - 100 Hz. A spectrum analyzer (*SD340 by Scientific Atlanta*) allows immediate observation of the spectral content of the incoming data.

Hourly averages of absolute tremor amplitude time series at stations KKN, LBH, and KLT, calculated from July 1, 1986 to February 28, 1987, are shown in figs.2 - 5. As a typical example, a seismogram is illustrated in fig. 6.

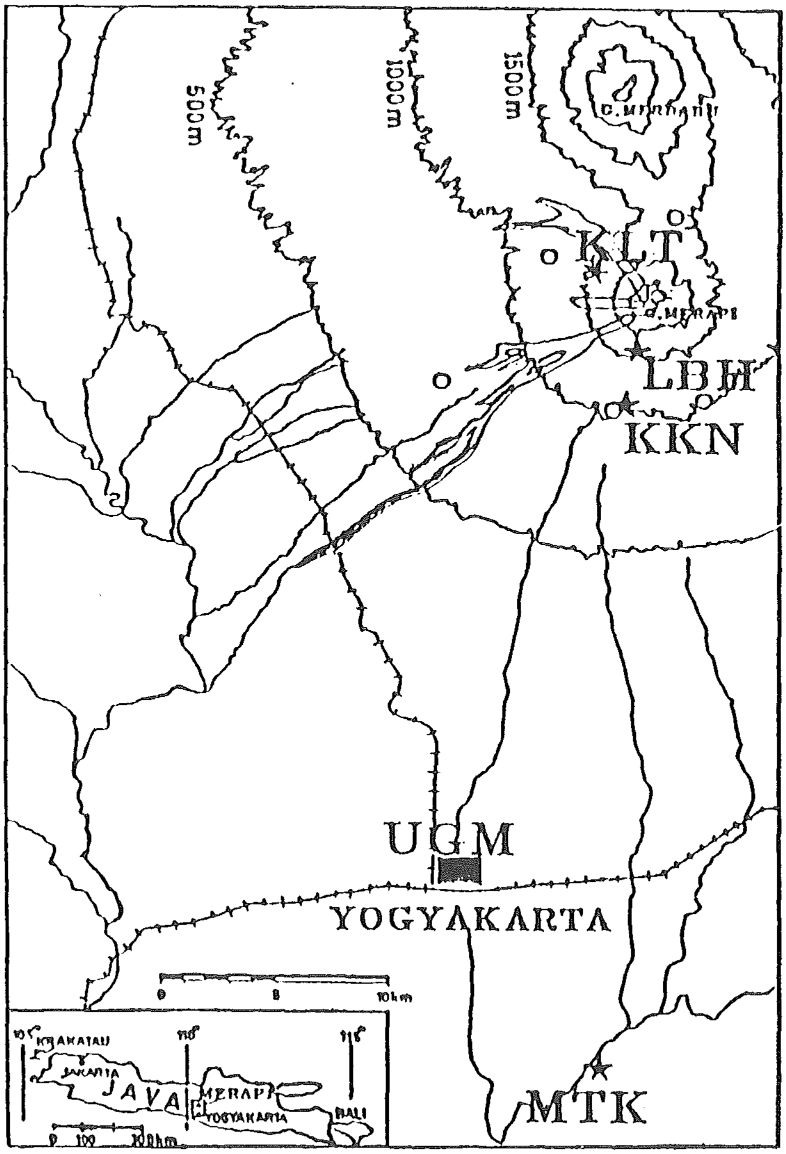

Fig. 1 Map showing locations of seismic stations (KLT, LBH, KKN, and MTK) used for data acquisition during this study.

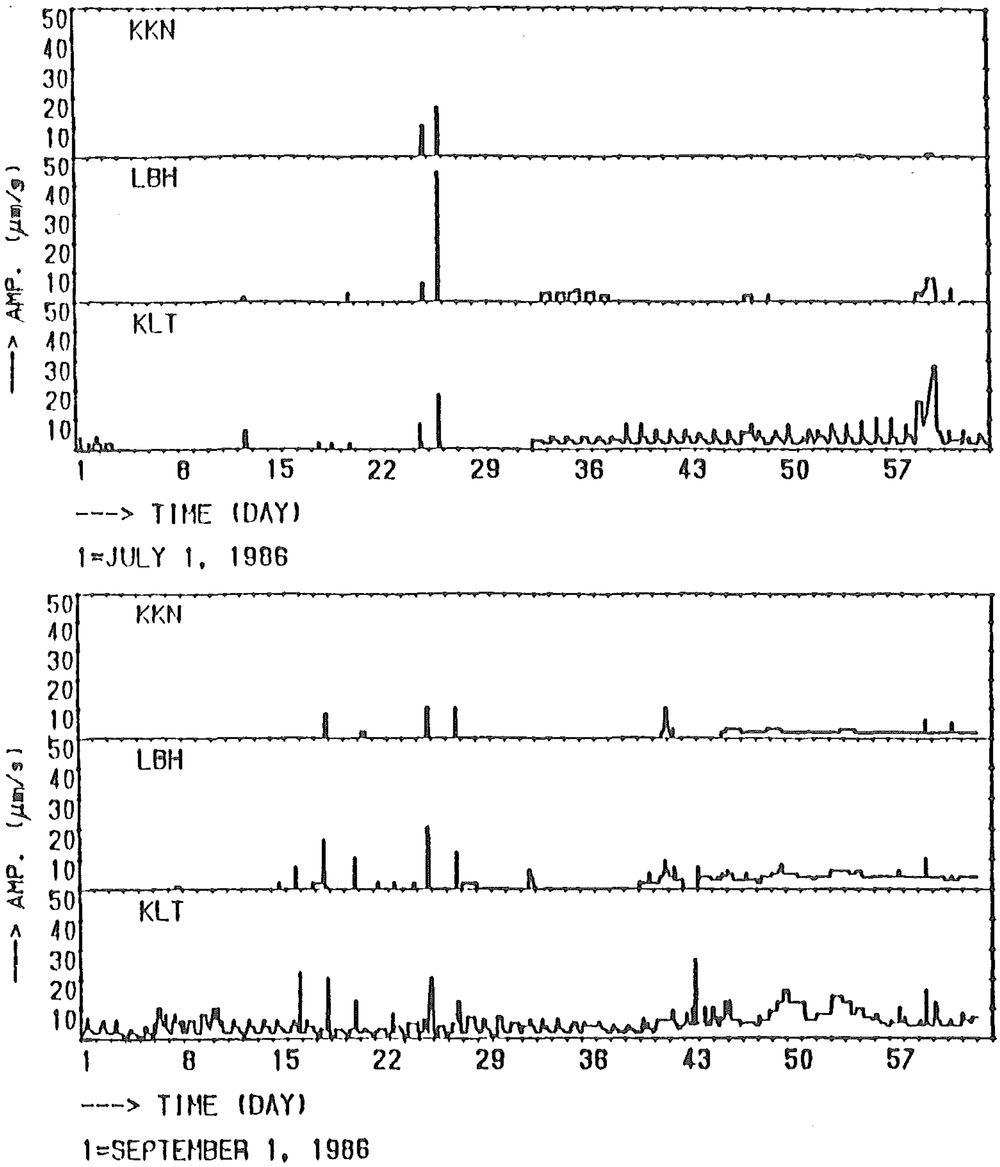

Figs. 2 and 3 Hourly averaged absolute tremor amplitude time series at stations KKN, LBH, and KLT, calculated from July 1, 1986 to August 31, 1986 (above) and from September 1, 1986 to October 31, 1986.

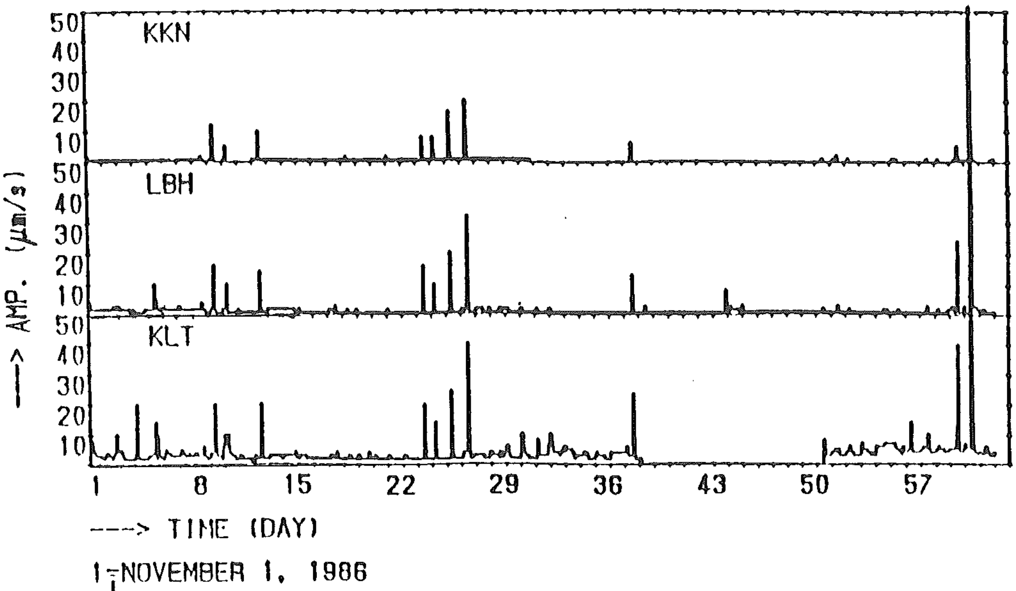

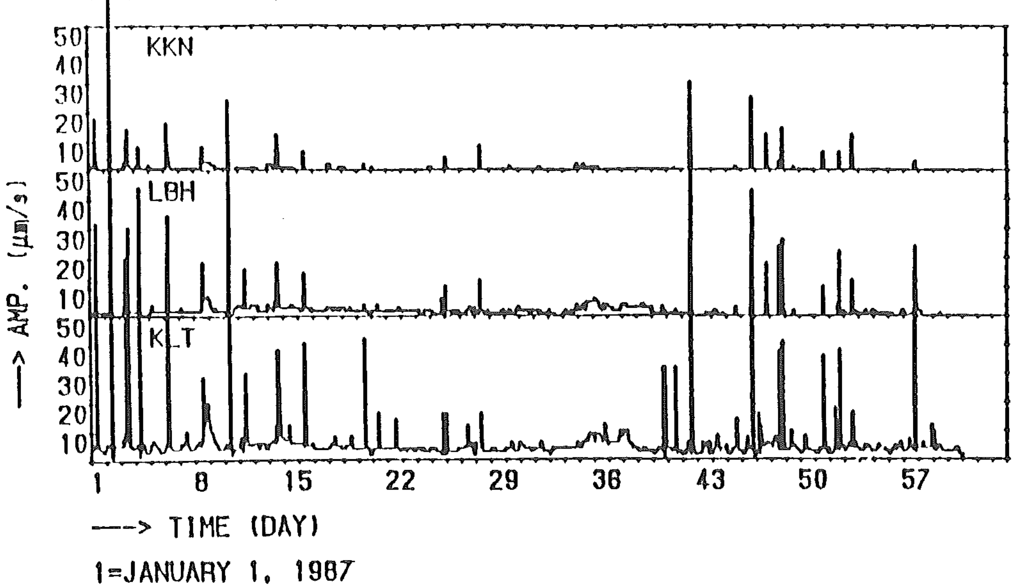

Figs. 4 and 5 Same as figs. 2 and 3, but from November 1, 1986 to December 31, 1986 and January 1, 1987 to February 28, 1987.

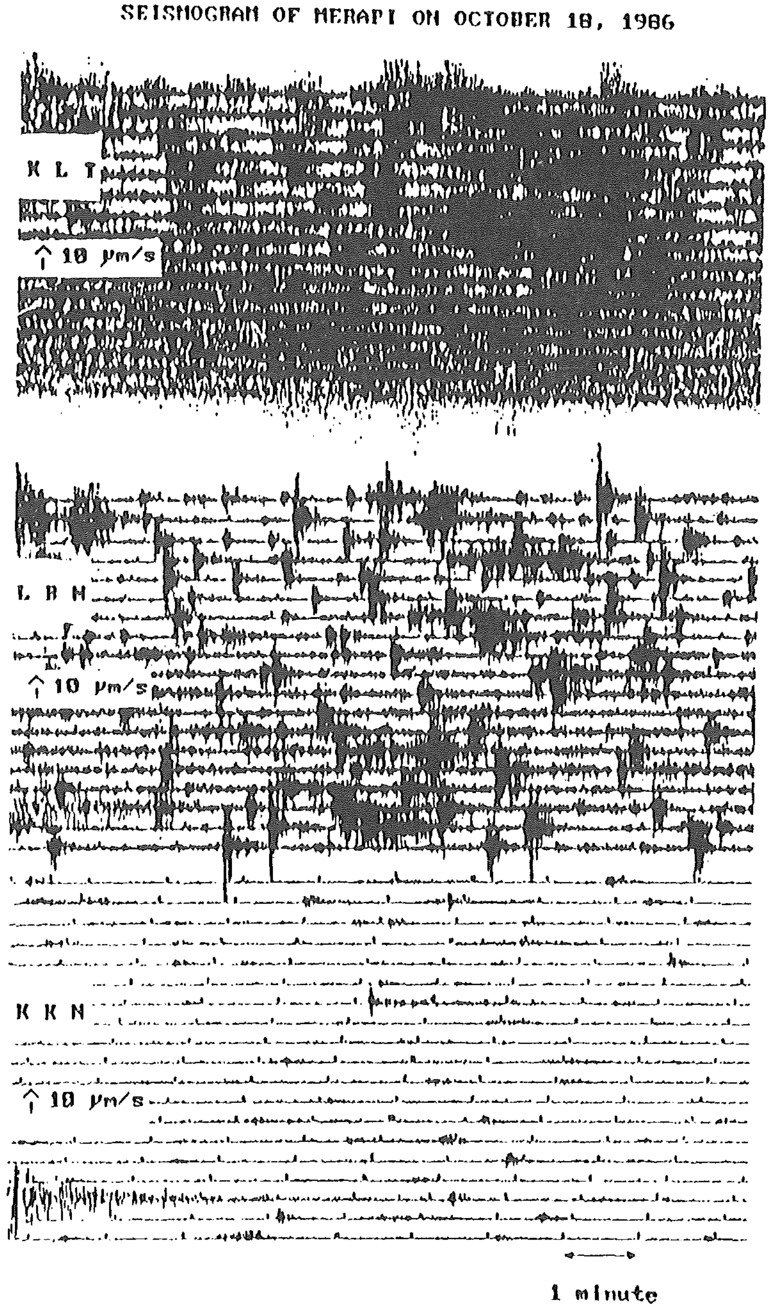

Fig. 6 Seismogram showing volcanic tremor and events recorded at KLT, LBH and KKN on October 18, 1986.

It can be seen in fig.2 that at KLT continuous volcanic tremor and at LBH intermittent tremor started at the beginning of August 1986. It followed transient tremor which was observed on July 24 and 25, 1986, recorded at KLT, LBH, and KKN. *Kirbani (1990)* calculated tremor source locations based on the relative amplitude ratios (*Fadeli, 1988*) of tremor measured at the three stations. The resulting source depths were 500 m ± 100 m from the summit. A calculation of the radiated power of the volcanic tremor, based on the assumption that the tremor consisted mainly of compressional waves (the tangential component of the tremor amplitude was smaller than the radial and vertical ones) and radiated spherically from a point source, yielded 35 watts. During the doming process the tremor source locations shifted to deeper (2800 m below the summit) parts of the volcano and the power signifi - cantly increased to 2400 watts.

FFT spectra of the volcanic tremor during this time are displayed in waterfall illustrations in figs. 7 - 9.

Visual vs. Tremor Observations

Although there exists an increase in the intensity of volcanic tremor during the starting phase in August 1986, there occurred no significant change in the visual activity, up to beginning of October 1986. The lava dome was still small (1.5 *

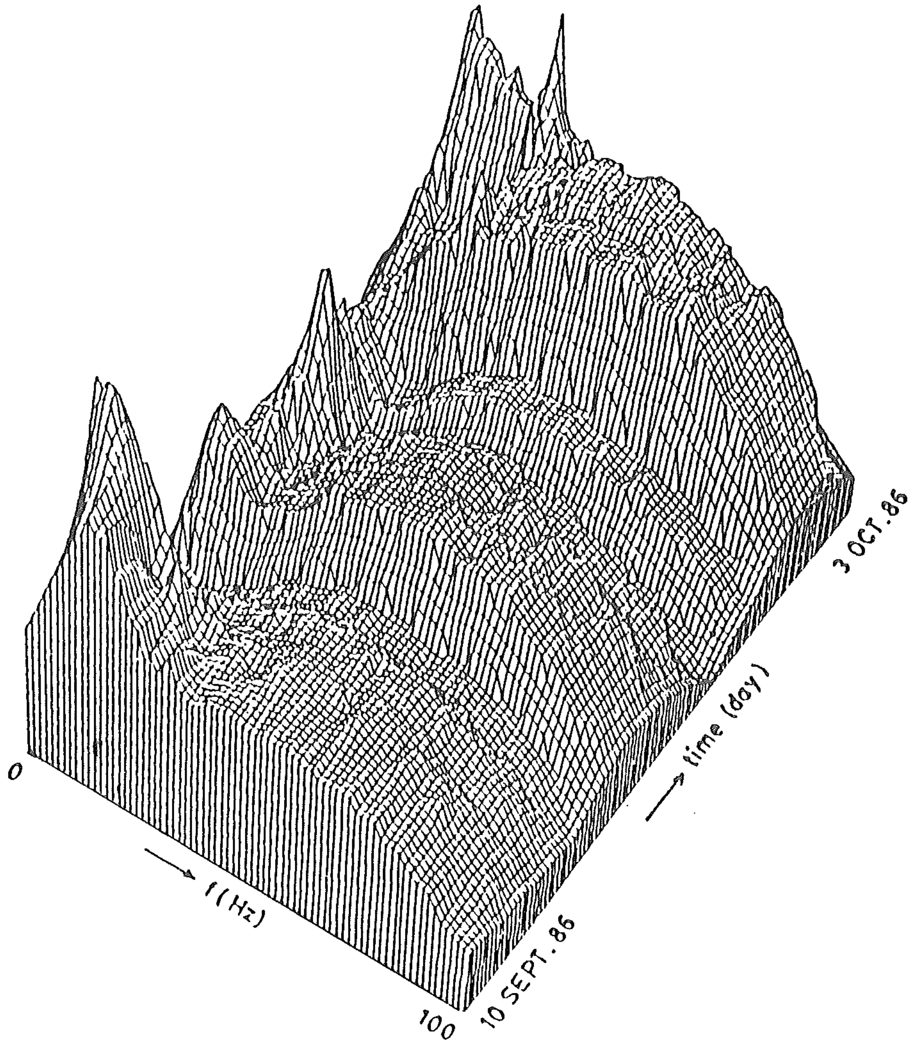

Fig. 7 Three dimensional view of spectra of tremor recorded at KLT before the lava dome building in October 1986.

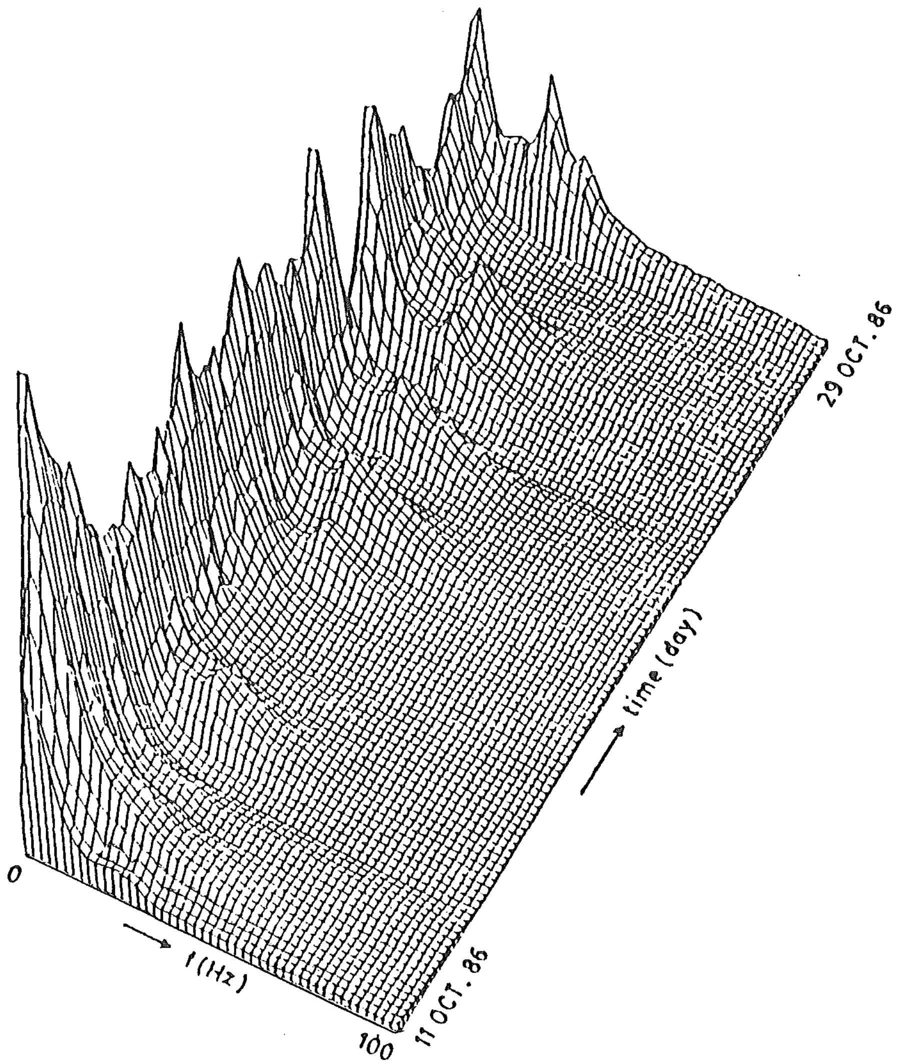

Fig. 8 Same as fig. 7, but during the dome building.

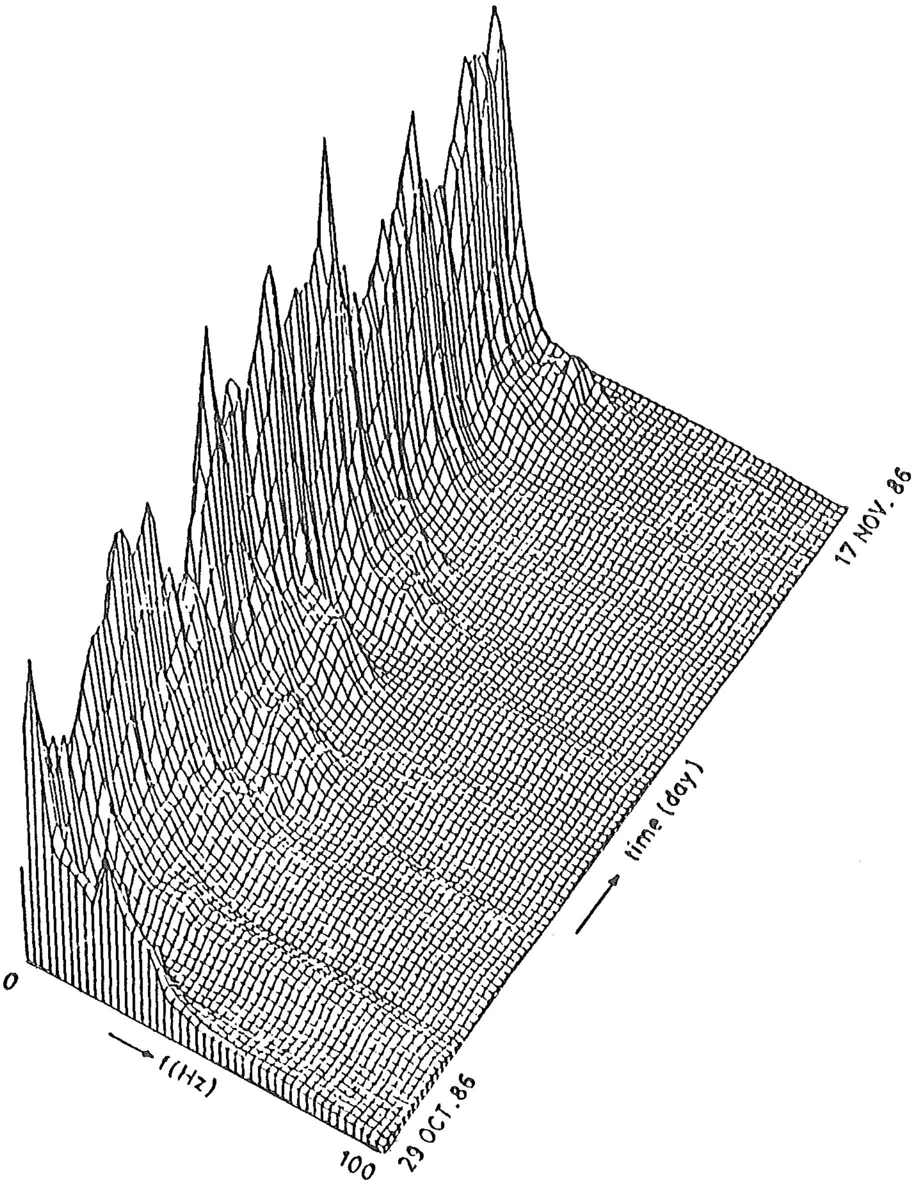

Fig. 9 Same as fig. 7, but after the doming episode.

10^6 m^3, *Ratdomopurbo, 1989*) and it showed an irregular shape. On October 17, 1986, the shape of the lava dome changed to a more rounded and larger bulge. The bottom part of the dome was glowing with a temperature around 1000 C. The water vapour emission from December 1986 to January 1987 was possibly influenced by the precipitation during the rainy season.

Three kinds of characteristic spectra corresponding to the stages before, during, and after the Merapi magma dome building can be distinguished (figs. 10 and 11 to 13).

Stage 1 (Before doming)

From the beginning of August 1986, there occurred more or less continuous volcanic tremor with a radiated power of 35 watts. The source location was in the upper part of the volcano and (500 ± 100) m below the summit. The spectra (figs. 7, 10 and 11) of the tremor show a pronounced broadband bulge in the higher frequencies. The lower frequency range ($f < 20$ Hz) shows a maximum peak varying from about 3 Hz to 10 Hz. There were only several transient tremor observed during this period.

Stage 2 (During Doming)

During this stage (October 11 to November 11, 1986), many events were recorded (fig. 6) superimposing continuous tremor with sometimes beating-like vibrations. The average power radiation

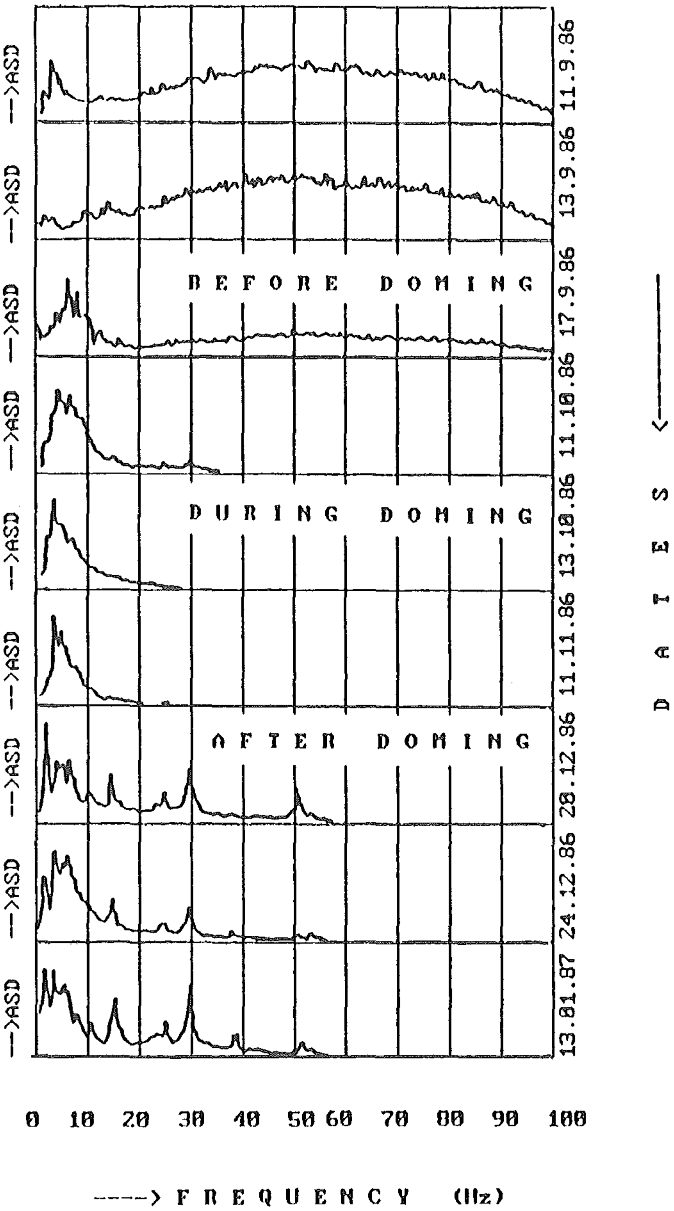

Fig. 10 Time varying spectral patterns before, during, and after the lava dome building in October 1986.

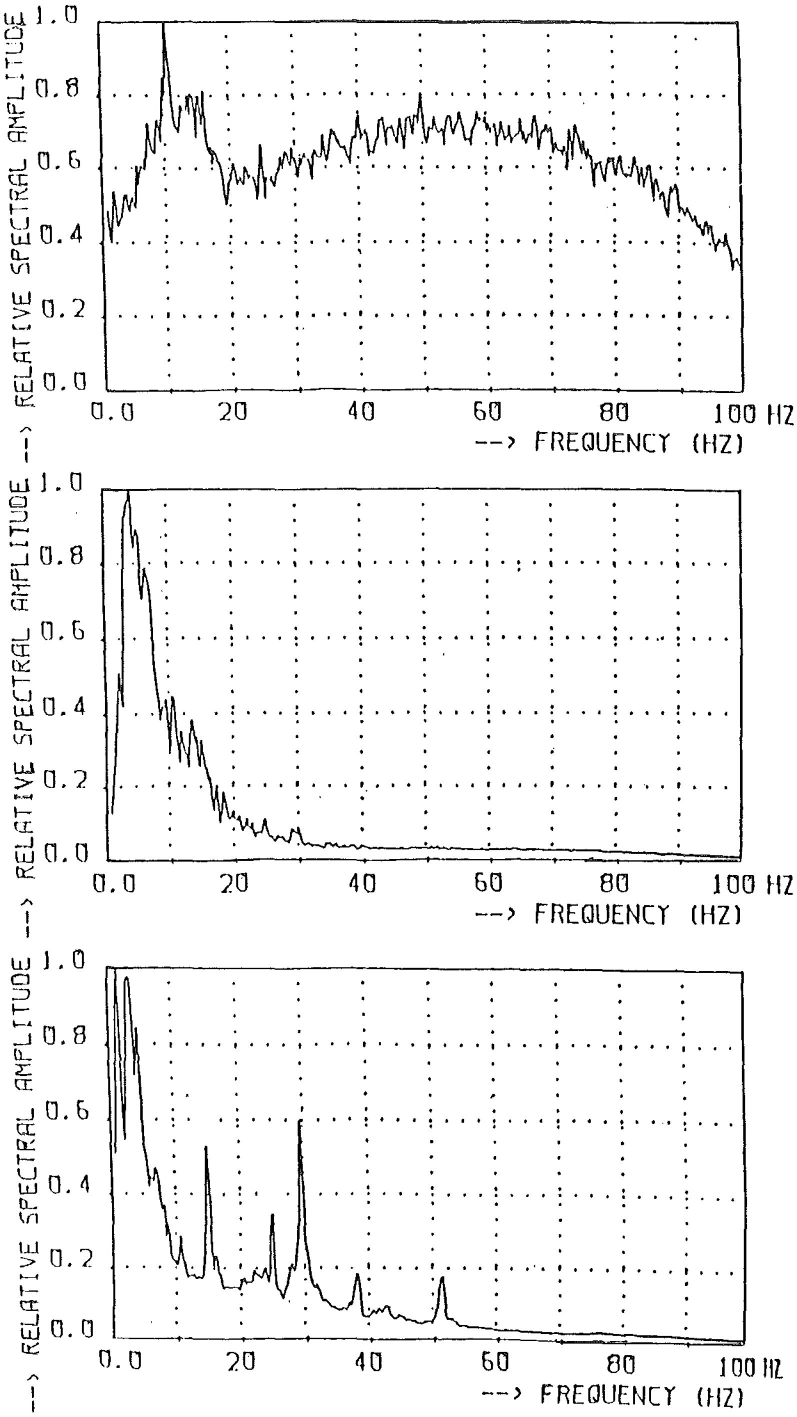

Figs. 11 (top), 12 (middle) and 13 (bottom) Amplitude frequency spectra of ground velocity vibrations detected at KLT showing characteristic spectral patterns, respectively, within episodes before, during and after doming process.

of the volcanic tremor was 2400 watts, with a source depth of (2800 ± 300) m beneath the summit. The spectra changed to a smaller bandwidth, and the bulge at the high frequency portion became negligible. The maximum peaks of the spectra concentrated between 2 to 6 Hz (figs. 8, 10 and 12).

Stage 3 (After doming)

After the doming episode, power radiation of the continuous tremor decreased to about 640 watts, with a source location similar to stage 2. Transient events were still recorded, but it seemed that beating-like tremor disappeared. During this stage, the spectral energy still concentrated below 10 Hz, but additonally there were stable peaks at 14.75 , 24.50 and 29.25 Hz (figs. 9, 10 and 13).

Interpretation

Volcanic tremor is seismic waves caused by pressure variations of the flowing magma to the solid conduit walls. The magma usually presents a multiphase fluid (liquid and / or gas phases, *Rittmann and Rittmann, 1978*). Pressure fluctuations inside the magma flow system should be the result of nonstationary flow, as stationary flow does not create a varying pressure field (*Moehring et al, 1983*).

Kirbani (1983, 1990) using the studies of *Morse and Ingard, 1968, Seidl et al, 1981 and Blake, 1986,* gave model graphs of tremor spectra caused by monopole, dipole and quadrupole flow, as well as bubble dynamics. Applications of this idea to tremor observations during various stages of the October 1986 lava dome building can be described in 3 stages. The dominant spectral components contributing to this interpretation are represented in fig. 14.

Stage 1 (Before Doming)

The shape of the spectrum as shown in figs. 7, 10 and 11 can be represented as a combination of a spectrum of random bubble inception and cavitation (fig. 14 a) superimposed on a spectrum of random quadrupole flow (fig. 14 b). The locations of the two sources with the different mechanisms are 1000 m and 3000 m from the KLT station, respectively, for the bubble and the quadrupole flow.

Stage 2 (During Doming)

The spectra of this stage as depicted in figs. 8, 10 and 12, which have a stable shape in the low frequency part (f < 20 Hz), correspond to a spectrum of random dipole flow (fig. 14 c). The dipole flow is situated about 2000 m from station KLT.

Stage 3 (After Doming)

The pattern of tremor spectra as shown in figs.

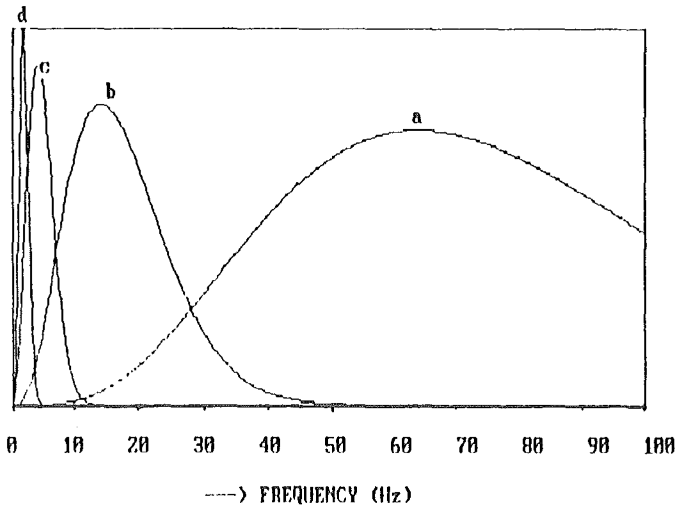

Model graphs calculated using the following formula (*Seidl et al, 1981 ; Kirbani, 1983 and 1990*) :

$$A(r,f) = \sum_i A_i \; (f)^{N_i} \exp\left(- \left(M_i \, f^2 + \frac{\pi f}{v * Q} \, r \right) \right)$$

Where :

$A(r,f)$	Spectral amplitude of volcanic tremor at a distance r from source at frequency f .
A_i	Vibration amplitude of the i^{th} source.
N_i	Terms of monopole, dipole, quadrupole flow and bubble dynamics, i = 1 . . . . 4 .
M_i	Mutual coupling coefficient.
v	Wave speed.
Q	Quality factor.
Graph a	Bubble dynamics ; N_i = 4 ; M_i = 1E-6 ; r = 1000 m.
Graph b	Quadrupole flow ; N_i = 3 ; M_i = 1E-3 ; r = 3000 m.
Graph c	Dipole flow ; N_i = 2 ; M_i = 5E-2 ; r = 2000 m.
Graph d	Quadrupole flow ; N_i = 3 ; M_i = 5E-1 ; r = 3000 m.

v = 1800 m/s and Q = 28 .

Fig. 14 Dominant components of model graphs fit to spectra shown in figs. 11, 12 and 13.

9, 10 and 13, can be represented as a combination of spectra of random quadrupole flow (in a location about 3000 m from KLT, fig. 14 d), random dipole flow (2000 m from KLT, fig. 14 c), and resonators (in the lava dome) contributing to sharp spectral peaks.

Discussions and Conclusions

Volcanic tremor is characterized by several physical parameters like for instance power radiation, frequency content, locations of the sources and the specific type of its vibrations e.g. transient, harmonic, or beating like.

Power radiation of volcanic tremor can be calculated only after the determination of the source location, shape of the source which determines the tremor radiation pattern, intensity of the vibrations at a certain position in relation to the source, and the type of waves, i.e. body or surface waves. This power radiation represents the level of activity inside the generator of the tremor, when acoustic coupling between the source and tremor propagating medium and also the acoustic effiency of the generator are known. There is reason to assume that the level of activity corresponds to the level of flow instability.

In the pre-doming process of Merapi in 1986, the tremor spectra are interpreted as a result of two kinds of sources : the shallow bubbling process and the deeper quadrupole flow. *Kirbani (1990)* assumed that the bubbling process took place in a magma column about 500 m underneath the old lava dome which could include the pyromagma (*Rittmann and Rittmann, 1978*) of Merapi. The quadrupole flow in the deeper part (about 3 km distance from KLT or 2.5 - 3 km below the summit) could be associated with convections in a magma chamber. During this period, power radiation of tremor was still low (about 35 watts), possibly due to inefficient acoustic coupling between the pyromagma of low impedance and the conduit wall of much higher mechanical impedance. The convection of the magma in the deeper part is also associated with a low efficiency acoustic generator because of the quadrupole flow pattern.

In the doming episode, the dominant magma flow corresponds to dipole flow in an intermediate depth, 2 km distance from KLT or 1.5 - 2 km below the summit. It might represent up and down flow in a magma pipe of Merapi which radiated 2400 watts of tremor waves. The process was associated with a transport of 1.5 million cubic meter of magma in about one month.

The post doming period was characterized by a combination of dipole flow, quadrupole flow and conduit resonances. Visually, Merapi showed steaming activity. It can be supposed that in the system of the lava dome some caverns existed which could act as resonators activated by steam jets. The dipole and quadrupole flow showed that there were still thermal instabilities inside the fluid system of Merapi. From December 1986 to August 1987, the lava dome was growing with various rates, lower than the rate of the lava doming in October 1986. During a 9 months interval, the magma dome increased by about one million cubic meters (*Ratdomopurbo, 1989*).

Assuming a 1000 m length of a vertical conduit from the summit of Merapi (*Fadeli et al, 1986*) and a density of magma of 2800 kg m^{-3} , the magma doming rate of $1.5 * 10^6$ m^3 per month means that considering potential energy alone and neglecting friction, the magma mass was transported against gravitational force with a power of $16.2 * 10^6$ watts. The tremor power radiation of 2400 watts was partially produced from this transportation or fluid flow power. Therefore, the power ratio between magma flow and tremor gives a value of $0.15 * 10^{-3}$. The acoustic effiency of dipole flow (*Morse and Ingard, 1968 ; Kirbani 1983 and 1990*) corresponds to the third power of the ratio between flow speed and sound speed of the magma. Using this power law and the acoustic effiency as calculated above, we can find a dipole flow speed of 1/19 of the acoustic wave speed in the magma. Assuming a wave speed of 1000 m/s (*Schick et al, 1982*) in liquid magma and 340 m/s in the gas, a dipole magma flow speed of about 50 m/s or 17 m/s, respectively, might follow. Sound speed in a fluid medium can be drastically reduced by the presence of gas or vapour in the liquid (*Wallis, 1969 ; Kieffer, 1977*), and even reach values much below the value of the sound speed of the single phase, e.g. 20 - 50 m/s. Therefore, the flow speed of the magma containing bubbles could even drop in the order of magnitude to a few meter per second.

The above calculation has not taken into acount the acoustic coupling between the tremor source and the propagating medium. The propagating medium of the tremor in a volcanic area, which is a combination of ash or tuffs, sand, lapilli and lava, has an average density of about 2500 kg m^{-3}, and this is usually lower in density than the fluid magma with a density around 2800 kg m^{-3}. On the other hand, the sound speed in the magma fluid which is 100 to 1000 m/s may be much less than that in the tremor propagating medium (1500 to 2000 m/s). In a qualitative sense, the acoustic coupling between the tremor source and the propagating medium will be worse when the fluid magma has higher void content. This may partly explain why in the episode before the doming, when the tremor spectral pattern showing bubble dynamics, the power radiation of tremor was very low due to the bubble dynamics.

Acknowledgements

This study was conducted in a joint project on physical volcanology between the Gadjah Mada University, Yogyakarta, Indonesia and the Institute of Geophysics, University of Stuttgart, Federal Republic of Germany.

The author would like to thank Prof. Dr. R. Schick and Dr. W. Bruestle for reviewing this manuscript.

This study was financially supported by BPPT Jakarta, LIPI Bandung, Nuffic Physics Project GMU-VUA Yogyakarta, Indonesia and Forschungszentrum (KFA), Juelich, Federal Republic of Germany.

References

Anonymous, 1987, Summary of recent volcanic activities in 1986, Bulletin of Volcanology 49 : 461 - 463.

Blake, W.K., 1986, Mechanics of flow-induced sound and vibration, Applied Mathematics and Mechanics V.17-II, Complex Flow-Structure Interactions, Academic Press Inc. Orlando.

Fadeli, A., 1988, Volcanic earthquakes at Merapi (Central Java) during the lava dome building beginning in October 1986, Paper presented at the International Workshop of Volcanic Seismology, IAVCEI, October 3-8, 1988, Capri, Italy.

Fadeli A., S.B. Kirbani, R. Mugiono, and R. Schick, 1986, Preliminary analysis of seismic data gathered with a new seismic station network on the Merapi volcano (Central Java, Indonesia), Paper submitted to The Journal Physics of the Earth, Japan.

Hartman, M.A., 1935, Die Ausbrueche des G.Merapi (Mittel Java) bis zum Jahre 1883, Neues Jahrbuch fuer Mineral Beil., V.75, p.127-162.

Kieffer, S.W., 1977, Sound speed in liquid-gas mixture ; Water and steam, Journal of Geophysical Research, V.82, No.20, p. 2895-2904.

Kirbani, S.B., 1983, Analysis and interpretation of volcanic tremor at Etna (Sicily, Italy), Institute of Geophysics, University of Stuttgart, Federal Republic of Germany, Publication No. 210, 1-106.

Kirbani, S.B., 1990, Analysis of volcanic tremor at Mount Merapi (Central Java, Indonesia) in order to understand internal magma flow, Doctor thesis of the Gadjah Mada University, Yogyakarta, Indonesia.

Moehring, W., E.A. Mueller, and F. Obermeier, 1983, Problems in flow acoustics, Reviews of Modern Physics, V. 55, No. 3.

Morse, P.M., and K.U. Ingard, 1968, Theoretical acoustics, McGraw - Hill Book Company, New York.

Ratdomopurbo, A., 1989, Annual report of the world volcanic eruptions in 1986, especially for Mt. Merapi (Central Java, Indonesia), Supplement to Bulletin of Volcanology 51.

Rittmann, A., and L. Rittmann, 1978, Volcanoes, Orbis Publishing, London.

Schick, R., G. Lombardo, and G. Patane, 1982, Volcanic tremors and shocks associated with eruptions at Etna (Sicily), September 1980, Journal Volcanology and Geothermal Research, V.14, 261-279.

Seidl D., R. Schick, and M. Riuscetti, 1981, Volcanic tremor at Etna : A model for hydraulic origin, Bull. Volcanol., V.44, p. 43 - 56.

Wallis, Graham B., 1969, One-dimensional Two-phase Flow, McGraw - Hill Book Company, New York.

Rayleigh-Bénard Convection in Extended Magma-Chambers

G.MEINHARDT
Lehr- und Forschungsbereich Theoretische Astrophysik der Universität Tübingen
Auf der Morgenstelle 12 C
7400 Tübingen

Abstract

The spectral analysis of volcanic tremor at Etna provides not only a structure model of the magma conducting system consisting of a flat magma chamber and pipes leading to the crater, but attaches the dipol hydrodynamic motion to the pipes and a quadrupole vortex flow to the magma chamber, too.

The seismic amplitude has a temporal behaviour comparable to typical stability problems, if the volcano gets more active.

The simplest physical model which might explain both the vortex flow as well as its temporal increase is that of the Rayleigh-Bénard convection. From synergetics an analytical solution was used for free-free boundary conditions, the fluid layer extended to infinity, to appreciate the time development of the convectional motion.

So three problems had been clarified:

1) The conditions for Rayleigh-Bénard convection are fulfilled for most of the magma chambers .
2) The Boussinesq approximation an assumption made for all calculations of Rayleigh-Bénard convection is valid in the magma parameter region.
3) From the analytical solution for the time behaviour of the convectional motion near the first instability follows that there is no correlation between the increase of the convectional motion and the seismic amplitude. Such a correlation for higher control parameter regions could not be excluded at all but this is very doubtful and could only be shown with the results of extended numerical calculations.

Introduction

Seismic measurements near active volcanoes such as Etna on Sicily or Merapi on Indonesia show signals consisting of a carrier frequency from 1 to 10 Hz and a modulation period from 10 sec to many hours. This phenomenon of volcanic tremor increases at the beginning of the eruptive phase until the amplitude reaches a maximum. Now the value remains either nearly constant for several hours and then decreases to the original value (Etna) or the seismic intensity slowly returns to the starting amplitude just after having reached the maximum (Merapi). The activity of the volcano is connected to the seismic amplitude in such a manner that the more active period which represents not necessarly an eruption starts with increasing amplitude and stops if the original amplitude is reached (Cosentino et.al., 1982, Schick et.al., 1982, Schick, 1981). This volcanic tremor needs an explanation.

Many phenomena support the hypothesis that the seismic intensity of the volcanic tremor depends on a not yet appointed power of the magma flow velocity. The magma leading system consists of a magma chamber lying several kilometers below the summit of the volcano. This magma chamber is linked to the crater surface through channels and dikes and there are connections to deeper lying magma reservoirs (Pichler & Schick, 1985).

A long-distance field expansion of a stochastic fluid flow in a monopole source, a dipol source and a quadrupole source associates the Fourier components of the seismic output with monopole, dipole and quadrupole motion (Morse & Ingard, 1968, Seidl et. al.,1985)

The M-value of the monopole term is equal to zero and the M-value of the quadrupole term is more than one order of quantity higher than that of the dipole term. This is the reason for the following conclusions. The dipole term belongs to the vertical up and down flow of the magma in the dikes and channels where the horizontal motion disappears. The quadrupole part of the seismic output can be identified as a vortex flow in the extended magma chamber (Kirbani, 1983).

The simplest model describing both the temporal course of the seismic amplitude being typical of stability problems, and the vortex flow in the large magma chamber, is that of the Rayleigh-Bénard-Convection.

The Rayleigh-Bénard Problem

In a fluid layer heated from below a certain volume element expands, thus the density is diminished resulting in a buoyancy force in the positive z-direction. The friction caused by the viscosity of the fluid particles prevents them to move upwards. This is the stationary case of heat conduction. Increasing the temperature gradient the buoyancy force grows and at a certain value of the temperature gradient the convectional motion sets in forming patterns of up and down motion such as hexagonal cells or rolls. Further heating leads over three-dimensional patterns and time-dependent convection to an irregular chaotic movement.

The reason for the transition from heat conduction to convection or from convectional motion to a higher order convection must be the increase of a control parameter, the temperature gradient. This could be accomplished, if hot magma from a deeper reservoir slowly enters the magma chamber. Supposing that the density of the entering magma is lower than that in the chamber a thin layer of hot and dense magma is formed at the bottom of the magma chamber heating the material above it.

The Rayleigh-Bénard-problem is a typical stability problem in physics and represents a good possibility to investigate the route to chaos. To compare the temporal course of the seismic amplitude with the time evolution of the convectional motion, we have to find a differential equation for the time dependence of the velocity. Starting with the basic equations and the solution of the linearized problem (Landau & Lifshitz, 1966; Chandrashekhar, 1966) we can get the generalized Landau-Gintzburg-equations for the velocity amplitude when we follow the methods developped in Synergetics (Bestehorn, 1983; Bestehorn & Haken, 1984; Haken, 1982; Wunderlin 1975).

From conservation of matter we obtain the continuity equation

$$\operatorname{div} \vec{u} = 0, \tag{1}$$

valid for incompressible fluids, whith the velocity-field $\vec{u}$.
Conservation of momentum leads to the Navier-Stokes-equation

$$\frac{\partial \vec{u}}{\partial t} + (\vec{u}\nabla)\vec{u} = \frac{1}{\varrho_0}\vec{F} - \frac{1}{\varrho_0}\nabla P + \nu \Delta \vec{u}, \tag{2}$$

The only external force is the gravitation $\vec{F} = \vec{g} \cdot \varrho$ with $\vec{g} = -|\vec{g}| \cdot \vec{e}_z$. The density ϱ is assumed being constant overall with the exception of this gravitational term. This fundamental assumption made for nearly all convection calculations is the well-known Boussinesq approximation (see also equation (4) and the chapter treating higher instabilities). P is the pressure distribution, ν is the cinamatic viscosity.

The conservation of energy provides us with the equation describing thermal conduction

$$\frac{\partial T}{\partial t} + (\vec{u}\nabla)T = \kappa \cdot \Delta T \tag{3}$$

where T is the temperature field and κ the temperature conductivity.

The boundary conditions for the temperature field are ideal conducting boundaries and the temperature distribution has to be homogenous. For the velocity field we have the conditions for free boundaries $u_z = \partial u_x/\partial z = \partial u_y/\partial z = 0$ or rigid boundaries $\vec{u} = 0$. The density is given after a Taylor expansion by the following equation of state, α being the expansion coefficient

$$\varrho(T) = \varrho_0(1 - \alpha(T - T_0)) \tag{4}$$

Together with the Boussinesq approximation we get the homogenous stationary solution of the problem

$$\vec{u} = 0. \tag{5}$$

$$T^{(s)} = \left(\frac{T_1 - T_0}{d}\right) \cdot z + T_0. \tag{6}$$

$$P^{(s)} = P_0 - \varrho_0 \cdot gz\left(1 + \frac{1}{2}\alpha\beta z\right). \tag{7}$$

Here, d is the layer thickness and β means the expression for the temperature gradient $\beta = (T_1 - T_0)/d$. The solution of the linearized problem can be obtained as follows. Introducing deviations from the stationary solution

$$\vec{u} = \vec{u}^{(s)} + \vec{u}' \tag{8a}$$

$$T = T^{(s)} + \Theta \tag{8b}$$

$$P = P^{(s)} + \varrho_0 \cdot w \tag{8c}$$

leads to the Rayleigh-Bénard problem adapted equations, if we scale all variables in the following way :

$$\vec{r} = d \cdot \vec{r}', \quad t = \frac{d^2}{\kappa} t', \quad \vec{u} = \frac{\kappa}{d} \vec{u}',$$

$$\theta = \frac{\nu\kappa}{\alpha \cdot g \cdot d^3} \theta', \quad w = \frac{\kappa^2}{d^2} w',$$

$$\frac{\partial}{\partial x} = \frac{1}{d} \cdot \frac{\partial}{\partial x'}, \quad \frac{\partial}{\partial t} = \frac{\kappa^2}{d^2} \cdot \frac{\partial}{\partial t'}$$

with d being the layer thickness.

Now we gain the equations adequate to the Rayleigh-Bénard problem

$$\operatorname{div} \vec{u} = 0 \tag{1'}$$

$$\frac{\partial \vec{u}}{\partial t} + (\vec{u}\nabla)\vec{u} = -\nabla w + P \cdot \Theta + P\Delta\vec{u} \tag{2'}$$

$$\frac{\partial \Theta}{\partial t} + (\vec{u}\nabla)\Theta = R \cdot u_z + \Delta\Theta \tag{3'}$$

where $P = \nu/\kappa$ is the Prandtlnumber and $R = \left(\alpha \cdot \beta \cdot g \cdot d^4\right) / (\nu \cdot \kappa)$ is the Rayleighnumber or the controlparameter of the system.
After linearizing the equations and several mathematical transformations (Chandrashekhar, 1966; Schlüter et.al., 1965; Zierep, 1981) we use the ansatz

$$u_3(r) = \Phi_3 \sin \pi l z \cdot e^{i\vec{k}\vec{x}} \cdot e^{\lambda t} \tag{9}$$

to obtain the following eigenvalues

$$\lambda_{1,2} = \frac{1}{2}(k^2 + l^2\pi^2)(P+1) \mp \frac{1}{2}\left[(k^2 + l^2\pi^2)(P+1) + \frac{4PRk^2}{k^2 + l^2\pi^2}\right]^{\frac{1}{2}} . \tag{10}$$

$\vec{k}$ represents the wave vector, k the wavenumber and l belongs to the mode.

If a λ_i becomes positive the solution is no longer damped and the system becomes unstable, i.e. the convection sets in. The lowest critical Rayleigh number is derived from finding the minimum of the marginal curve given by

$$R(k) = \frac{(k^2 + l^2\pi^2)^3}{k^2} \tag{11}$$

For $l = 1$ this critical Rayleigh number reads

$$R_c = \frac{27}{4}\pi^4 \text{ where } k_c = \frac{\pi}{\sqrt{2}} \tag{12}$$

is the inherent wave vector for free boundaries.

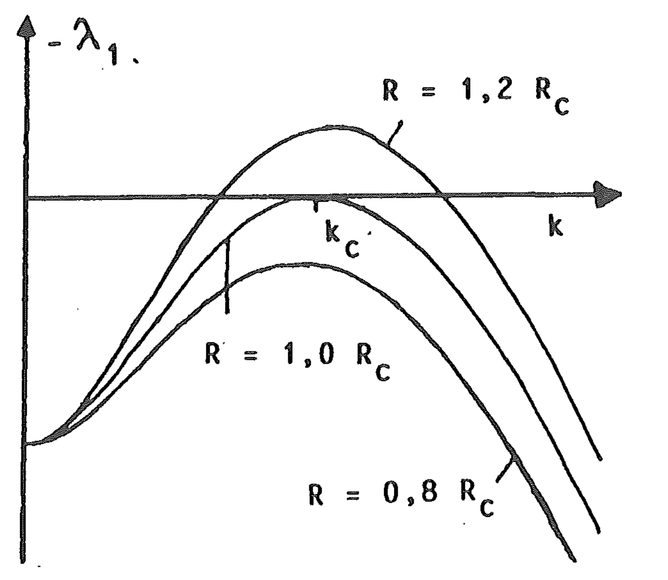

Figure I:
Eigenvalue λ_1 plotted over the wavenumber k. At R = R_c the solution just becomes unstable.

The remaining velocity components, the pressure distribution and the temperature field could be calculated by solving the eigenvalue problem

$$-\lambda_j \underline{S}\, q_j = \underline{L}\, q_j$$

(Chandrashekar 1966; Schlüter et.al.,1965; Haken, 1982).

With the linearized solution and the knowledge at which value of the control parameter R the system becomes unstable, we now have to solve the nonlinear problem, trying the following superposition ansatz for the time-dependent modes of the velocity, temperature and pressure field

$$\vec{q}(x, y, z, t) = \sum_{\vec{k},l} \xi_{\vec{k},l}(t)\vec{q}_{\vec{k},l}(\vec{x}, z) \tag{13}.$$

Entering with this ansatz into the nonlinear problem

$$\underline{S}\dot{\vec{q}} = \underline{L}\vec{q} + N(\vec{q})$$

the equations for the time-dependent amplitudes get the following structure after some lengthy mathematical calculations and transformations (Wunderlin, 1975; Bestehorn, 1983; Bestehorn & Haken 1984)

$$\dot{\xi}_{\vec{k},l}(t) = \lambda(\vec{k},l)\xi_{\vec{k},l}(t) - \sum_{\substack{\vec{k}',l' \\ \vec{k}'',l''}} A_{\vec{k},l;\vec{k}',l';\vec{k}'',l''}\xi_{\vec{k}',l'}(t)\xi_{\vec{k}'',l''}(t). \tag{14}$$

Splitting the equation system in one for the stable modes and one for the unstable modes, we can write the equation for the unstable modes in the following form, when we have chosen a specific direction $\vec{k}_c$ from the infinite degenerated set of roll axis directions

$$\dot{\xi}_{\vec{k}_c,1} = \frac{3}{2}\pi^2 \frac{P}{P+1}\left(\frac{R-R_c}{R_c}\right)\xi_{\vec{k}_c,1} + \frac{2\sqrt{2P}}{9\pi^2(P+1)}\xi_{\vec{k}_c,1}\xi_{0,2}. \tag{15}$$

The equation for the stable modes reduces if we put only terms $\propto |\xi_{\vec{k}_c,1}|^2$ into account

$$\dot{\xi}_{0,2} = -4\pi^2\xi_{0,2} - \frac{2\sqrt{2P}}{9\pi^2(1+P)}|\xi_{\vec{k}_c,1}|^2. \tag{16}$$

Invoking the principle of adiabatic elimination (Haken, 1982) we put the time derivatives of the stable modes equal to zero. A Taylor expansion of the eigenvalue leads to

$$\lambda_1(\vec{k}_c, R-R_c) = \frac{3}{2}\pi^2 \frac{P}{P+1}\left(\frac{R-R_c}{R_c}\right). \tag{17}$$

Solving the equation (16) to the stable modes and inserting them into the equation (15) we finally have obtained the Landau-Ginzburg-equation for the unstable modes of the system for the region of R near to R_c and the direction $\vec{k}_c$

$$\dot{\xi}_{\vec{k}_c,1} = \frac{3}{2}\pi^2 \frac{P}{P+1}\left(\frac{R-R_c}{R_c}\right)\xi_{\vec{k}_c,1} - \frac{P}{6\pi^2 R_c(1+P)^2}|\xi_{\vec{k}_c,1}|^2\xi_{\vec{k}_c,1}. \tag{18}$$

To solve this differential equation for the order parameter we have to eliminate the absolute value $|\xi_{\vec{k}_c,1}|^2$ with the transformation $|\xi_{\vec{k}_c,1}| = \psi(t)e^{i\phi}$. Dividing through the time-indpendent phases $e^{i\phi}$ the differential equation for the temporal evolution of the velocity reads

$$\dot{\psi} = \frac{3}{2}\pi^2 \frac{P}{P+1}\left(\frac{R-R_c}{R_c}\right)\psi - \frac{P}{6\pi^2 R_c(1+P)^2}\psi^3. \tag{19}$$

Separation, partial fractional decomposition and final integration and solving to $\psi(t)$ provides the temporal evolution of the velocity amplitude

$$\psi(t) = \sqrt{\varepsilon \cdot \frac{e^{2\gamma t}}{e^{2\gamma t} - 1}}. \tag{20}$$

The solution of the nonlinear problem near the first instability can now be written as

$$\vec{q}(x, y, z, t) = N_1(\vec{k}_c, 1)\vec{q}_{\vec{k},1}(\vec{x}, z)\psi(t) \cdot e^{i\phi} + O(|\xi_{\vec{k}_c,1}|^2). \tag{21}$$

Convecting Conditions in a Magma Chamber

Before we compare the expression (20) with the course of the seismic amplitude, we have to examine whether there are conditions in an extended magma chamber so that the Rayleigh-Bénard convection could set in. A simple entropy consideration for compressible fluids without viscosity can be cited to clarify this question (Landau & Lifshitz 1966).

The condition that there is no convection can be derived from an expansion of entropy terms for an infinitesimal fluid volume at a certain altidude z and that at an altitude z + ζ :

$$\frac{dT}{dz} > -\frac{gT}{c_p V}\left(\frac{\partial V}{\partial T}\right)_p \tag{22}$$

where

$$\frac{1}{V}\left(\frac{\partial V}{\partial T}\right)_p = \alpha \tag{23}$$

is the coefficient of heat conduction which is greater than zero for the most materials. This leads to the condition for overadiabatic temperature stratification for compressible nonviscose fluids

$$\left|\frac{dT}{dz}\right| > \left|\frac{g \cdot \alpha \cdot T}{c_p}\right|. \tag{24}$$

After putting in the material parameters the result is that the temperature gradient should be greater than 10^{-4}K/m .

The condition for convection in an extended magma chamber for the more realistic case of incompressible viscose liquids is the passing of the critical Rayleigh number, where the convectional motion starts. For

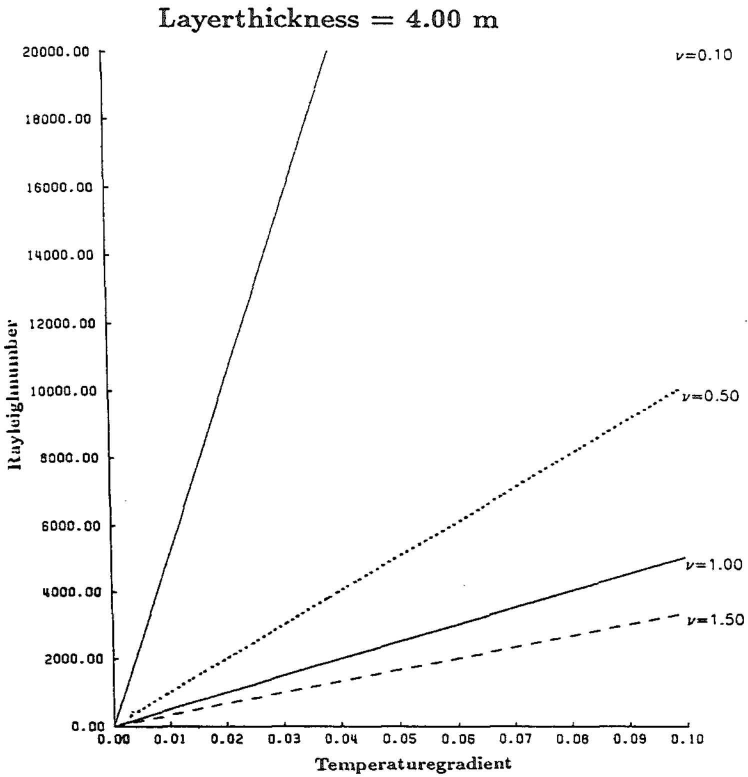

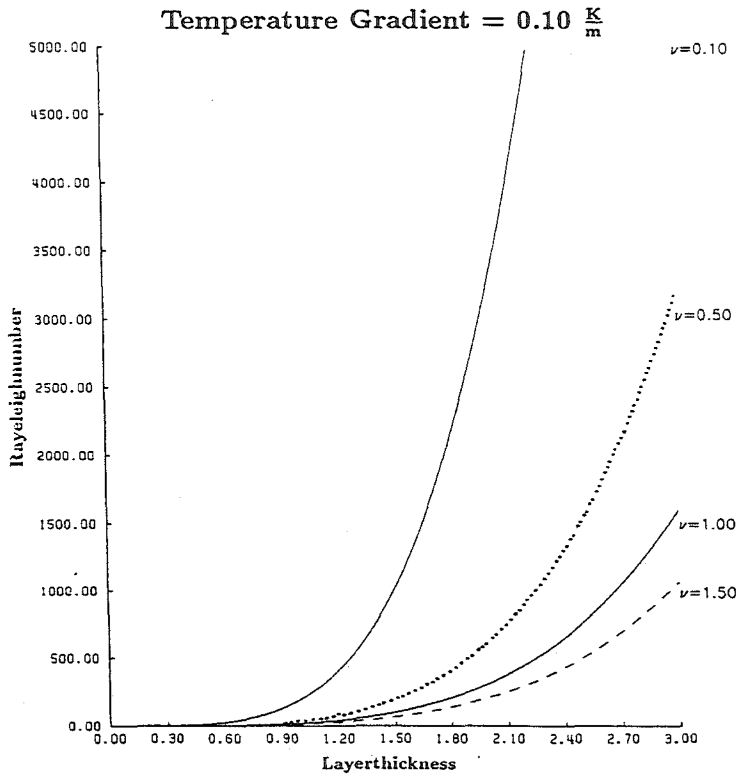

Figure II:
Dependence of the Rayleighnumber from the temperature gradient with a constant layer thickness of 4 m.

bei

Figure III:
Dependence of the Rayleighnumber from the layer thickness with a constant temperature gradient of 0.1 K/m

einem

free boundaries this critical Rayleigh number is $R_c = 657,51$, for rigid boundaries numerical calculation give the result of $R_c = 1708$ (i.e. Chandrasekhar, 1966). Setting in again the material parameters for magma from table 2 the results are from order 10^{-4}K/m for free and near 10^{-3}K/m for rigid boundaries and so the temperature gradient for the existence of convection must be greater than 10^{-3}K/m at the worst. This is realized in nearly each magma chamber what can be easily concluded from the figures II and III.

The validity of the Boussinesq Approximation

Further the validity of the Boussinesq approximation must be guaranteed because it is the assumption made for all calculations executed for convectional problems.

The strict Boussinesq approximation is applicable, if nonlinear terms are only 10 % from the amount of the linear terms leading to the following relations which must be fulfilled (Gray & Giorgini, 1976)

$$\left| \varepsilon_{11} \frac{T_0}{\beta} \right| \leq 0.1, \tag{25}$$

$$|\varepsilon_{11}| \left(\frac{P}{R} \right)^{\frac{1}{2}} \leq 0.1 \frac{1}{(P \cdot R)^{\frac{1}{2}}} \tag{26}$$

with

$$\varepsilon_{11} = \frac{\alpha_0 \cdot g\beta \cdot L}{c_{p_0}}. \tag{27}$$

The insertion of the known material parameters for magma leads to

$$\frac{L}{\beta} \leq \frac{0.1 c_{p0}}{\alpha_0 \cdot g \cdot T} = \frac{0.1 \cdot 1490 \frac{\mathrm{J}}{\mathrm{K \cdot kg}}}{10^{-5}\ \mathrm{K}^{-1} \cdot 9.81 \frac{\mathrm{m}}{\mathrm{s}^2} 1200^o\mathrm{C}} = 1.0311 \cdot 10^3 \frac{\mathrm{m}}{\mathrm{K}}, \tag{28}$$

$$L \leq \frac{0,1 \cdot c_{\mathrm{p}0}}{\alpha_0 \cdot g \cdot P} = \frac{0.1 \cdot 1490 \frac{\mathrm{J}}{\mathrm{K \cdot kg}}}{10^{-5}\ \mathrm{K}^{-1} \cdot 9.81 \frac{\mathrm{m}}{\mathrm{s}^2} 2 \cdot 10^6} \approx 0.759 \ \ \mathrm{m}. \tag{29}$$

From the relation (29) we can see that the strict Boussinesq approximation is only valid up to a layer thickness of 0.759 m.

But there is a way to extend the validity region, if we have another look at the expression of the last relation

$$\frac{\alpha_0 \cdot g \cdot L}{c_{p0}} \left(\frac{P}{R}\right) \cdot \Phi$$

where

$$\Phi = \frac{1}{2} \left(\frac{\partial v_i}{\partial x_j} + \frac{\partial v_j}{\partial x_i} - \frac{2}{3} \frac{\partial v_k}{\partial x_k} \delta_{ij} \right) \left(\frac{\partial v_i}{\partial x_j} + \frac{\partial v_j}{\partial x_i} \right) \tag{30}$$

is the term of the friction heat. The friction heat can be neglected because it has no significant influence at magma temperatures from 1100°C to 1200°C .

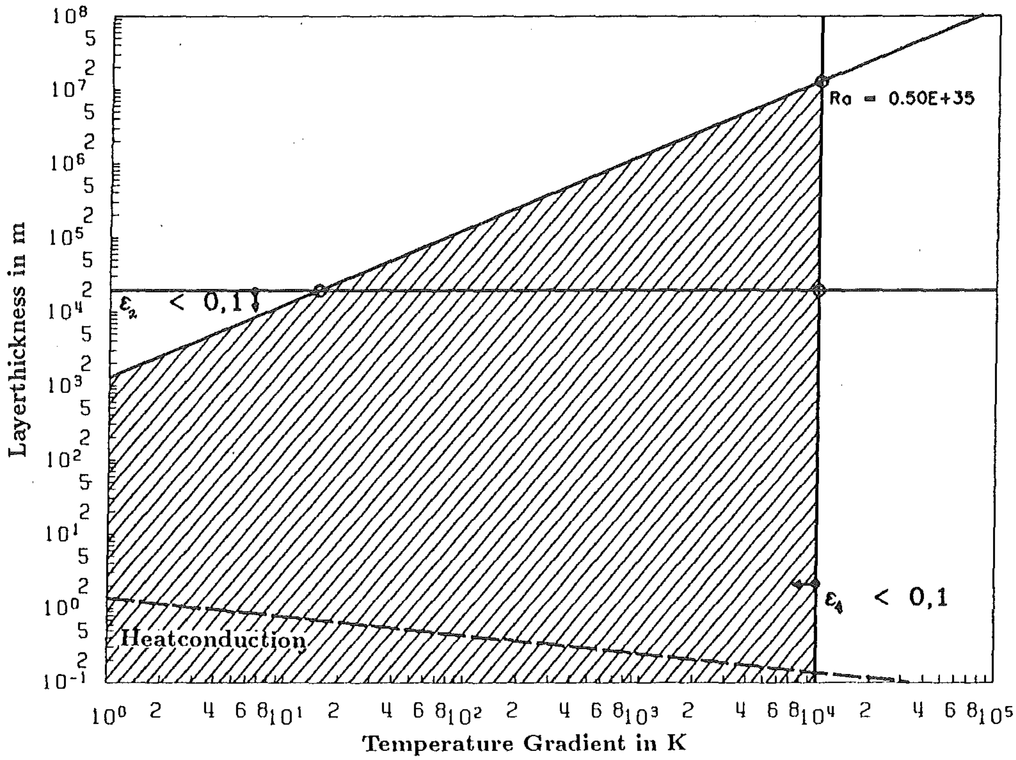

Figure IV:
The regions of validity of the Boussinesq approximation for magma (T_0 = 1150° C, P = 1 atm). The second order terms of the basic equations had not been considered yet, because the matter parameters were too vague.

The influence of the linear variation of the density with pressure and temperature is

$$\varepsilon_1 = \alpha_0 \cdot \beta \quad \text{und} \quad \varepsilon_2 = \varrho_0 \cdot \sigma_0 \cdot g \cdot L \tag{31}.$$

$$\beta = \frac{0,1}{1 \cdot 10^{-5}\ \mathrm{K}^{-1}} = 10^4\ \mathrm{K}, \tag{32}$$

$$L = \frac{0,1}{2 \cdot 10^{-6}\ \mathrm{bar}^{-1} \cdot 2670 \frac{\mathrm{kg}}{\mathrm{m}^3} \cdot 9,81 \frac{\mathrm{m}}{\mathrm{s}^2}} = 19\,090\ \mathrm{m} \approx 20\ \ \mathrm{km}. \tag{33}$$

For variations of second order the exponential decrease of the viscosity with growing temperature $c = \mu^{-1}\, \partial\mu/\partial T$ is important.

But most material parameters for magma which are needed to give a useful estimation of the influence of the quadratic terms are rather uncertain. Here we have to wait until more data are available. The validity region of the Boussinesq approximation shows figure IV.

Results obtained from the Analytic Solution

After having shown that a convectional motion is realized in nearly every magma chamber, we are now able to compare the time evolution of the Rayleigh-Bénard convection with the temporal course of the seismic amplitude. First we have to define an ingenious time constant for the temporal increase of the velocity. A very clear but not exact procedure represents the following grapical evaluation.

If we plot the amplitude ξ over the normalized time $t' = (\kappa/d^2) \cdot t_{real}$ (for example see figure V., VI.) one cannot exactly decide where the convectional motion starts and where the velocity has reached its ending value. To start the convection the system has to be deviated by external forces, fluctuations of the velocity, temperature and pressure field which were neglected in the calculation to solve the problem analytically. The negative time values originate in the freedom of choosing the starting conditions.

We define the increasing time adding the absolute value of the time at the point where the amplitude is just zero to the time where the amplitude has just reached its maximum. For water, for example, we have the absolute value of $t' = -0.07$ added to 0.03 equal 0.10. Table 1 shows some characeristic values for some experimental measurable materials and two magmas, one at a Rayleigh number of $R = 660$ the other at $R = 5000$.

The objection that the calculation is not valid for such high Rayleigh numbers is only justified for Prandtl numbers lower than 10. For high

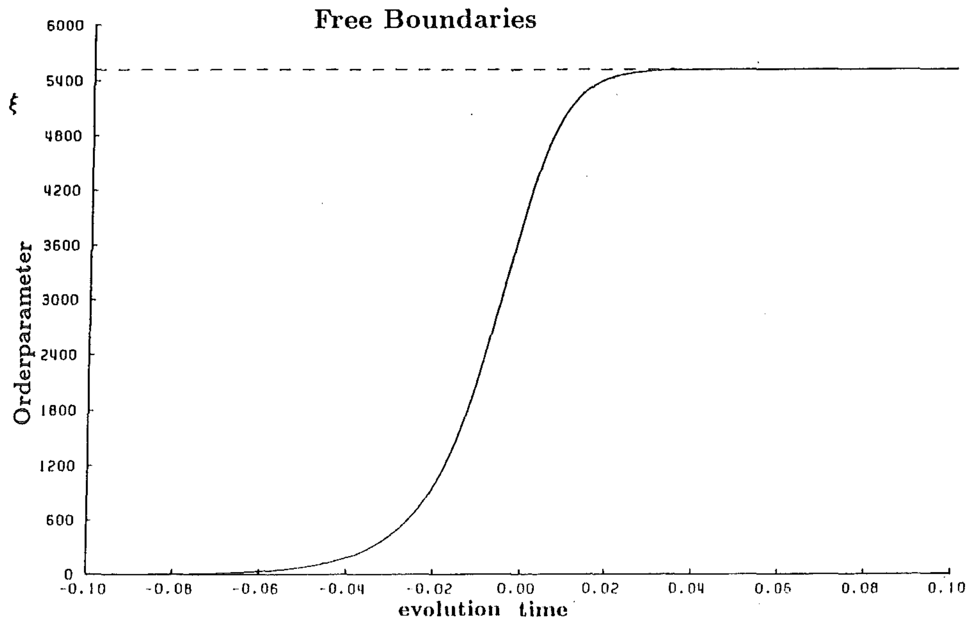

Rayleighnumber = 5000 **Prandtlnumber = 7.00**

Figure V:
Temporal evolution of the order parameter ξ, the first mode of the velocity amplitude for water at a Rayleighnumber of 5000.

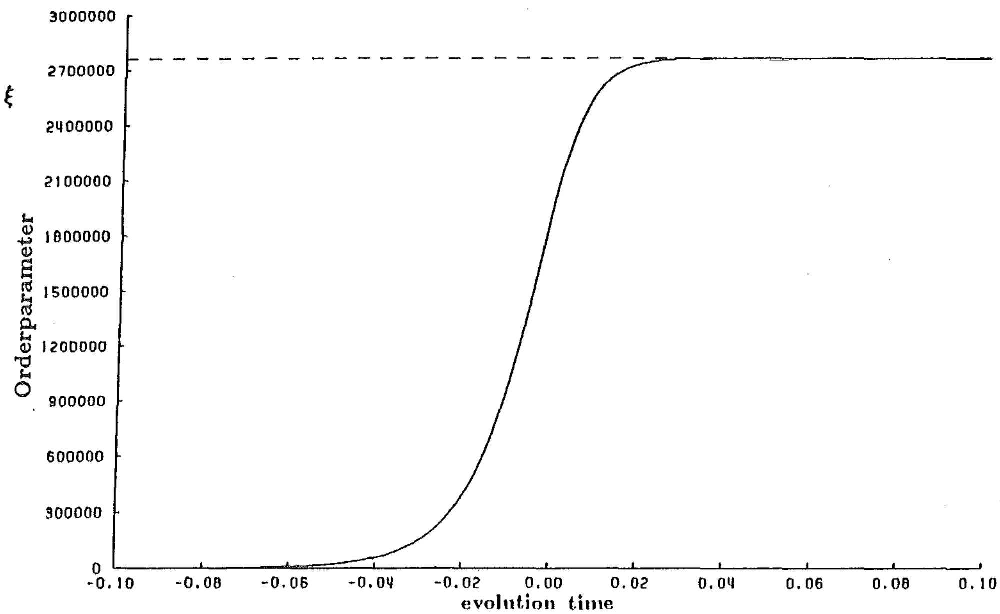

Rayleighnumber = 5000 **Prandtlnumber = 200 000**

Figure VI:
Temporal evolution of the order parameter ξ, the first mode of the velocity amplitude for Dacitmagma at a Rayleighnumber of 5000.

Material	normalized Time	heatconducting Number	Layer-thickness	evolution Time
Nitrogen	0.225	$2.21 \cdot 10^{-5}$ m^2/s	15.2 mm	2.29 s
Water	0.10	$1.43 \cdot 10^{-7}$ m^2/s	15.0 mm	157.34 s
Siliconeoil	0.11	$1.09 \cdot 10^{-7}$ m^2/s	15.0 mm	206.42 s
Magma (highviscose & viscose)	0.11	$5.00 \cdot 10^{-7}$ m^2/s	20.0 m	$8.8 \cdot 10^7$s = 2.79 y
Magma*	150	$5.00 \cdot 10^{-7}$ m^2/s	20.0 m	$1.2 \cdot 10^{11}$ s = $3.8 \cdot 10^3$ y

Table 1:

Some characteristic evolution times of the vertical velocity componenent for magma and some experimental available materials, appointed by graphical evaluation. The Rayleigh number was 5000, for * it was 660.

Prandtl numbers the region of two dimensional convection reaches a Rayleigh number of 20 000, and the comparision with experimental results shows a good agreement which is more than sufficient for appreciating the evolution time of convection in a magma chamber (figure X).

The evolution time remains constant in the high Prandtl number region, e.g., there is no difference between Dacit- and Basaltmagma.

The great difference of more than two orders between the evolution time of the convection and the increasing time of the tremor amplitude which is about ten to twenty minutes cannot be caused by the error made in graphical evaluation.

Nevertheless, we can introduce two more computational procedures to determine the time constant. The first one is comparable to time constant definitions for a R-C-network in electrical engineering. Fitting an exponential function

$$\psi(t) = \sqrt{\varepsilon \cdot \frac{e^{2\gamma t}}{e^{2\gamma t} - 1}} \approx \sqrt{\epsilon}(1 - e^{-2\gamma t}) \tag{34}$$

we define a characteristic time as the time where the amplitude has reached $(1 - 1/e)$ of the maximum:

$$t = \tau = \frac{1}{2\gamma} = \frac{1}{3\pi^2} \frac{P+1}{P} \left(\frac{R_c}{R - R_c} \right) . \tag{35}$$

Another possibility to get a time constant represents a procedure analogous to the graphical evaluation. Here the characteristic time can be

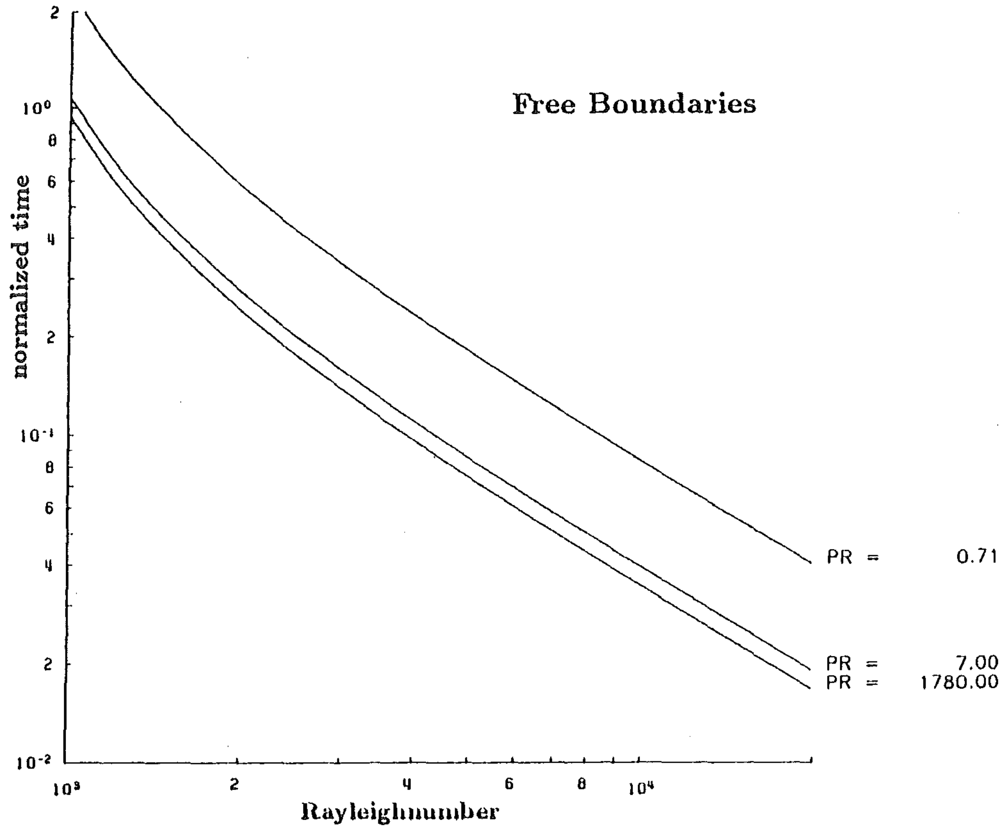

Figure VII:
Normalized evolution time of the cellular convection for nitrogen, water and siliconeoil M 200 dependent from the Rayleighnumber. The determination was made in analogy to the graphical procedure. The correspondence to experimental results is more than sufficient (Bühler et. al., 1979, Oertel jr., 1979, Kirchartz, 1980)

defined as the transition time from 1 % of the final amplitude to 99 % of this value. That means we sum over the absolute values of the time between the point where the velocity amplitude is 1/100 of the maximal amplitude and that one where the amplitude is only 1/100 far away from its maximum. There we define the convection as completely developped.

$$\tau = \left| t\left(\frac{\sqrt{\varepsilon}}{100}\right) \right| + \left| t\left(\sqrt{\varepsilon} - \frac{\sqrt{\varepsilon}}{100}\right) \right|, \tag{36}$$

$$\tau = \frac{1}{2\gamma}\left[\left|\ln\frac{1}{9999}\right| + \left|\ln\frac{9801}{199}\right|\right] = \frac{1}{3\pi^2}\frac{P+1}{P}\left[\left|\ln\frac{1}{9999}\right| + \left|\ln\frac{9801}{199}\right|\right]. \tag{36'}$$

The very good agreement with experiments justifies this method, which is the most exact one of the three presented (figure VII, VIII).

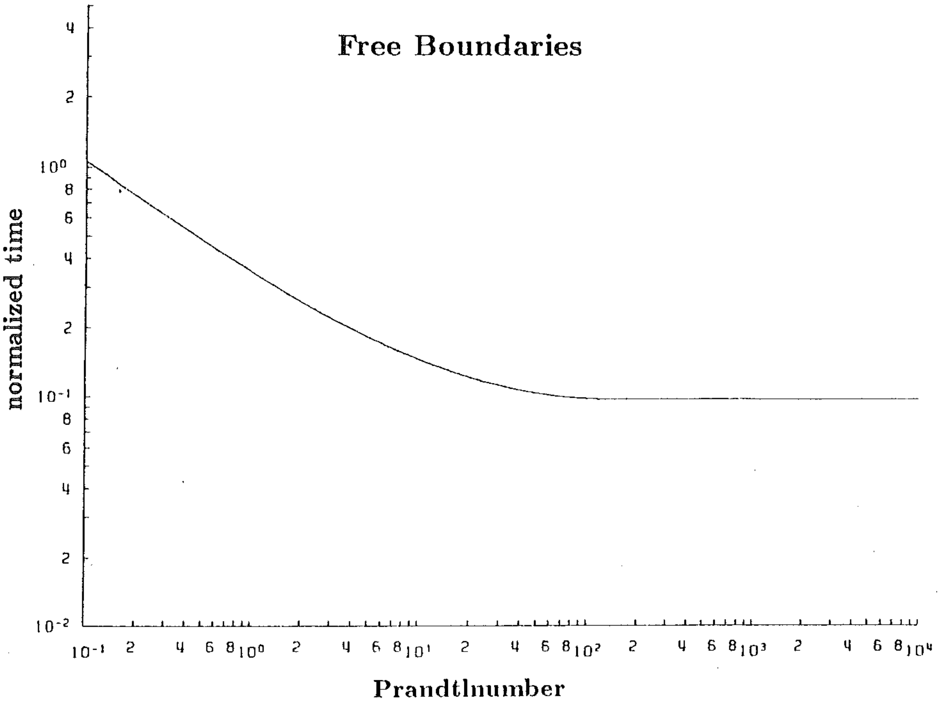

Rayleighnumber = 4000

Figure VIII:
Normalized evolution time of the cellular convection dependent from the Prandtlnumber. The determination was made in analogy to the graphical procedure. The correspondence to experimental results is more than sufficient (Bühler et. al., 1979, Oertel jr., 1979, Kirchartz, 1980)

The determination of the time constant with the exponential approach is rather faulty and a factor one third too low. In spite of this, the evolution time calculated for a Prandtl number region of $60\,000 < P < 200\,000$ and a Rayleigh number of $R = 5\,000$ with this method is

$t_{\exp} = 4,09 \cdot 10^6$ s $= 47,73$ d which is two orders too high. The other method provides $t_{\mathrm{amp}} = 5,362 \cdot 10^7$ s $= 1,7$ y which is more than three orders higher than the increasing time of the tremor amplitude.

Numerical calculations for rigid boundaries has been carried out by Bestehorn (Bestehorn, 1983; Bestehorn & Haken, 1984). He chosed an $\epsilon = 0.1$ so that the synergetic calculation has been valid in any case. After rescaling the normalized time he obtained for circular layers $t_{\mathrm{circ}} = 1.27 \cdot 10^{10}$ s $= 403,5$ y and for quadratic layers $t_{\mathrm{quad}} = 4,8 \cdot 10^{10}$ s $= 1523$ y. Since the Rayleigh number is much lower than in the cases above, the transition time seems very long now. But if we calculate the time constant for this Rayleigh number as well we get nearly the same results.

If the seismic output does not depend on the third root of the magma flow velocity the hypothesis cannot be maintained that the increasing of the tremor amplitude is evocated by the inset of the Rayleigh-Bénard convection.

Higher Instabilities of the Rayleigh-Bénard Convection

The results of the nonlinear treatment are valid only near the critical Rayleigh number for the transition from heat conduction to convection. Which statements can be made about the higher Rayleigh number region of fluids with high Prandtl numbers like magma?

The best experimental work for this region was carried out by Krishnamurti, 1970 a,b. First she investigated the Rayleigh number region from $10^3 < R < 10^5$ for fluids with Prandtl numbers from 1 to 10 000. As fluid layer she used a cell with large aspect ratio and rigid boundaries. For her experiments she registrated the heat flux obtained by the Nusselt number and simultaneously took photos from the current pattern. The result was a more effective heat transport above a Rayleigh number of $13 \cdot R_c$ than below this value. Looking at the photos a change of the current pattern could be recognized. At this point, the two-dimensional rolls alter to a bimodale three-dimensional pattern where two roll movements overlay perpendicular to each other.

With rising Rayleigh number it could be acertained that at a Rayleigh number of $35 \cdot R_c$ and once more at $105 \cdot R_c$ the heat flux became more and more effective than below this values. Watching the convection patterns,

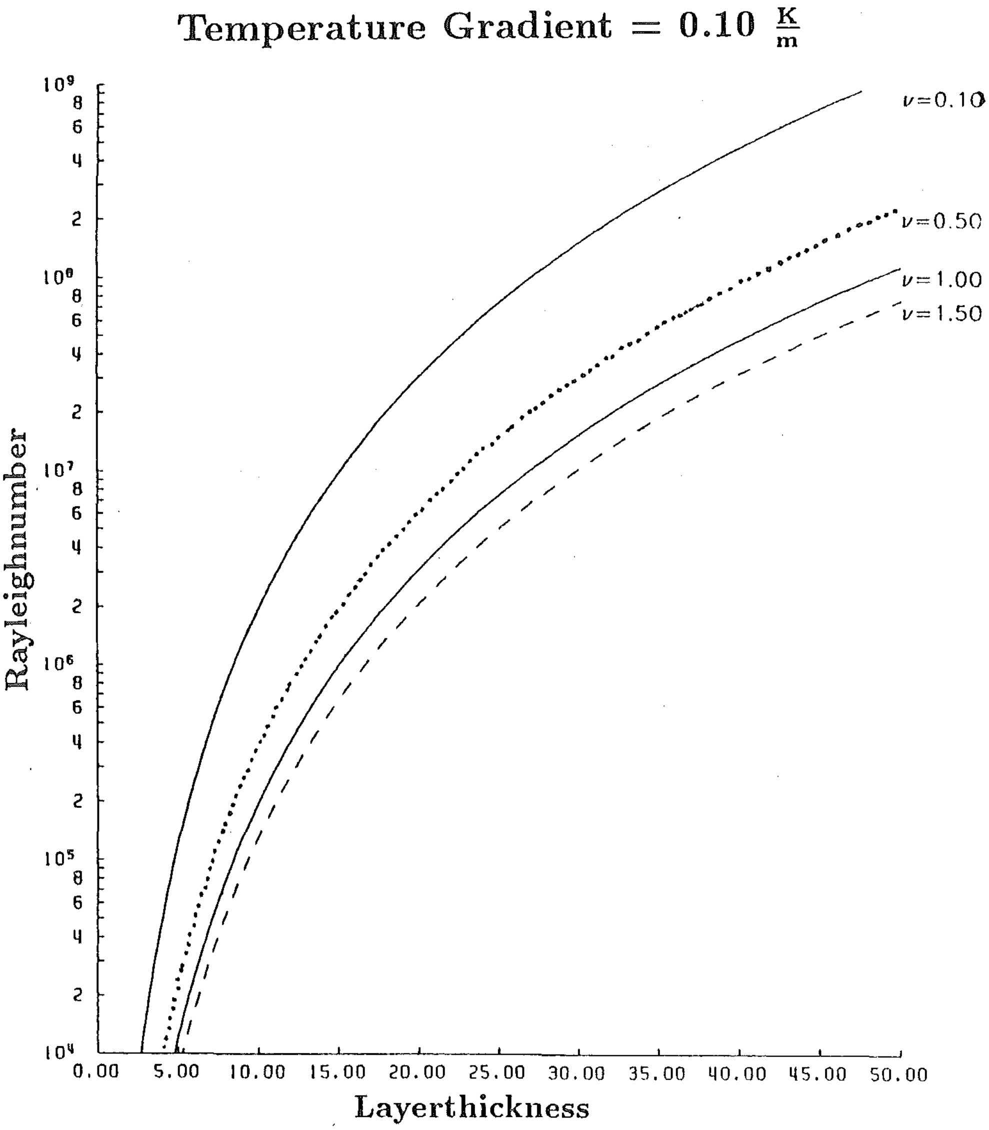

Figure IX:
Dependence of the Rayleighnumber from great layer-thicknesses for several magma viscosities.

Krishnamurti found a time dependent motion with oscillating character. First, the whole stationary pattern moves by a phase diffusion. Raising the Rayleigh number the oscillating three dimensional convection turns over to the spoke pattern, see figure 5.7a from Swinney & Gollup, 1981.

Now a stochastic turbulent up and down motion superimposes this pattern. This is already the turbulent region. If the Rayleigh number gets higher the motion becomes more chaotic until the wide meshed structure yields an irregular unstructered movement. Lowering the Rayleigh number again results in an effect of hystheresis, i.e., the transitions to lower convection modes take place at lower Rayleigh numbers than those for rising the Rayleigh number. The heat flux runs higher for decreasing the Rayleigh number than for increasing it.

The results for rising Rayleigh number were summarized in a stability diagram shown in figure X.

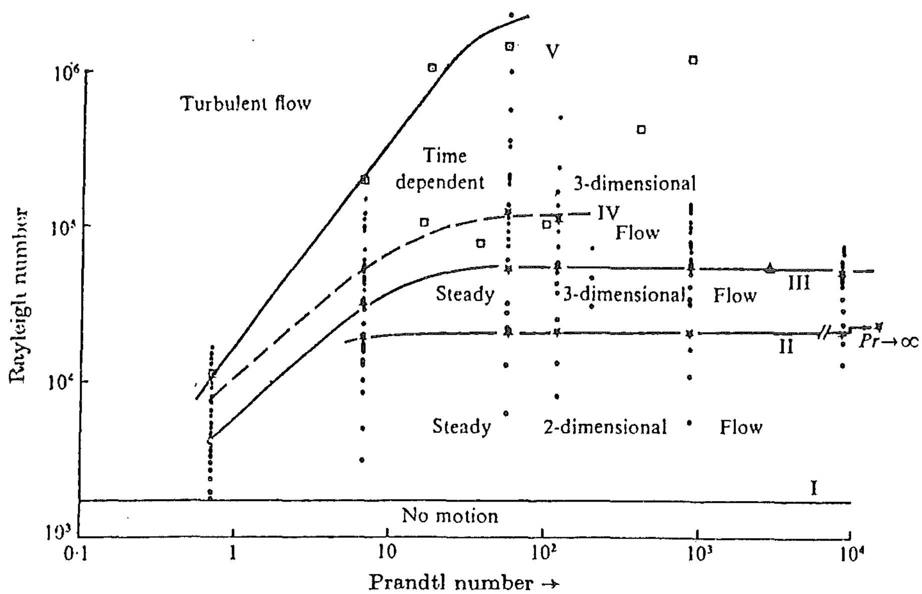

Figure X:
The régime diagram. The circles represent steady flows, the circular dots represent time-dependent flows. The stars represent transition points. The open squares are Rossby's observations of time-dependent flow, the squares with a dot in the centre are Willis & Deardorff's observations for turbulent flow. The triangle is Silvston's point of transition to time-dependent flow (R. Krishnamurti, 1970 b)

One can easily see that the transition from heat conduction to convection is independent of the Prandtlnumber. For Prandtl numbers greater than 100 all the other transitions are independent of the Prandtl number, too, so that an extrapolation to $P \rightarrow \infty$ and, of course, to the Prandtl numbers of the various magmas is justified. The values for $P \rightarrow \infty$ calculated by Busse, 1978, are marked in this figure. Note that the transition from three dimensional convection to turbulence is not yet surely described in this picture. Looking at the figures II, III and IX one can recognize that only for very small values of the temperature gradient and the layer thickness the Rayleigh number is in the region of the critical Rayleigh number for the first transition. On the contrary, first of all with rising layer thickness the turbulent regime is soon reached. So all kinds of convection could be realized in a magma chamber.

It would be useful if one could define a time constant for the transitions to higher convection modes. Busse, 1978, had made an extension of the linear stability theory to higher instabilities. But the evolution times cannot be calculated with an analytical approach. For the higher instabilities a numerical scheme should be used by solving the complete nonlinear equations.

Another time scale to compare with the seismic amplitude of volcanic tremor is the period of the temperature oscillations which are correlated with an oscillating movement. These knots of a time-dependent bimodale convection tend to oscillate. Krishnamurti (1970 b) has measured the frequency for a fluid with the Prandtl number of 8500. Rescaling the normalized time constants gives a frequency range of $1.25 \cdot 10^{-8}\ \mathrm{s}^{-1} < f < 1,25 \cdot 10^{-7}\ \mathrm{s}^{-1}$ which cannot be found neither in the tremor spectre of Etna nor of Merapi. Although the estimation is very uncertain the error should not amount to seven orders of quantity.

Perhaps the small oscillations superimposed on the tremor with greater period are caused by turbulent flow of the magma. Convection cells with a large aspect ratio represent a system with many degrees of freedom. Actually the possible directions of the diffraction patterns, their wave vectors, are very degenerate in a nearly to infinity extended layer. So the system gradually tends to a chaotic motion. This begins with the spoke pattern which is overlayed by small stochastic fluctuations. The transition to turbulence looks more like the theoretical model of Ruelle-Takens, saying that the solutions for the behaviour of a system, which tends to turbulence, approaches a strange attractor in the phase space, following the subharmonic way to chaos. The route to turbulence over intermittency, in which the appearing of a well-defined frequency with more and more superimposing noise is characteristic is followed only for convection cells with low aspect ratio. (i.e. Dubois & Bergé, 1981)

Final Conclusions

With the results of the analytic calculation the supposition that the Rayleigh-Bénard convection in a large magma chamber is the source of the volcanic tremor must be rejected for the first instability. For higher instabilities the results of extended numerical calculations of the evolution time would give the right answer whether the tremor amplitude is correlated with the increasing velocity of the convectional motion. The conclusions, however, which had been made for higher instabilities are not very hopeful to affirm this.

Other mechanisms could exist also evoquating seismic oscillations, for example, boundary layer effects, two phase convection or something more complicate. But before trying to describe the volcano with more complicate systems than the Rayleigh-Bénard convection rejecting one by one, a more systematic proceeding is desirable. First one has to investigate how complicate the system volcano in reality is. This could be reached if the fractal dimension from the time series of the seismic output is determinated. If the fractal dimension is low the system can possibly consist of few variables. High fractal dimension might mean that the system is very complicated and chaotic, so that an adjusted simplication must be found to characterize it.

The work of Strigl at the Geophysikalisches Institut, Stuttgart, who tried to find the fractal dimension of the volcanic tremor output represents a good contribution to advance the studies about volcanoes in this direction (see also the next contribution by himself in this volume).

But the theoretical modelling of a volcano must be the subject of further investigations.

Acknowledgements

I am indepted to K. Strobach who received me kindly in his institute and refereed my thesis, H. Haken who gave helpful advices and who co-refereed my thesis and R. Schick always sacrificing his time for discussions as a helpful supervisor. Grateful thanks due to following members of the Institute of Theoretical Physics & Synergetics for their helpfulness and pleasentness in supporting this work : M. Bestehorn, H. Bunz, R. Friedrich, T. Grauer and A. Wunderlin. Special thanks for R. Mayer, who introduced me with many hints in the use of computers, W. Hirsching, P. Sachs and the other members of the Institute of Geophysics for their useful discussions. A. Wunderlin and W. Hirsching read the proofs of this contribution to whom I thank very much for further discussions, corrections and advices. Without all them this work wouldn't have been possible.

References

Behringer, R. P. Rayleigh-Bénard-Convection and Turbulence in liquid Helium, Rev.Mod.Phys. Vol.57 no.3 part 1, pp 657 - 686, 1985

Bestehorn, M. Musterbildung beim Bénard-Problem der Hydrodynamik, Diplomarbeit, Univ. Stuttgart, Institut für theoretische Physik, 1983

Bestehorn, M., H.Haken Transient patterns of the Convection Instability: a Model Calculation, Condensed Matter, Zeitschr. f. Physik B, Springer, 1984

Birch, F., J.F.Scheirer, H.C.Spicer Handbook of Physical Constants, Geolog.Soc.America Spec.Pap., 1942

Bühler, K., K.R.Kirchartz, H.Oertel jr. Steady Convection in a horizontal Fluid Layer, Acta Mechanica, Vol. 31 pp 155 - 171, 1979

Busse, F.H. Nonlinear Properties of Convection, Rep.Prog.Phys. Vol 41, pp 1929 - 1967, 1978

Carrigan, C.R. A Heat Pipe Model for Vertical Magma-filled Conduits, J.Volcanol.Geotherm.Res. Vol.16, pp 279 - 298, 1983

Chandrasekhar, S. Hydrodynamic and hydromagnetic Stability, Oxford University Press, 1966

Cosentino, M., G.Lombardo, G.Patane, R.Schick, A.D.L.Sharp Seismological Researches on Mount Etna, State of Art and recent Trends, Mem.Soc.Geol.Ital. Vol.23 pp 159 - 202, 1982

Crutchfield, J.P., J.D.Farmer, N.H.Packard, R.S.Shaw Chaos, Spektrum der Wissenschaft Feb. 1987

Dubois, M., P.Bergé   Instabilités de Couche limite dans un fluide en Convection: Évolution vers la Turbulence, J.Physique Vol.42, pp 167 - 174, 1981

Gray, D.D., A.Giorgini   The Validity of the Bousinesq-Approximation for Liquids and Gases, Int.J.Heat Mass Transfer Vol.19 pp 545 - 551, 1976

Haken, H.   Synergetik - Eine Einführung, Springer, Berlin - Heidelberg - New York, 1982

Haken, H.   Erfolgsgeheimnisse der Natur, DVA, Stuttgart, 1981

Haken, H.   Advanced Synergetics, Springer, Berlin - Heidelberg - New York, 1982

Hardee, H.C.   Convective Heat Extraction from molten Magma, J.Volcanol.Geotherm.Res. Vol.10 pp 175 - 183, 1981

Hardee, H.C., J.C.Dunn   Convective Heat Transfer in Magmas near Liquidus, J.Volcanol.Geotherm.Res. Vol.10, pp 195 - 207, 1980

Hernance, H.E., J.L.Colp   Kilauea Iki Lava Lake: Geophysical Constraints on its Present Physical State, J.Volcanol.Geotherm.Res. Vol.13 pp 31 - 61, 1980

Keller, G.V., L.T.Grose, J.C.Murray, C.K.Stokan   Results of an experimental Drill Hole at the Summit of Kilauea Volcano, Hawaii, J.Volcanol.Geotherm.Res. Vol.5, pp 345 - 385, 1979

Kirbani, S.B.   Analysis and Interpretation of Volcanic Tremors At Etna, Inst.Geophys.Univ.Stuttgart, Publication 210, 1983

Kirchartz, K.R.   Zeitabhängige Zellularkonvektion in horizontalen und geneigten Behältern, Dissertation, Univ.Karlsruhe, Institut für Strömungsmechanik, 1980

Krishnamurti, R.   On the Transition to turbulent Convection, Part I, The Transition from two- to threedimensional Flow, J.Fluid Mechanics Vol.42 part 2, pp 295 - 307, 1970

Krishnamurti, R.   On the Transition to turbulent Convection, Part II, The Transition to time-dependent Flow, J.Fluid Mechanics Vol.42 part 2, pp 309 - 320, 1970

Landau, L.D., E.M.Lifschitz Lehrbuch der Theoretischen Physik VI, Hydrodynamik, Akademie Verlag, Berlin, 1966

Libchaber, A., J.Maurer A Bénard-Experiment: Helium in a small Box, in: Nonlinear Phenomena at Phase Transitions and Instabilities, ed. T.Best, pp 259 - 286, 1982

Manghani, M.H., S.I.Akimoto High Pressure Research - Applications in Geophysics, Accademic Press, Inc., New York, 1977

McLaughlin, J.B., P.C.MArtin Transition to Turbulence in a Statically stressed System Phys.Rev. Vol.12, pp 186 - 203, 1975

Morse, P.M., K.U.Ingard Theoretical Acoustics, McGraw-Hill Book Company

Normand, C., Y.Pomeau, P.Velarde Convective Instability: A Physicists Approach, Rev.Mod.Phys. Vol.49, pp 581, 1977

Oertel jr., H. Thermische Zellularkonvektion Habilitationsschrift, Univ.Karlsruhe, Institut für Strömungsmechanik, 1979

Pichler, H., R.Schick Der Ätna, Spektrum der Wissenschaft Vol.1, 1985

Schick, R., G.Lombardo, G.Patane Volcanic Tremors and Shocks associated with Eruptions at Etna (Sicily), September 1980 J.Volcanol. Geotherm.Res. Vol.14, pp 261 - 279, 1982

Schick, R. Source Mechanism of volcanic Earthquakes Bull.Volcanol. Vol.44-3, 1981

Schlüter, A., D.Lortz, F.H.Busse Rayleigh-Bénard-Convection, J.Fluid Mechanics Vol.23, 1965

Schreyer, W. High Pressure Researches in Geoscience, Nägele u. Obermüller, Stuttgart, 1982

Schuster, H.G. Deterministic Chaos, Vieweg, 1984

Seidl, D., R.Schick, M.Riuscetti Volcanic Tremors at Etna: a Model for hydraulic Origin, Bull.Volcanolog. Vol. 44-1, 1981

Swinney, H.L., J.L.Gollup Hydrodynamic Instabilities and the Transition to Turbulence Springer, Berlin - Heidelberg - New York, 1981

Wunderlin, A. Statistische Methoden und ihre Anwendungen auf Gleichgewichts- und Nichtgleichgewichtssysteme, Dissertation, Univ. Stuttgart, Institut für theoretische Physik, 1975

Zierep, J., H.Oertel jr. (ed.) Convective Transport and Instability Phenomena G.Braun, Karlsruhe, 1982

Zierep, J. Lineare Theorie der instationären thermischen Konvektion bei überkritischen Temperaturgradienten, Acta Mechanica Vol.39, pp 271 - 275, 1981

Table2:

(see next page) Material properties of magmas, lavas and volcanic rocks, including some experimentally wellmeasurable materials for the comparision with the theory. Datas come from Birch et. al., 1942, Kirchartz (K), 1980, Schreyer, 1982 and from the author.

Material	dynamic Viscosity μ in g/(cm · s)	cinematic Viscosity ν in m²/s	Expansion Coefficient α in K^{-1}	Density ρ in g/cm³	Heat-Capacity c_p in J/(g · K)	Heatcon-ductivity K in W/(m · K)	Temperature conductivity κ in m²/s	Prandtl-Number ν/κ
Nitrogen								
−100oC	$0.114 \cdot 10^{-3}$	$9.116 \cdot 10^{-6}$		$1.2505 \cdot 10^{-3}$	1.083 (20°C)	$16.4 \cdot 10^{-3}$	$1.2647 \cdot 10^{-5}$	0.7208
-50oC	$0.141 \cdot 10^{-3}$	$1.128 \cdot 10^{-5}$				$20.5 \cdot 10^{-3}$	$1.5809 \cdot 10^{-5}$	0.7132
0°C	$0.165 \cdot 10^{-3}$	$1.3195 \cdot 10^{-5}$			1.037 (0°C)	$24.2 \cdot 10^{-3}$	$1.8862 \cdot 10^{-5}$	0.7071
20°C	$0.175 \cdot 10^{-3}$	$1.3994 \cdot 10^{-5}$	$3.41 \cdot 10^{-3}$			$25.5 \cdot 10^{-3}$	$1.8829 \cdot 10^{-5}$	0.7432
50°C	$0.182 \cdot 10^{-3}$	$1.4554 \cdot 10^{-5}$		1.16		$30.7 \cdot 10^{-3}$	$2.2669 \cdot 10^{-5}$	0.6420
100°C	$0.208 \cdot 10^{-3}$	$1.6633 \cdot 10^{-5}$			1.08 (500°C)	$37.0 \cdot 10^{-3}$	$2.7321 \cdot 10^{-5}$	0.6088
200°C	$0.246 \cdot 10^{-3}$	$1.9627 \cdot 10^{-5}$			1.21	$56.0 \cdot 10^{-3}$	$4.135 \cdot 10^{-5}$	0.4757
500°C	$0.340 \cdot 10^{-3}$	$2.7189 \cdot 10^{-5}$			(1200°C)			0.71 (K)
Water 0°C	$1.792 \cdot 10^{-2}$	$1.7952 \cdot 10^{-6}$				0°C: 5.524	$1.3233 \cdot 33 \cdot 10^{-7}$	13.567
20°C	$1.002 \cdot 10^{-2}$	$1.0038 \cdot 10^{-6}$				10°C: 5.692	$1.3635 \cdot 10^{-7}$	
50°C	$0.54848 \cdot 10^{-2}$	$5.4899 \cdot 10^{-7}$	$2.04 \cdot 10^{-4}$	0.9982		20°C: 5.580	$1.4035 \cdot 10^{-7}$	7.1521
80°C	$0.355 \cdot 10^{-2}$	$3.5564 \cdot 10^{-7}$				30°C: 6.026	$1.4435 \cdot 10^{-7}$	7.0 (K)
100°C	$0.282 \cdot 10^{-2}$	$2.8251 \cdot 10^{-7}$				40°C: 6.194	$1.4838 \cdot 10^{-7}$	
150°C	$0.181 \cdot 10^{-2}$	$1.8133 \cdot 10^{-7}$				50°C: 6.351	$1.5238 \cdot 10^{-7}$	3.6028
						70°C: 6.696	$1.6040 \cdot 10^{-7}$	
						80°C: 6.863	$1.6440 \cdot 10^{-7}$	2.1633
Siliconeoil M200		$1.94 \cdot 10^{-4}$	$9.6 \cdot 10^{-4}$	0.970			$1.09 \cdot 10^{-7}$	1780 (K)
Magma		0.1 — 1	$1 \cdot 10^{-5}$	2.70			$5.0 \cdot 10^{-7}$	$2.00 \cdot 10^{6}$
Olivinbasalt (Gembudō)								
1150°C	37900	1.4411	$8.2 \cdot 10^{-6}$		0°C: 0.85	$22 \cdot 10^{-3}$	$9.1482 \cdot 10^{-7}$	$1.4644 \cdot 10^{6}$
1200°C	3180	$1.2091 \cdot 10^{-1}$			200°C: 1.04			
1300°C	296	$1.255 \cdot 10^{-2}$	$5.4 \cdot 10^{-6}$		400°C: 1.14	bis	bis	bis
1400°C	137	$5.2091 \cdot 10^{-3}$	(Gabbros u.		800°C: 1.32			
			Diabasen)		1200°C: 1.49	$18 \cdot 10^{-3}$	$8.0518 \cdot 10^{-7}$	$6.46 \cdot 10^{-3}$
(Kōnura)								
1200°C	732	0.0278		2.63				$2.8249 \cdot 10^{4}$
1300°C	173	0.0066						bis
1400°C	120	0.0046						$0.5712 \cdot 10^{4}$
Andesitbasalt (Motomura)								
1150°C	80000	3.0418						$3.0909 \cdot 10^{3}$
1200°C	31200	1.1863						bis
1300°C	260	0.0099						
1400°C	140	0.0053						$6.582 \cdot 10^{3}$
Nephelinbasalt (Nagahama)			$7.0 \pm 2 \cdot 10^{-6}$					
1200°C	190	0.0072						$7.316 \cdot 10^{3}$
1300°C	97	0.0037						bis
1400°C	80	0.0030						$3.725 \cdot 10^{3}$
Lava (Mt. Vesuvio)								
1100°C	28300	1.076						$1.0933 \cdot 10^{6}$
1200°C	2760	1.076						bis
1300°C	730	0.0278						$0.1179 \cdot 10^{6}$
1400°C	250	0.0095						

Eigenvibrations of magma-filled dike systems with complex geometry

T. Dahm , Geophysikalisches Institut Karlsruhe, Hertzstr. 16
D-7500 Karlsruhe

Introduction

There is an increasing interest in using seismic data to characterize the state of volcanic activity and to forecast possible eruptions. One special type of volcanic seismicity are volcanic tremors. Volcanic tremors are linked to volcanic activity. They are characterized by peaked spectra with frequencies preferently ranging from 0.15 Hz to 10 Hz. Tremor signals can last from minutes to many hours with almost constant amplitude and frequency content. In general the seismograms do not show clear first arrivals of the tremors.

Although many tremor models have been established in recent years (see Chouet (1988) and Schick (1988) for latest reviews) the source mechanism of volcanic tremor is still controversial. Based on the long duration of volcanic tremor and the relatively stable, sharply peaked tremor spectra, their generating mechanism is often associated with resonance effects connected to conduit, crack or magma chamber geometry.

Several models have been proposed in which fluid vibration plays an active role (St. Lawrence and Quamar, 1979, Seidl et.al., 1981, Ferrick et.al., 1982 and others). Ferrick et.al. (1982) studied analytically the hydraulic transients of a magma filled conduit with constant cross sectional area. They showed that this system can generate a harmonically peaked spectrum which can be a first approximation to observed tremor spectra.

In this paper the model of a magma filled dike is extended to more complex geometry . A finite element method (Kirschke, 1974) is used and results are compared to analytical results.

Geometry and boundary conditions

A schematic diagram of a simplified geometry of a dike system is shown in Fig. 1. The dike system is approximated by many dikes with constant cross-sectional area branched or placed in series. During an active state of the volcano the magma in the dike system could possibly be excited to

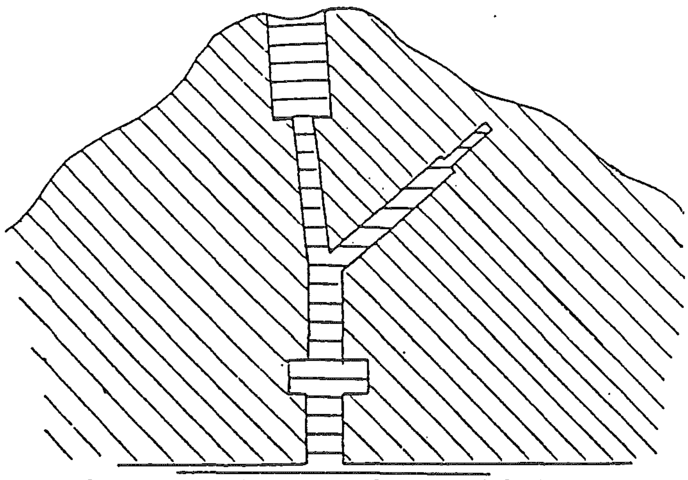

Figure 1: Schematic diagram of a simplified dike system

resonance by instationarities within the fluid (compare Seidl et.al, 1981, Ferrick et.al.,1982). In this paper the excitation mechanism is disregarded and only the eigenvibrations of the fluid filled system are studied. The main question is to find the transfer function of a dike system, build up by many dikes placed in series or branched. In a first step two dikes placed in series are chosen. In order to simplify the analysis several assumptions are introduced :

- With the examples presented, a magma is assumed which contains no gas bubbles. Thus tremor generated in the more shallow region of the feeding conduits are not considered.
  The effect of viscous damping of the waves within the magma is disregarded here and discussed in Dahm (1989).

- Perfectly rigid surrounding rock . The interaction between the fluid and the surrounding material is small if the impedance contrast (acustic velocity times density) between them is large . By directly estimating the seismic energy content in the tremor records obtained by Fehler (1983), Ferrick and St. Lawrence (1984) conclude that to first order the contribution to fluid system damping of elastic wave generation is negligible.

- Adiabatic propagation of plane waves within the dike system . Adiabatic propagation is realistic if the amplitude of the pressure pulses within the magma are not too big. The plane wave assumption is justified if the diameter of the dike sytem is small compared to the wave length considered. The typical frequency content of volcanic tremor is smaller than $10Hz$. This confines the wavelength λ by $\frac{\alpha}{\lambda} = f \leq 10Hz$ (α is the acoustic wave velocity in the magma). If the acoustic wave velocity is for example $\alpha = 1200\frac{m}{s}$, the wavelength is $\lambda \geq 120m$. In other words this simple conception could possibly explain the relatively sharp cut off frequency observed for volcanic tremor, because for higher frequencies the propagation of plane waves within the dike system is not possible and thus destructive interference is more likely.

Numerical examples

The numerical models are calculated with a Finite Element Method (Kirschke, 1974). Later, the numerical solutions are compared with analytical transfer functions.

In Fig. 2 the well known single dike solution for one closed end (bottom) and a reservoir or open end (top) is shown. The dike is divided into finite elements by the program as seen at the left of Fig. 2. To calculate the synthetic impulse response the system is excited at the top at time $t = 0$ with a pressure pulse. For each of the elements the pressure oscillation and the accompanying amplitude spectrum are calculated and plotted in Fig. 2.

In this case in each element the pressure oscillations have constant amplitudes and each spectrum shows the same eigenfrequencies, which are odd harmonics of the fundamental eigenfrequency. The shape of the different modes is given at the top of Fig. 2.

The impulse response of the single dike is a harmonic peaked spectrum which may be inverted to yield the geometry of the generating system.

Several dike systems are treated in Fig. 3. Two dikes are placed in series, both of the same length l_0 but different cross sectional areas A_1 and A_2. The boundary conditions at the left and right end are the same as in Fig 2, i.e. reservoir and closed end . The model of Fig. 3b is exactly the same as the one in Fig. 2. In order to simplify the representation in Fig. 3a - 3d only one element of the system is considered (element 3) and the time series and the spectrum of this element are shown.

Due to partial reflections between the dikes the time series of model a, c and d do not have this simple shape as in model b. In the case of a strong characteristic impedance contrast (contrast of cross sectional areas) between the two dikes in series, as seen in model 3d, a relatively long beating period occurs. In this case the spectral peaks approximate the harmonic solution of the two single dikes.

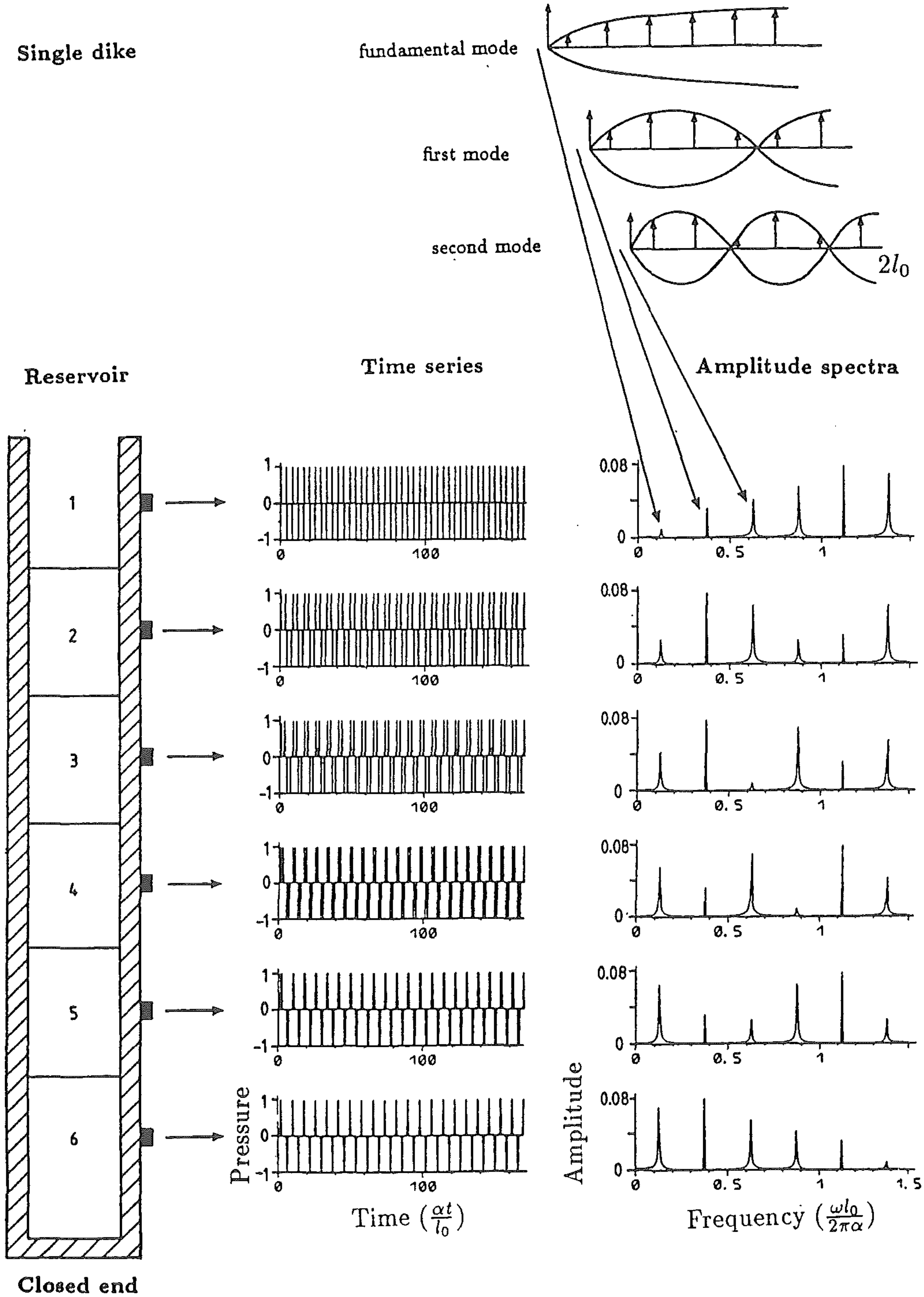

Figure 2: Impulse response of a single dike with length $2l_0$. (α: acoustic velocity in the magma, t: time, ω: frequency)

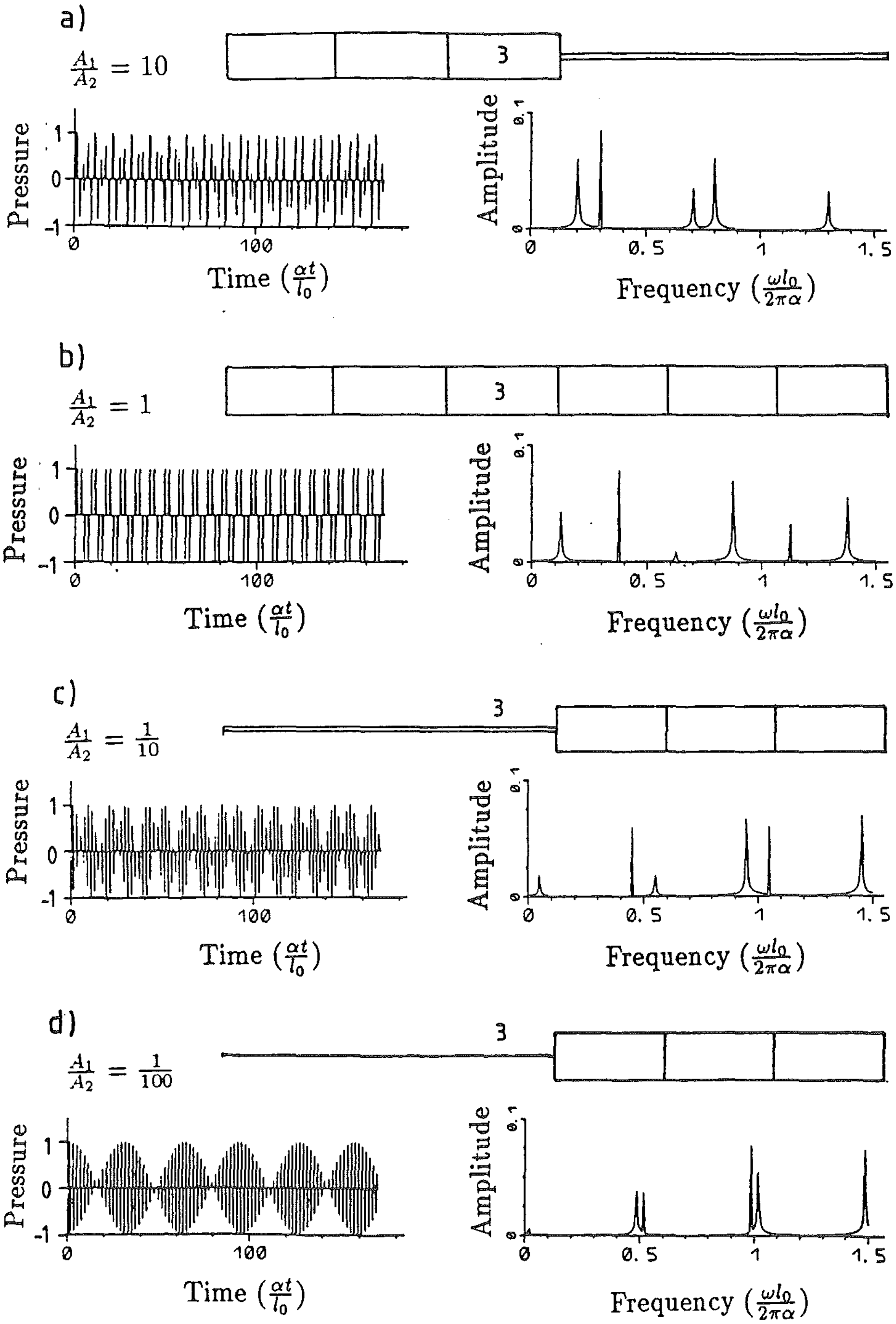

Figure 3: Impulse response of two dikes with length l_0 and characteristic impedance contrast $\frac{A_1}{A_2}$ placed in series. All models have a reservoir boundary condition at the left end and a closed end at the right

For model 3c and 3d the fundamental frequency is much lower than that obtained by using a single dike (model 3b). For example, the very long period volcanic tremor (periods up to $7s$) reported by Sassa (1935) on Mount Aso may be generated by a dike system of modest size. Assuming a measured fundamental period of $\frac{2\pi}{\omega} \approx 7$ sec and an acoustic velocity of $\alpha \approx 1200\frac{m}{s}$ the total length $l = 2l_0$ of the dike of model 3b would be $l \approx 2km$, for model 3c $l \approx 800m$ and for model Fig. 3d $l \approx 200m$.
Another important feature seen in the amplitude spectra of Fig. 3a, 3c and 3d is that the peaks are not evenly distributed on the frequency axis. In other words, higher eigenfrequencies are neither even nor odd harmonics of the fundamental frequency.

To give prominence to this behaviour in Fig. 4 the calculated eigenfrequencies of two dikes in series (both of length l_0) are plotted against the characteristic impedance contrast $\log \frac{Z_{c2}}{Z_{c1}}$ (= $\log \frac{A_1}{A_2}$, contrast of cross sectional areas) between them .
The crosses represent eigenfrequencies for one reservoir and one closed end (compare Fig. 3) and the circles represent these for two reservoir boundary conditions at both ends. In the case of a frictionless system it is possible to find an analytical solution, which is plotted in Fig. 4 as a continuous line. By first looking at the crosses one can notice that the eigenfrequencies are shifted symmetrically to periodic points on the frequency axis. These points are marked with small arrows. They are a function of $\frac{l_0}{\alpha}$ (see mathematical description). With these symmetry points it is possible to solve the inverse problem and to determine the length of both dikes placed in series.

Looking at the circles, one can notice that changing only one boundary condition from closed end to reservoir is sufficient to significantly alter the solution . Here the location of the eigenfrequencies is independent of the characteristic impedance contrast between the dikes. This is because all eigenfrequencies occupy points of symmetry which are independent of the characteristic impedance contrast. For dike systems with more dikes placed in series or branched, the structure of the solution in principle remains the same. In Fig. 5 the impulse response of three dikes in series and a reservoir boundary condition at both ends is shown. The synthetic impulse reponse shows nonharmonic peaked spectra with points of symmetry at $\frac{\omega l_0}{2\pi\alpha} = 0.25, 0.5, \ldots$. The "characteristic" length l_0 is the biggest common real divisor of the lengths of the dikes placed in series. Note that the characteristic length l_0 in Fig.3 and Fig.4 is not the same as in Fig. 5. In Fig.6 the impulse response of a system with branching dikes is shown. Note that symmetry points are characteristic phenomena.

Calculated eigenfrequencies of two dikes with length l_0 placed in series.

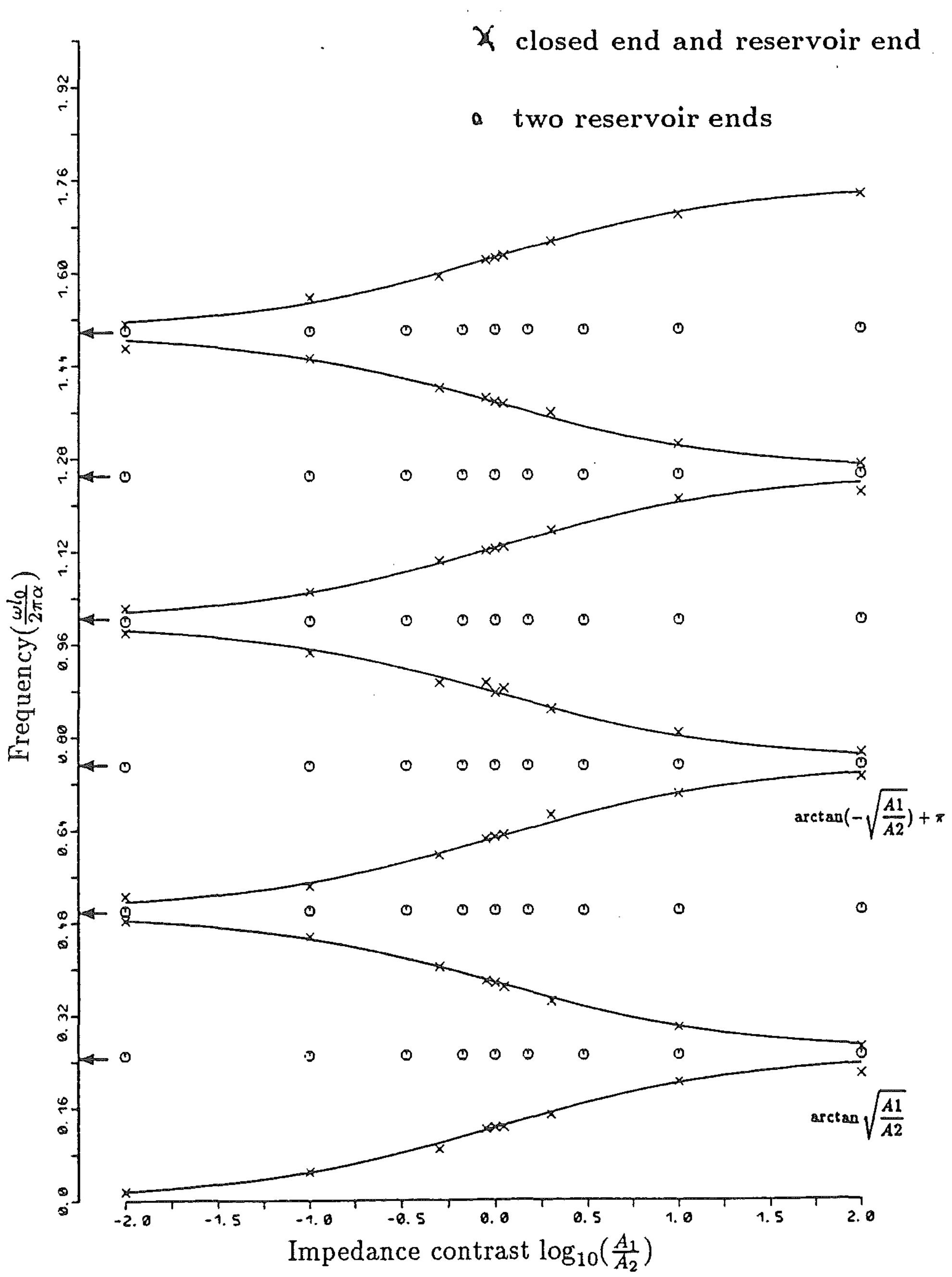

Figure 4: Relation between eigenfrequencies and characteristic impedance contrast

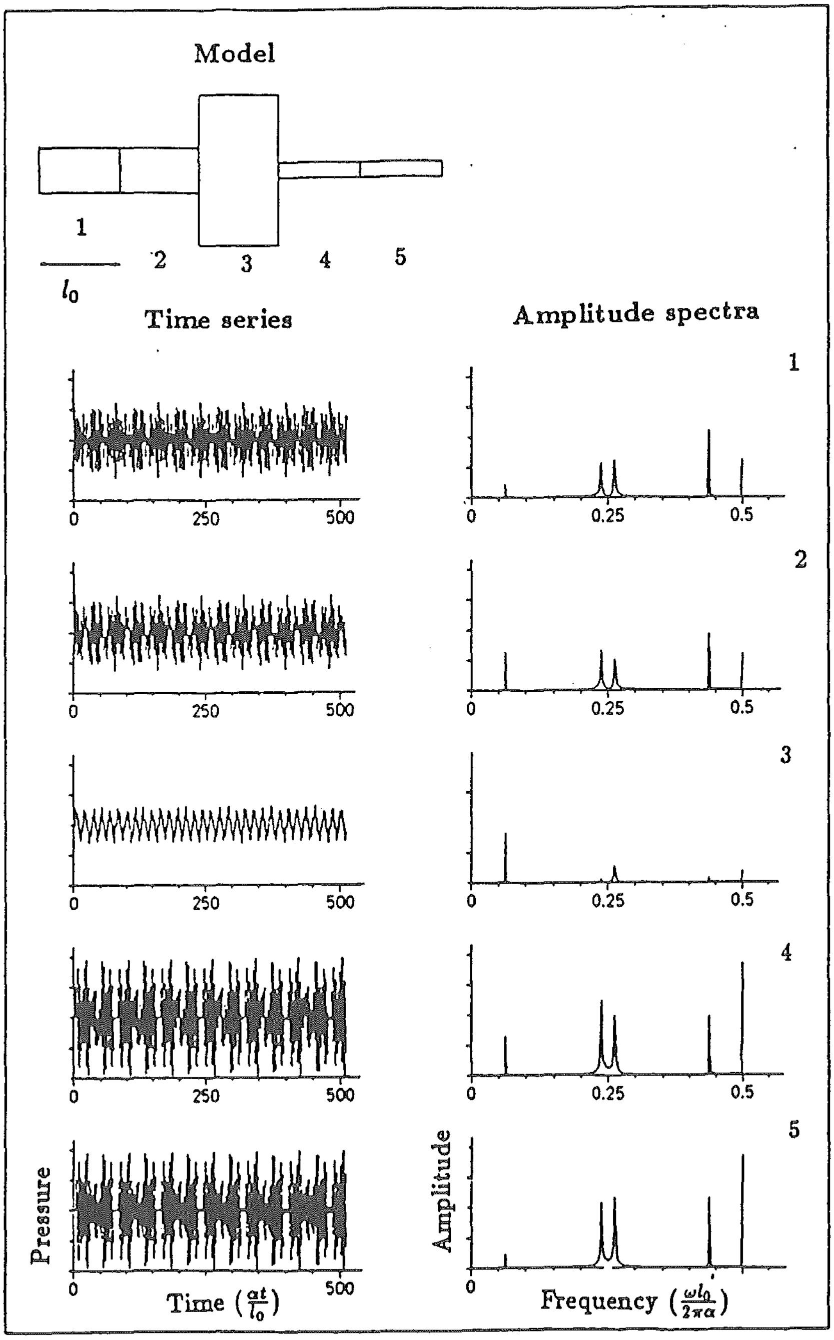

Figure 5: Impulse response of a dike system with reservoir boundary conditions at both ends

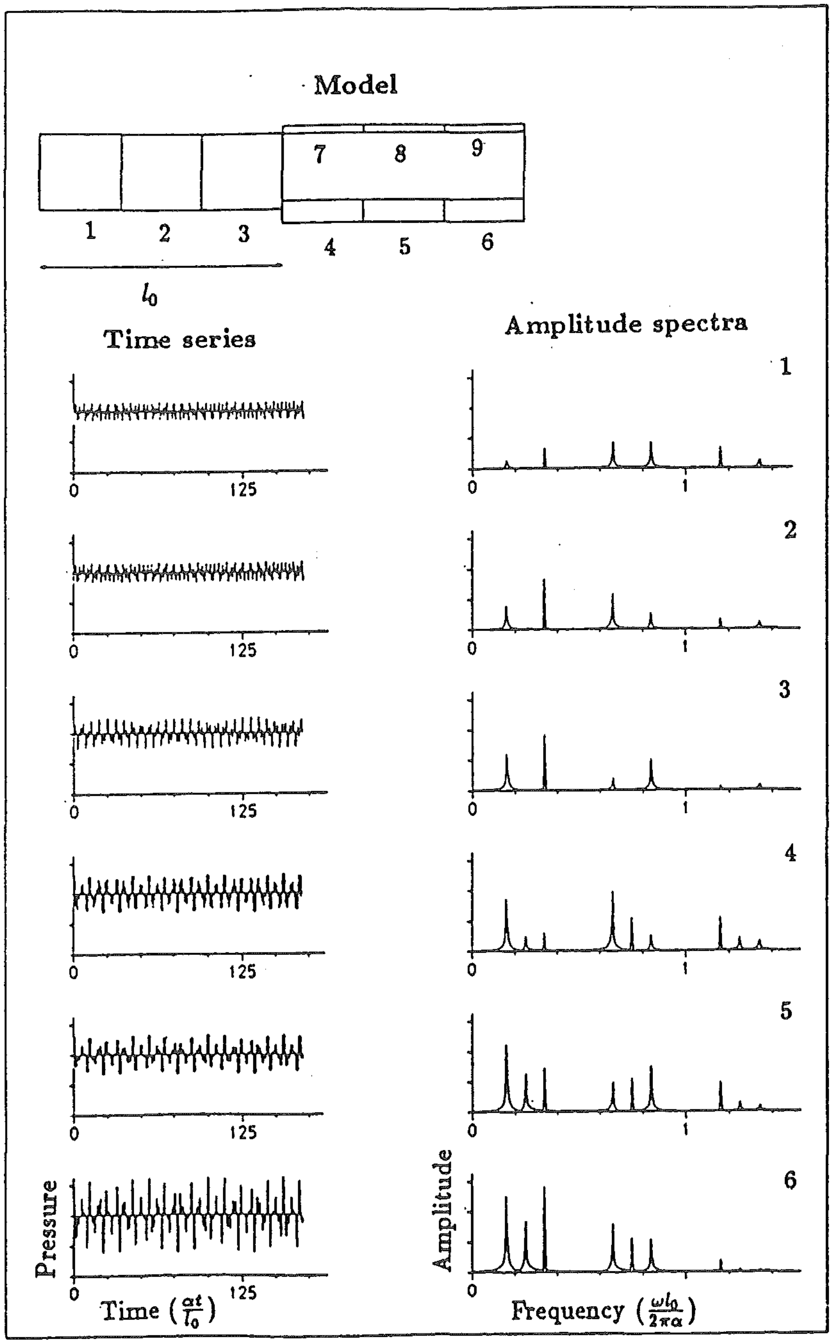

Figure 6: Impulse response of a dike system with more complex geometry

Analytical study

Transfer function of a single dike

Wylie and Streeter (1978) and Meyer and Neumann (1975) used so-called transient equations to describe the dynamics of a single pipe. With the assumption of plane waves the problem is reduced to a one dimensional problem and the equations may also be used for the dike systems considered here .

The pressure P and the hydraulic discharge $Q = uA$ (u is the fluid velocity, A the cross sectional area) can be divided into mean values $\bar{P}$ and $\bar{Q}$ and oscillatory components p' and q' .

$$P(x,t) = \bar{P}(x) + p'(x,t), \qquad Q(x,t) = \bar{Q}(x) + q'(x,t)$$

Wylie and Streeter (1978) derived the following equations for the pressure oscillations and the oscillations of the hydraulic discharge of a one ended, infinite pipe with constant cross section A.

$$\begin{aligned}
p' &= e^{st}P(x) && (1)\\
q' &= e^{st}Q(x) && (2)\\
P(x) &= P(x=0)\cosh(\gamma x) - Z_c Q(x=0)\sinh(\gamma x) && (3)\\
Q(x) &= \frac{-1}{Z_c}\Big(P(x=0)\sinh(\gamma x) - Z_c Q(x=0)\cosh(\gamma x)\Big) && (4)
\end{aligned}$$

with

$Z_c =$	$\frac{\gamma\rho\alpha^2}{sA}$ $(= \frac{\rho\alpha}{A}$ for $R = 0$)	(characteristic impedance)
$\gamma^2 =$	$Cs(Ls + R)$	(complex wavenumber)
$s =$	$\sigma + i\omega$	(complex frequency)
$L =$	$\frac{1}{gA}$	(fluid inertance)
$C =$	$\frac{gA}{a^2}$	(fluid capacitance)
$P(x=0),$	$Q(x=0)$	(boundary conditions at $x = 0$)
ρ		(density of the fluid)
α		(acoustic wave velocity of the fluid)
g		(gravitational acceleration)
A		(cross sectional area of the pipe)
R		(friction term)

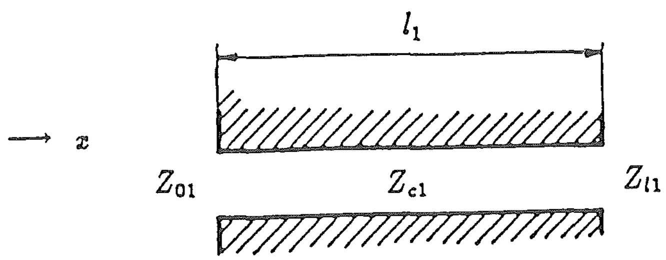

Figure 7: Single dike with characteric impedance Z_{c1}, length l_1 and boundary conditions Z_{01} and Z_{l1}

Remark: Wylie and Streeter (1978) introduced the hydraulic "gradline" $H = \frac{P}{\rho g}$. Here I use p' instead of h' and therefore the relation for the characteristic impedance Z_c differs from that given by Wylie and Streeter. With $Z_c = \frac{\rho \alpha}{A}$ $(R = 0)$ the pressure reflection coefficient between two dikes with characteristic impedances Z_{c1} and Z_{c2} is $r = \frac{Z_{c2} - Z_{c1}}{Z_{c1} + Z_{c2}}$.

By introducing the acoustic impedance $Z(x) = \frac{P(x)}{Q(x)}$ the single dike can be described by one equation (compare Fig. 7).

$$Z_{01} = Z_{c1} \frac{Z_{l1} + Z_{c1} \tanh \gamma l_1}{Z_{c1} + Z_{l1} \tanh \gamma l_1} \tag{5}$$

with $Z_{01} = \frac{P(x=0)}{Q(x=0)}$ and $Z_{l1} = \frac{P(x=l_1)}{Q(x=l_1)}$ as boundary conditions .
For example $Z_{01} = 0$ is a reservoir boundary condition at $x = 0$ and $Z_{l1} = \infty$ is a closed end boundary condition at $x = l_1$. With both boundary conditions no outflow of oscillatory energy occurs, i.e. the reflection coefficient is $+1$ or -1 .
The solution of (5) represents the well known organ pipe modes and are discussed in Ferrick et.al. (1982). The solution for a reservoir boundary condition at $x = 0$ and for $R = 0$ (fluids without viscosity) is:

$$\begin{aligned}
Z_{l1} > Z_{c1} : \qquad \omega_n &= n \frac{\pi}{2} \frac{\alpha}{l_1} \qquad n = 1, 3, \ldots \\
\sigma &= \frac{\alpha}{2 l_1} \ln\left(\frac{Z_{l1} - Z_{c1}}{Z_{c1} + Z_{l1}}\right) \\
Z_{l1} < Z_{c1} : \qquad \omega_n &= n \frac{\pi}{2} \frac{\alpha}{l_1} \qquad n = 2, 4, \ldots \\
\sigma &= \frac{\alpha}{2 l_1} \ln\left(\frac{Z_{c1} - Z_{l1}}{Z_{c1} + Z_{l1}}\right)
\end{aligned} \tag{6}$$

The implicit form of (5) with $R = 0$ is

$$Z(Z_{01}, Z_{l1}, Z_{c1}, \tanh(\frac{\sigma + i\omega}{\alpha} l_1)) = 0 \tag{7}$$

where Z_{01}, Z_{l1}, Z_{c1} are constant.
From (7) it is clear that the solution must be periodic with $\frac{i\omega l_1}{\alpha} = i\pi$ since $\tanh z = \tanh(z + i\pi)$.

Transfer function of two dikes placed in series

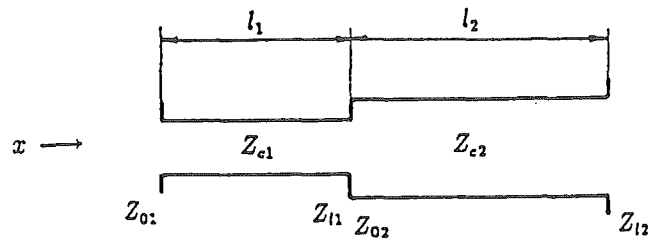

Figure 8: Two dikes placed in series with characteristic impedances Z_{c1}, Z_{c2}, length l_1, l_2 and boundary conditions Z_{01}, Z_{l2}

After Wylie and Streeter (1978) at $x = l_1$ the pressure $P(x,t)$ and the hydraulic discharge Q(x,t) is continuous so that a new boundary condition can be introduced (compare Fig. 8) in the form:

$$Z_{l1} = Z_{02} \tag{8}$$

With (8) the transfer function of the first and the second dike can be coupled. The implicit form of the new transfer function of the two coupled dikes placed in series is written in the form:

$$Z(Z_{01}, Z_{l2}, Z_{c1}, Z_{c2}, \tanh(\gamma l_1), \tanh(\gamma l_2)) = 0 \tag{9}$$

Solving this equation with respect to ω yields the eigenfrequencies of the system. With that principle of coupling transfer functions a dike system with many dikes placed in series can be constructed.
The number of independent variables in (9) can be reduced by introducing a characteristic length l_0 as the biggest real common divisor of the length l_1 and l_2 of the dikes placed in series, i.e.

$$l_1 = al_0, \qquad l_2 = bl_0 \qquad \text{a,b are integers}$$

Equation (9) may now be written as :

$$Z(Z_{01}, Z_{l2}, Z_{c1}, Z_{c2}, \tanh(\gamma l_0)) = 0 \tag{10}$$

For $R = 0$ a comparison with (7) shows that the solution must be periodic with $\frac{i\omega l_0}{\alpha} = i\pi$. This simple concept visualizes the points of symmetry seen in the plots.

The principle of reducing the number of independent variables in the impedance function of the system can also be used for more complex geometries such as more dikes placed in series or branching systems. Therefore the solution is always periodic with $\frac{\omega l_0}{\alpha} = \pi$. With

$$\binom{n}{n-k} = \binom{n}{k} = \begin{cases} \frac{n!}{k!(n-k)!} & 0 \leq k \leq n \\ 0 & 0 \leq n \leq k \end{cases} \qquad n, k \in N$$

equation (10) can be written as (see Dahm, 1989 ;equation (28)) :

$$B_{01} = \sum_{p=0}^{i > \frac{a+b}{2}} \frac{f_0^{2p} B_{l2}\left(S_p^0 + K_{12} S_p^{12}\right) + f_0^{2p+1}\left(K_{12} S_p^1 + S_p^2\right)}{f_0^{2p}\left(K_{12} S_p^0 + S_p^{12}\right) + f_0^{2p+1} B_{l2}\left(S_p^1 + K_{12} S_p^2\right)} \tag{11}$$

with

$$\begin{aligned}
S_p^0 &= \sum_{q=0}^{p} \binom{a}{2q}\binom{b}{2p-2q} \\
S_p^{12} &= \sum_{q=0}^{p} \binom{a}{2q+1}\binom{b}{2p-2q-1} \\
S_p^1 &= \sum_{q=0}^{p} \binom{a}{2q+1}\binom{b}{2p-2q} \\
S_p^2 &= \sum_{q=0}^{p} \binom{a}{2q}\binom{b}{2p-2q+1} \\
f_0 &= \tanh(\gamma l_0) \\
B_{01} &= \frac{Z_{01}}{Z_{c1}} \\
B_{l2} &= \frac{Z_{l2}}{Z_{c1}} \\
K_{12} &= \frac{Z_{c1}}{Z_{c2}}
\end{aligned}$$

Solving this equation with respect to ω yields the eigenfrequencies of the two dikes placed in series. S_p^0, S_p^1, S_p^2, S_p^{12} are sums of products of binomial

coefficients and are dependent of a and b, i.e. of the ratio of the lengths of the two dikes placed in series.
Discussing (8) for special boundary conditions B_{01} and B_{l2} one can obtain information about the structure of the solution.

Example :
$l_1 = al_0$, $l_2 = bl_0$, where a and b are odd and reservoir boundary conditions at both ends ($B_{01} = 0, B_{l2} = 0$) (compare circles of Fig. 4)
This leads to :

$$Z_{c1}\frac{C_{a+b-1}f^{a+b-1} + C_{a+b-3}f^{a+b-3} + \ldots + C_3f^3 + C_1f}{C_{a+b}f^{a+b} + C_{a+b-2}f^{a+b-2} + \ldots + C_2f^2 + C_0} = 0 \qquad (12)$$

with constant coefficients C_n and $f = \tanh(\frac{i\omega l_0}{\alpha})$, ($R = 0$).

In this example $f = 0$ and $f = \infty$ are solutions of (12), independent of the coefficients C_n, i.e. independent of the impedance contrast between the dikes. $f = 0$ is equivalent to $\frac{\omega_n l_0}{\alpha} = n\frac{\pi}{2}$, $n = 2, 4, 6, \ldots$ and $f = \infty$ respectively for $n = 1, 3, \ldots$. These are exactly the points of symmetry in Fig. 4.
Between any two poles of f (odd harmonic points of symmetry) (12) has $a + b - 1$ roots of the nominator, that means $a + b - 1$ eigenfrequencies .

In this example all points of symmetry are occupied by eigenfrequencies and the number of eigenfrequencies between the odd harmonic points of symmetry ($f = \infty$) determine the length $l = l_1 + l_2$ of the two dikes placed in series. In other words by recognizing the symmetry in the spectrum of the impulse response half of the inverse problem can be solved. For more than two dikes placed in series the estimation of the geometry of the generating systems is not unique (see Dahm, 1989).

More realistic impedance contrast between two dikes

From the above discussion it is clear that for a dike system with small characteristic length l_0 many eigenfrequencies must be known to find periodicity in the spectrum of the impulse response of such a system. Due to the "cut off frequency" at $\approx 10Hz$ for volcanic tremor the number of observable eigenfrequencies is restricted. To discuss this problem the impulse response

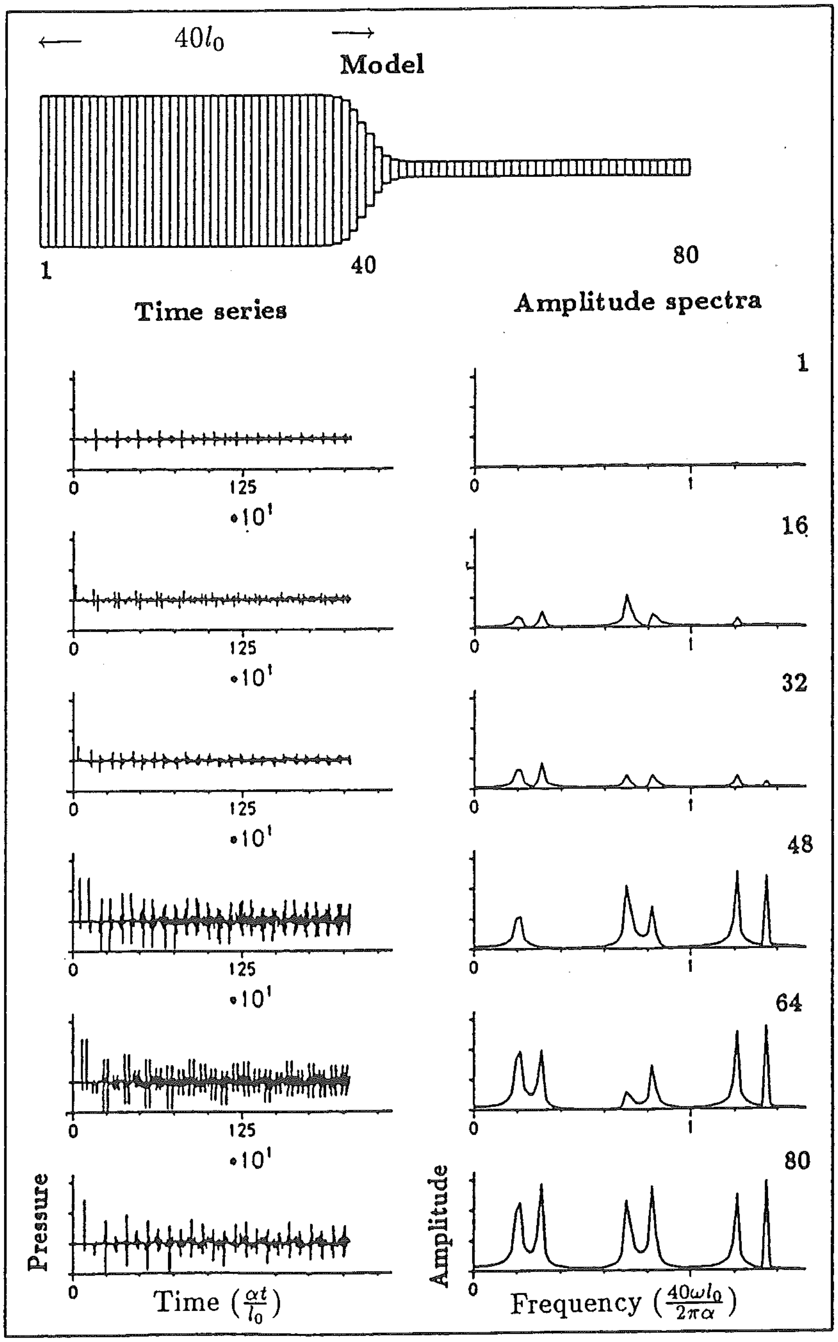

Figure 9: Impulse response of a dike system with a reservoir boundary condition at the left end and a closed end boundary conition at the right end

of a system like that in Fig. 9 was calculated. The model is comparable to that of Fig. 3a, except of the smoother impedance contrast between the dikes. As a consequence of this alteration the characteristic length of the model is much smaller than that in Fig. 3a ,i.e. the first point of symmetry in Fig. 9 should be between the 20th and 21th overtone. To make the spectra in Fig. 9 comparable to that of Fig. 3a the frequency axis in Fig. 9 is enlarged.

This example shows that the symmetry of Fig. 3a appears in the impulse response of the deepest eigenfrequencies in Fig. 9. In Dahm (1989) it is shown that this behaviour is dependent on the "wavelength" of the smooth impedance contrast. For eigenfrequencies with wavelengths bigger than the transition length of the smooth impedance contrast this contrast can be considered as discontinuous. This situation encourages to suppose simple geometries in tremor models like that suggested in this paper.

Conclusions

At present, the source mechanism of volcanic tremor is still unknown. The shape of tremor signals observed on many volcanoes suggests resonance effects to many scientists as a cause for volcanic tremor. A simple model to explain the data is a magma-filled resonating pipe or dike. This study is an extension of this model to a magma-filled resonating dike system with complex geometry. Our goal was to calculate the theoretical eigenfrequencies of such a dike system. Knowing the transfer function of a dike system one can easily calculate the synthetic response due to an arbitrary excitation function or use the transfer function to invert for the excitation function.

The extended model has many advantages in comparison with the single dike model. For example it is possible to explain a tremor spectrum with dominant peaks which are not harmonically situated. Such spectra have been observed from many volcanoes.

Likewise the fundamental frequency of a dike system with complex geometry can be much lower than that of a single dike of comparable length.

During an eruption some peaks in the tremor spectra might be shifted while others remain stable. Such phenomena have been observed on active volcanoes. This is due to a changing impedance contrast between the branches in the dike system and can be explained by the ideas introduced in this paper.

A common characteristic of this extended model is the symmetry and periodicity in the nonharmonic peaked tremor spectra. This symmetry is a function of a characteristic length l_0 in the model, or more generally, a

function of a characteristic time $t_0 = \frac{l_0}{\alpha}$ (α is the acoustic velocity in the magma). The characteristic length l_0 is the biggest real common divisor of the lengths of the single dikes, placed in series or branched. With the aid of this symmetry it is possible to make predictions about the geometry of the generating dike system. In general these predictions are not unique and more a priori information is needed to solve the inverse problem. One important source of information would be the amplitude distribution of a tremor spectrum as a function of distance from the source.
For complex dike systems the characteristic length l_0 is small. In other words many eigenfrequencies are needed to recognize the periodicity and to estimate the characteristic length. In general this is not possible because of the "cut off frequency" at $\approx 10Hz$ for volcanic tremor.
Another application of this presented method is to calculate the eigenfrequencies of a known or conjectured dike system with complex geometry. In this way the finite element program can be used as a tool to prove models by calculating synthetic tremor signals.
This study has demonstrated the potential of using hydraulic transients to model volcanic tremor and future research will aim to solve the inverse problem.

Acknowledgments

I would like to thank Prof. Dr. Rolf Schick an Dr. Walter Zürn for helpful assistance and discussions througout this work. I also gratefully appreciate the careful reviews of Heiner Igel and Dr. Wolfgang Brüstle.

References

Chouet,B., R.Koyanagi, and K. Aki , The origin of volcanic tremor in Hawaii, Part 2: Theory and discussion, *U.S. Geol. Surv. Prof. Pap., 1350,* 1259-1280, 1987

Chouet, B. , Resonance of a fluid-driven crack: Radiation properties and implications for the source of long-period events and harmonic tremor, *J. Geoph. Res., 93,* 4375-4400, 1988

Dahm, T. , Eigenschwingungen magma-gefüllter Klüfte mit komplexer Geometrie *Diplomarbeit, Geophys. Inst. Karlsruhe,* 1989

Fehler, M. , Observations of volcanic Tremor at Mount St. Helens volcano *J. Geoph. Res., 88,* 3476-3884, 1983

Ferrick, M.G., A. Quamar, and W. F. St. Lawrence , Source mechanism of volcanic tremor, *J.Geophys. Res. 87,* 8675-8683, 1982

Ferrick, M.G. and W.F. St.Lawrence , Comments on "bservations of volcanic tremor at Mount St. Helens volcano" by Michael Fehler *J.Geophys. Res. 89,* 6349-6350, 1984

Kirschke, K. , Druckstoßvorgänge in wassergefüllten Felsklüften *Veröff. Inst. Bodenmech. und Felmech. 61, Uni Karlsruhe* , 164S : 1974

Meyer E. und E.G. Neumann , Physikalische und Technische Akustik *Vieweg , Braunschweig* , 380S ; 1975

Sassa, K. , Volcanic micro-tremors and eruption-earthquakes, *Mem Coll. Sci. Univ. Kyoto, Ser. A, 18* , 255-293, 1935

Schick, R. , Volcanic tremor-source mechanism and correlation with eruptive activity *Nat. Hazard 1,* 125-144 , 1988

Seidl, D., R. Schick, and M. Riuscetti , Volcanic tremors at Etna: A model of hydraulic origin, *Bull. Volcanol., 44,* 43-56, 1981

St. Lawrence, W., and A. Quamar , Hydraulic transients: A seismic source in volcanous and glaciers, *Science, 203,* 654-656, 1979

Wylie, E.B., und V.L. Streeter , Fluid Transients *McGraw-Hill,* 1978

Dimensional Analysis of Volcanic Tremor

Joachim Strigl

Institut für Geophysik Richard-Wagner-Straße 44 D-7000 Stuttgart 1

Introduction

'Volcanic tremor' is a collective name for the intensive ground motion which can be observed at many volcanoes, even in a non-eruptive state. Pressure fluctuations in the fluid system of the volcano are, by definition, the origin of tremor. The exact source mechanism is nevertheless controversial, and it is by no means clear, that tremor always stems from the same type of source.

Up to now, traditional tools like power spectrum estimation have been used in analysing tremor time series. If the tremor generating system should be chaotic, i.e. if it displays sensitive dependence on initial conditions, a dimensional analysis is much more appropriate an instrument [Mayer-Kress, 1986]. It will reveal the number of degrees of freedom relevant in the generation of tremor, if this number is not too high. Let the number of degrees of freedom be k. If this has been found out we know that the analysed signal can be generated by a set of k coupled ordinary first order differential equations: valuable information for the discussion of tremor source models.

Let us suppose, that the state of our system is described by the f-dimensional phase space vector $\underline{q}$, its time evolution by a set of first order differential equations:

$$\underline{\dot{q}}(t) = \underline{F}(\underline{q}(t)) \qquad (1)$$

The number of degrees of freedom will then a priori be f. If the system is dissipative, dynamics will asymptotically be confined to a lower dimensional subsection of phase space, an attractor. The strange realm, where chaotic behaviour takes place in a dissipative system is called strange attractor. Strange attractors often possess a self-similar structure. In contrary to 'normal' attractors, they always have a non integer fractal dimension. In any case, the number of relevant degrees of freedom will reduce in the course of time from f, the dimension of phase space, to the dimension of the manifold containing the attractor (in the case of non strange attractors, the manifold is identical with the attractor).

Due to self-organisation, even an infinite dimensional dissipative system, which is non linear and thermodynamically open (necessary for selforganisation) can have low dimensional, non trivial (i.e. no fix points) attractors [Broomhead & King, 1986]. These conditions are surely fulfilled by the fluid system of a volcano. Thus there is hope to find one or more low dimensional attractors in volcanic activity. Corresponding to the nonperiodic tremor signals with their often broad spectrum, we might expect strange attractors. Our aim is to check, if the 'chaotic' looking tremor signals are the effect of many independent events, a sort of noise, or if they are chaotic in the sense of deterministic chaos, i.e. governed by a moderate number of degrees of freedom.

To accomplish this task, two steps are necessary:

- reconstruction of the dynamics in phase space from a time series. Because every trajectory attracted by an attractor will 'fill' the latter in the course of time, an attractor can be reconstructed by the method described below, if the time series is long enough

- determination of the dimension of the reconstructed attractor

a) Reconstruction

The essential idea is the construction of n-dimensional vectors $\underline{x}_i$ from a sampled time series $\{R_1, R_2, R_3, \ldots\}$ by

$$\underline{x}_i = (R_i, R_{i+\tau}, R_{i+2\tau}, \ldots, R_{i+(n-1)\tau}) \tag{2}$$

The resulting (sampled) trajectory $\underline{x}_1$, $\underline{x}_2$, ... in the n-dimensional embedding space is, under certain conditions, similar to the original trajectory in the phase space of the system producing the time series. Similar here means that the trajectory in embedding space is the image of the original trajectory under a differentiable and invertible map between the manifolds containing the two trajectories. If the dimension of the original manifold is f, a theorem of Takens requires $n \geq 2f + 1$ in order to make the similarity a generic property [Broomhead & King, 1986].

Unfortunately, we usually don't know f in advance. It is therefore convenient to increase n, until the dimension of the reconstructed set of points saturates, i.e. becomes independent of n. The question of how to choose the 'time delay' τ is controversial. We usually take $\tau \approx$ sampling rate $*$ T/4, with T being the dominant period of the signal.

b) Determination of the dimension

The now well known Grassberger & Procaccia algorithm is used to determine the dimension of the reconstructed set of points. Their correlation dimension D is one of the possible generalisations of the notion 'dimension'. It is defined by [Grassberger & Procaccia, 1983]

$$D = \lim_{l \to 0} \frac{\log(C(l))}{\log(l)}$$

$$C(l) = \lim_{N \to \infty} \frac{1}{N(N-1)} * Z$$

$$Z = \left(\text{number of pairs of points } (i, j) \text{ with distance} < l\right)$$

C(l): correlation integral (self pairs are not counted!)
N: number of points

In practice, D is determined from the slope of a log(C(l))/log(l) plot. If there exists a region with constant slope, this is easily done. One possible reason for the absence of such a region is, that the point set in embedding space is not 'dense' enough and we can only see the gross structure of the attractor, because the time series used for reconstruction is not long enough. In this case, any interpretation of results gained from averaged slopes is at least hazardous, if not dubious.

Noise should always result in D = n. If a signal is disturbed by additional noise, the log/log plot will show two regions with different slopes. For small distances l - compared with the average noise amplitude - we get slope = n, for greater distances the slope reveals the correlation dimension of the original system (without noise).

For the computation of distances, we use the maximum norm or the euclidean norm. In order to save computation time, sometimes not all N(N-1)/2 distances are computed. The application of an algorithm proposed by Bingham and Kot [Bingham & Kot, 1989] results in computing all distances below a certain limit, and only some (but not all) greater distances. The latter are disregarded for the determination of the slope. Also disregarded are all distances of pairs (i, j) with $|i - j| < 5$. Otherwise we possibly would see a region with slope one in the log(C(l))/log(l) plot, because our point set lies on one trajectory [Grassberger].

Results

Some results of the examination of synthetic and tremor time series are presented below (figures 5 - 12). A representative section of every time series is shown, as well as a power spectrum estimation, a plot of correlation dimension versus embedding dimension and a log(C(l))/ log(l) plot for different embedding dimensions. In contrary to the definition given above, C(l) is not normalised to a maximum value of one in the graphics. The power spectrum usually is computed from 4096 points. In order to reduce the variance of one power spectrum value, sixteen adjacent values at a time are averaged. The absolute time and frequency values for the synthetic time series are arbitrary.

a) Synthetic signals

There is certainly some modification of tremor signals on their way from the source to the seismometer. Thus it is useful to examine, how the modification caused by the propagation through a stratified medium (like a volcano) affects the correlation dimension of different types of signals. We use a recursive filter to simulate the effect of a medium with three homogenous layers over a homogenous half space (fig. 1).

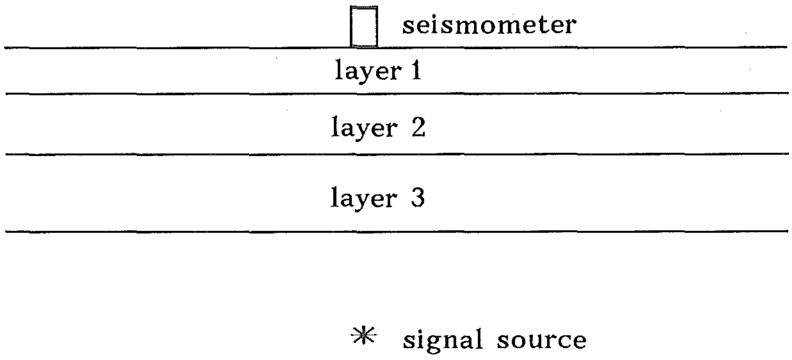

fig. 1: layer model

The seismic velocity is assumed to diminish from bottom to top. Dispersion is not taken into account. The signal at the seismometer, Y, is obtained from the samples X_i of the source signal as follows:

$$Y_i = X_i - 0.30Y_{i-4} - 0.34Y_{i-7} - 0.33Y_{i-17} \qquad (3)$$

Filter coefficients are not derived from real layer data but chosen with respect to the source signals. The impulse response of our filter is given below:

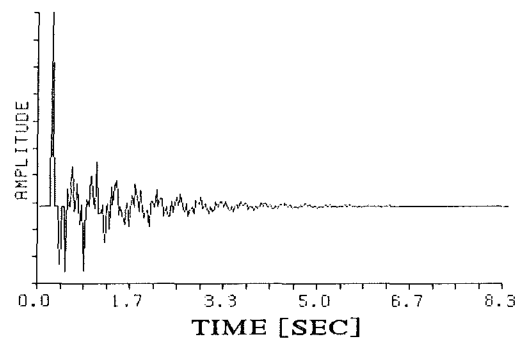

fig. 2: impulse response of filter (3)

α) Henon map

One of the most popular examples of a discrete map is the Henon map. It is defined by [Grassberger & Procaccia, 1983]

$$
\begin{aligned}
x_{n+1} &= y_n + 1 - ax_n^2 \\
y_{n+1} &= bx_n
\end{aligned}
\tag{4}
$$

For a = 1.4 and b = 0.3 the generated point set has D = 1.25 [Grassberger & Procaccia, 1983]. Here, we use a 'time series' composed of 3000 values x_i, which has been filtered according to (3). It yields D ≈ 6.3 (see figure 5).

For a time series filtered by a propagation medium with only one or two layers, we get D ≈ 2.2 respectively D ≈ 3.6 (not documented in this paper).

β) Lorenz model, periodic

The famous Lorenz equations look like this [Jetschke, 1989]:

$$
\begin{aligned}
\dot{q}_1 &= s(q_2 - q_1) \\
\dot{q}_2 &= -q_1 q_3 + r q_1 - q_2 \\
\dot{q}_3 &= q_1 q_2 - b q_3
\end{aligned}
\tag{5}
$$

For s = 16, b = 8/3 and r = 320, the system possesses a (stable) limit cycle. As time series we take 4000 values of the variable q_1. This series yields D = 1, as one would expect (not documented in this paper). From a version filtered with (3), we get the same result, D = 1 (figure 6).

γ) Lorenz model, chaotic

With s = 10, b = 8/3 and r = 28, the (strange) Lorenz attractor arises. For a time series of 3000 values q_1, we get a correlation dimension of ca. 2.1 (figure 7), quite close to the literature value of 2.05.

The application of filter (3) on this series, combined with subsequent high pass filtering according to the transfer function of a 1.2 Hz seismometer, results in a really 'chaotic looking' time series. Nevertheless, the correlation dimension is not greater than 3.3 (figure 8).

reconstruction of the lorenz attractor

reconstruction from the filtered series

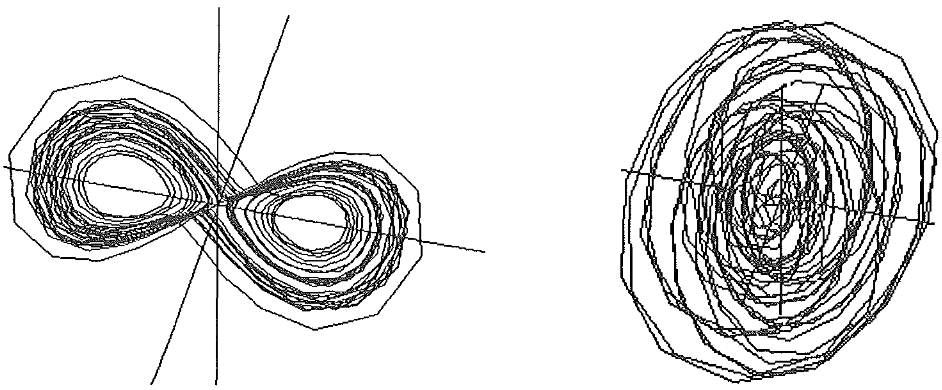

fig. 3: lorenz attractor and reconstruction from filtered series

The influence of the wave path on a source signal can be described by a linear filter. Linear filtering does not generate frequencies, which are not already present in the source signal. Therefore, periodic signals remain periodic and quasiperiodic signals generally remain quasiperiodic. Propagation through a stratified medium will in no case increase the correlation dimension of a periodic or quasiperiodic signal. On the other hand, the correlation dimension of nonperiodic (but not random) signals increases, if we increase the number of layers.

b) Tremor time series

The tremor time series stem from measurements of the vertical component of the ground velocity. The series presented here were recorded with seismometers of ca. one Hz eigenfrequency. Hence frequencies fairly below one Hz, which can be present in tremor, could not be recorded. Before digitizing with a 12-bit A/D converter, the series were low pass filtered to prevent aliasing. Another reason for filtering is, that high frequencies in tremor generally are rather associated with boiling ground water, than with magma and/or gas movements [Schick].

α) Aetna, normal activity

The results given in figure 9 stem from a time series recorded at Aetna during normal (i.e. non eruptive) activity, at a crater distance of 6.5 km. The correlation dimension is calculated from 5000 points. It increases with increasing embedding dimension, hence we can not determine the number of degrees of freedom of our system (signal source plus propagation path).

In the power spectrum, we have the typical peak at 1.6 Hz, which can be found in all Aetna spectra.

β) Aetna, ash eruption

Here, we use 7000 points of a time series recorded during an ash eruption (figure 10). Due to the crater distance of only 0.4 km, higher frequencies predominate in the power spectrum. Nevertheless, the 1.6 Hz peak still is present, as can be seen after low pass filtering.

Again, there is no saturation of the correlation dimension.

γ) Aetna, strong ash eruption

The results presented in figure 11 are gained from a time series recorded during a strong ash eruption, at a crater distance of 6.5 km. The spectrum is quite monochromatic. This is genuine, not an effect of low pass filtering before the digitizing. We calculate the correlation dimension from 7000 points: no saturation is visible.

Figure 4 is a picture of the point set reconstructed from our time series for embedding dimension two, i.e. it shows the points $\underline{x}_i$ (defined in (2)) for n = 2. In contrary to all other 'phase portraits' that we made from tremor series, it clearly shows a (spiral) structure. A linear, damped oscillator, which is 'kicked' now and then, could, for example, produce such a picture.

fig. 4: point set reconstructed from tremor series

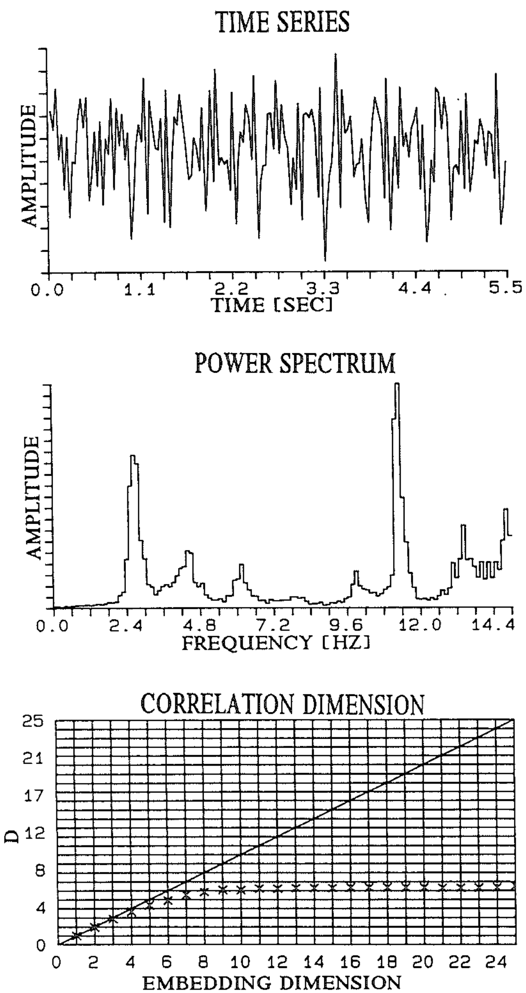

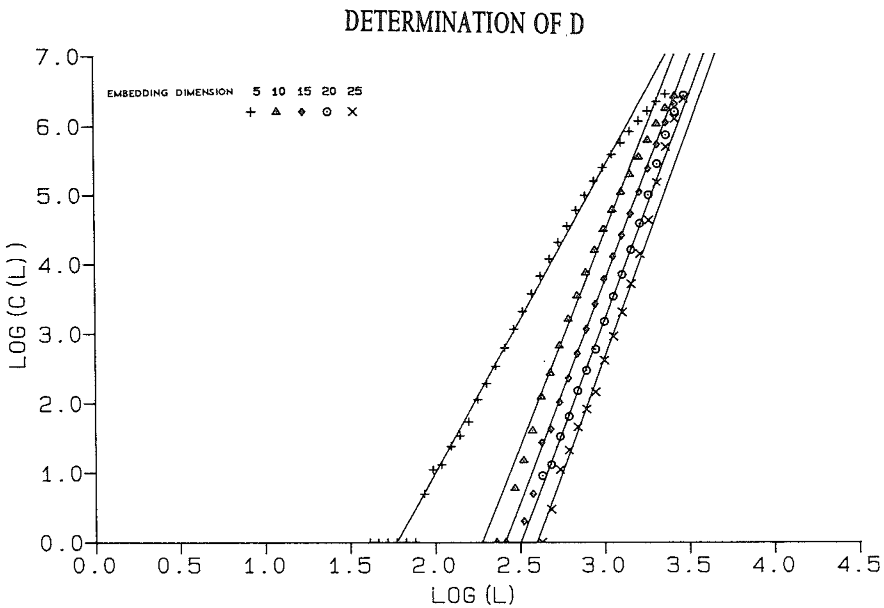

fig. 5	origin of time series	: Henon map, filtered with (3)
	length of series	: 3000 points
	time delay τ	: 1
	result for D	: 6.3

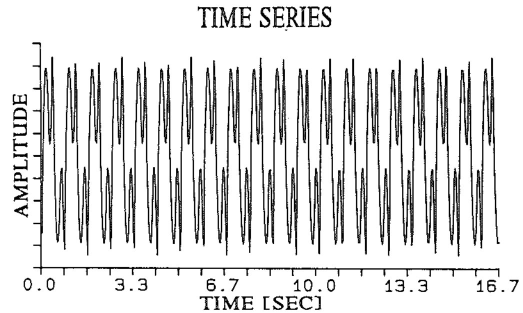

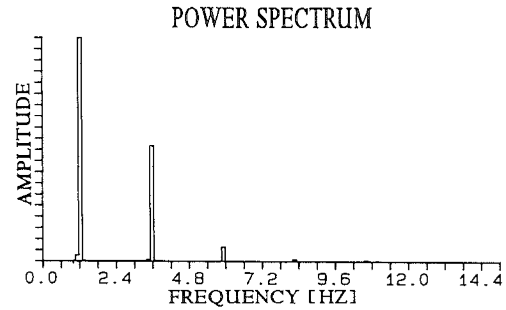

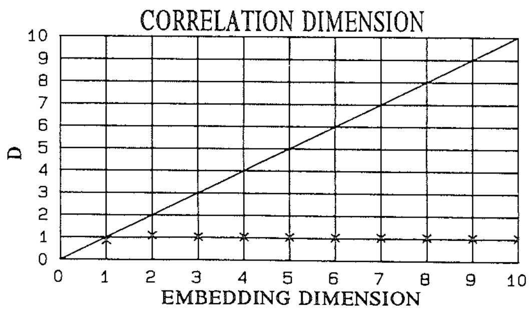

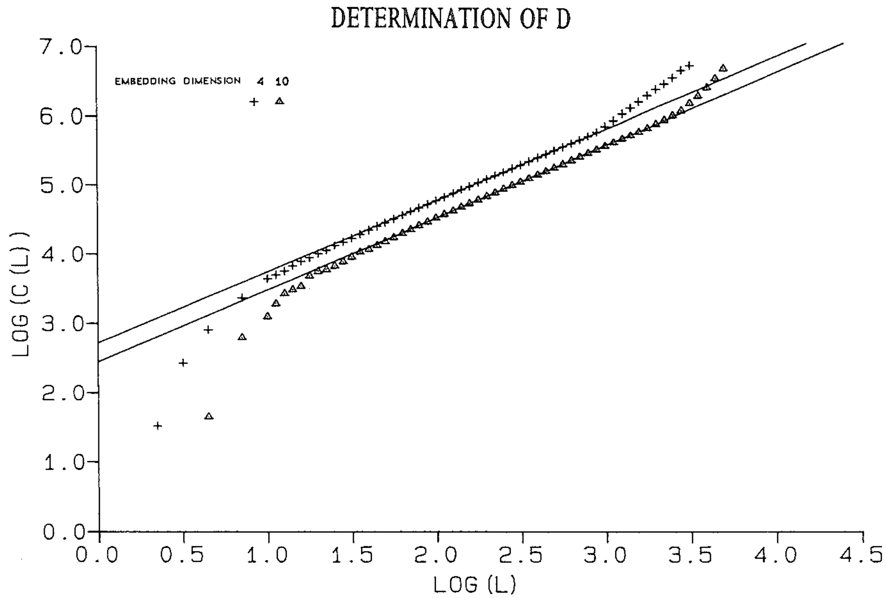

fig. 6 origin of time series : Lorenz equations (periodic), filtered with (3)
length of series : 4000 points
time delay τ : 6
result for D : 1

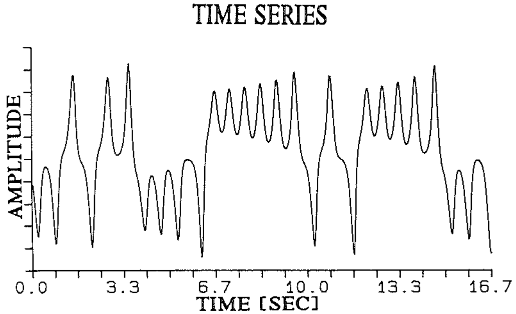

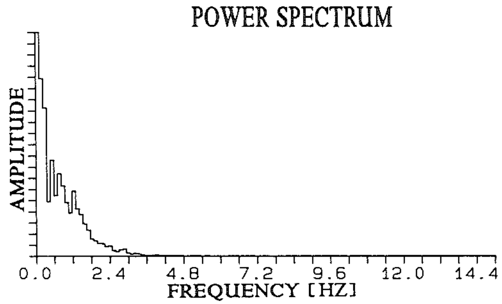

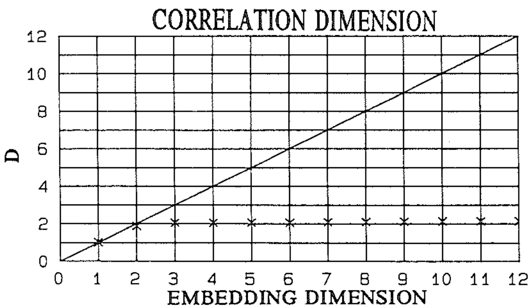

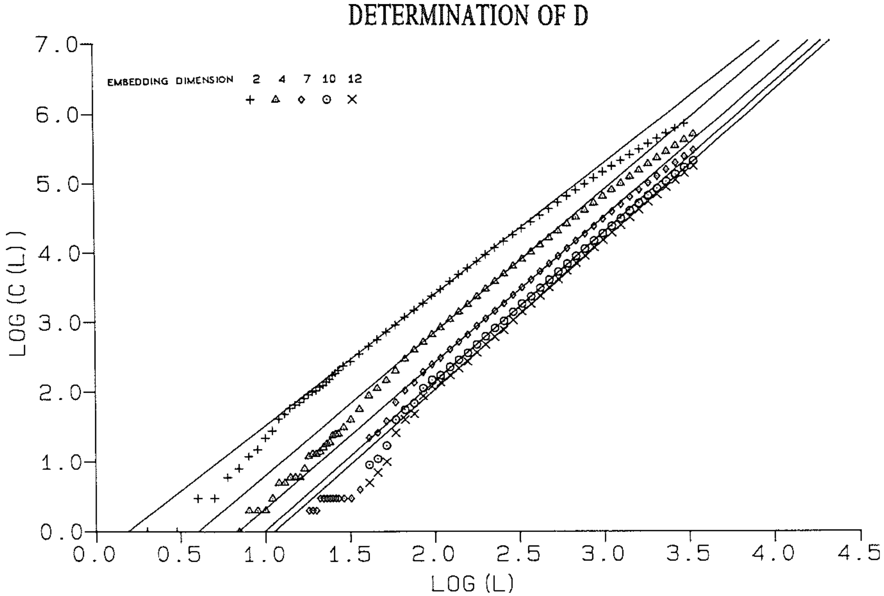

fig. 7	origin of time series	: Lorenz equations (chaotic)
	length of series	: 3000 points
	time delay τ	: 1
	result for D	: 2.1

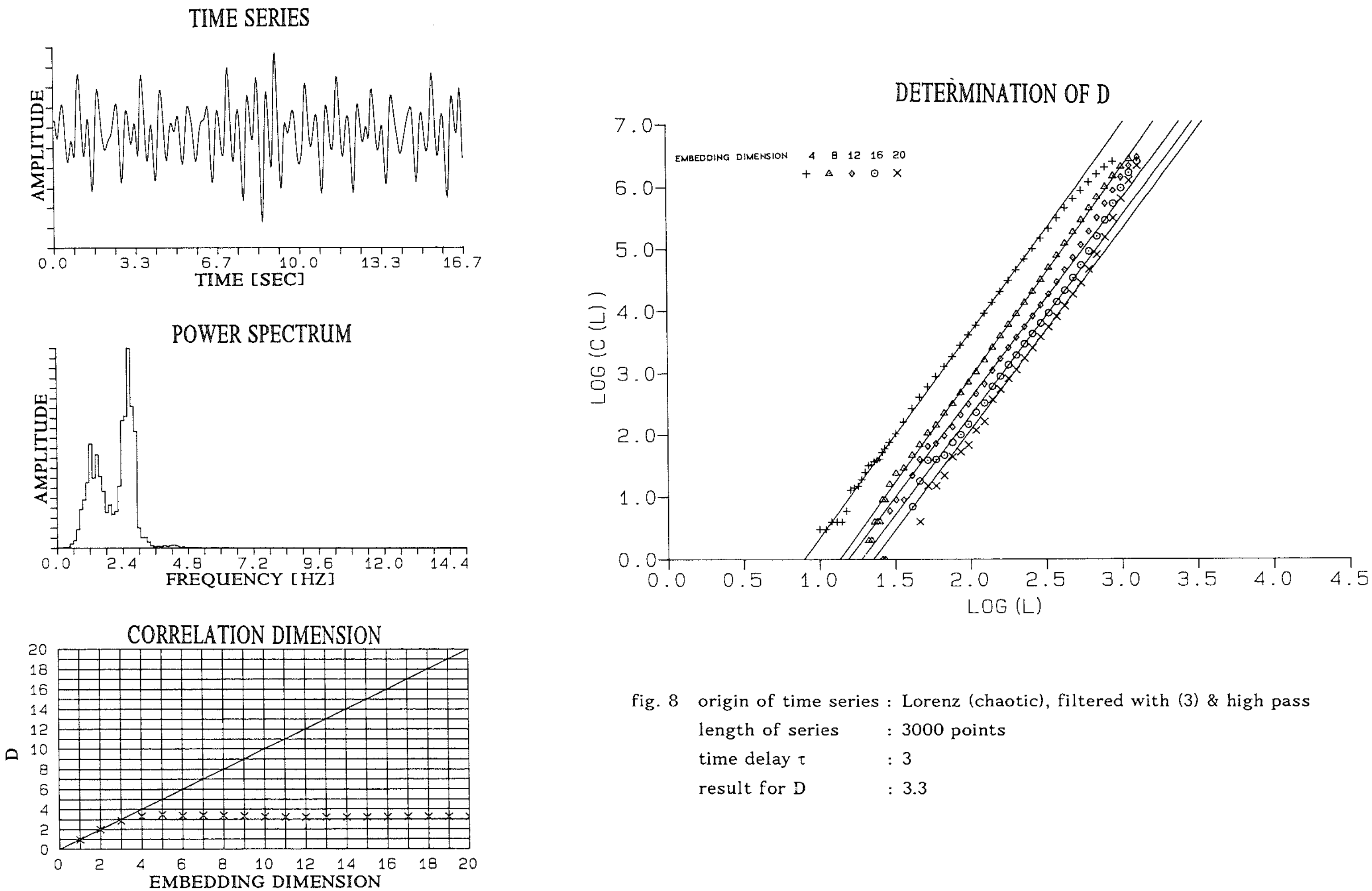

fig. 8 origin of time series : Lorenz (chaotic), filtered with (3) & high pass
length of series : 3000 points
time delay τ : 3
result for D : 3.3

TIME SERIES

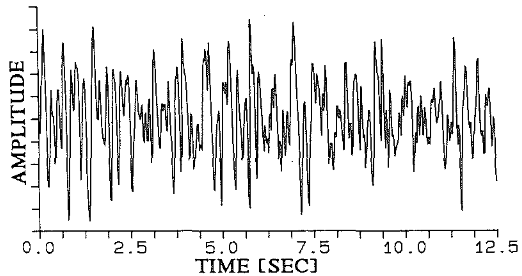

POWER SPECTRUM

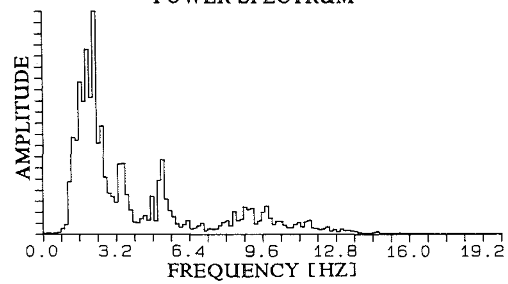

CORRELATION DIMENSION

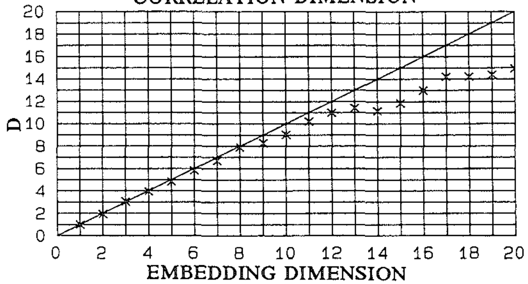

DETERMINATION OF D

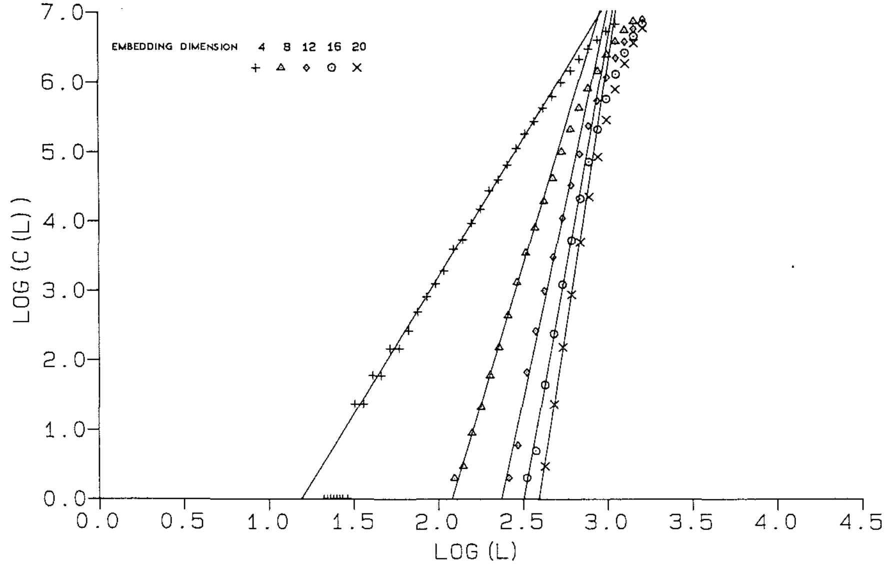

fig. 9	origin of time series	: Aetna, normal activity, crater distance 6.5 km
	length of series	: 5000 points
	cut-off frequ. low pass	: 20 Hz
	sampling rate	: 40 Hz
	time delay τ	: 5
	result for D	: no saturation

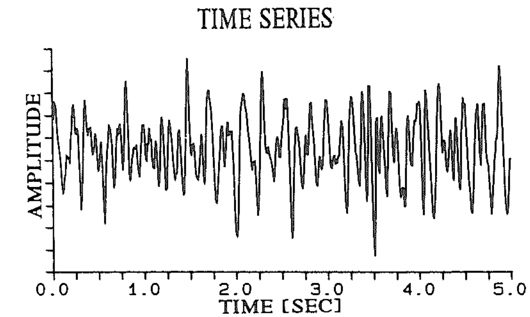

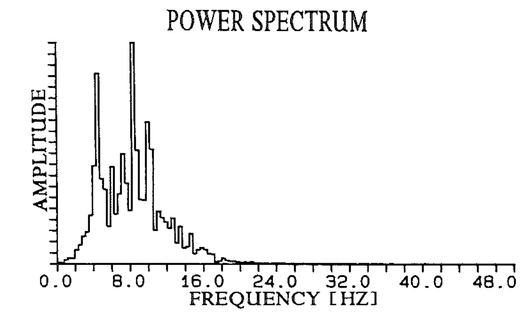

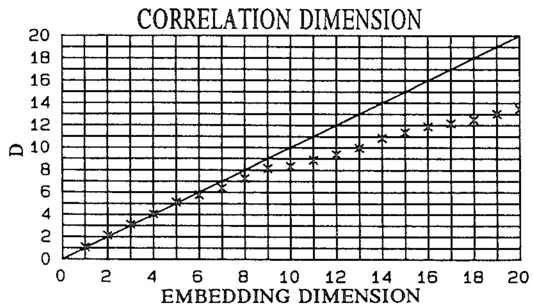

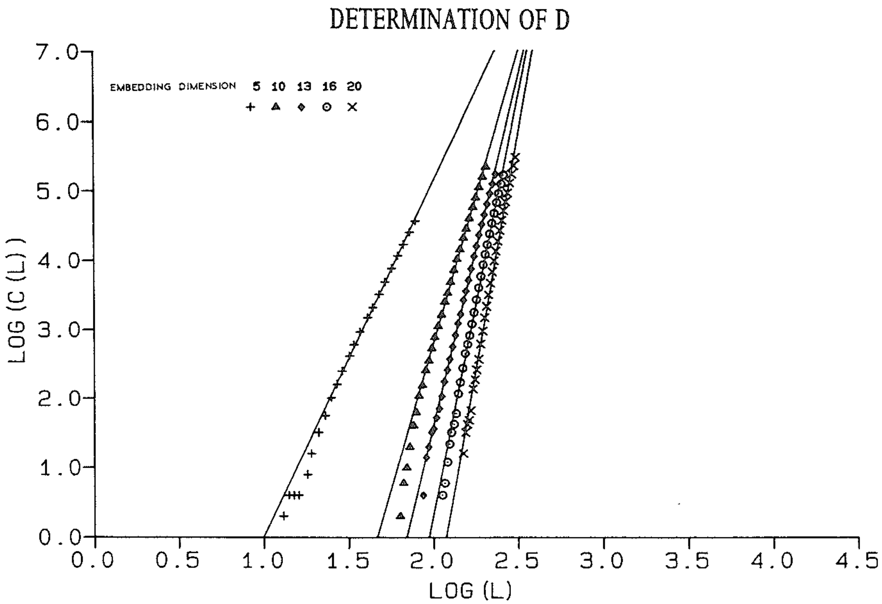

fig. 10	origin of time series	: Aetna, ash eruption, crater distance 0.4 km
	length of series	: 7000 points
	cut-off frequ. low pass	: 50 Hz
	sampling rate	: 100 Hz
	time delay τ	: 3
	result for D	: no saturation

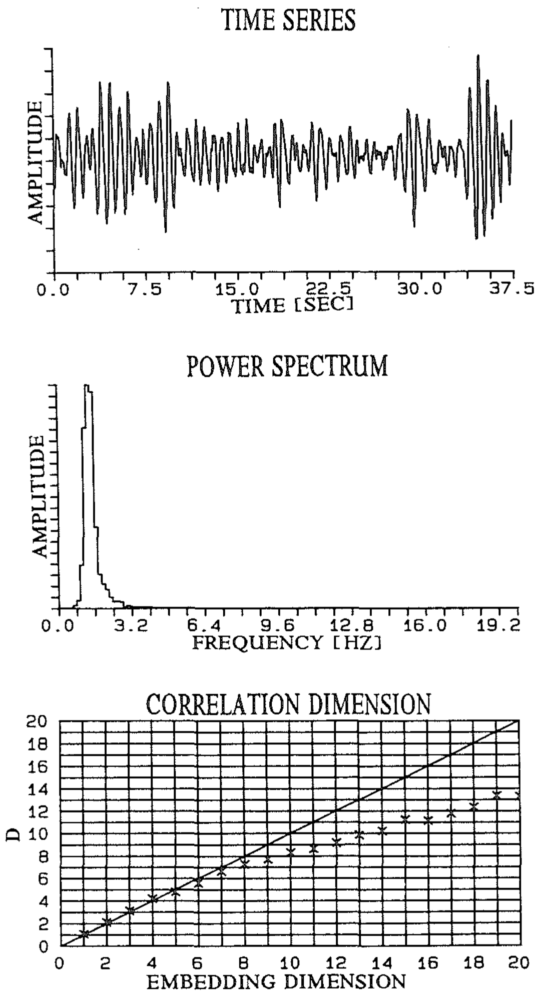

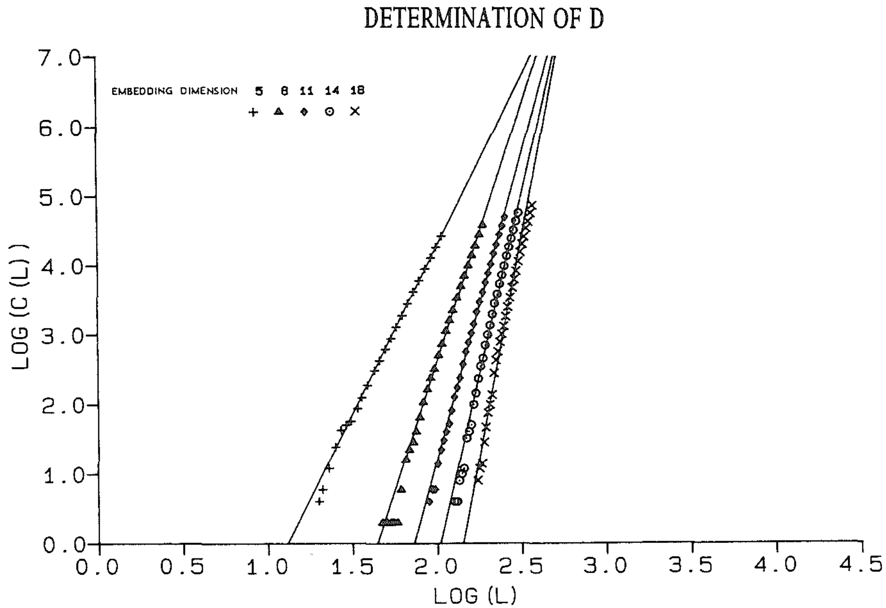

fig. 11 origin of time series : Aetna, strong ash eruption, crater distance 6.5 km
length of series : 7000 points
cut-off frequ. low pass : 20 Hz
sampling rate : 40 Hz
time delay τ : 7
result for D : no saturation

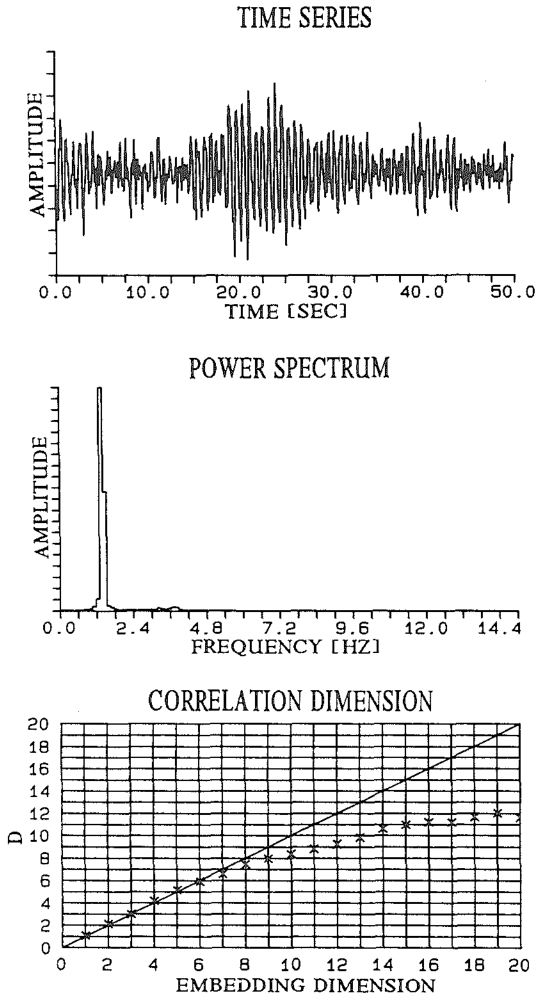

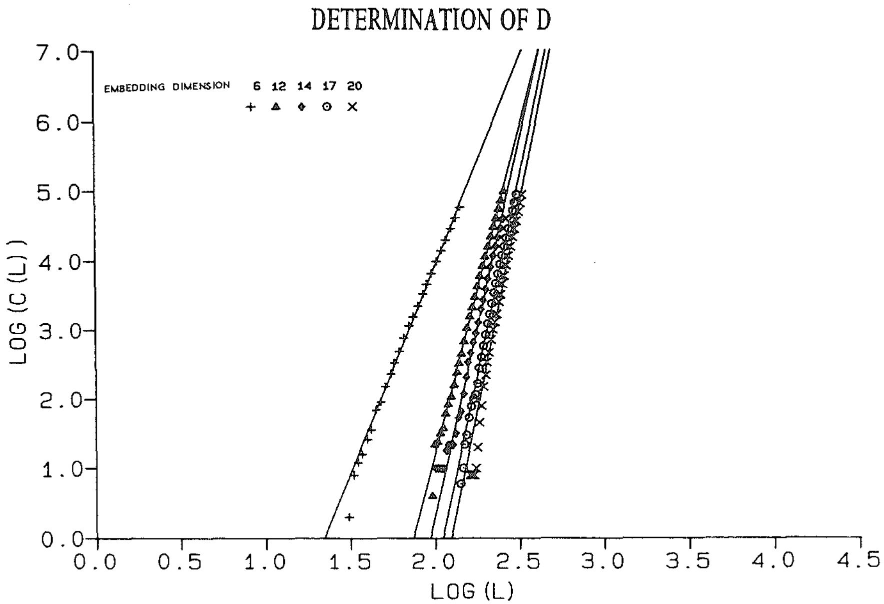

fig. 12	origin of time series	: Merapi, no activity, crater distance 1.5 km
	length of series	: 10000 points
	cut-off frequ. low pass	: 5 Hz
	sampling rate	: 30 Hz
	time delay τ	: 5
	result for D	: no saturation

δ) Merapi

Figure 12 shows the results from a time series from Merapi/Central Java. It was recorded at a crater distance of 1.5 km. The power spectrum looks extremely monochromatic, only partly an effect of the low pass filtering.

As in α) –γ), there is no clear saturation of the correlation dimension, which in this case is calculated from 10000 points of the time series.

In investigations not documented here, we used other time series, up to 20000 points and embedding dimensions up to 30, but the result did not change. No dimensional analysis of tremor series showed a clear cut saturation of correlation dimension.

Conclusions

The investigated tremor time series can obviously not be generated by a set of few differential equations. The plots of correlation dimension versus embedding dimension look more like 'noise' than like low dimensional deterministic dynamics. Up to a embedding dimension of ca. nine, tremor correlation dimensions do not differ from results gained from random number series, where we get correlation dimension ≈ embedding dimension. Correlation dimensions for greater embedding dimension are difficult to determine in the case of tremor: there is no region with really constant slope in the log(C(l))/log(l) plots. Perhaps this problem could be solved by using longer time series.

Without being imprudent, we can state, that the dimension of our systems is not less than eight (that is roughly the slope we get with embedding dimension nine). Our system is composed of tremor source and propagation medium. That's why we can not exclude a low dimensional tremor source mechanism: we can not isolate the source signal, and the signal recorded somewhere on the surface of the volcano can give a greater correlation dimension, as we learn from the synthetic examples.

Acknowledgements

I thank all people who supported me: Prof. Schick, Prof. Wielandt, all members of the Institut für Geophysik in Stuttgart, Dr. Wunderlin and Prof. Grassberger. Last but not least, thanks for many nice tremor time series to the Istituto di Vulcanologia in Catania/Sicily and the Institute of Geophysics in Yogyakarta/Java.

References

Bingham, S. and M. Kot, 1989: *Multidimensional Trees, Range Searching, and a Correlation Dimension Algorithm of reduced Complexity*, Physics Letters A 140 (6), p. 327

Broomhead, D.S. and G.P. King, 1986: *Extracting qualitative Dynamics from experimental Data*, Physica 20D, p. 217

Grassberger, P., personal communication

Grassberger, P. and I. Procaccia, 1983: *Measuring the Strangeness of Strange Attractors*, Physica 9D, p. 189

Jetschke, G., 1989: *Mathematik der Selbstorganisation*, Vieweg

Mayer–Kress, G. (editor), 1986: *Dimensions and Entropies in Chaotic Systems*, Springer

Schick, R., personal communication

Location of Seismic Sources of Merapi (Central Java) with Impulsive Character

Abdulrahman Fadeli
Physics Department, Gadjah Mada University,
Yogyakarta, Indonesia

Abstract

The seismicity at mount Merapi is characterized by the continuous occurrence of volcanic shocks and sporadic volcanic tremor, where the former have impulsive character. Using the amplitude ratios of the impulsive seismic signals recorded by three stations the locations of the foci show the following features : During the "normal" state of activity the volcanic shocks are dominated by those with shallow depths (less than 1 km below the summit). It is suggestive that these shocks are caused by cracks or fractures in the lava dome. But when the lava doming episode occurred in October 1986, the number of deeper volcanic earthquakes increased. The source locations of these shocks moved upward from depths of about 5 km to 1 km in a time interval of about two months.

Introduction

Mount Merapi which is located in Central Java ($7^{\circ}32'30''$ S, $110^{\circ}26'30''$ E) and has a height of 2911 m above sea level is one of 26 active volcanoes in Indonesia *(Data Dasar Gunung Api di Indonesia, 1979)*, and is among a dozen volcanoes in the world which are in a state of persistent eruption *(Tazieff, 1983)*. The historical eruptions which are recorded from the year 1600 until 1984 show that in the average small eruption occur in about 2-3 years intervals and larger eruptions in intervals of 9 to 16 years *(van*

Bemmelen, 1949). The latest two big eruptions in 1930 and 1964 killed 1369 and 64 people, respectively. It is suggestive that the continuously eruptive activity of Merapi is a consequence of an intersection of two fracture system lying under the volcano *(Tazieff, 1983)*. The Merapi is also well known for its lava dome building process which has been observed since 1883 *(Data Dasar Gunung Api di Indonesia, 1979)*. This process on the active vent of Merapi is classified as a type A eruption i.e. eruptions which are associated with the magma movements in the absence of gas *(Hartman. 1935 ; Kirbani, 1990)*. This type of eruption is not explosive, the magma rises slowly and piles up above the vent to form a lava dome, usually in the shape of a tongue.

It is still not clear how a volcanic eruption, either explosive or intrusive, is initiated, but it is generally accepted that the state of the volcanic activity is associated with the dynamics of magma inside the volcano. As this magma movement cannot be directly observed, surface phenomena which are supposedly related to the magma flux might provide a better mean to determine the state of volcanic activity. Furthermore, in order to get valid interpretations concerning the eruptive activity, fundamental parameters which are supposedly related with the eruptive process have to be observed and cross-correlated. There is no doubt that seismicity of a volcano is one of the most important phenomena indicating the state of the activity. The origins of the seismic sources can be used to trace the foci of the magma movements, leading to some knowledge about eruptive mechanisms.

The seismicity at Merapi is characterized by a continuous occurrence of volcanic shocks and sporadic tremor (*Fadeli et al.; 1987)*. The former which have impulsive character may be caused by material failure in the medium surrounding the magma conduits as a consequence of excessive magma pressure (*Schick, 1988)*, or may be caused by shear failure in the fracture system. In this paper the migration of the origins of the volcanic shocks associated with lava dome building episode of Merapi volcano in October 1986 is presented and disscused.

Instrumentation

The seismic data used in this study are recorded by three seismic stations (KLT, LBH and KKN) which are located on the summit area of Merapi with a radius of about 5 km (for exact locations see *Sri Brotopuspito Kirbani,* fig. 1; this volume). A fourth station, MTK, which is located on the southern flank at a distance of about 50 km from the summit can be used to distinguish qualitatively between volcanic (Merapi) and non volcanic earthquakes. The transducer for ground vibrations used at each station is a 1 Hz vertical seismometer (L4A by Mark-Products), and solar panels are used for power supply. The analog seismic data are radio telemetered to the Institute of Geophysics, Gadjah Mada University, Yogyakarta by means of frequency modulation (System Lennartz-Electronics).

Data Analysis

Figure 1 shows the mean hourly frequency of volcanic earthquakes recorded at the three stations within one year starting on August 1, i.e. about 2 months before the doming process which occurred at the beginning of October 1986. The mean value were calculated with a 48 hours time window and then smoothed by a 5-point moving average filter. During the normal state of activity the number of volcanic shocks at Merapi is dominated by those which are only recorded at the station KLT (the closest one to the summit), i.e. about 5 times as many as recorded at LBH. KKN, the most distant station from the summit, recorded 50 % less than LBH did. This indicates that the origins of the events were at a shallow region close to the summit. Using the station MTK as a reference about 2-5 non-volcanic earthquakes per day are found. From the value of the frequency contents it is suggestive that the latter events are associated with

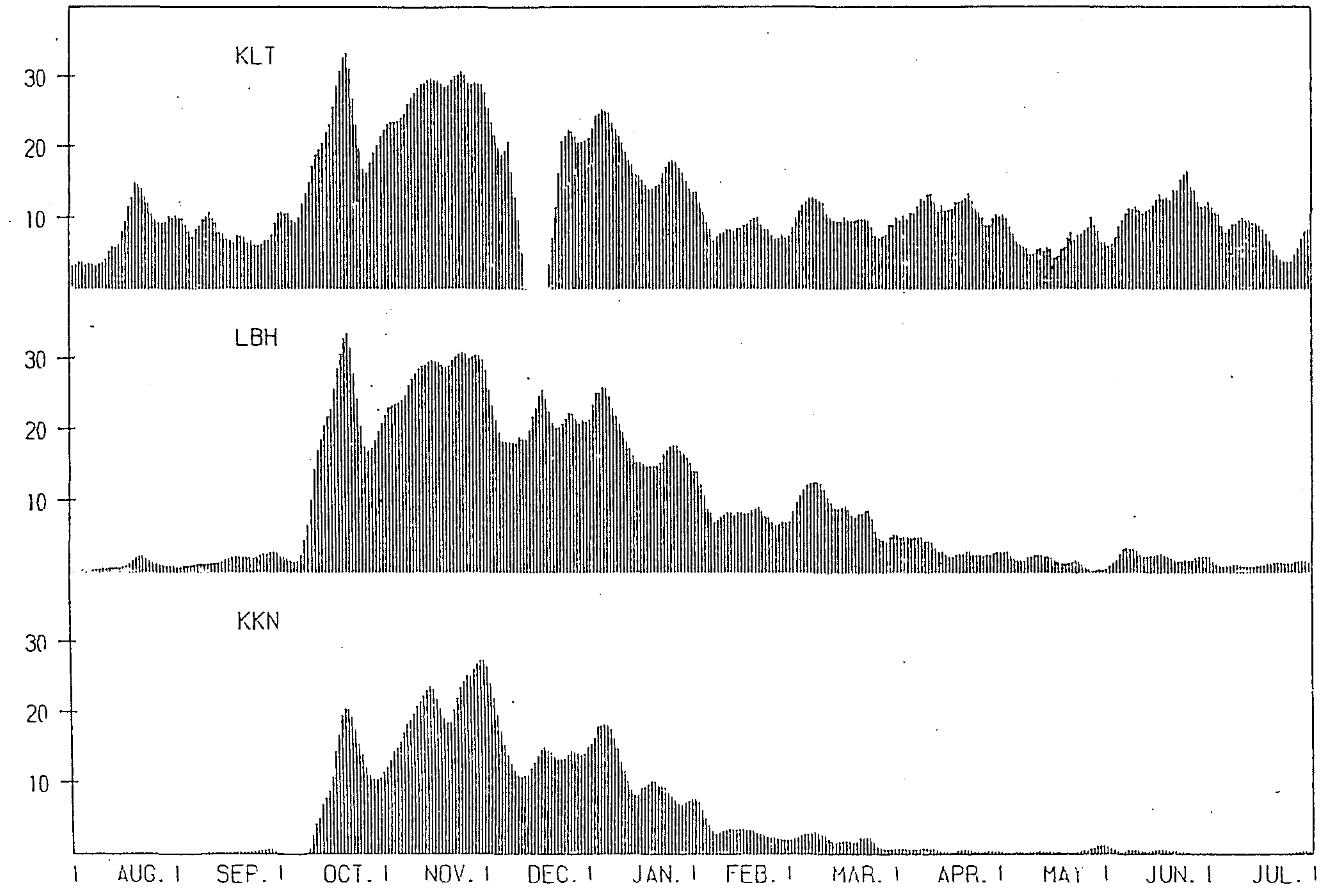

Fig. 1. Average number of volcanic shocks per day at Merapi in one year period started on August 1, 1986.

the fracture system under the Merapi. On October 9, 1986, a new swarm of volcanic shocks started. the ratio of the number of recorded shocks at the three stations changed significantly, indicating deeper source depths. Figures 2 and 3 show examples of seismograms recorded during the quiet state (in August 1986) and in the period of lava dome building in October 1986.

Since we use only three seismic stations and the arrival time of some volcanic shocks cannot be accurately determined, the source locations are estimated using the maximum amplitude ratios of the seismograms recorded at the three stations. In the calculations the medium assumed to be homogeneous and isotropic. The dissipation of seismic energy is mainly caused by internal friction. The amplitude of a body wave at a distance r from the source is then :

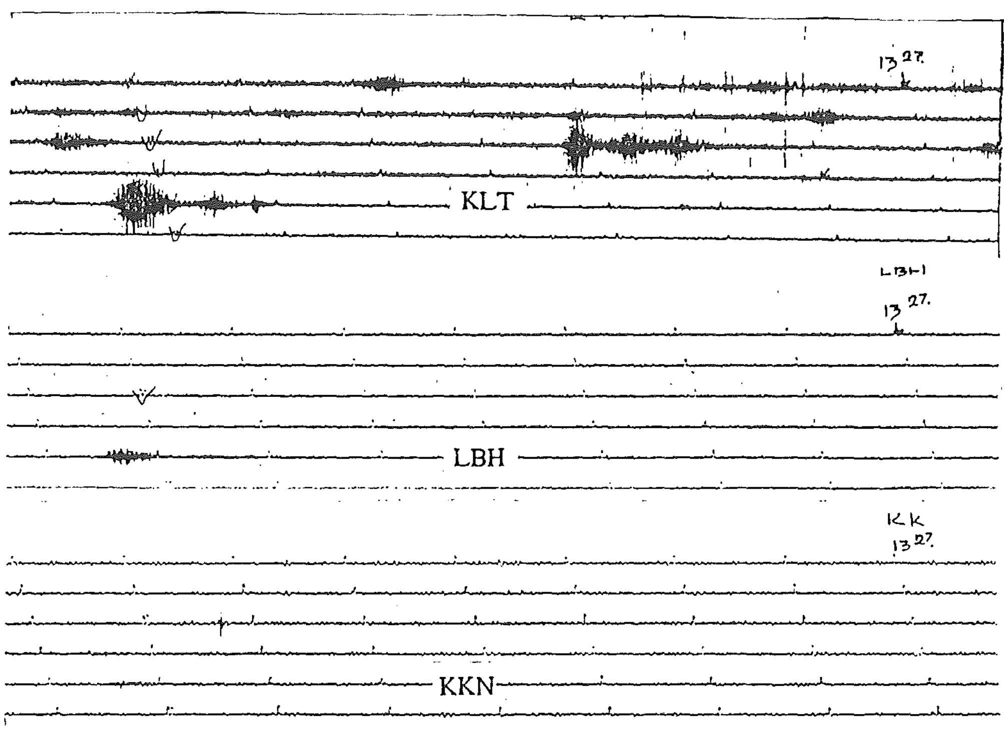

Fig. 2. Example of seismograms recorded at stations KLT, LBH and KKN in August 1986, indicating a "normal" state of activity.

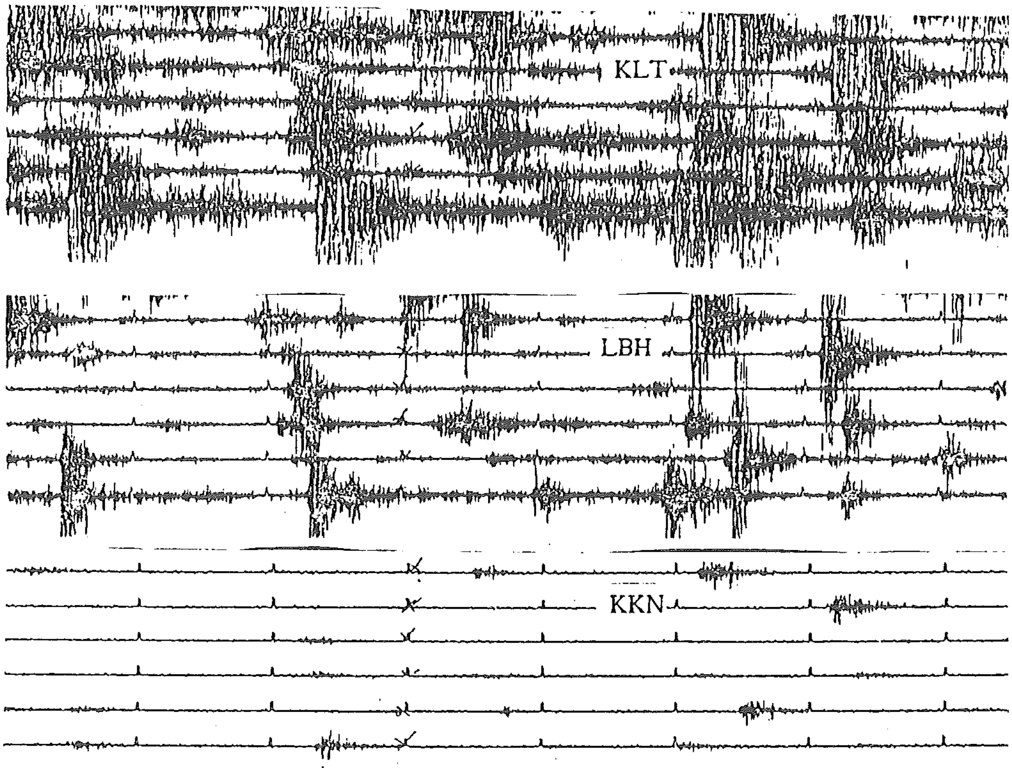

Fig. 3. Section of seismograms recorded at the three stations during the lava doming process in October 1986.

$$A(r) = \frac{A_0}{r} \exp (- \alpha r) \tag{1}$$

where α is the attenuation coefficient and A_0 is the amplitude of the body wave at the source. Here $r = \{(x-x_0)^2 + (y-y_0)^2 + (z-z_0)^2\}^{1/2}$, where (x_0,y_0,z_0) and (x,y,z) are the coordinates of the seismic source and the station respectively.

The amplitude ratio of seismograms recorded at two station is :

$$\frac{A(r_1)}{A(r_2)} = \frac{r_2}{r_1} \exp (r_2 - r_1) \alpha \tag{2}$$

With only three stations on Merapi, there are only 2 independent equations of amplitude ratios for one event. This is not enough to analitically compute x_0, y_0 and z_0. Therefore to estimate the location of the source a trial-and-error method was used. For given values of x_0, y_0 and z_0 in the region inside and under the summit area of the volcano, the amplitude ratios LBH/KLT and LBH/KKN are calculated. The result of the calculation is shown in table 1. In the calculation the medium was treated as sedimentary rock or sandstone with attenuation coefficient between 0.2 and 0,35 km^{-1}. With a wave velocity of 3 km/s and a frequency of 5 Hz, i.e. the dominant frequency of the seismic wave, these parameters are comparable to Q-values ranging from 30 to 50.

Table 1 List of depths, in km, calculated for different values of LBH/KLT and KKN/LBH amplitude ratios.

LBH/KLT KKN/LBH	0.1	0.3	0.5	0.7	0.9
0.1	--	0.4-1.8	0.2-2.3	0.4-1.5	0.2-1.8
0.3	0.6-1.4	1.8-2.3	2.5-3.4	2.9-3.9	3-4.7
0.5	--	--	3.5-4.1	4.7-5.4	4.8-5.5
0.7	--	--	--	5.4-6	--
0.9	--	--	--	--	--

To search for the migration of the sources associated with the lava doming process, the change in the amplitude ratios was studied. Tables 2 to 5 show the frequency distribution of amplitude ratios of four consecutive time periods, including periods before and during the lava doming process which started at the beginning of October 1986. From the distributiom of their amplitude ratios shown in the the tables, it seems useful to devide the volcanic shocks according to their source locations in 3 gorups. First, volcanic shocks having zero value of KKN/LBH amplitude ratio and with LBH/KLT ratio less than one. Extrapolating table 1 for smaller values of KKN/LBH amplitude ratio, these shocks are associated with source locations at depths less than 1 km. Second, shocks with KKN/LBH and/or LBH/KLT amplitude ratios having values larger than one, showing events originated from regions deeper than 10 km or outside the edifice of the volcano. Third, shocks with values of KKN/LBH and LBH/KLT amplitude ratios less than one. These shocks are associated with source locations at depths less than 6 km. If we take into account the number of days of the period in the tables, the distributions of volcanic shocks of the first and third group are almost constant in periods before and during the lava doming process. With the second group, it can be clearly seen from tables 2 to 5 that the mode of the

Table 2. Frequency distribution of KKN/LBH and LBH/KLT amplitude ratios in a period :Aug. 1-21, 1986

LBH/KLT KKN/LBH	0.1	0.3	0.5	0.7	0.9	1.1	1.3	1.5	1.7	1.9
0	129	127	44	16	12	2	0	3	0	1
0.1	0	10	7	4	0	1	0	0	1	0
0.3	0	5	3	1	3	0	0	0	0	0
0.5	1	4	4	8	4	2	0	0	0	0
0.7	0	3	5	16	5	1	0	2	0	1
0.9	4	2	6	9	8	1	0	0	1	1
1.1	0	0	1	1	6	1	4	1	0	0
1.3	0	1	3	6	5	3	1	3	1	0
1.5	0	1	1	4	1	1	0	0	0	0
1.7	0	0	0	1	0	0	0	0	0	0
1.9	1	1	1	2	0	0	1	0	0	0

Table 3. The same as t table 2, but in a period :
Sept. 25 - Oct. 7, 1986

LBH/KLT KKN/LBH	0.1	0.3	0.5	0.7	0.9	1.1	1.3	1.5	1.7	1.9
0	61	169	93	38	13	1	1	1	0	1
0.1	2	2	13	6	1	0	0	0	0	0
0.3	0	1	4	4	6	1	1	1	0	0
0.5	1	1	3	10	7	1	1	0	0	0
0.7	0	0	7	10	8	1	2	1	0	0
0.9	2	6	5	5	7	1	1	1	0	0
1.1	0	0	2	1	1	0	0	0	0	0
1.3	0	2	1	1	0	0	0	0	0	0
1.5	0	1	0	0	1	0	0	0	0	1
1.7	0	0	0	0	1	0	0	0	0	0
1.9	0	2	0	0	0	0	1	0	0	0

Table 4. The same as table 2, but in a period :
Oct. 9 - 11, 1986

LBH/KLT KKN/LBH	0.1	0.3	0.5	0.7	0.9	1.1	1.3	1.5	1.7	1.9
0	8	103	143	77	21	1	0	2	0	1
0.1	0	8	44	42	39	3	0	1	0	0
0.3	1	3	8	5	8	0	0	0	0	0
0.5	0	0	4	0	5	0	0	0	0	0
0.7	1	0	2	2	4	0	0	0	0	0
0.9	0	0	0	1	1	0	0	0	0	0
1.1	0	0	0	0	0	0	0	0	0	0
1.3	0	0	0	0	0	0	0	0	0	0
1.5	0	0	0	0	0	0	0	0	0	0
1.7	0	0	0	0	0	0	0	0	0	0
1.9	0	0	0	0	1	0	0	0	0	0

Table 5. The same as table 2, but in a period : Oct. 23 - 24, 1986

LBH.KLT / KKN/LBH	0.1	0.3	0.5	0.7	0.9	1.1	1.3	1.5	1.7	1.9
0	1	43	46	19	7	1	0	0	0	0
0.1	0	10	39	96	169	19	5	0	0	0
0.3	0	2	4	12	35	2	0	0	0	0
0.5	0	1	0	0	1	0	1	0	0	0
0.7	0	0	0	1	2	0	0	0	0	0
0.9	0	0	0	1	1	0	0	0	0	0
1.1	0	0	0	0	0	0	0	0	0	0
1.3	1	0	0	0	0	0	0	0	0	0
1.5	1	0	0	0	0	0	0	0	0	0
1.7	1	0	0	0	0	0	0	0	0	0
1.9	0	0	1	0	0	0	0	0	0	0

distributions shifted to lower values of KKN/LBH amplitude ratio for times closer to the beginning of the lava doming process. These changes correspond to the upward movements of the source locations from depths of about 5 km to 1 km, in an interval of about 2 months.

Results and Disscussion

In summary, an analysis of volcanic shocks at Merapi related to a lava dome building episode which occurred at the beginning of October 1986 leads to the following results :

1. Volcanic shocks at Merapi which are only detected at station KLT or at stations KLT and LBH (the two closest stations from the summit) are originated from a region within or close to the lava

dome. The focal depths are less than 1 km. During a quiet state of activity the number of these shocks is dominant. It is suggestive that these seismic signals are caused by cracks or fractures in the lava dome.

2. The deeper volcanic earthquakes, i.e. shocks which are detected by the three stations, could be responsible for the activity of the volcano. During the lava dome building in October 1986, the source locations of these shocks were moving upward from depths of about 5 km to 1 km. Following *Schick* (*1988*), these seismic signals could be caused by material failure in the medium surroundimg the moving magma in the conduits.
3. With the number of about 2 to 5 events per day, there are observed at Merapi earthquakes at depths more than 10 km. *Shimozuru et al. (1969)* reported that during their field measurements more than ten earthquakes were located near Yogyakarta. It still needs further observations, but these earthquakes could be originated from two fault lines where the intersection is located under the volcano.

Acknowledgements

The work was done in a joint project on physical volcanology between Gadjah Mada University, Yogyakarta and the Institute of Geophysics, University of Stuttgart, and financially supported by Badan Pemgkajian dan Penerapan Teknologi (BPPT), Indonesia and Kernforschungsanlage (KFA) Juelich, the Federal Republic of Germany. The author thanks J. Neuberg for critically reading the manuscript and S.B. Kirbani for useful discussions.

References

Fadeli, A., S.B. Kirbani, R. Mugiono and R. Schick, 1987, Preliminary analysis of seismic data gathered with a new seismic station network on the Merapi volcano (Central Java, Indonesia), 1967 Contributions of the Merapi Research Group, Gadjah Mada University, Sekip Unit III, Yogyakarta, Indonesia.

Kirbani, S.B., 1990, Analysis of volcanic tremor at Mount Merapi (Central Java, Indonesia) in order to understand internal magma flow, Doctor thesis of Gadjah Mada University, Yogyakarta, Indonesia.

Tazieff, H., 1983, Monitoring and interpretation of activity on Mt. Merapi , Indonesia, 1977-1980: an example of practical, "civil defence, volcanology, In : Tazieff, H., and J.C. Sabroux (eds), Forecasting volcanic events, Development in volcanology 1.

Schick, R., 1988, Volcanic tremor - Source mechanism and correlation with eruptive activity, Natural Hazard 1, 125-144.

Shimozuru, D., T. Miyazaki, N. Gyoda, and J. Matahelumual, 1969, Volcanological survey of Indonesian volcanoes, Part 2. Seimic observation at Merapi volcano, Bulletin of the Earthquake Research Institute, vol. 47, pp 969-990.

Study on Characteristics and Origin of Volcanic Seismic Signals

Jürgen Neuberg and Wahyudi

Physics Department, Gadjah Mada University, Yogyakarta, Indonesia

1. Introduction

Volcanoes provide a wide variety of seismic signals which vary in a much wider range than seismograms of earthquakes recorded in areas of nearly homogeneous geological structure. In addition to the difficulty of often showing a rather emergent first arrival, the seismograms do not allow us to associate single phases with any distinct ray path. Following the widely used concept of describing a seismic signal as a convolution of a source-time function and a propagation operator for the seismic wave, we find in the case of a volcano an even more complicated ambiguity: on the one hand the geological structure of a volcano with its highly inhomogeneous layering results in a very sophisticated transfer function for wave propagation; on the other hand the generation of seismic energy can be described by a wide variety of source models which are currently far from being understood.

In order to explain the unusual charateristics of the seismograms, it is helpful to split the contributions to the convolution and to consider only one of the two processes, which are referred to in the following as the *path* and the *source*. In the first case the seismogram contains all the information about the source and can be used to model the suorce dynamics. In the second case the seismogram is a superposition of a fairly large number of different ray paths through a highly complicated structure. Even though we are aware of the fact that only a combination of these processes will bring us closer to reality, this strict distinction seems to be promising to start with.

Riuscetti et al. (1977) found that dominant features in the frequency spectrum of volcanic seismic signals do not show a dependence on azimuth or distance from the crater. They consequently associated these features with the source rather than with the path. Seidl et al. (1990) found for Mount Merapi coherent spectral energy using Maximum Entropy Spectral Analysis (MESA) of long events recorded at different stations. They concluded their approach to be a qualitative confirmation of the resonator-ensemble model. This means that the coherent spectral features are also solely associated with the source. Schick (1988) gave an overview of all kinds of source models for a wide variety of signals. Malone (1983) analyzed seismic signals from Mount St. Helens and suggested in a rather phenomenological approach a very careful classification of seismic events which range from high- over low-frequency signals (assuming a frequency-depth correlation) to surface events like steam or gas bursts and avalanches.

The main objective of this paper is a description of source characteristics of seismic signals recorded at Mount Merapi. We will demonstrate that the data available from Merapi are not sufficient to generally solve for either the source process or the internal structure through which the seismic energy propagates. But some observations lead to the evidence of a rather smooth transfer function for the path leaving spectral features solely with the source.

The source location is particularly important as even small changes in the source position in these highly inhomogeneous surroundings result in significant differences in the waveform.

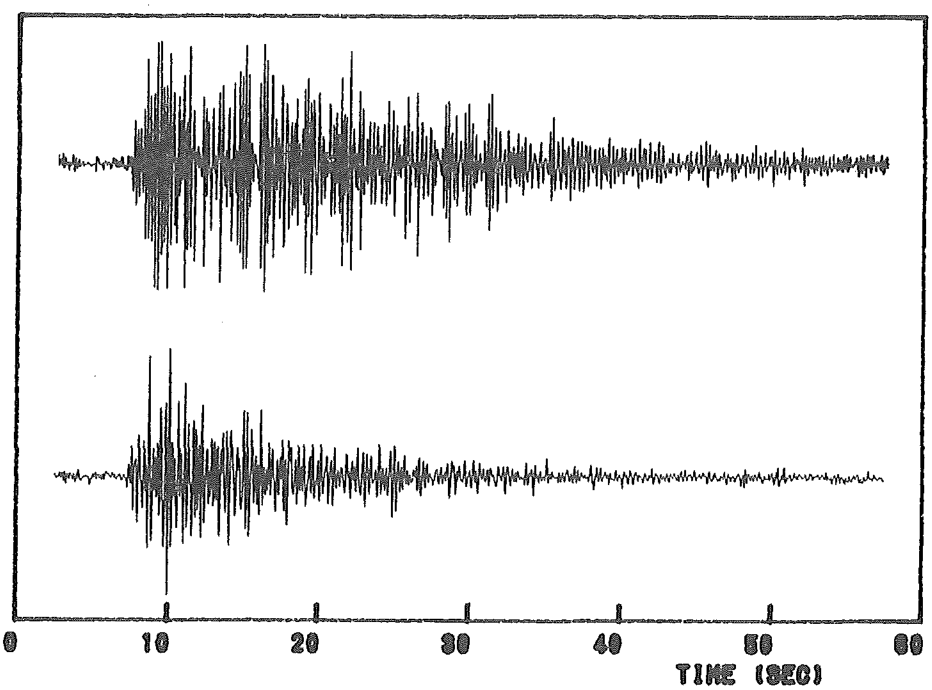

Fig. 1 Seismic event on October 28, 1986, recorded at KLT (upper trace) and LBH (lower trace)

Therefore, in the section that follows the data description we use a cross-correlation method to investigate the waveform of adjacent sources. We use the $\lambda/4$-hypothesis (Geller and Mueller, 1980) for this investigation. In the next section we search for similarities in the spectra of seismograms in order to find joint features for either one event recorded at different stations or a number of events recorded at one station. In Section 5 we dicuss the impact of our findings to a classical location technique, and in Section 6 we present a short summary and some conlusions.

2. Data

We consider throughout this investigation a shock-like type of seismic event of a duration of about 100 s in contrast to a 'harmonic tremor' with a longer duration and mostly emerging onset. The seismograms have been recorded at three stations: Klathakan (KLT), Labuhan (LBH), and Kalikuning (KKN) with distances to the summit (crater) of 1.5 km, 2.5 km, and 5 km, respectively. All events occured in October 1986 during a period of significantly higher rate of growth of the lava dome. Fig. 1 shows two examples of seismograms recorded at KLT and LBH.

3. Relative event location by cross-correlation of waveforms

Clusters of earthquakes sometimes produce nearly identical seismograms over the entire length of the record (Ishida and Kanamori, 1978). Furthermore, it has been found that initial pulse widths and corner frequencies of earthquakes with magnitudes smaller than 2 or 3 remain constant if seismic energy emerges from a certain region and is recorded at a particular station. Geller and Mueller (1980) formulated the hypothesis that earthquakes which have identical waveforms must have similar focal mechanisms and hypocenters within one quarter of the shortest wavelength λ for which the similarity is observed. We refer to this in the following as the $\lambda/4$-hypothesis.

Assuming for volcanic events both a source process which is sufficiently similar and a source region which is sufficiently limited, we apply the $\lambda/4$-hypothesis to volcanic events in order to determine the size of the source region. We follow in a first attempt the approach by Bergthora et al. (1987) and bandpass filter the data for [1-2]Hz, [2-4]Hz, and [4-8]Hz, and cross-correlate the filtered traces in pairs. The resulting cross-correlation coefficients are displayed in 'cross-correlation matrices', one for each bandpass (Fig. 2).

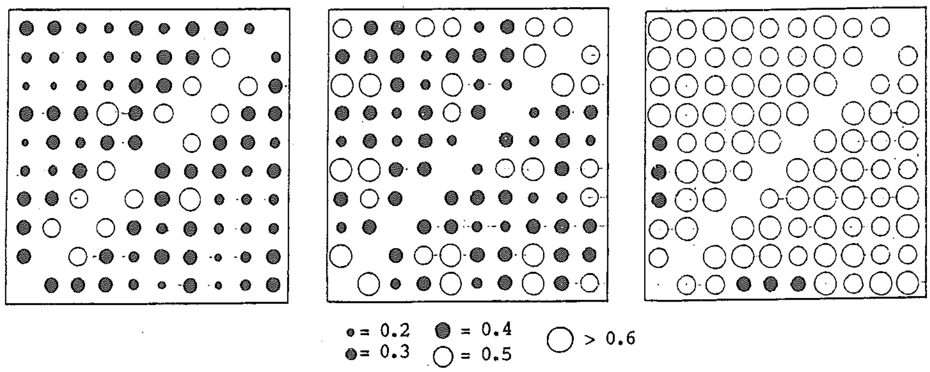

Fig. 2 *Cross-correlation coefficients for correlation of paired seismograms. The traces have been bandpass filtered for [4-8]Hz (left), [2-4]Hz (center), and [1-2]Hz (right).*

We observe the highest cross-correlation for the [1-2]Hz band and are in complete agreement with Bergthora et al. (1987), who applied this method to a pattern of quarry blasts. In a second attempt, however, we keep the bandwidth of the filter operator constant and now find similar cross-correlation values for any frequency range (Tab. 1). This means that the cross-correlation factor is a function of the bandwidth rather than of the center frequency of the passband. The procedure of Bergthora et al. (1987) will be critically reviewed elsewhere but we like to point out here that it is possible to prove the failure of the $\lambda/4$-hypothesis in two ways, at least for our data set.

Table 1 *Cross-correlation coefficients for a constant bandwidth of 1 Hz in comparison with variable bandwidths.*

Bandwidth	Cross-corr.coeff.	Bandwidth	Cross-corr.coeff.
[1-2]Hz	0.595	[1-2]Hz	0.595
[2-3]Hz	0.559	[2-4]Hz	0.473
[3-4]Hz	0.570	[4-8]Hz	0.320
[4-5]Hz	0.516		

(1) A simple example of time series consisting of random numbers clearly shows the strong dependence of the cross-correlation

factor on the bandwidth. The narrower the passband the more we approach a single frequency and no matter which one we choose, we will get a perfect correlation with 'monofrequent' signals (Tab. 2).

(2) If one finds for the [1-2]Hz band a high cross-correlation, then, according to the $\lambda/4$-hypothesis, the inclusion of lower frequencies (e.g.[0-2]Hz) should not change the correlation of waveforms because longer wavelengths are not affected by differences in the travel path. The dropping of the mean cross-correlation coefficient from 0.5 to 0.3 demonstrates that this is not the case.

Table 2 Cross-correlation coefficients for a constant bandwidth of 1 Hz in comparison with variable bandwidths for two random number time series.

Bandwidth	Cross-corr.coeff.	Bandwidth	Cross-corr.coeff.
[1-2]Hz	0.495	[1-2]Hz	0.495
[2-3]Hz	0.501	[2-4]Hz	0.419
[3-4]Hz	0.554	[4-8]Hz	0.391
[4-5]Hz	0.540		

Besides some general objections against the narrow band filter technique prior to cross-correlation in Bergthora et al. (1987), the failure of the $\lambda/4$-hypothesis for our data set might point to a very heterogeneous geological structure which strongly affects waves emerging from the same source region. All this is only relevant, of course, if the main assumption of limited source region and similar source process is at all valid.

4. Search for spectral similarities

4.1. Spectra

In this section we try to compare and interpret some spectral similarities from recordings which have been obtained either at two stations at the same time or at one station in a certain time range. Similar features in spectra derived from the same event at different stations point to source characteristics, while differences in these spectra are caused by the different path or different source location. We refer here to the term *event* as radiation of seismic energy at a certain time, not necessarily from a single source. Similarities in spectra derived at one station can be associated with charateristics of the path from the source region to the receiver and/or with the surroundings of the receiver.

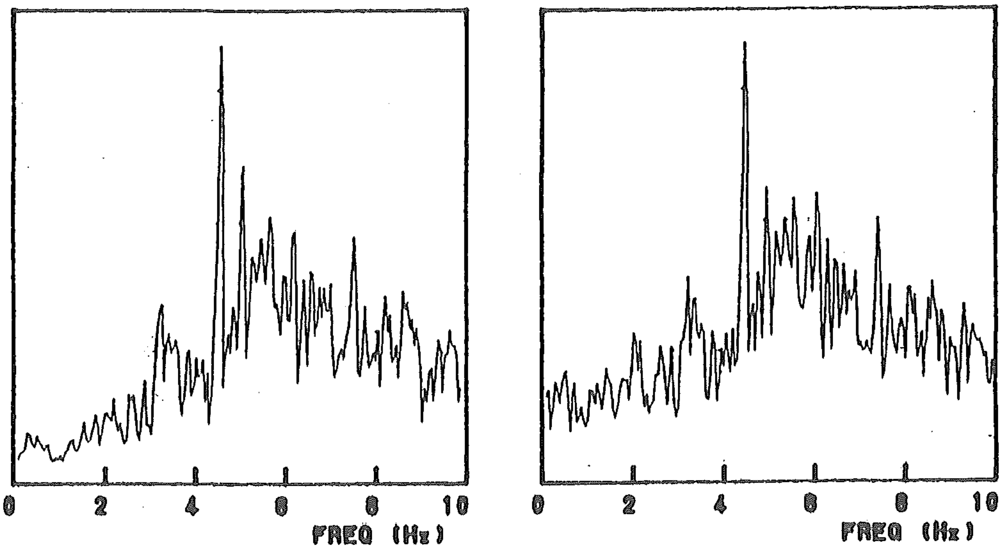

Fig. 3 *Frequency spectra of category (a) obtained at KLT (left) and LBH (right). The amplitudes are normalized and approximately differ by a factor 4 (KLT/LBH). The example shows a good coherence.*

In the following we consider events recorded at stations KLT and LBH; Fig. 3 through 5 show the spectra. The spectra which are grouped into category (a) are those where the main frequency peaks can be found in either spectrum and the similarities between spectral features are obvious (Fig. 3). Category (b) contains events where only a few spectral features are coherent (Fig. 4), and finally, category (c) incldudes events which do not permit any matching of frequency peaks. The matching was done by computing the coherency spectra and one for each category is displayed in Fig. 6.

4.2. Speculative explanations

The examples in category (a) provide evidence for the existence of one single source which produces seismic energy recorded at LBH and KLT. The influence of the different paths are presumably small and leads to a rather smooth transfer function containing only weak attenuating and/or dispersive effects. These merely change the amplitudes of single frequency peaks while the shape of the whole spectrum is left unchanged. In this case the spectra in category (a) represent the pure source function.

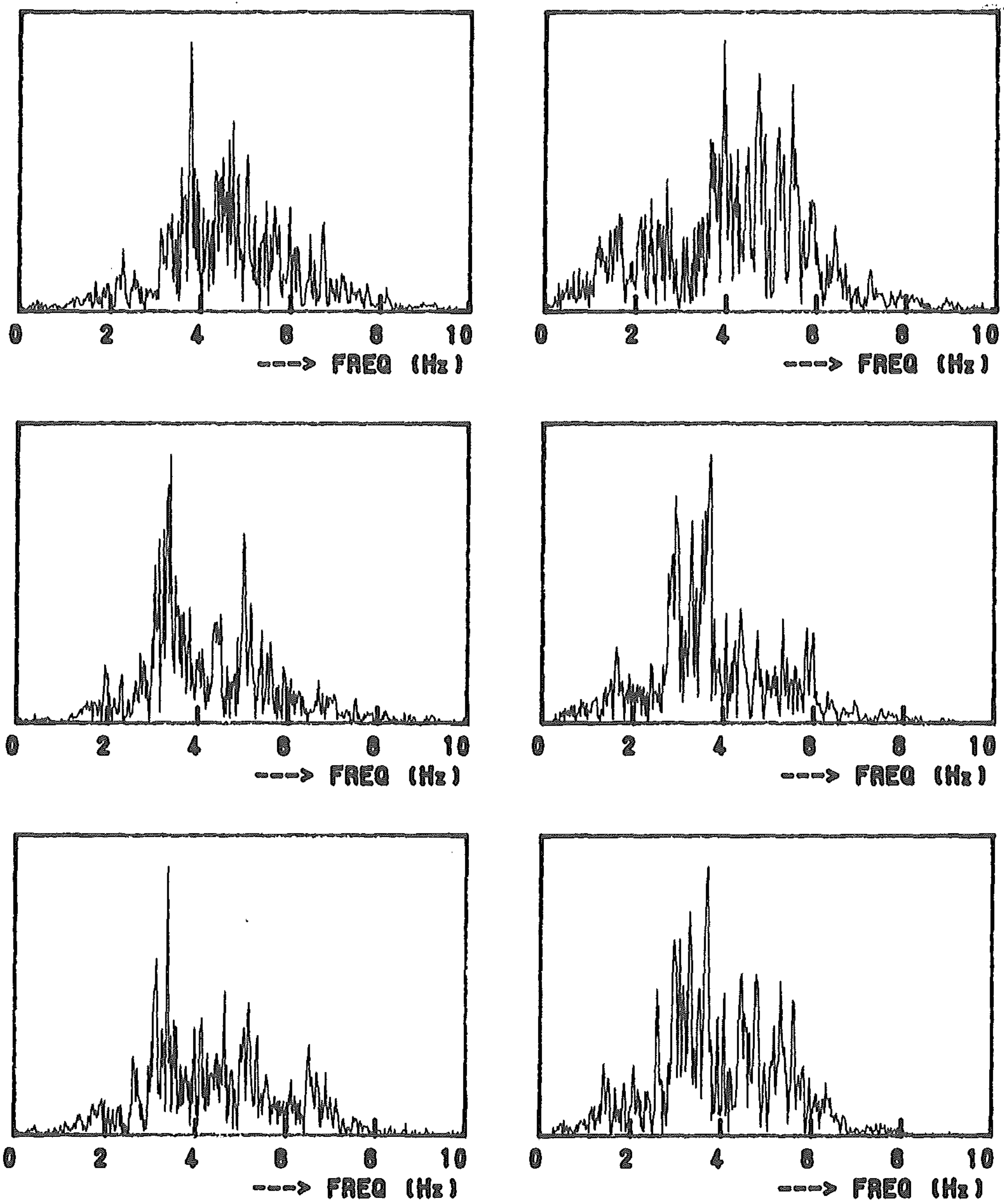

Fig. 4 *Frequency spectra of category (b) obtained at KLT (left) and LBH (right). The amplitudes are normalized and approximately differ by a factor 4 (KLT/LBH). The three examples show some similarities.*

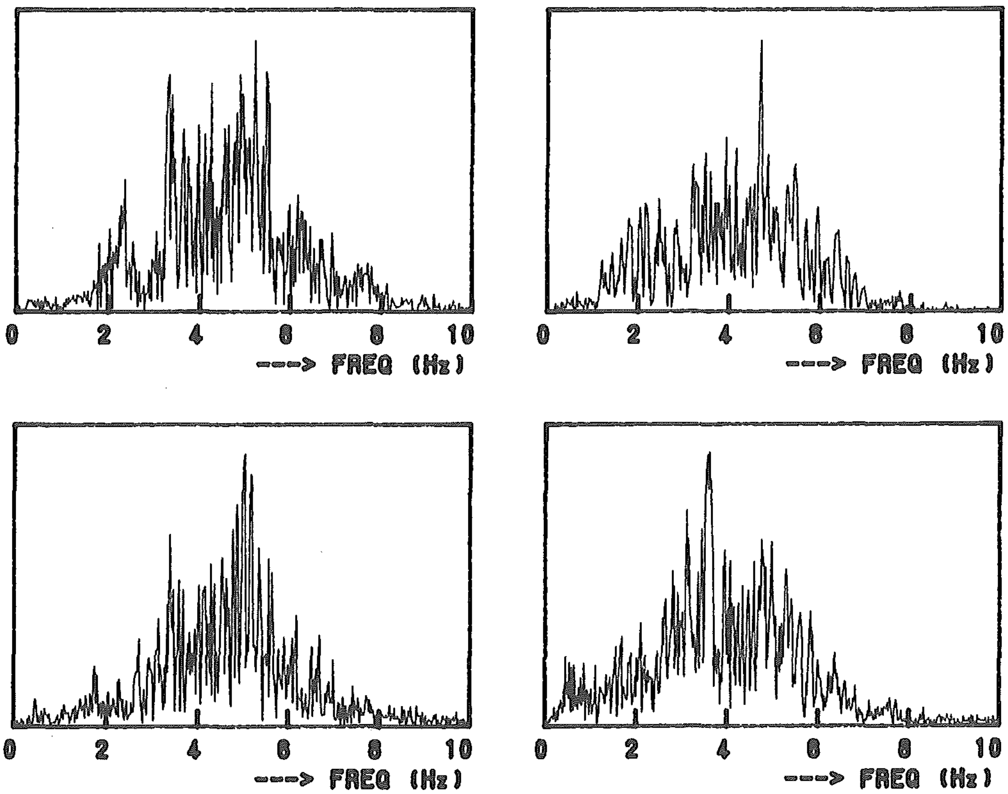

Fig. 5 *Frequency spectra of category (c) obtained at KLT (left) and LBH (right). The amplitudes are normalized and approximately differ by a factor 4 (KLT/LBH). The two examples show no similarities at all.*

The spectra in category (b) indicate more complicated conditions. Coherent spectral energy can be explained as in (a) but non-coherent features raise some questions. The path can hardly be held responsible for the differences if, at the same time, its smooth transfer function is required in (a). Alternatively, we could distinguish between two different kinds of paths, one having a smooth transfer function and the other producing sharp spectral peaks. In our opinion, however, the responsibility for spectral differences is more likely to be shifted to the source side. That is, we consider a number of different sources to be radiating energy at the same time. Such a cluster of sources could cover a wide area and could have a common energy feeding system which provides the simultaneousness. A possible source model could consist of an entire 'plumbing system' rather than a single magma conduit. The magma itself does not need to play a direct role in generating an event,

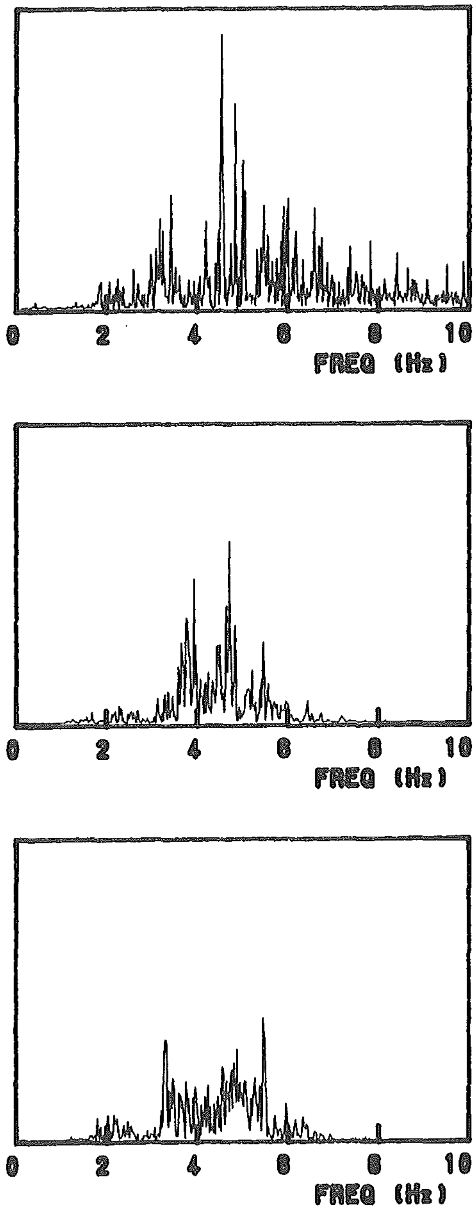

Fig. 6 *Coherency spectra for category (a) (above), category (b) (center), and category (c) (below).*

but is instead only a common source of stress change in the rocks penetrated by the 'plumbing system'. This kind of system has to be adequately extended so that different stations record significantly different parts of the superimposing seismic signals.

Such a model can easily explain the spectra of category (c) as well. In this case the contributing seismic sources are so far apart that one receiver can catch only a certain cutout of the entire signal.

Another speculative model tries to explain the spectral differences by a radiation pattern which changes the frequency characteristics of the emerging seismic waves. Such a model is likely for shallow events. Studies at Mount St. Helens (e.g. Malone, 1983) showed the shallow geological structure to be characterized by high velocity contrasts giving rise to highly dispersive surface waves since their energy is trapped in such a near-surface structure.

The majority of events which clearly belong to category (b) and (c) could be generally explained by the inhomogeneous geological structure through which the seismic waves propagate. The events of category (a), however, provide evidence for a minor influence of the path and the fact that almost identical spectra can be observed at different stations leads to the idea of an extended source system to explain (b) and (c).

4.3. Maximum Entropy Spectral Analysis

Aware that a frequency spectrum contains only information averaged over an entire time range, we investigate some events by Maximum Entropy Spectral Analysis (MESA). For details about the method see Kanasewitch (1981) and Press et al.(1986). This method provides an estimation on frequency spectra for time series which can be modelled by an autoregressive process and yields a high resolution for even short time series. Seidl et al. (1990) applied this technique to so-called 'tremor-storms' and 'beating-tremors' which were recorded at Merapi.

Following the idea that some sharp frequency peaks in the spectra are produced by 'resonators' with a certain eigenfrequency and damping properties we now try to match single frequency peaks which are not stationary over the entire time range of the seismogram. This means that we gain resolution in the time domain as well as resolving spectral lines in the frequency domain. Fig. 7 shows two examples and gives some specifications about MESA calculations. The examples correspond to category (b) and (c).

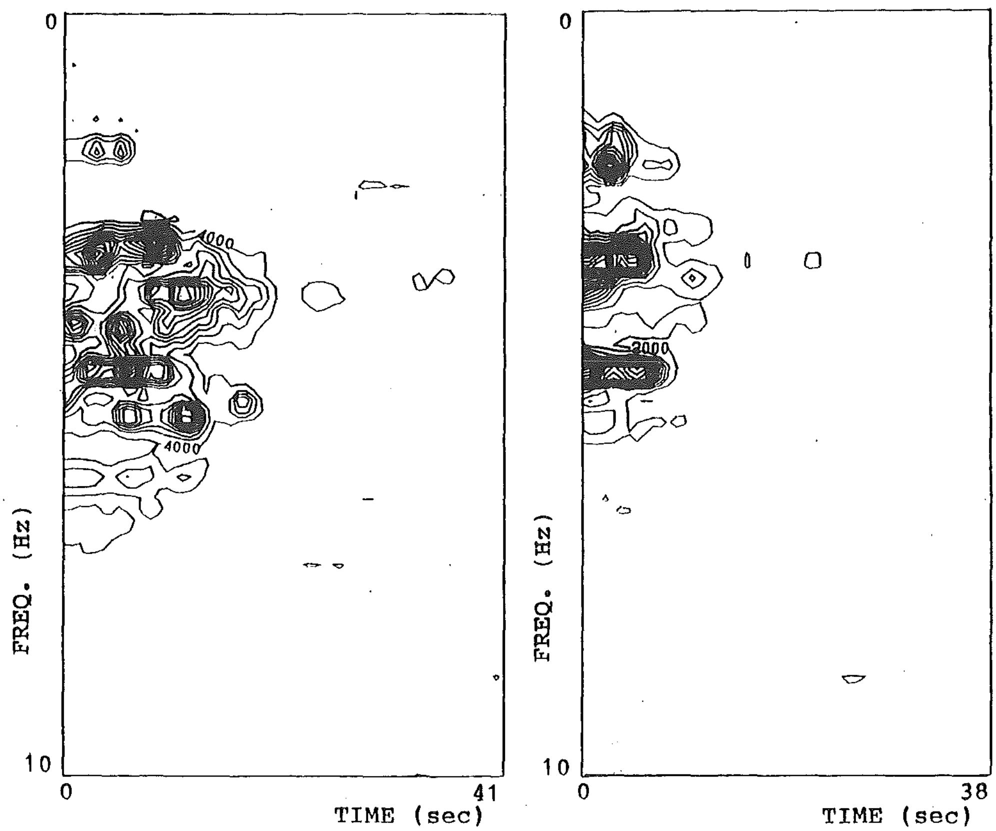

Fig. 7a *MESA spectra for a time series of category (b). KLT (left), LBH (right), some coherent energy can be found. The segment lengths is 5.0 s and the order of MESA-spectrum is 100.*

We cannot find a good spectral coherency for the majority of shock-type events. This unsurprisingly corresponds to our findings from ordinary spectra. Seidl et al. (1990) found for a tremor-storm an excellent coherence over the entire duration of a signal with a correlation coefficient of 0.87. In a second example the authors report an improvement of the correlation from 0.66 to 0.73 by shifting the entire spectrum, unfortunately without further elaborating the physical consequences of that shift. We also wonder if their first example infact represents the majority of tremors which would indicate a single tremor source with characteristic eigenfrequencies.

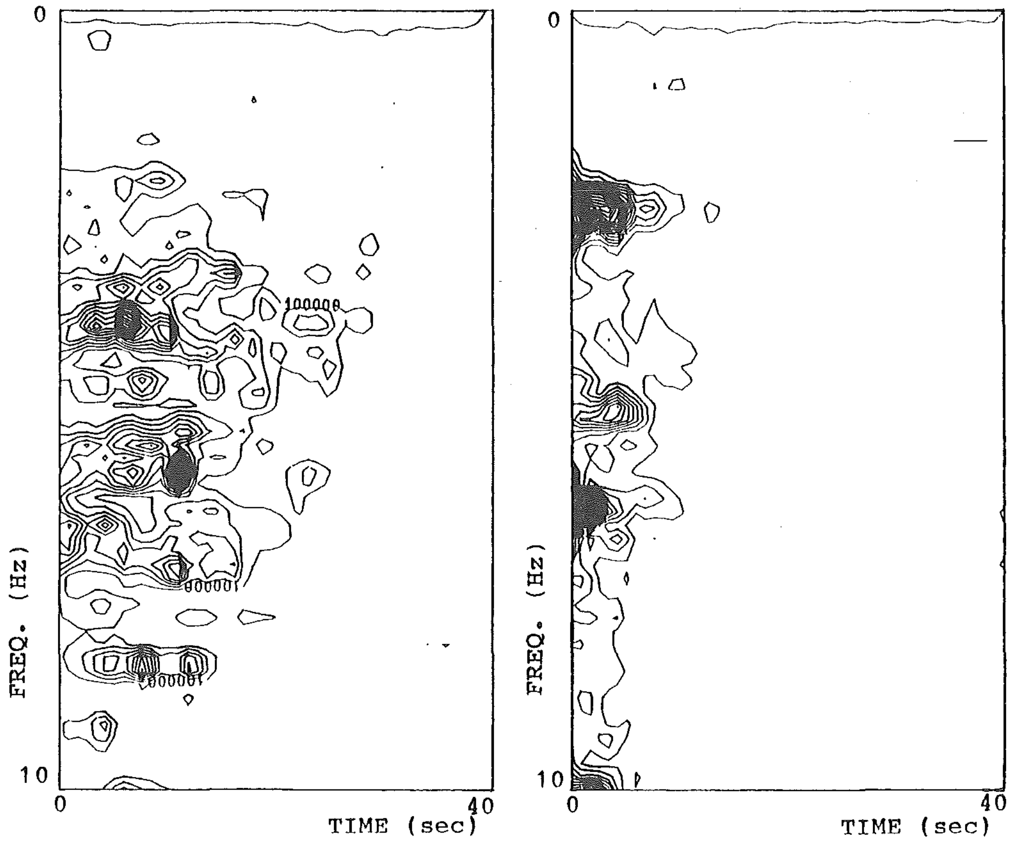

Fig. 7b *MESA spectra for a time series of category (c). KLT (left), LBH (right), the frequencies cannot be matched. The segment length is 5.0 s and the order of MESA-spectrum is 100.*

4.4. Spectra at one station

After comparing the spectra of one event at two stations, we examine the spectra obtained at one station for similarities. Referring to Fig. 3 through 5 again, we find varying spectral peaks which we associate with the sole influence of the source. This is based on the assumption that frequency shifts are caused by different source-time functions due to changes in physical parameters (e.g. Chouet, 1988) rather than by the medium through which seismic waves travel. All KLT spectra have energy around 3 Hz and 5 Hz, without matching perfectly. The LBH spectra tend to be broader and have reduced amplitudes due to the larger distance from the source region and the corresponding geometrical spreading.

5. Location of seismic events

Seismic events with a sharp onset can be used for a classical hypocenter determination. Our findings in the previous section, however, have a principal impact on any location procedure. The implicit model behind such a location is always a simple point

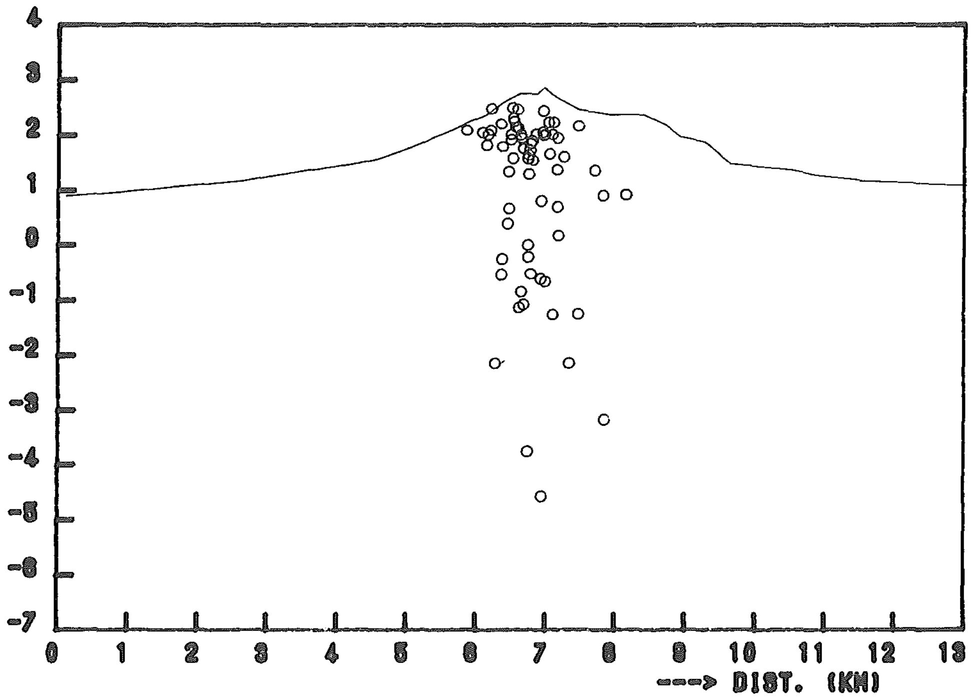

Fig. 8 *Depth distribution of seismic events at Mount Merapi derived by a least-squares hypocenter determination.*

source even if the surrounding medium is represented by a very sophisticated velocity model. In case of a widely extended source region (in comparison to the distance to the station) the hypocenter determination can hardly be successful. Even if a result from such a procedure seems to be reliable, the convergence in such an inversion and the behavior of the parameter to be fitted must be carefully examined. Malone (1983) encountered this type of problem that many of his hypocenter determinations failed to converge. This convergence failure generally results in poor depth determination of the point sources. Fig. 8 shows the depth determination routinely performed by the Volcanological Survey of Indonesia (VSI). Besides some problems which could be caused by the wrong location model as explained in the previous section, the depth determination strongly suffers from a trade-off between origin time and depth caused by a symmetrical and therefore unfavorable distribution of stations around the summit.

6. Summary and conclusions

We investigated a certain type of short-period volcanic event in order to obtain some constraints on the distinction between the characteristics of both the seismic source and the medium through which the seismic energy propagates. The failure of the $\lambda/4$-hypothesis points to more complicated conditions than in usual earthquake seismology without specifying on which side, path or source, those complications occur.

Based on the analysis of coherent features in spectra obtained in two different stations, we speculate about the existence of an entire source-system, somehow connected and simultaneously radiating energy. We emphasize that such a speculation is based on the contrary observation of almost identical spectra derived at different stations. This suggests a rather smooth transfer function for the path and leaves the responsibility of the different spectral features with the source. Therefore, we conclude that different spectra are most probably caused by different sources which are simultaneously active. This holds for the majority of events.

A further investigation should include a careful location of sources or an estimation of the extent to which a source region can be confined. A more systematic classification of seismic signals according to depth and frequency contents could then be helpful to recognize major changes in the behavior of the volcano.

Acknowledgments

We thank A. Fadeli for providing the spectra for Fig. 3, the Volcanological Survey of Indonesia for assistance in accessing seismic data, and Karen Herschell for critically reading the manuscript. One of the authors (JN) was supported by the Center for International Migration and Development, Frankfurt, Germany.

References

Bergthora, S., Thorbjarnardottir, B.S., Pechmann, J.C., 1987, Constraints on relative earthquake locations, Bull. Seism. Soc. Am., 77, 1626-1634.

Chouet, B., 1988, Resonance of a fluid-driven crack: radiation properties and implications for the source of long-period events and harmonic tremor, J. Geophys. Res., 93, 4375-4400.

Geller, R.S., Mueller, C.S., 1980, Four similar earthquakes in Central California, Geophys. Res. Letters, 7, 821-824.

Ishida, M., Kanamori, H., 1978, The foreshock activity of the 1971 San Fernando earthquake, California, Bull. Seis. Soc. Am., 68, 1265-1279.

Kanasewich, E.R., 1981, Time sequence analysis in geophysics, The University of Alberta Press, Edmonton, 480 pp.

Malone, S.D., 1983, Volcanic earthquakes: examples from Mount St. Helens, Earthquakes: observation, theory, and interpretation, Eds. Kanamori and Boschi, North Holland Pub., Amsterdam, 436-455.

Press, W.H., Flannery, B.P., Teukolsky, S.A., Vetterling, W.T., 1986, Numerical recipes, Cambridge University Press, Cambridge, 818 pp.

Riuscetti, M., Schick, R., Seidl, D., 1977, Spectral parameters of volcanic tremors at Etna, J. Volcanol. Geotherm. Res., 2, 289-298.

Schick, R., 1988, Volcanic tremor-source mechanisms and correlation with eruptive activity, Natural Hazard, 1, 125-144.

Seidl, D., Kirbani, S.B., Brüstle, W., 1990, Maximum entropy spectral analysis of volcanic tremor using data from Etna (Sicily) and Merapi (Central Java), Bull. Volcanol., 52, 460-474.

On Volcanic Shocks at Merapi and Tidal Triggering

A. Fadeli[1], P.A. Rydelek[2,3] , D.Emter[3], W.Zürn[3].

1 Introduction

The phenomenon of tidal triggering of earthquakes has been clearly observed in lunar seismicity (LAMMLEIN et al., 1974) but has not been demonstrated unambiguously in catalogs of global or large-regional seismicity on Earth (SCHUSTER, 1897; KNOPOFF, 1964; SIMPSON, 1967; SHLIEN and TOKSÖZ, 1970; SHUDDE and BARR, 1977). Correlations with varying levels of significance between lunar/solar phases and earthquake origin times, however, have been found in regional and localized catalogs (SHLIEN, 1972; KLEIN, 1976; YOUNG and ZÜRN, 1979; KILSTON and KNOPOFF, 1983; PALUMBO, 1986; ULBRICH et al., 1987; SHIRLEY, 1988). The few cases where tidal triggering seems likely, involve classes of events which perhaps are the most easily affected by small tidal stresses, namely earthquakes occuring in volcanic zones (McNUTT and BEAVAN, 1981; McNUTT and BEAVAN, 1984; EMTER et al., 1986; RYDELEK et al., 1988). The promising results of these studies have prompted us to investigate the possibility of tidal triggering at Mount Merapi, one of the most active volcanoes in the world.

2 The Seismic Catalogs

The data used in this investigation comes from the records of the Merapi seismic network (see KIRBANI, this volume). We are concerned here with "shocks" similar to the B-type events after Minakami's classification (MINAKAMI, 1974; see also SCHICK, 1981). They are distinguished from the so called "tremors" by their impulsive character (see Fig.6 of KIRBANI this volume) and by a short duration of less than 100 s. The relatively slow emergence of the seismic signal precludes an accurate determination

[1]Physics Department, Gadjah Mada University, Sekip Unit III, P.O.Box BLS 21,Yogyakarta, Indonesia.

[2]now at: Center for Earthquake Research and Information, Memphis State University, Memphis, Tennessee 38152, USA.

[3]Black Forest Observatory Schiltach, Heubach 206, D-7620 Wolfach, FRG.

of source locations from source-to-receiver traveltimes. Nevertheless, the recorded amplitudes at the three stations KLT, LBH and KKN, at different distances from the central vent, allow a rough estimate of the source locations; these are believed to be close to the vent, within a depth range of 200 to 4000 m. This idea is also supported by the inverse relation of the number of recorded shocks versus distance from the volcano at the three stations (see Table 1). Shock magnitude is below 1 (energy $< 10^{13}$ erg), and it is well established that the frequent lava avalanches at Merapi do not produce measurable seismic signals with shock-like features.

The shocks were read from seismograms from the three stations and then binned into hours (local time) to form the catalogs used in this study. Shocks were only used when their amplitudes were 2 mm above the noise level or above the tremor amplitude (if and when tremors occurred); therefore, an influence of the tremor activity on the number of recorded shocks cannot be excluded. The seismogram paper is changed every day, but not at exactly the same time. The number of shocks missed during the change of paper is estimated to be not larger than 4 events, even at times of the highest seismic activity; thus we exclude this possiblity as a source of man-made periodicity in the catalogs. There are some gaps in the records occurring usually several hours after midnight because of battery run-down due to insufficient power from the solar panel on the previous day, but they amount to only a small percentage of the record length (see Table 1). Their influence on periodicities, however, was checked and found non-significant (see below). The time series of the number of events per hour for the stations KKN, LBH

Table 1:

Station	distance from vent	number of events	gaps(%)
KKN	4.0 km	53,985	3.6
LBH	2.2 km	100,369	2.7
KLT	1.5 km	189,576	7.5

and KLT constitute the catalogs we have analysed. Each catalog starts on April 1, 1985 and lists the hourly count for 1005 days (Figure 1a). The total number of events in the three catalogs are given in Table 1. This data set, especially that for station KLT, is to our knowledge, the largest catalog of volcanic seismic events ever analyzed.

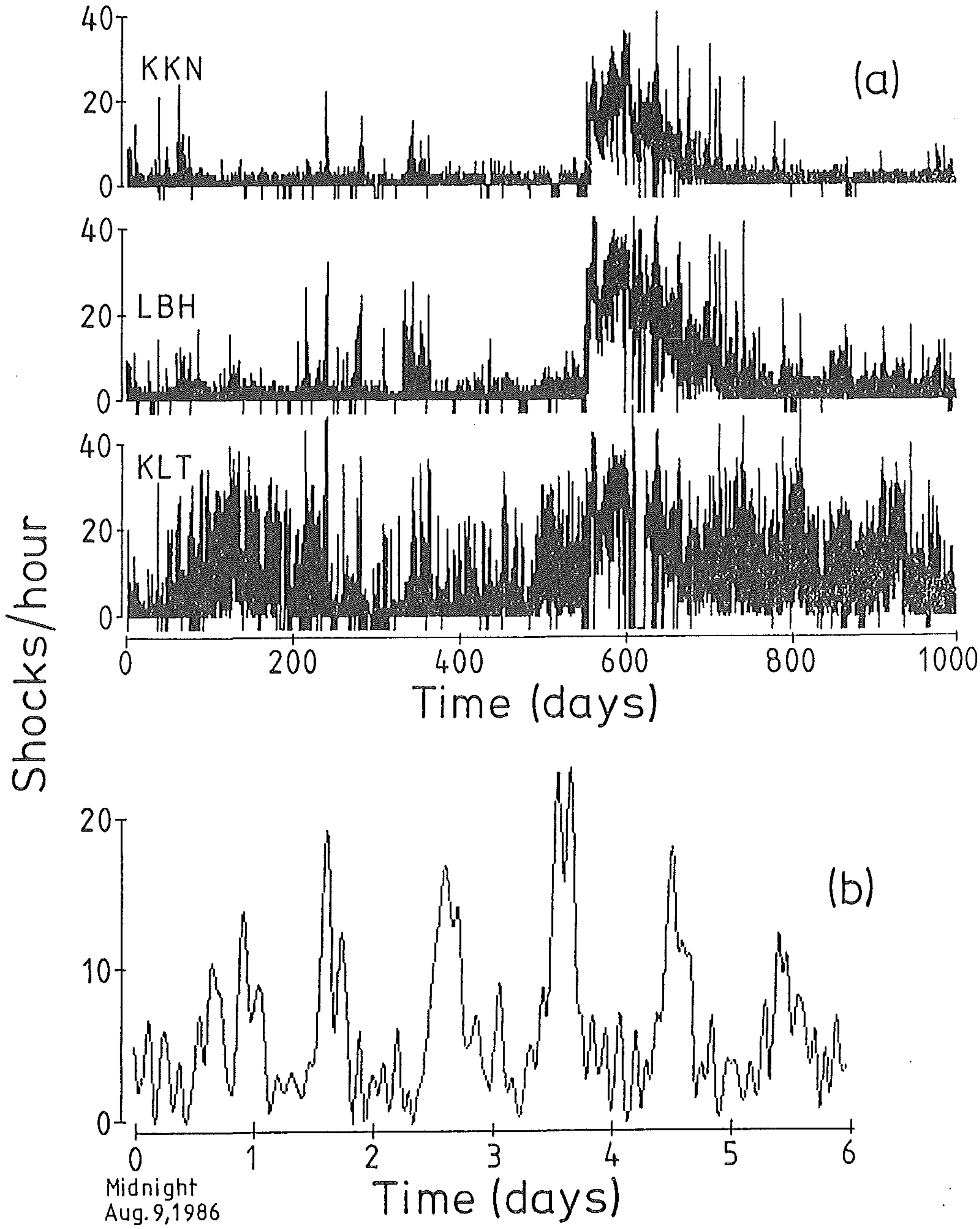

Figure 1. (a) Plot of the number of events per hour versus time for the three Merapi catalogs: KKN, LBH, KLT. Data gaps are plotted as negative values. (b) blowup of a section of the KLT catalog.

All three catalogs show a pronounced increase in seismic activity starting at the beginning of October, 1986 (about day 550 in Figure 1a) and ending about three months later. In mid-October, 1986, Mount Merapi entered an active dome building phase which lasted for about one month and resulted in a volumetric increase of the lava dome of almost 2 million cubic meters. Dome building continued at a slower pace for another 8 months, forming another 2 million cubic meters of material. The ratio of the recorded number of events between the three stations (KLT:LBH:KKN) changed from about 10:2:1 to roughly 1:1:1 during the three months of increased seismic activity (see Figure 1a). This can be explained by either deeper sources and/or larger magnitudes of the events. Moreover, spectral analysis of seismograms recorded during the dome building phase showed significant variations in spectral composition, indicating continual changes in the source of the earthquakes or the structural features of the volcano, or both (see KIRBANI, this volume).

3 Description of the Schuster Test

The Merapi catalogs in Figure 1a were tested for evidence of tidal triggering by a method following SCHUSTER (1897) which is described in detail by HEATON (1975). Briefly, for each hour (local time is used at Merapi) a tidal phase, for a certain tidal function, is calculated from the position of the hour with respect to adjacent tidal maxima which are defined to be 360^o apart. Each event in the hour is thus represented by a phasor of unit length having the tidal phase angle as defined above. The vector sum of all the phasors from the N events in the catalog produces a phasor sum (or walkout) of length R. The probability of obtaining R from random data with the Schuster test is: prob = $\exp(-R^2/N)$. If the phase angles of the events are uniformly randomly distributed, then the path of the walkout resembles Brownian motion, and the expected length after N steps is $\sqrt{N}$. When the probability becomes smaller than 0.05 (0.01), the null hypothesis of random distributed event phases can be rejected at 95% (99%) confidence, and there is a significant correlation between the occurrence of earthquakes and the tidal function. In this study, the tidal potential at Merapi computed from formulas adapted from LONGMAN (1959) was used to determine the tidal phases. The Schuster method is more simply defined for the case of strictly periodic phenomena; for example, when a 24-hour sinusoid is used the local time defines the phase (midnight = 0^o, noon = 180^o). RYDELEK

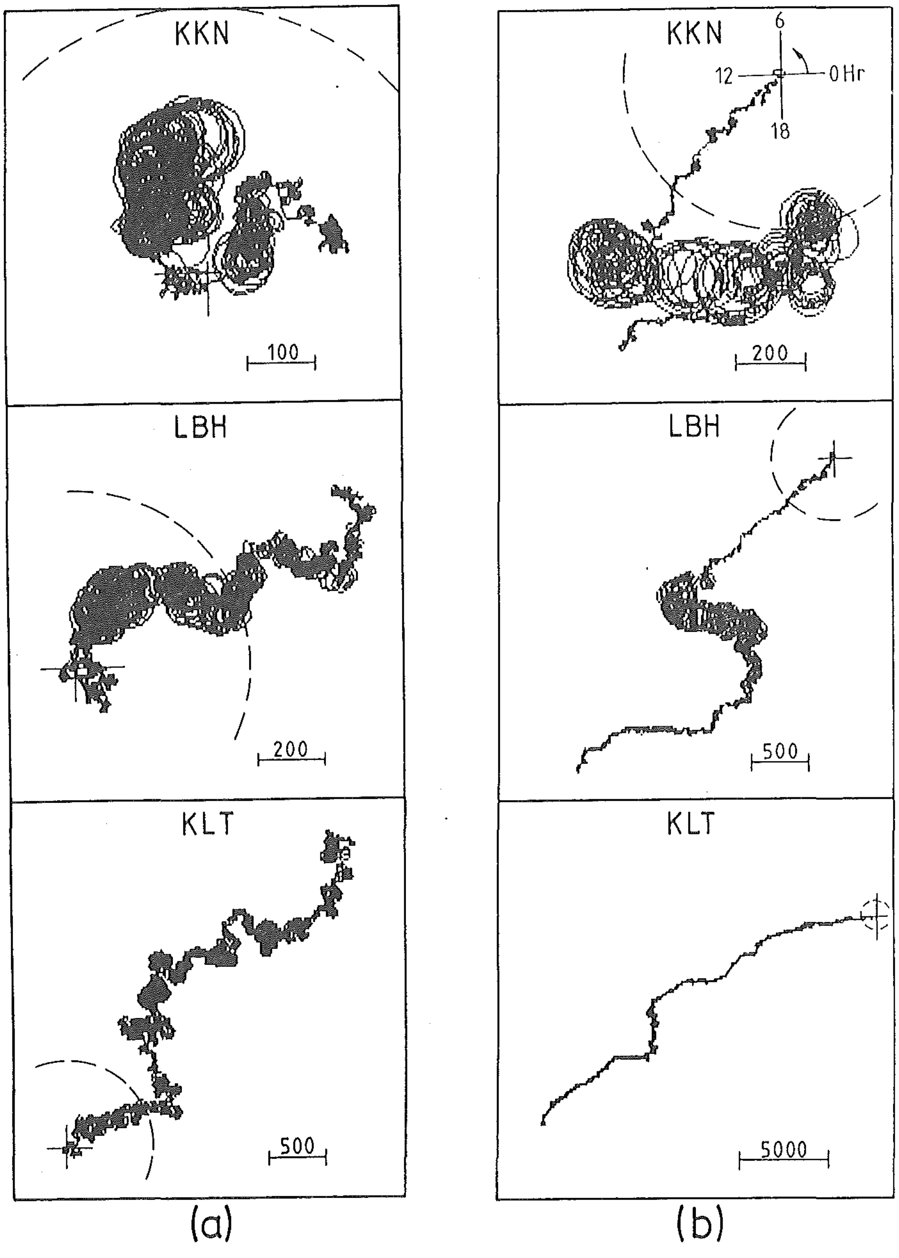

Figure 2. Phasor walkouts from the Schuster method when the Merapi catalogs are tested against: (a) the tidal potential, and (b) a 24-hour sinusoid. The crosses locate the origins, and the dashed circles are drawn at 95% confidence levels. The length of N unit phasors is given by the scale bar, where N is the number on the scale bar.

and SACKS (1989) used this method to develop a completeness test for earthquake catalogs based on such a 24-hour clock.

4 Schuster Test Results: Tidal Potential

The phasor walkouts from the Schuster method are plotted in Figure 2a for the three catalogs. The dashed circles in the figure, which represent the 95% confidence levels of non-random walkout, are drawn from the probabilities calculated from the Schuster test. Thus based solely on the results in the figure, the answer to the question of whether tidal triggering occurs at Merapi would be: no at station KKN, but definitely yes at stations LBH and KLT; the Schuster test probabilities for the catalogs from these stations are 0.51, 8.1×10^{-5}, and $< 10^{-20}$, respectively. However, we do not accept these positive results as evidence of tidal triggering because of other important findings described below.

5 Spectral Analyses

If the seismicity at Merapi, and especially at station KLT, was genuinely influenced by the tides at the extremely high level of confidence indicated by the Schuster test (Figure 2a), then tidal effects in the catalog should be detectable with standard, classical methods of analysis, such as Fourier analysis. We performed a fast Fourier transform on the KLT catalog, after first filling the gaps in the data with zeros, and then applying a Hanning window. The amplitude spectra are shown in Figure 3 for the semidiurnal and diurnal tidal bands. No evidence of a spectral peak at the frequency of the largest tidal component M_2 is seen, although this tide makes-up a substantial portion of the total tidal potential at equatorial latitudes. The lack of an O_1 tidal peak is not unexpected since the diurnal tides are small at the latitude of Merapi (7.6°S) (in theory, the diurnal tides vanish on the equator, while the semidiurnal tides have maximum amplitudes). Therefore, the significance of the positive results from the Schuster test in the previous section must be controlled by other, smaller tidal components, which is very puzzling.

The spectra, however, reveal strong broad-band peaks centered on frequencies of exactly 1 and 2 cpd (S_1 and S_2); the spectral amplitude of the former is about twice as large as the latter. In addition, the S_1 peak has a bandwidth which spans across the frequencies of the tidal components P_1 and K_1 (see Figure 3b). A spectral peak at S_2 would be consistent with a tidal influence on the seismicity, if it were not for the fact that M_2, always twice as large as S_2 in theory, is not observed. The lack of an M_2 peak is strong evidence that tidal triggering does not occur at Merapi. In fact, our suspicion at this point is that the S_2 peak is a harmonic of the S_1 peak, and that the presence of one or both of these terms is influencing the Schuster test and producing a false positive result. Possible sources of the S_1 term are discussed in a separate section.

6 Schuster Test Results: 24-hour Sinusoid

Shown in Figure 2b are the phasor walkouts when the Merapi catalogs are tested against a 24-hour (or S_1) sinusoid. The figure confirms the results of Fourier analysis and shows that all three catalogs contain an extremely strong S_1 term in the seismicity, the significance of which increases in the order: KKN, LBH and KLT. The average walkout is directed towards approximately 14:00 hours local time. A daily periodicity is also readily noticed in the section of the KLT catalog shown in Figure 1b.

Another form of display of this periodicity is shown in a rose plot of the KLT catalog in Figure 4. The length of each wedge in this plot is drawn proportional to the total number of shocks in the catalog within the local hour of the day indicated. On average, shock activity is found to be fairly constant during the night and then gradually increases during the day with a broad peak at 14:00 to 16:00 hours.

The above results demonstrate that the seismicity at Merapi has a tendency to peak daily at 14:00-16:00 hours local time. Although the gap structure of the data has a 24-hour periodicity, which is almost exactly 180^o out of phase with respect to the peak seismic time, (e.g. Figure 4, 2:00 am versus 2:00 pm), it cannot explain the long walkout observed, especially for station KLT. This was verified by filling the gaps in the KLT catalog with 30 events/hr (a large number compared to the average event/hr, see Figure 1a) and then redoing the Schuster test: the new result still showed a highly significant walkout at 14:00 hours. Indeed, the seismicity is clearly seen to peak in the afternoon hours, even in sections of data without gaps, e.g. Figure 1b.

In Figure 2, the peculiar behavior of the phasor walkouts near the middle of the paths (most obvious for KKN because of high resolution in the plot)

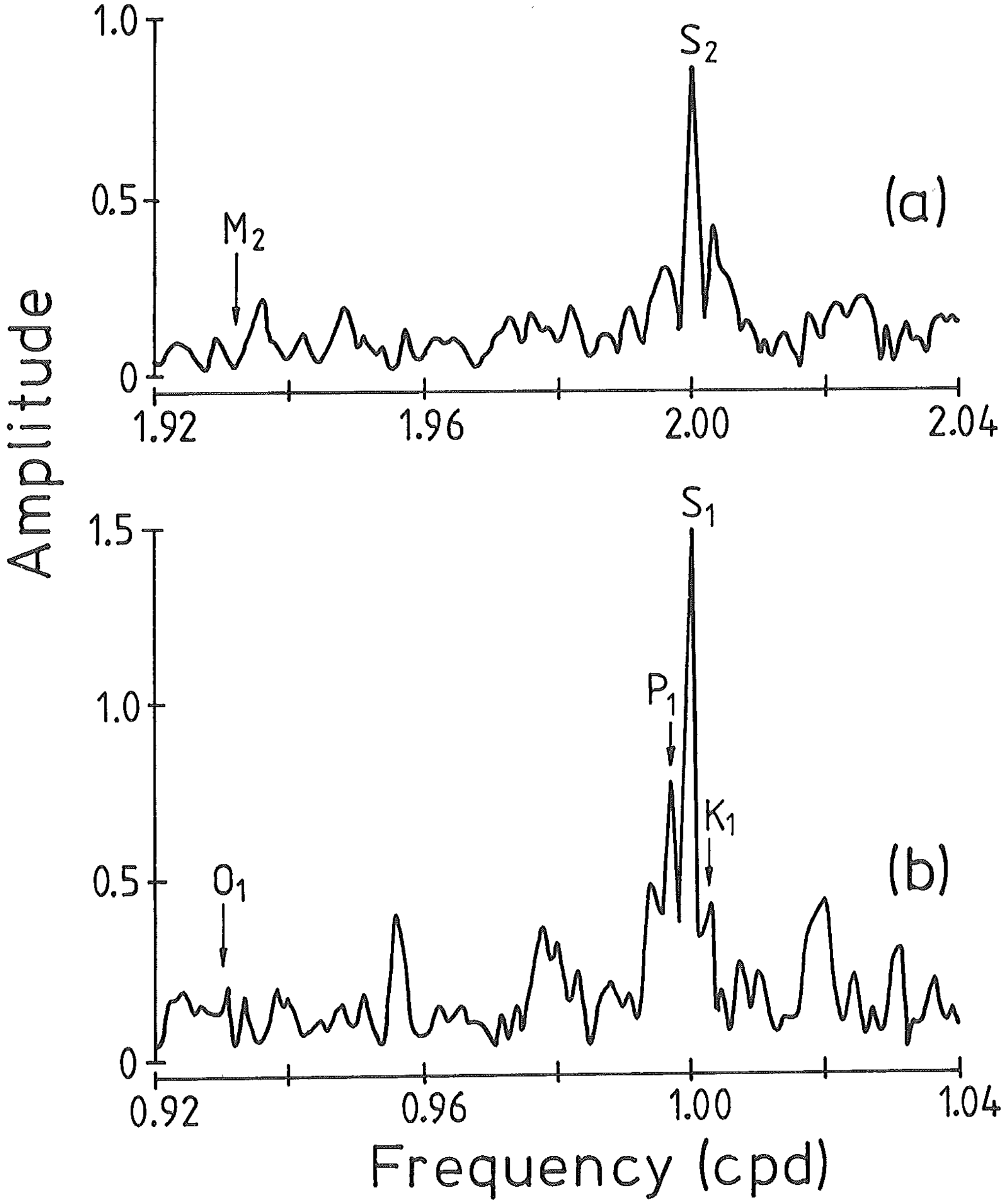

Figure 3. Amplitude spectra of the KLT catalog in the (a) semidiurnal and (b) diurnal tidal bands.

is a result of the increased seismic activity during the dome building phase noted previousy. During this time, the seismicity increased to the point of almost a constant number of events, on average, for each hour (see Figure 1a). This has the effect of producing a circular pattern in the phasor walkout because the phase angle changes from 0° to 360° almost continuously, while the amplitude remains practically unchanged, i.e. the number of shocks per hour is roughly constant. We found that this section of the catalog could be dropped from the analysis with no change in the conclusions from the Schuster test for either the tidal potential or the 24-hour sinusoid. Perfectly triggered events would appear as a linear walkout in the Schuster plot, and random data, as explained previously, would resemble Brownian motion.

7 Synthetic Catalogs

In order to determine whether the S_1 and/or S_2 term in the seismicity can affect the outcome of the Schuster method, noise-free synthetic earthquake catalogs were tested against the tidal potential at Merapi. These catalogs were generated by creating a pure sinusoidal variation of the number of events per hour: $A[\cos(2\pi t/T) + 1]$, where T is the period of the sinusoid and t is the local time of the hourly samples. (The amplitude of the sinusoid is not important since the Schuster probablilty is normalized to the total number of events.) In the first case, a catalog with a pure S_1 term (i.e. 24.00 hours) was generated and tested. The results of the Schuster test revealed no significant tidal triggering (prob > 0.15) and the path of the phasor walkout was rather inconspicuous; thus the positive results in Figure 2a cannot be explained by the presence of a pure S_1 term in the Merapi catalogs alone. Next a synthetic catalog with a pure S_2 (12.00-hour) variation of seismicty was tried. In this case, a very long walkout resulted (prob$< 10^{-20}$), which demonstrates that an S_2 term in the catalog is capable of greatly affecting the results of the tidal Schuster test at Merapi. Because of the broad-band nature of the spectral peak at S_1 (Figure 3b), which is presumably caused by slow temporal variations of the amplitude of the daily peak, we also tried a third catalog having a modulated S_1 periodicity in the seismicity. The modulation was formed by superimposing side-band waves onto the S_1 carrier. The side-bands were assigned to have the freqencies of the diurnal tidal components P_1 and K_1, and with amplitudes chosen to resemble the observed spectral amplitudes of these waves relative to S_1 in Figure 3b, i.e. $P_1/S_1 = 1/2$, and $K_1/S_1 = 1/4$. The Schuster test on this catalog using the tidal potential also resulted in a highly significant walkout (prob $< 10^{-20}$), thus demonstrating that a modulated S_1 is also capable of affecting the Schuster test at the latitude of Merapi.

There is no doubt that the catalogs from Merapi contain a large daily variation of the seismicity. As can be seen in Figure 1b, this variation resembles a S_1 sinusoid, but one that is heavily distorted and noisy; thus the harmonic overtones (i.e., S_2, S_3, etc) should also exist in the catalog. In addition, any long-period modulation of the daily pattern, such as a summer-winter effect, will produce a smearing of the S_1 spectral peak, as observed in Figure 3b. This in turn results in leakage of S_1 spectral energy into nearby tidal frequencies P_1 and K_1, at least in the KLT catalog we have spectrally analysed. Since the tidal potential at Merapi contains the terms P_1, K_1 and S_2, the presence of either the S_2 harmonic and/or the modulated S_1 in the catalog is large enough to produce false positive results when the catalog is tested against the tidal potential with Schuster's method, even though the potential contains only a very weak S_1 term in theory (at any location). This is the reason why we do not accept the positive results of the Schuster test for tidal triggering in the LBH and KLT catalogs. Notice that from the length of the walkouts in Figure 2b, these catalogs show the strongest daily variation in seismicity.

8 Discussion

The question of whether tidal triggering occurs at Merapi has now changed to the question of why the catalogs have a daily variation in seismicity, with peak activity biased towards afternoon hours. Several possibilities are discussed below, but no definitive answers can be given at present.

8.1 Tremor Amplitude Variations

Shocks are recorded when their amplitudes are 2 mm above the noise level or above the tremor amplitude, if and when tremors occur at Merapi. Since small shocks are missed during the tremors, a daily variation of tremors would thus produce a daily variation in shocks. At times, the hourly-count of the tremors does show a daily periodicity (see KIRBANI et al., 1988), but tremor activity is biased towards early morning hours (about 7:00), which cannot explain the observed phasor walkout at 14:00 for the shocks. There should be a 180° phase relation between shocks and tremors, with regard

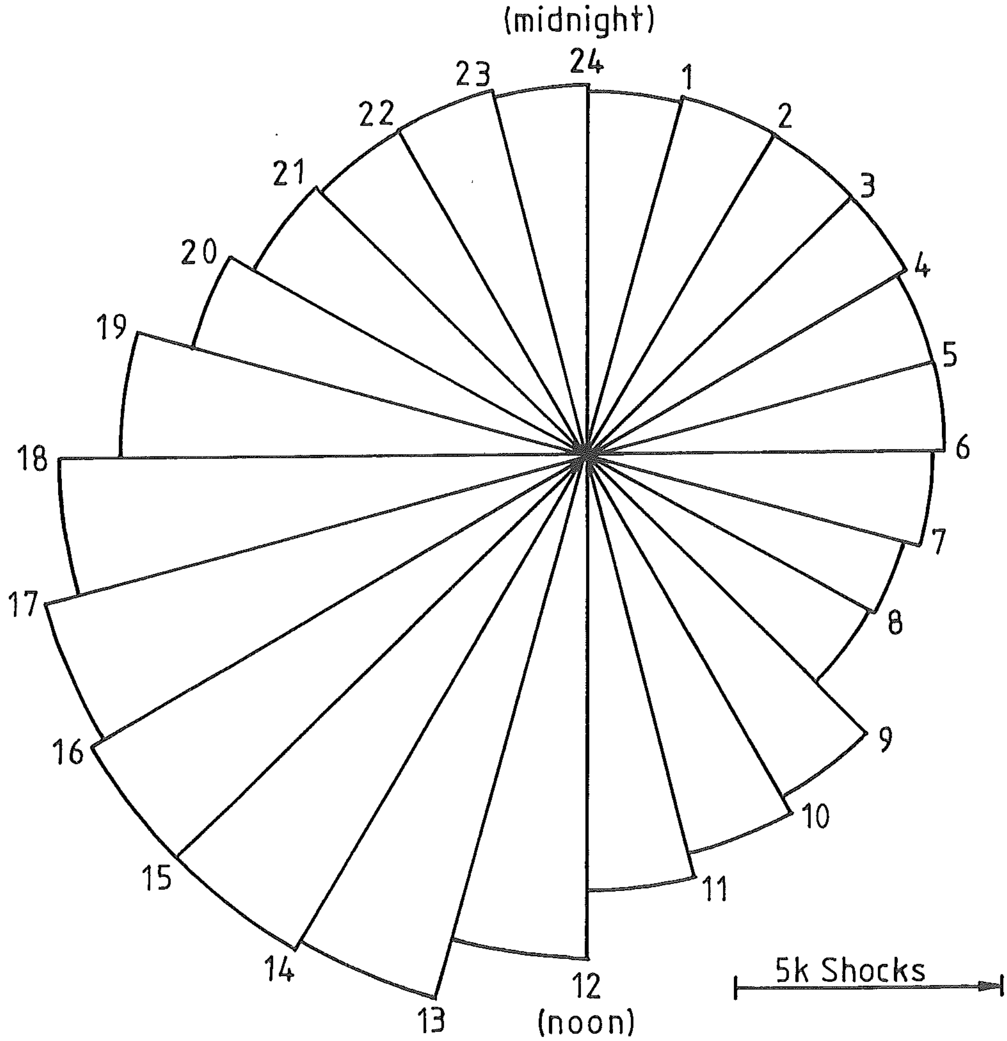

Figure 4. Histogram of the local time of the shocks in the KLT catalog.

to the time of day, if the former are missed because of the latter (see also RYDELEK and SACKS, 1989). In any case, blaming the tremors for hiding the shocks only would shift the problem to why tremor activity varies with a daily periodicitiy.

8.2 Man-Made Sources

It is well known that man-made activities such as routine maintenance, power outages, quarry and construction blasts, local road traffic, etc, produce disturbances with mostly daily periodicities. To the best of our knowledge, quarry and construction blasts pose no problems in the Merapi catalogs since these activities are minimal in Central Java. Also, the different number of events at the three stations is inconsistent with sources distant from the volcano. The self-contained seismic stations are remotely located on the slopes of the volcano; at heights from 1100 to 1700 m and about 14 km from the nearest main road, they are presumably well isolated from any man-made influences. In addition, there seems to be no apparent way in which a strong 24-hour variation in seismicity can enter into the catalogs from human errors in the procedure of recording the shocks from the seismograms. Man-made sources might be suspected if the daily variation in seismicity was a small effect, but we find it difficult to imagine how any localized non-seismic disturbances can produce the large daily pattern seen in Figure 1b.

8.3 Barometric and Temperature Effects

Hourly samples of barometric pressure and air-temperature with lengths of 3 months (June, July and August, 1986) and 1 month (August, 1986), respectively, are available from the city of Semarang, located 50 km north of Mt. Merapi. The spectra of these records have features similar to those found in the spectra of the catalogs, namely broad-band spectral peaks at both 1 and 2 cpd (see FADELI, 1988). In the case of pressure, the S_1 and S_2 peaks are roughly the same size, while for temperature the S_1 peak is almost 3.5 times as large at the S_2 peak.

The similarity of the spectra suggests the possibility that daily variations in seismicity might be caused by barometric and/or temperature effects. In order to check this possibility, correlations between the seismic catalogs and the above climatic data were performed. Figure 5a shows a plot of the number of shocks per hour versus the pressure (at Semarang) when the shocks

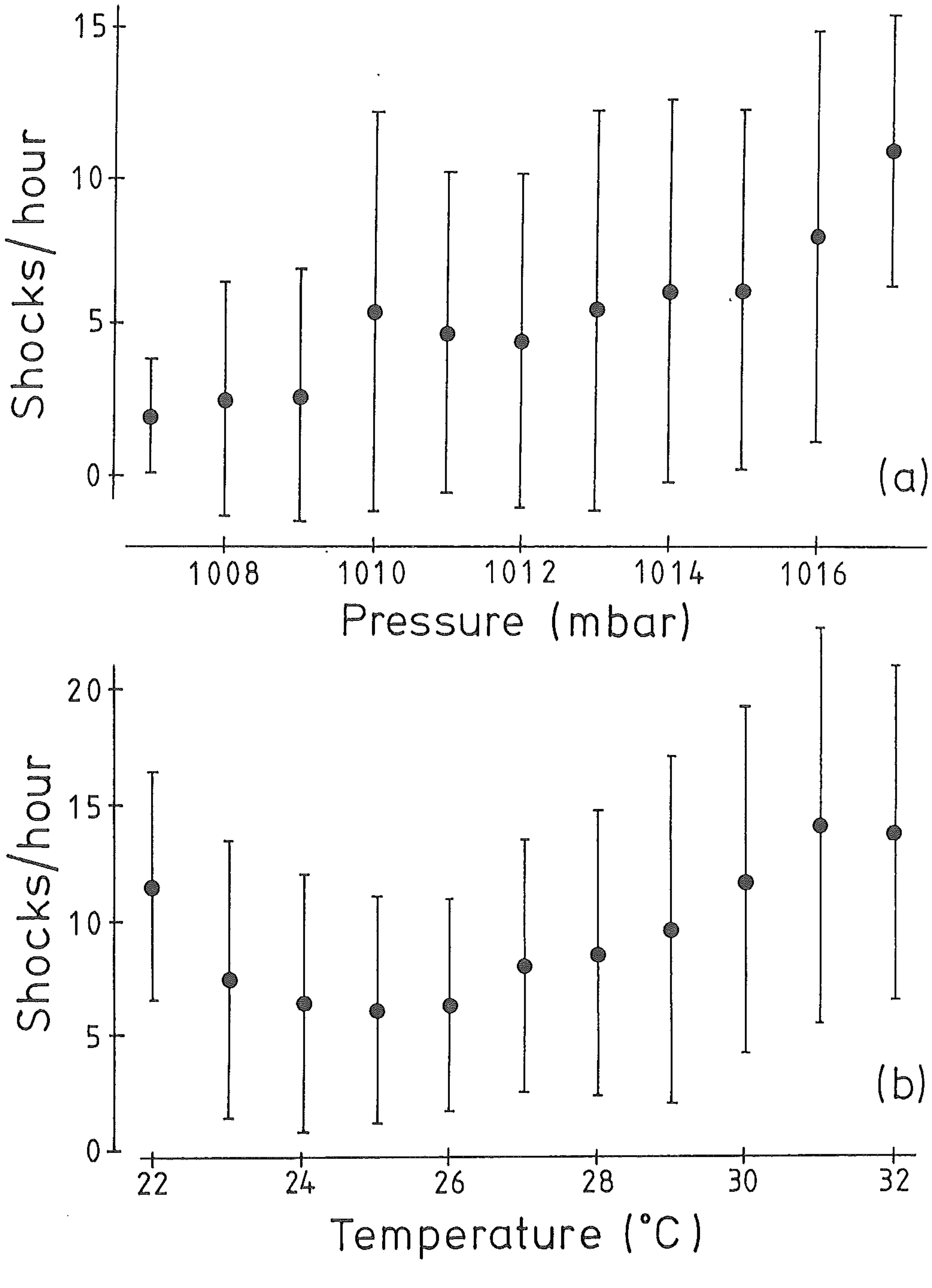

Figure 5. Plot of the pressure (a) and temperature (b) versus the average number of shocks, with 1 σ standard deviations. Shock data from KLT; pressure and temperature data is from Semarang, 50 km north of Merapi.

were recorded; Figure 5b is a similar plot, but for temperature. In both figures, mean values of the number of shocks per hour with 1 σ uncertainties are plotted, while the abscissa values are assumed to be error-free. Figure 5 shows a weak bias of more shocks occurring at higher pressures and temperatures, but in view of the error-bars in the plots, we must conclude that strong climatic effects are not dominant in the data we have analysed, albeit for climatic data recorded at some distance from Mt. Merapi. Other models, such as non-linear effects, multi-channels or phase shifts between data channels, could be investigated but then much longer and more representative pressure and temperature time series should be used than are available to us at present.

8.4 Thermo-Elastic Effects: Albedo

The air temperature measured at a coastal site 50 km away is probably not a reliable estimate of the conditions at Merapi, and especially since the central vent of the volcano is almost 3000 m above sea level. The sun could be shining brightly on the summit of Merapi, while the coast is experiencing cloudy conditions; thus the air-temperature at Semarang would be an erroneous measure of the ground temperature at Merapi.

FRIEDERICH and WILHELM (1986) have found that temperature changes in the ground resulting from the solar radiational heat-flux are a source of time-dependent thermoelastic deformations. A key point in their work is that spatial variations in the radiation balance (i.e. albedo contrasts) are more important as a disturbing influence then the absolute value of the input radiation. A mountain peak with a different face sunlit during certain times of the day would be affected because of such albedo contrasts. And a rain storm would also cause a sudden change in the radiation balance.

The stresses associated with thermo-elastic deformations are comparable to tidal stresses and could provide a trigger mechanism for the seismicity; the resulting effect would have a strictly daily periodicity because of the direct solar influence. Compared to the depth of the shocks, however, the penetration depths of these deformations are rather small (100's of meters or less), although these estimates are for an elastic half-space with local, abrupt albedo changes. The penetration depths may increase when topography is considered but this remains to be determined. In any case, it appears that only very shallow events could be triggered by such stresses; for example events in the magma dome.

Another idea worth mentioning are possible temperature effects on lava.

The viscosity of the lava that continuously builds the dome on Merapi is certainly a strong nonlinear function of the temperature, and thermo-viscoelastic effects (also with a daily periodicity) due to solar-radiative heating of this dark basaltic rock can be imagined.

9 Conclusions

Because of large daily variations in seimicity we have observed in the seismic catalogs, we are unable to answer the question of whether tidal triggering occurs at Merapi with the Schuster method of analysis. At the present time, we can offer no conclusive explanations for these variations, and only discuss some possibilities. But from our experiences in testing synthetic catalogs, and analysis of other earthquake catalogs, we can issue the general warning: the Schuster test for tidal triggering should be used with extreme caution on catalogs with demonstrated strong daily variations in seismicity, if at all.

References

Emter, D., Zürn, W., Schick, R., and G. Lombardo, 1986. Search for tidal effects on volcanic activities at Mt. Etna and Stromboli, In: R. Vieira (Editor), *Proc. 10th Int. Symp. on Earth Tides*, Consejo Superior de Investigaciones Cientificas, Madrid, pp. 213-219.

Fadeli, A, 1988. Volcanic earthquakes at Merapi (Central Java) during lava dome building beginning in October 1986, *Paper presented at the International Workshop of Volcanic Seismology, IAVCEI, October 3-8*, Capri Italy.

Friederich, W. and H. Wilhelm, 1986. Solar radiational effects on earth tide measurements, In: R. Vieira (Editor), *Proc. 10th Int. Symp. on Earth Tides*, Consejo Superior de Investigaciones Cientificas, Madrid, pp. 865-879.

Heaton, T.H., 1975. Tidal triggering of earthquakes, *Geophys. J. Roy. astr. Soc., 43*: 307-326.

Kilston, S. and L. Knopoff, 1983. Lunar-solar periodicities of large earthquakes in southern California, *Nature, 304*: 21-25.

Kirbani, S.B., Fadeli, A. and R. Mugiono, 1988. A review of the development of a geophysical volcano research laboratory to investigate the Merapi volcano in Central Java, Indonesia, *Paper presented at The Project-Site Seminar on Sabo Works, October 11-13*, Yogyakarta, Indonesia.

Klein, F.W., 1976. Earthquake swarms and the semidiurnal solid earth tide, *Geophys. J. Roy. astr. Soc., 45*: 245-295.

Knopoff, L., 1964. Earth tides as a trigger mechanism for earthquakes, *Bull. Seismol. Soc. Am., 54*: 1865-1870.

Lammlein, D.R., G.V. Latham, J. Dorman, Y. Nakamura, and M. Ewing, 1974. Lunar seismicity, structure and tectonics, *Rev. Geophys., 12*: 1-21.

Longman, I. M, 1959. Formulas for computing the tidal accelerations due to the moon and the sun, *J. Geophys. Res., 64*: 2351-2355.

McNutt, S.R. and R.J. Beavan, 1981. Volcanic earthquakes at Pavlof Volcano correlated with the solid earth tide, *Nature, 294*: 615-618.

McNutt, S.R. and R.J. Beavan, 1984. Patterns of earthquakes and the effect of solid earth and ocean load tides at Mount St. Helens prior to the May 18, 1980, eruption, *J. Geophys. Res., 89*: 3075-3086.

Minakami, T, 1974. Seismology of volcanoes in Japan, In: L. Civetta, P. Gasperini, G. Luongo, and A. Rapolla (Editors), *Physical Volcanology*, Elsevier Sc. Publ., Comp., Amsterdam, pp. 1-27.

Palumbo, A., 1986. Lunar and solar tidal components in the occurrence of earthquakes in Italy, *Geophys. J. Roy. astr. Soc., 84*: 93-99.

Rydelek, P.A., P.A. Davis and R.Y. Koyanagi, 1988. Tidal triggering of earthquake swarms at Kilauea Volcano, Hawaii, *J. Geophys. Res., 93*: 4401-4411.

Rydelek, P.A. and I.S. Sacks, 1989. Testing the completeness of earthquake catalogues and the hypothesis of self-similarity, *Nature, 337*: 251-253.

Schick, R., 1981. Source mechanism of volcanic earthquakes, *Bull. Volconol., 44-3*: 491-497.

Schuster, A., 1897. On lunar and solar periodicities of earthquakes, *Proc. Roy. Soc., 61*: 455-465.

Shirley, J.H, 1988. Lunar and solar periodicities of large earthquakes: Southern California and the Alaska-Aleutian seismic region, *Geophys. J., 92*: 403-420.

Shlien, S. and M. N. Toksöz, 1970. A clustering model for earthquake occurrences, *Bull. Seismol. Soc. Am.,60*: 1765-1787.

Shlien, S., 1972. Earthquake-tide correlation, *Geophys. J. Roy. astr. Soc., 28*: 27-34.

Shudde, R. H and D. R. Barr, 1977. An analysis of earthquake frequency data, *Bull. Seismol. Soc. Am., 67*: 1379-1386.

Simpson, J.F., 1967. Earth tides as a triggering mechanism for earthquakes, *Earth and Planet. Sci. Letters, 2*: 473-478.

Ulbrich, U., L. Ahorner and A. Ebel, 1987. Statistical investigations on diurnal and annual periodicity and on tidal triggering of local earthquakes in central Europe, *J. Geophys, 61*: 150-157.

Young, D. and W. Zürn, 1979. Tidal triggering of earthquakes in the Swabian Jura?, *J. Geophys., 45*: 171-182.

Volcanic Activity Parameters

Rolf Schick

Institut fuer Geophysik Rich.-Wagner-Str.44 D-7000 Stuttgart-1

Introduction

The origin of seismic signals on an active volcano is of manifold nature: Shear and tensile fractures, collapse of cavities, gas explosions and pressure fluctuations of the non-stationary fluid flow of magma and/or gas. The resulting seismic ground vibrations consequently cover a wide range of amplitudes and a broad frequency band. At least at times of higher volcanic activity, seismic signals generated by the activity of a volcano are nearly continuously observed, a fact which prohibits data reduction by event triggering methods. A seismic station with three components, an amplitude resolution of 16 bits and a frequency bandwidth of 100 Hz requires a data storage capable of handling up to 100 MBytes/day. High data rates not only cause technical difficulties, they also hamper obtaining a quick overview on the information content of the incoming signals and of recording gap free data.

Volcanic Activity Parameters

The quantitative description of a complex and multi parameter process like an active or eruptive volcano must be very subjective at the present state of our knowledge about the internal working of a volcano. Giuseppe Imbo, director of the Vesuvius observatory for a long time, was one of the first volcanologists who recognized that an appropiate reduction of the recorded seismic data results in 'numbers' which are useful in describing the strength and type (effusive-explosive) of activity and which furthermore permits studies of relationships between the strength of external forces (barometric pressure, tidal forces, and others) and the occurrence of eruptive activity. Imbo calculated these numbers corresponding approximately to hourly averages of volcanic tremor amplitudes and called them 'indici dell'intensita eruttiva' (IMBO, 1954). Recent studies, mainly from the analysis of volcanic tremor and volcanic shocks, confirm the utility of 'numbers' derived from the information content of seismic signals. 'Volcanic Activity Parameters' might be an appropiate appelation for these 'numbers'. ENDO and MURRAY (in press) and HURST (1989) also report on convenient analog and digitally working data acquisition systems for tracking the seismic activity of a volcano. The definition of 'Volcanic Activity Parameters' must be subject to a trade-off between their significance describing the eruptive activity of a volcano, the applicability of the method in a real-time calculation and the size of needed data storage. At our present state of knowledge of volcanic processes and with a moderate cost of the equipment for the data acquisition, 'activity parameters' may be calculated according to the following procedures:

1. Transient events per time unit (SCHICK and MUELLER,1988)
2. Distribution functions of transient signals
3. Power values (RMS) per time unit (ENDO and MURRAY, 1990)
4. Non-stationarity of signal envelopes
5. Patterns of signal envelopes (periodicities)
6. Spectral parameters (COSENTINO et.al., 1989)
7. Polarization analysis (SEIDL and HELLWEG, this volume)

Instrumentation.

A block diagram of the instrumention being in construction and partly in use, is shown in fig. 1. Low or moderate cost circuit boards and parts are used throughout, and the straightforward and uncomplicated design allows the assembly of the data converter in a small workshop without sacrificing performance. The frequency range of the induced seismic signals by magma/gas flow is broad and extends over at least 12 octaves, as was observed with volcanic tremor recordings at Stromboli volcano (FALSAPERLA et. al., to be published). This property requires at least two different seismic sensors. For our application, we prefer to use GURALP CMG-3 or CMG-4 instruments, or seismometers of the Wielandt-Streckeisen type (STS-1 or STS-2). Unfortunately, cost of these instruments is high (especially for three component stations), and delivery times from the manufacturers are long. Many long-period seismometers, as used in earthquake seismology, are not usable on volcanoes, because the high frequency part of the tremor spectrum can excite all kinds of spurious resonances in the seismometer system, causing intermodulation products which may strongly disturb essentially the long period part of the spectrum. For the short period part of the spectrum (larger 10 Hz), low-cost accelerometers can be used without problems. The output of the broad-band seismometer is separated into two parts by high- and low pass filtering at 1 Hz cut-off frequency. Filtering is performed with Burr-Brown 'Universal Active Filters' UAF41. Each component of the seismic data stream consists of 3 parts according to signal bandwidths: 0.01-1 Hz, 1-10 Hz and 10-100 Hz. An RMS-DC converter (4341 from B.B.) computes a DC voltage proportional to the RMS value of the signal, corresponding to the envelope of the seismic waveform. The value of the time constant with which the output signal of the converter is filtered must be chosen according to the size of the data storage, as well as to the available man-power for evaluating the recorded information. We prefer currently a time constant between 5-10 s which seems to be a useful compromise between needed data storage and the identification of shocks (FADELI et. al., this volume). The analog to digital conversion of these signals is performed with a data logger type 'Tattletale V' by ONSET Comp. Corp., Falmouth, USA. This datalogger has several, for our purpose desirable features: small size, resolution 10 bits (with a 12 bit option), 11 input channels, very low power consumption, easily programmable, RS232 interface and up to 2 MBytes memory size. Oversampling the incoming data by a factor of 100 increases the effective resolution of the data to better than 12 (14) bit. In case this dynamic range is not sufficient, a logarithmic amplifier (f.i. LOG100 by B.B.) in one component of each seismic sensor provides an amplitude range of close to 100 dB.

There are now 3 options of data storage and data transfer:

1. The Tattletale data logger may be used as a stand-alone device. This permits the installation of a remote located field station on a volcano with a very low power consumption and uncomplicated installation. The data files from the logger are transferred in regular intervals to a laptop computer by persons visiting the station.

2. A laptop computer is permanently connected to the data logger. The harddisk of the computer increases the memory size of the station by a factor of 20 or more. Furthermore, a more sophisticated signal processing (f.i. with the polarisation analysis) may be performed in the computer.

3. The Tattletale data logger is connected to a 'Terminal Net Controller' (TNC2). This is a simple MODEM-interface between the datalogger and a UHF-transceiver. The communication is based on the protocol AX25, a modification of the X25 standard, and developed for amateur radio (Anonymous, 1990). With standard and unmodified 'handie-talkie' transceivers, data transfer with 1200 baud in 2 s packets is used. Provided the radio telemetry path is reasonably stable, a communication baud rate of better than

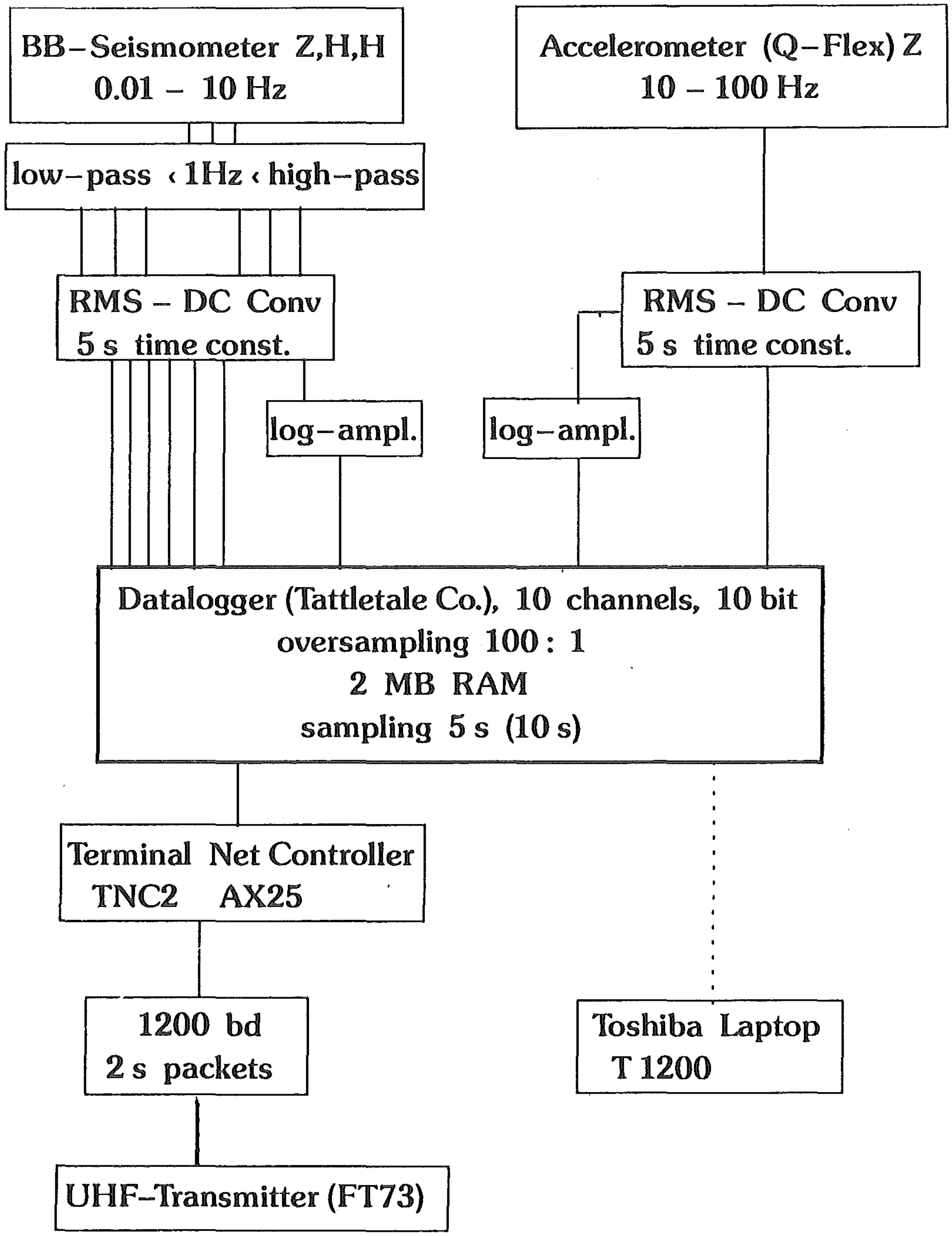

Fig. 1 : Block diagram of data acquisition system

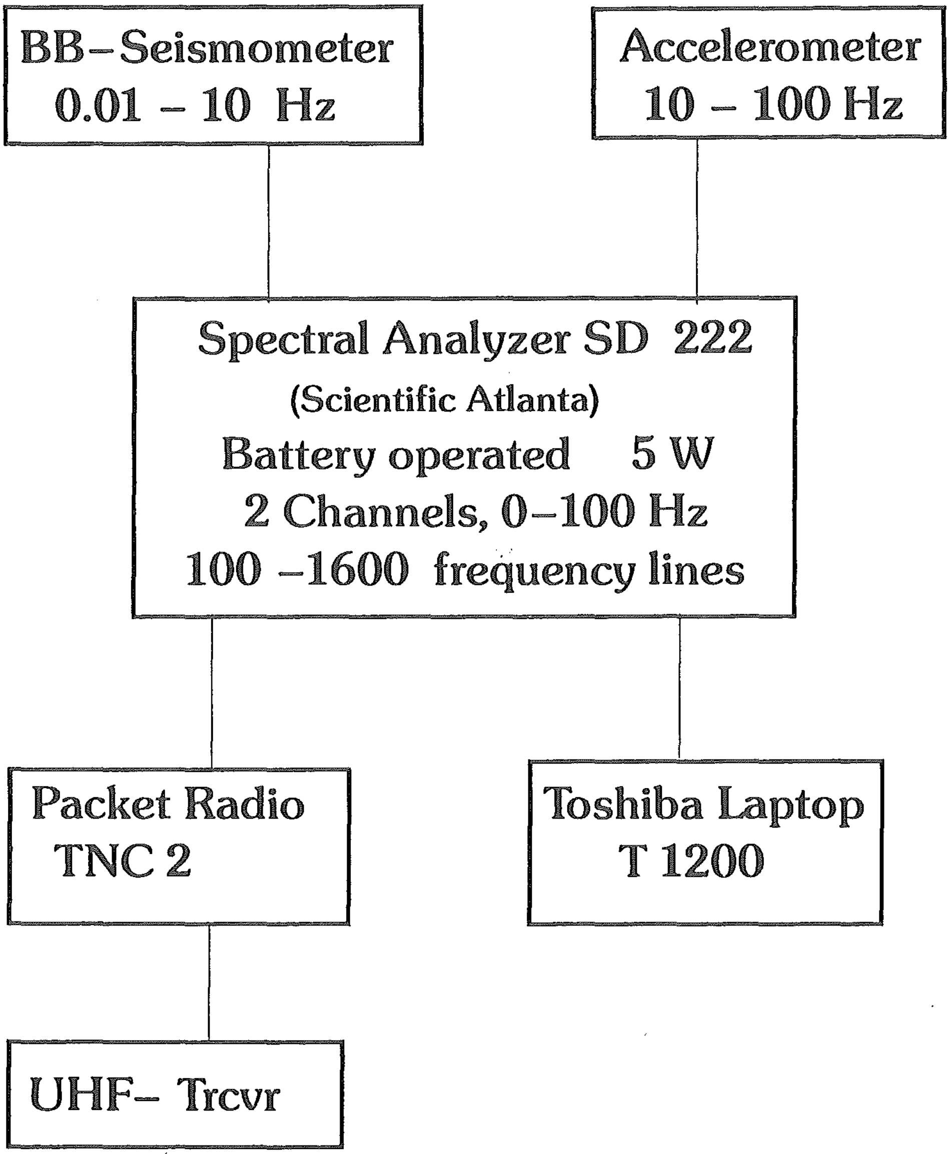

Fig. 2 : Block diagram of data acquisition for spectral estimates.

400 can easily be obtained with an error free data transfer. 'Digipeaters' which are simple to install can be put between an observing station and the field stations, if communication is otherwise not possible due to large distances or mountain obstacles, or if power consumption at the field recording station has to be kept very low. Several stations may work simplex on a common radio frequency. An alternative or supplementary version to the system of fig. 1 is illustrated in fig. 2. It can be of advantage when spectral parameters of the tremor are important in the evaluation of the eruptive activity. The main part of the system consists of a two channel FFT analyzer (model SD222 by Scientific Atlanta, San Diego, USA) which is designed for field use and has a power consumption of only 5 W. Spectral estimates and selected or decimated time functions can be calculated with many options and either stored in the instrument (up to 500 spectra), transferred directly to a laptop computer, or sent by packet-radio telemetry in an error-free communication mode to a central observatory.

Acknowledgements

P. Rydelek and W. Zuern read the manuscript.

References.

Anonymous (1990): Digital Communication. In: The Radio Amateur's Handbook, Published by the American Amateur Radio League, Newington, CT., USA

Cosentino, M., G. Lombardo and E. Privitera (1989): A Model for Internal Dynamical Processes on Mt. Etna. Geophys. J., Vol. 97, p. 367-379.

Endo, E.T. and T. Murray (in press): Real-time Seismic Amplitude Measurement (RSAM): A Volcano Monitoring and Prediction Tool. Bull. Volcanology.

Hurst, A.W.(1989): Monitoring Volcanic Tremor at the Chateau Observatory. Technical Report No. 105, Geophysics Division, Dept. of Sc. and Ind. Res., Wellington, N.Z.,46 p.

Schick, R. and W. Mueller (1988): Volcanic Activity and Eruption Sequences at Stromboli during 1983-1984. Modeling of Volcanic Processes, Ch.Y. King and R. Scarpa eds., Vieweg, Braunschweig, p.120-139.

Automatic Event Recording

A. Fadeli [1], S.B. Kirbani[1] and R. Schick[2]

1) Lab. Geofisika Gadjah-Mada-Univ. Yogyakarta Indonesia
2) Institut fuer Geophysik Rich.-Wagner-Str.44 D-7000 Stuttgart

The high rate of seismic events on an active volcano and their correlation of the frequency of occurrence, wave form and energy with the state of eruptive activity makes an automatic recording desirable. It is not seldom that more than 100 events per hour are observed with the seismic activity at Merapi volcano. Furthermore, an automatic recording with an on-line display permits an easy and quick overview on the activity of the volcano (Endo and Murray, in press). The instrumentation which is used for our event detection is described in the article by Schick (this volume). A cut-off frequency of 0.2 Hz is chosen for the low-pass filter following the rms-dc conversion. The value is a trade-off between the loss of information and the needed size of the data storage. Fig. 1 shows in such a way decimated data of a time series recorded at the station KKN at Merapi (see Kirbani, this volume). As can be seen, it is easily possible to determine the time of occurrence of a shock, its maximum amplitude and its energy content. These values may be plotted on-line in an observatory. The increasing amplitude offset at the end of the series illustrated in fig. 1 is due to starting volcanic tremor ('tremor storm') which superimposes the events. The data base can also serve for correlation analysis, as for instance described by Fadeli et. al. (this volume).

Fig. 2 shows a spectral analysis of the time series of fig. 1. The pronounced amplitude peak at about 100 s indicates a non-random character of the time intervals between the shocks. A continuous observation of such event periodicities and their variation in time may present information on the kind of activity of the volcano.

References

Endo, E.T. and T. Murray (in press): Real-time Seismic Amplitude Measurement (RSAM): A Volcano Monitoring and Prediction Tool. Bull. Volc.

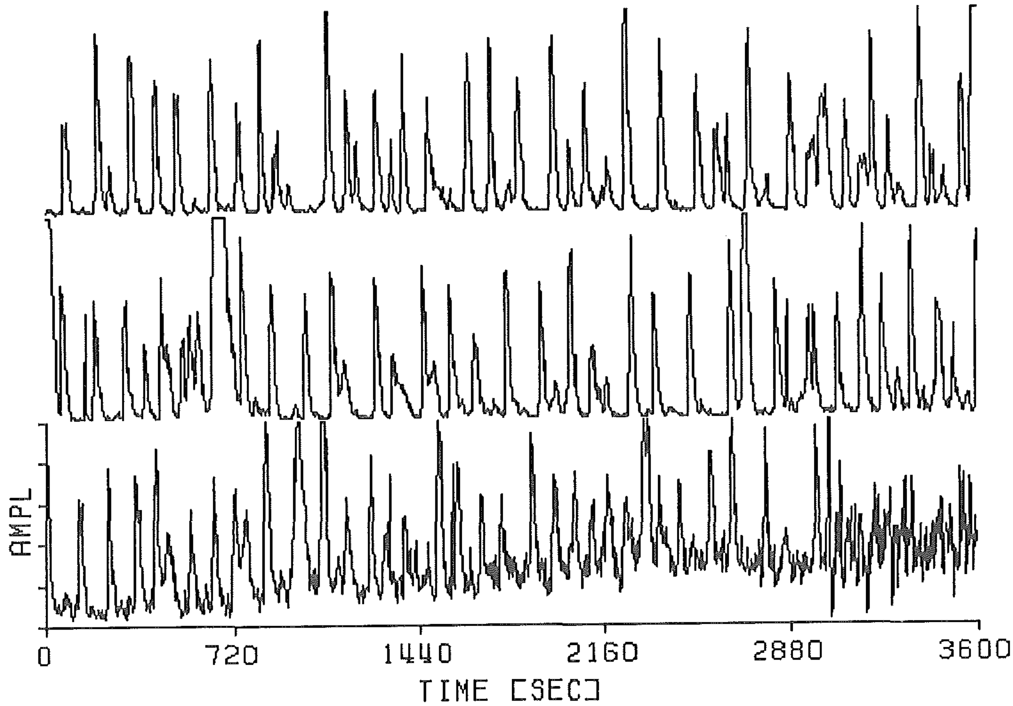

Fig. 1 : Low-pass filtered RMS values of seismogram containing tremor and shocks. Note start of tremor at end of series.

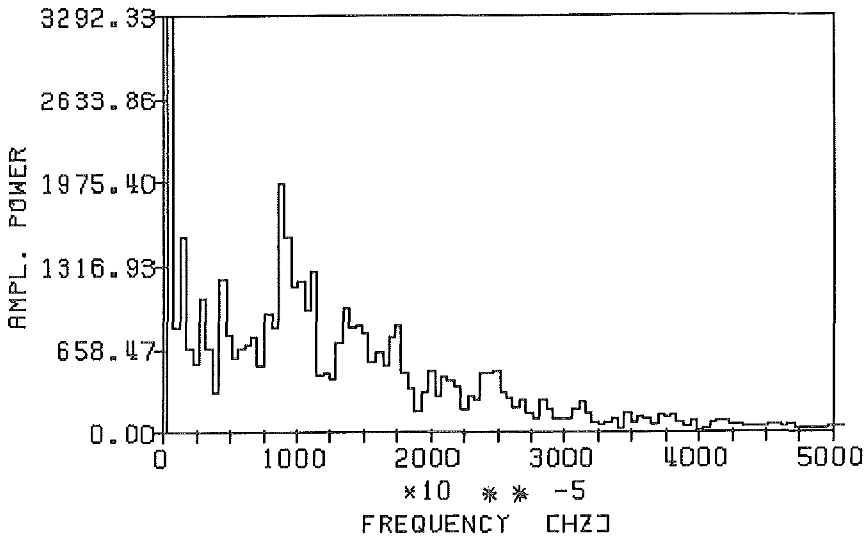

Fig. 2 : Spectral analysis of time series illustrated in fig. 1. Note pronounced peak at about 100 s.

A New Long-Baseline Tiltmeter for Volcanic Application

Dieter Emter[1], Edi Meier[2] and Rolf Schick[3]

Abstract

A new type of long-baseline fluid tiltmeter has been operated in the Black Forest Observatory Schiltach (BFO) for several years. Instead of the fluid levels at both ends the pressure difference at the center of the instrument is used as a measure for tilt. This type of instrument is easy to install and to maintain and has proven to be superior to short-baseline tiltmeters in the case of quantitative measurement of tidal tilt. Attempts have been undertaken to construct a similar, less sophisticated and less sensitive instrument for field measurements in volcanic areas. Those instruments are equipped with commercially available differential pressure transducers. One of these instruments reached tidal sensitivity at a baselength of 20 m and showed a remarkable long-term stability.

1 Introduction

The continuous measurement of tilt in the vicinity of volcanoes has a long history: JAGGAR and FINCH (1927) reported about the first tilt measurements in Hawaii and MINAKAMI (1942) started with tilt measurement at Asama volcano in Japan already in 1934. Long-period seismometers and horizontal pendulums with short baselines were used in these investigations. It was soon realized, however, in the volcanic observatories of Hawaii and in Japan that short-baseline instruments are much more affected by small-scale perturbations than long-baseline tiltmeters. Therefore most of these observatories were equipped with long-baseline tube tiltmeters first developped by HAGIWARA (1947) and EATON (1959) and improved later on. The signals of those tiltmeters are used as one input for multichchannel prediction e.g. in Hawaii (KLEIN, 1984) or for computer based online warning systems e.g. at Sakurajima (KAMO and ISHIHARA, 1989).
Tilt signals as precursors of volcanic eruptions have been measured with nearly all different types of tiltmeters. They are sometimes so strong that

[1]Black Forest Observatory Schiltach, Heubach 206, D-7620 Wolfach, FRG
[2]Hard 4, CH 8408 Winterthur, Switzerland
[3]Institute of Geophysics, Richard-Wagner-Str.44, D-7000 Stuttgart, FRG

no highly sensitive tiltmeter is needed to detect them qualitatively. If tilt signals, however, should be used to distinguish between different models for magmatic intrusions before an eruption, precise quantitative tilt measurements are required at different distances from the volcano.

2 Differential Fluid Pressure Tiltmeters

2.1 General

The previously existing types of tube tiltmeters, the Michelson type with a half-filled tube (MICHELSON, 1914) and the pot-and-tube tiltmeter after HAGIWARA (1947) and EATON (1959) have some advantages and disadvantages against each other but all of them need absolute fluid-level measurements at both ends of the instrument. A newly designed instrument (HORSFALL and KING, 1978) reduces the two fluid-level measurements to only one measurement of the pressure difference at the center of the instrument.

2.2 The Horsfall Tiltmeter

2.2.1 The BFO Installation

One of the prototypes of the Horsfall tiltmeter is operated since some years in the BFO. The first basic results of this installation have been published by ZÜRN et al. (1986). A detailed description of the instrument and the installation together with the final results is given by EMTER et al. (1989). Therefore only a brief description is outlined here.
A pot-and-tube tiltmeter is blocked in its middle by the diaphragm of a differential pressure transducer (see Fig.1), the tilt-related height differences at both ends are measured in this way as a pressure difference. The diaphragm is made relatively stiff; this makes the dynamic response of the instrument fast but on the other hand requires the measurement of very small displacements of the diaphragm. These displacements (about 10^{-7}m for tidal tilt) are measured with a capacitive sensor directly in the tiltmeter fluid which therefore has to be a perfect insulator. A substituted fluorocarbon was chosen as a fluid with ideal properties but it is very expensive and not easy to get everywhere.
A great advantage of the Horsfall tiltmeter is the ease of installation; the tube can follow existing galleries of a mine and has not to be layed out

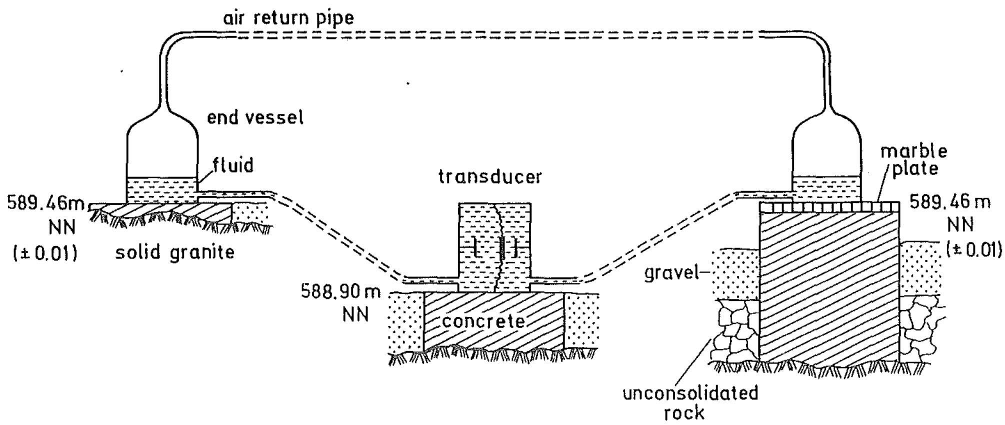

Figure 1: Principle of operation of the differential fluid pressure tiltmeter (Example of the BFO installation).

exactly along the baseline. In the case of a good temperature stability not much care has to be taken to level the tube. Furthermore the instrument can easily be dug in in the field as Horsfall did with his first prototype in the vicinity of the Cambridge institute (HORSFALL, 1977).

2.2.2 Tidal and Long-Term Results

The greatest advantage of tube tiltmeters is that their baselength can be made as long as the local circumstances allow and that the influence of local elastic perturbations (HARRISON, 1976) can be minimized in this way. This could be clearly demonstrated for the case of tidal tilt in the BFO. The results obtained over a measuring base of 170 m agree much better with the tidal tilts predicted for an elastic earth model including the ocean effects than all the previous results from the different types of short-baseline tiltmeters in the same observatory (ZÜRN et al, 1986; EMTER et al., 1989). From this we conclude that tilt amplitudes are measured the more representatively the longer the baseline of the tiltmeter is. This should be valid for all types of tilts that are accompanied with simultaneous elastic

deformations of the earth's crust i.e. for volcanic tilts as well as for tidal tilts.
The instrument showed a nearly constant drift over years with a rate between 2 and 3 μrad/year over a baselength of 170 m. It could be demonstrated (EMTER et al., 1989) that the biggest part of this drift stems from the mechanical part of the sensor i.e. the metallic diaphragm and might be caused by creep due to aging of the copper-beryllium alloy.

2.3 Towards a "Volcanic" Tiltmeter

2.3.1 General Considerations

Within the bilateral cooperation in geosciences between the Federal Republic of Germany and Indonesia the question arose whether to install one or more tiltmeters at the Merapi Volcano in Java. It was clear from the beginning that a long-baseline instrument would give the most reliable results but that the Horsfall instrument would be too sophisticated and too expensive to be operated in a greater number in remote areas. It was decided to develop a similar instrument in cooperation with the engineering firm of E. Meier. This tiltmeter should consist mostly of parts that are commercially available thus having a reasonable price and being reproducible in an adequate number. Furthermore, the tiltmeter should be operated with water instead of a special, expensive fluid.
Which specifications should such a tiltmeter fullfill? Tilt signals observed at volcanoes are normally much larger than tidal tilt and they show rates generally larger than some μrads/day during preeruptive periods, corresponding to extrapolated values between 200 and 10000 μrad/year (e.g. KLEIN, 1984; SWANSON et al., 1985). A "volcanic" tiltmeter should therefore resolve at least 1 μrad; better would be tidal resolution in order to control the coupling of the instrument to the earth's crust. The instrumental drift under stable conditions should not exeed 10 μrad/year in order to be well below possible volcanic tilt rates.

2.3.2 First Attempts

The basic conception of the new tiltmeter is that it consists of an industrial differential pressure transducer connected by a copper tube with end vessels of glas or metal. Such industrial transducers are different from the Horsfall transducer (EMTER et al., 1989) as they can be operated with nearly all fluids and especially with water. They have a measuring cell filled with

a special fluid which is coupled by two diaphragms to two fluid systems between which the pressure difference can be measured; these can be the two arms of a water-filled tube tiltmeter for instance. The specifications given by the manufaturers are intended for engineering applications therefore they often do not include the ultimate resolution which is limited by the electronic noise level and informations about the long-term stability. Therefore each type has to be tested under stable conditions for this special application.
A first test series was obtained with differential pressure transducers fabricated by HARTMANN u.BRAUN. After some negative experiences a selected transducer was found with a resolution of better than 0.1 μrad in connection with a water-filled tube tiltmeter with a baselength of 10 m. The long-term stability extrapolated from a time series of only two weeks corresponded to about 20 to 30 μrad/year. This tiltmeter was sent to Indonesia and installed in a tunnel near Merapi volcano. Because of logistical problems (power supply and data logging) no continuous data set was obtained before the tiltmeter electronics was completely damaged by lightning.

2.3.3 The Albigna Tiltmeter

In the meantime one of us (E.M.) constructed a new tiltmeter which was installed with a baselength of 20 m at the bottom of a hollow chamber inside the Albigna dam in the Swiss alps (MEIER, 1990). The transducer has ceramic diaphragms instead of metallic ones, the former are expected to show smaller creep due to aging. The data are stored in a local data logger and can be transfered by telephone line to a central computer. The results obtained within nearly one year of observation are very encouraging. The zero point of of the transducer was stable to about 4 μbar within 9 months corresponding to a tilt stability of about 3 μrad/year. As expected, the tilt measured in front of the dam correlated nearly linearly with the water height behind the dam. When this influence was removed by linear regression the residuals showed variations below the μrad-level mainly due to imperfect correction or to meteorological noise. During a period when the water level was kept constant, the residuals showed a clear semidiurnal periodicity. A comparison with theoretical tidal tilt calculated for the geographical coordinates (46,34°N, 9.6°E) and the azimuth of the tiltmeter (NS) proves clearly (Fig.2) that tidal tilts have been resolved.
One of the greatest advantages of the new tiltmeter is a system of magnetic valves that can be switched by remote control and by which different fluid systems can be connected one after the other to the two sides of the differen-

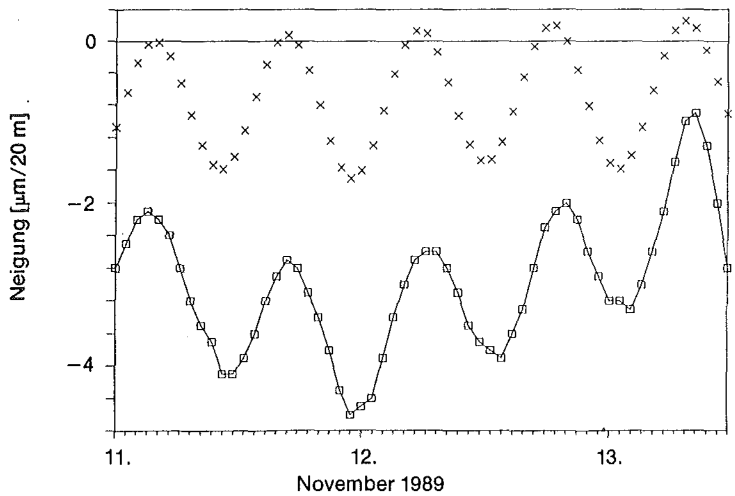

Figure 2: Reproduction from MEIER (1990): Solid line represents measured tilt residuals, crosses represent theoretical tidal tilt (units correspond to 0.05μrad).

tial pressure transducer without any transport or loss of liquid. This offers a possiblity for the control and correction of the zero drift of the transducer which is known (EMTER et al., 1989) to give the biggest contribution to the instability of the complete tiltmeter. A sketch of the different configurations of this system is given in Fig.3. In configuration 1 one endvessel of the tiltmeter AB can be connected to both sides of the transducer to measure its zero point. In configuration 2 the normal measurement is performed which can be repeated in configuration 3 by reversing the two arms of the tiltmeter. The average of the measurements in configurations 2 and 3 should again give the zero position of the transducer and coincide with the value from configuration 1. If a second pot-and-tube system CD with the same dimensions is installed which is equalized all the time by an open pipe, measurements in configurations 4 and 5 allow an additional control of the tiltmeter stability including evaporation and temperature effects. Configuration 6 of the valve system is free for adding a second tiltmeter e.g. in perpendicular direction or with a longer baseline for redundancy.
An example of a sequence of measurements with different configurations is given in Fig.4 as a function of time. It can be seen that the value of

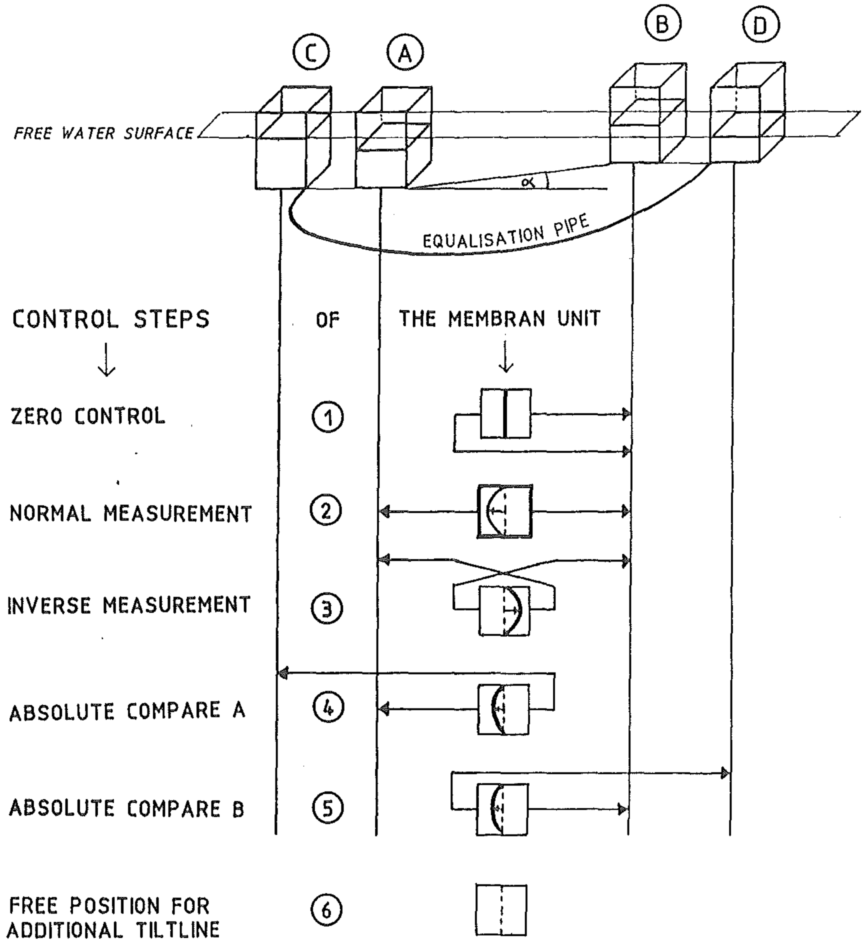

Figure 3: Schematic sketch of the different measuring configurations with the magnetic valve system. Description see text.

configuration 1 is exactly the average of those of configurations 2 and 3. Furthermore, the fast response of the system is demonstrated; the time constant of the Albigna tiltmeter is about 6 s, the damping is aperiodic. Time constant and damping can be adjusted within a certain range for a given tube length by the choice of the tube diameter (see EMTER et al., 1989). Aperiodic damping without overshooting may provide the best performance.

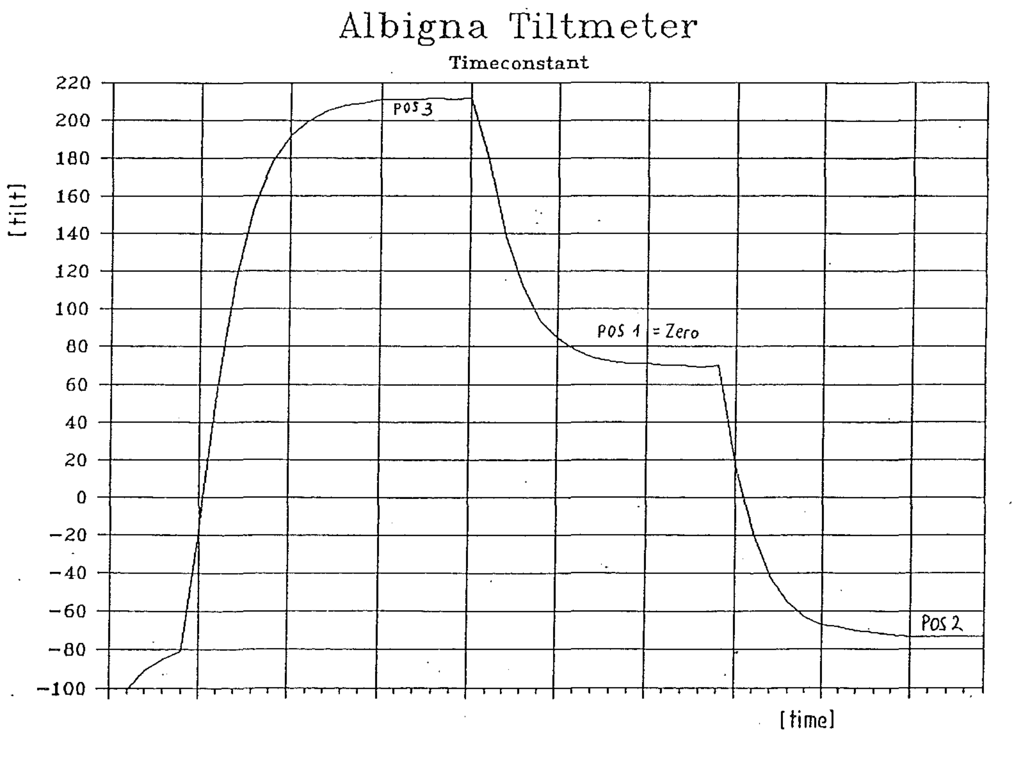

Figure 4: Sequence of measurements in different configurations of the valve system (vertical units correspond to 0.05μrad, units of the time scale are 2 s).

3 Conclusions

Any representative measurement of ground tilt is the better the longer the baseline of a tiltmeter is. This could recently be demonstrated for the case of tidal tilt by comparison of the results obtained with short- and long-baseline tiltmeters at one and the same site (EMTER et.al., 1989). In this context it should be kept in mind that the first high quality measurements of tidal tilt have been performed with a long-baseline instrument (MICHELSON, 1914). These findings can be transfered to volcanic tilts as they undergo the same small-scale elastic perturbations as tidal tilts. A tiltmeter for the quantitative measurements of tilts related to volcanic activities should therefore have a baseline as long as the local circumstances allow. The differential fluid pressure tiltmeter after HORSFALL (1977) will be a very promising alternative but a version for field measurements in remote areas has to be built. A similar system developed in Switzerland (MEIER, 1990) seems to fullfill the minimum requirements as it has shown tidal sensitivity and a good long-term performance. The zero control by the valve system offers the possibility to use even transducers which are not as stable as the one used in the Albigna tiltmeter. This might be necessary as not all transducers of the same manufacturer and the same type have the same stability. This showed up when a second transducer of the same type was tested in the BFO and showed higher noise and stronger drift. The reasons are not yet clear, as the transducer fullfills the engineering specifications. There remain different possibilities for the future. The first will be to select low-noise and low-drift transducers out of a greater number of serial transducers, this will be expensive or demand the cooperation of the manufacturer. The second will be to find and to exchange noisy electronic parts which will be elaborate, and the third will be to rely on the valve system for zero correction. In any way, more and especially more long-term tests will have to be performed before those tiltmeters can be used for reliable field measurements.

Acknowledgements

We thank H. Otto and W. Großmann for technical support during the installation and testing of tiltmeters in the BFO. H.G. Wenzel and W. Zürn critically read the text. All this is gratefully acknowledged.

References

EATON, J.P., 1959: A portable water-tube tiltmeter. Bull Seismol.Soc.Am., **49**, 301-306.

EMTER, D.; ZÜRN, W.; MÄLZER, H., 1989: Underground measurements at tidal sensitivity with a long baseline differential fluid pressure tiltmeter. Dt.Geod.Komm., Reihe B, **288**, 74 p.

HAGIWARA, T., 1949: Observations of changes in the inclination of the earth's surface at Mt.Tsukuba. Bull.Earthqu.Res.Inst., Univ.Tokyo, **25**, 27-32.

HARRISON, J.C., 1976: Cavity and topographic effects in tilt and strain measurements. J.Geophys.Res., **81**, 319-328.

HORSFALL, J.A.C., 1977: A new geophysical tiltmeter. PhD thesis, Cambridge University, 156 p.

HORSFALL, J.A.C.; KING, G.C.P., 1978: A new geophysical tiltmeter. Nature, **274**, 675-676.

JAGGAR, T.A.; FINCH, R.H., 1927: Tilt records for thirteen years at the Hawaiian volcano. Bull.Seismol.Soc.Am., **19**, 38-51.

KAMO, K.; ISHIHARA, K., 1989: A preliminary experiment on automatic judgement of the stages of eruptive activity using tiltmeter records at Sakurajima, Japan. In: IAVCEI Proceedings in Volcanology 1, Volcanic Hazards (Ed. J.H.Latter), pp. 585-598, Springer Berlin-Heidelberg.

KLEIN, F.W., 1984: Eruption forecasting at Kilauea Volcano, Hawaii. J.Geophys. Res., **89**, 3059-3073.

MEIER, E., 1990: Ein Neigungsmesser. Wasser, Energie, Luft, **1/2**, pp. 26-30, Verbandszeitschrift Schweizerischer Wasserwirtschaftsverband, Baden (Schweiz).

MICHELSON, A.A., 1914: Preliminary results of measurements of the rigidity of the earth. Astrophys.J., **39**, 105-138.

MINAKAMI, T., 1942: On volcanic activities and tilting of the earth's surface. Bull.Earthqu. Res.Inst., Univ.Tokyo, **20**, 431-504.

SWANSON, D.A.; CASADEVALL, T.J.; DZURISIN, D.; HOLCOMB, R.T.; NEWSHALL, C.G.; MALONE, S.D.; WEAVER, C.S., 1985: Forecasts and predictions of eruptive activity at Mt.St.Helens, USA. J.Geodyn., **3**, 397-423.

ZÜRN, W.; EMTER, D.; HEIL, E.; NEUBERG, J.; GRÜNINGER, W., 1986: Comparison of short and long baseline tidal tilts. In: Proc. 1Oth Int.Symp.Earth Tides (Ed. R.Vieira), pp.61-69, Cons.Sup.Inv. Cient.Madrid.

previously published in this series

Climatic Zones and Rural Housing in India
Editors: N.K. Bansal, G. Minke
GERMAN-INDIAN COOPERATION
ISBN 3-89336-008-5

Titanium Nitride Coatings
Preparations, Characteristics and Applications
S. Marinković, Z. Marinković and H. Kötter
GERMAN-YUGOSLAV COOPERATION
ISBN 3-89336-010-7

The Nappe Structure of the North Sporades in Greece
The Glossa Unit of Skopelos
V. Jacobshagen and D. Matarangas
GERMAN–GREEK COOPERATION
ISBN 3-89336-015-8

Impact of Green on the Urban Atmosphere in Athens
M. Horbert, A. Kirchgeorg, A. Chronopoulou-Sereli, J. Chronopoulous
GERMAN-GREEK COOPERATION
ISBN 3-89336-016-6

Development and Improvement of Identification Methods for Time Varying and Nonlinear Industrial Processes
Bilateral Cooperation between Technische Hochschule Darmstadt and Univerza "Edvarda Kardelja" Ljubljana
GERMAN-YUGOSLAV COOPERATION
ISBN 3-89336-022-0

Digital Adaptive Control
edited by: K. Schwamberger, A. Schumann and D. Matko, B. Zupanćić
GERMAN-YUGOSLAV COOPERATION
ISBN 3-89336-021-2

Boron Nitride Coatings
Preparation, Characteristics and Applications
S. Marinković and Z. Marinković with collaboration of H. Kötter and Ch. Meixner
GERMAN-YUGOSLAV COOPERATION
ISBN 3-89336-024-7

A Test Method for Solar Water Heaters Characterisation
by M. Bosanac
GERMAN-YUGOSLAV COOPERATION
ISBN 3-89336-032-8

Selected Studies of Adsorption on Metal and Semiconductor Surfaces
by B. Gumhalter, M. Milun and K. Wandelt
GERMAN-YUGOSLAV COOPERATION
ISBN 3-89336-034-4

Osnovi nauke o materijalima (neue Werkstoffe)
by G. Ondracek and I. Stamenković
GERMAN-YUGOSLAV COOPERATION
ISBN 3-89336-036-0

Scientific Series of the International Bureau

1 Fundamentos do Método de Correntes Parasitas
S. Stegemann (1990)

2 Diamond and Diamondlike Coatings
S. Marinković and Z. Marinković with S. Krawcynski (1990)

3 Environmental Research in Acquatic Systems
M. Branica (1990)

4 Volcanic Tremor and Magma Flow
edited by R. Schick and R. Mugiono (1991)

ISBN 3-89336-058-1